UNIVERSITY OF COPENHAGEN

FACULTY OF SCIENCE

PhD Thesis

Vanessa Rück

DNA-stabilized Silver Nanoclusters

From Photophysical Characterization to Bioimaging Applications

Name of department: Department of Chemistry and Nano-Science Center

Author: Vanessa Rück

Title and subtitle: DNA-stabilized Silver Nanoclusters

From Photophysical Characterization to Bioimaging Applications

Supervisor: Professor Tom Vosch

Submitted on: 31. August 2024

This thesis was submitted to the PhD School of the Faculty of Science in partial fulfillment of the academic degree of PhD. Following the submission, an oral defense will take place.

Preface

The work presented in this thesis was obtained during the period from 1st September 2021 to 31st August 2024 under the supervision of Professor Tom Vosch at the Department of Chemistry and Nano-Science Center at the University of Copenhagen, Denmark.

This thesis is a synopsis based on four selected peer-reviewed articles published during the three-year PhD enrolment. The selected published articles are included in the appendix, while a brief but informative introduction to the thematic background relevant to the publications is given in several chapters. The order in this thesis does not correspond to the chronological order in which the projects were carried out or published.

As part of the PhD program, I completed a research stay from February to April 2024 in the group of Associate Professor Stacy Copp at the University of California Irvine, USA. During my time abroad, I worked on several projects, including the high-throughput screening of DNA-AgNCs and the investigation of dual-emitting DNA-AgNCs with emission in the NIR range. These projects are still ongoing and are not included in this thesis.

Acknowledgment

First of all, I would like to thank Tom Vosch for giving me the opportunity to do my PhD in his group and for his great support. You gave me a lot of freedom to implement ideas and caught me when I got lost in my perfectionism. In addition to scientific skills, you also taught me to take things a little easier and to stay positive. I have learned a lot during these exciting years.

I would also like to thank the whole group for the friendly, cheerful, and helpful working atmosphere and the support I received in the different phases of my PhD time. My special thanks go to Cecilia Cerretani for her wonderful mentoring. I really enjoyed the close collaboration, we went through many ups and downs together and it was great to share the fascination and enthusiasm for DNA-stabilized silver nanoclusters with you. Moreover, I would like to thank Mikkel B. Liisberg for the always helpful exchange on data and his support, especially during the writing of my thesis. Thank you for always being willing to try out all sorts of ideas with me on our home-built microscope.

I would also like to thank our collaborator Stacy Copp for allowing me to work in her lab at the University of California Irvine. It was a great experience and I enjoyed it very much. A big thank you also goes to Anna Gonzàlez-Rosell and Rweetuparna Guha for making my time in the US unforgettable.

Furthermore, I would like to thank the people from the BWL and TJS groups for the fantastic evenings over a few beers and pizzas. I will never forget the wonderful time we spent together. My special thanks go to Rasmus K. Jakobsen and Stine G. Stenspil. Thank you for always having an open door for me and for your help and advice. I would also like to thank the HGK Group for the always fun lunch breaks and for welcoming me into their running team for the DHL relay.

Last but not least, I would like to thank my family, my boyfriend, and my friends. Thank you for always encouraging and supporting me. With your support, I have been able to surpass myself over the past few years. Thank you for the countless phone calls that have brightened up my days. Thank you for always having my back. I am so grateful that your love and our bond of friendship are stronger than the geographical distance between us. I love you all so much.

- Vanessa

Abstract

DNA-stabilized silver nanoclusters (DNA-AgNCs) are fascinating emitters comprised of a few silver atoms that are stabilized by one or more DNA oligomers. Their emission tunability from the visible to near-infrared (NIR) range, high quantum yields, photostability, and biocompatibility make this class of emitters highly attractive. To promote DNA-AgNCs for applications, a fundamental understanding of their formation, structure, and properties is essential. My work in this research field included fundamental investigations of structural and spectroscopic properties as well as application-oriented studies.

Unraveling the correlation of the photophysical properties with the structure of the cluster is crucial for the prediction of DNA-AgNCs with tailored properties. However, only a few crystal structures are currently known, as obtaining high-quality crystals of DNA-AgNCs is challenging. My structure elucidation attempts resulted in a partially solved structure of a green-emitting DNA-AgNC. Unfortunately, the encapsulating DNA structure remained unresolved, but the arrangement of the silver atoms in the cluster core was determined. Despite the missing information on the structural arrangement of the DNA, the cluster core already provides valuable insights into the structure-property relationships.

Due to the advantages of the NIR transparency window, the discovery of DNA-AgNCs in this spectral region is of great interest. I have explored the fundamentals of a NIR-emitting DNA-AgNC with outstanding and unusual properties. The cluster shows a dual emissive behavior which can be used as a light intensity meter on the nanoscale.

DNA-AgNCs are promising candidates for biological applications. The success of their implementation depends on the controlled and targeted conjugation. I investigated the rational conjugation using copper-free click chemistry. The key to ensure this rational conjugation strategy is a solved crystal structure. The NIR-emitting DNA-Ag$_{16}$NC with a known structure was successfully linked to three different peptides and a small protein. The spectroscopic properties of the cluster remained unchanged and bioimaging studies demonstrated the large potential for biological applications.

Dansk resumé

DNA-stabiliserede sølvnanoklynger (DNA-AgNC'er) er fascinerende fluoroforer, der består af nogle få sølvatomer, som er stabiliseret af en eller flere DNA strenge. Deres emission kan tunes fra det synlige til det nær infrarøde (NIR) område, høje kvanteudbytter, fotostabilitet og biokompatibilitet gør denne klasse af fluoroforer meget attraktiv. For at fremme anvendelsen af DNA-AgNC'er er det vigtigt med en grundlæggende forståelse af deres dannelse, struktur, og egenskaber. Mit arbejde inden for dette forskningsfelt omfattede grundlæggende undersøgelser af strukturelle og spektroskopiske egenskaber samt anvendelsesorienterede studier.

Afdækning af sammenhængen mellem klyngens fotofysiske egenskaber og struktur er afgørende for at kunne designe DNA-AgNC'er med skræddersyede egenskaber. Der kendes dog kun få krystalstrukturer i øjeblikket, da det er en udfordring at få DNA-AgNC krystaller af høj kvalitet. Mine forsøg på at opklare strukturen af en grønt-emitterende DNA-AgNC resulterede i en delvist løst krystal struktur. Desværre forblev strukturen af den indkapslende DNA uopklaret, men strukturen af sølvatomerne i klyngen blev bestemt. På trods af de manglende oplysninger om det strukturelle arrangement af DNA, giver klyngekernen allerede værdifuld indsigt i forholdet mellem struktur og egenskaber.

På grund af fordelene ved NIR-transparensvinduet har opdagelsen af DNA-AgNC'er i dette spektralområde stor interesse. Jeg har udforsket de grundlæggende egenskaber for en NIR-emitterende DNA-AgNC, som er både enestående og usædvanlige. Klyngen viser en dobbelt emitterende adfærd, som kan bruges som en lysintensitetsmåler på nanoskala.

DNA-AgNC'er er lovende kandidater til biologiske anvendelser. Deres succesfulde implementering afhænger af at kunne konjugere klyngerne kontrolleret til specifikke mål. Jeg undersøgte en rationel konjugationsstrategi ved hjælp af kobberfri klik-kemi. Nøglen til at kunne benytte denne rationelle konjugationsstrategi er en løst krystalstruktur. Den NIR-emitterende DNA-Ag$_{16}$NC, med en kendt struktur, blev succesfuldt koblet til tre forskellige peptider og et lille protein. Klyngens spektroskopiske egenskaber forblev uændrede, og fluorescens mikroskopi af celler viste potentialet for deres biologiske anvendelser.

List of abbreviations

A	adenine
$AgNO_3$	silver nitrate
BCN	bicyclononyne
C	cytosine
CHO	Chinese hamster ovary
CuAAC	copper-catalyzed azide-alkyne cycloaddition
DFT	density functional theory
DNA	deoxyribonucleic acid
DNA-AgNC	DNA-stabilized silver nanocluster
D_2O	deuterium oxide
ESI	electrospray ionization
FC	Franck-Condon
FCS	fluorescence correlation spectroscopy
FLIM	fluorescence lifetime imaging microscopy
G	guanine
HPLC	high-performance liquid chromatography
hIR-B	human insulin receptor B
H_2O	water
IRF	instrument response function
MeOH	methanol
microED	microcrystal electron diffraction
ML	machine learning
MOPS	3-(N-morpholino)propanesulfonic acid

MPD	2-methyl-2,4-pentanediol
MS	mass spectrometry
m/z	mass-to-charge ratio
$NaBH_4$	sodium borohydride
NH_4OAc	ammonium acetate
NIR	near-infrared
OADF	optical activated delayed fluorescence
PEG	polyethylene glycol
QY	quantum yield
SC-XRD	single crystal X-ray diffraction
SPAAC	strain-promoted azide-alkyne cycloaddition
T	thymine
TADF	thermally activated delayed fluorescence
TCSPC	time-correlated single photon counting
TEAA	triethylammonium acetate
TOF	time-of-flight
TRES	time-resolved emission spectra
UV	ultraviolet
UV-vis	ultraviolet-visible
WC	Watson-Crick

List of Publications

<u>Included in thesis:</u>

1. **Vanessa Rück**, Vlad A. Neacşu, Mikkel B. Liisberg, Christian B. Mollerup, Park Hee Ju, Tom Vosch, Jiro Kondo, Cecilia Cerretani. Atomic Structure of a DNA-Stabilized Ag_{11} Nanocluster with Four Valence Electrons.
    Adv. Optical Mater. **2024**, *12* (7), 2301928. DOI: 10.1002/adom.202301928.

2. **Vanessa Rück**, Mikkel B. Liisberg, Christian Brinch Mollerup, Yanmei He, Junsheng Chen, Cecilia Cerretani, Tom Vosch. A DNA-Stabilized Ag_{18}^{12+} Cluster with Excitation-Intensity-Dependent Dual Emission.
    Angew. Chem. Int. Ed. **2023**, *62* (39), e20230976. DOI: 10.1002/ange.202309760.

3. **Vanessa Rück**, Narendra K. Mishra, Kasper K. Sørensen, Mikkel B. Liisberg, Ane B. Sloth, Cecilia Cerretani, Christian B. Mollerup, Andreas Kjaer, Chenguang Lou, Knud J. Jensen, Tom Vosch. Bioconjugation of a Near-Infrared DNA-Stabilized Silver Nanocluster to Peptides and Human Insulin by Copper-Free Click Chemistry.
    J. Am. Chem. Soc. **2023**, *145* (30), 16771-16777. DOI: 10.1021/jacs.3c04768.

4. **Vanessa Rück**, Cecilia Cerretani, Tom Vosch. How Inert is Single-Stranded DNA Towards DNA-Stabilized Silver Nanoclusters? A Case Study.
    ChemPhotoChem **2024**, e202400014. DOI: 10.1002/cptc.202400014.

<u>Not included in thesis:</u>

-   Giacomo Romolini, Cecilia Cerretani, **Vanessa Rück**, Mikkel B. Liisberg, Christian Mollerup, Tom Vosch. Analytical method for the determination of the absorption coefficient of DNA-stabilized silver nanoclusters.
    Nanoscale **2024**, *16* (26), 12559-12566. DOI: 10.1039/D4NR01765J.

-   Mikkel B. Liisberg, **Vanessa Rück**, Giacomo Romolini, Cecilia Cerretani, Tom Vosch, Hydration Sensitive Orthogonal Dual Emission of a DNA-Stabilized Silver Nanocluster.
    Adv. Optical Mater. **2024**, *12* (19), 2400345. DOI: 10.1002/adom.202400345.

- Mikkel B. Liisberg, **Vanessa Rück**, Tom Vosch. Time gated Fourier transform spectroscopy with burst excitation for time-resolved spectral maps from the nano- to millisecond range.
Chem. Commun. **2023**, *59* (84), 12625-12628. DOI: 10.1039/D3CC03961G.

- Cecilia Cerretani, Mikkel B. Liisberg, **Vanessa Rück**, Jiro Kondo, Tom Vosch. The effect of inosine on the spectroscopic properties and crystal structure of a NIR-emitting DNA-stabilized silver nanocluster.
Nanoscale Adv. **2022**, *4* (15), 3212-3217. DOI: 10.1039/D2NA00325B.

- Anna Gonzàlez-Rosell, Rweetuparna Guha, Cecilia Cerretani, **Vanessa Rück**, Mikkel B. Liisberg, Benjamin B. Katz, Tom Vosch, Stacy M. Copp. DNA Stabilizes Eight-Electron Superatom Silver Nanoclusters with Broadband Downconversion and Microsecond-Lived Luminescence.
J. Phys. Chem. Lett. **2022**, *13* (35), 8305-8311. DOI: 10.1021/acs.jpclett.2c02207.

Table of contents

1 Introduction

1.1 What are DNA-AgNCs?

DNA-stabilized silver nanoclusters (DNA-AgNCs) are exceptional emitters that were first introduced by Petty et al. in 2004.[1] This special type of ligand-stabilized metal nanoclusters consists of a limited number of silver atoms and cations, usually 2-30, stabilized by one or more DNA strands.[2] DNA-AgNCs are characterized by tunable emission from the visible to near-infrared (NIR) region, often with high fluorescence quantum yields,[3,4] large Stokes shifts,[5] and high chemical stability and photostability.[6]

In the metal nanocluster, the metal atoms are kept together by metal-metal and metallophilic interactions. The small size of nanoclusters leads to attractive optical and electronic properties. The electronic structure of metal clusters is characterized by discrete energy levels, in contrast to the continuous electronic bands observed in the bulk structure (Figure 1).[7,8] This distinction explains why DNA-AgNCs exhibit molecular-like behavior. Additionally, other metal clusters composed of gold (Au), copper (Cu), platinum (Pt), and palladium (Pd), to name a few, are known.[8] However, silver is particularly interesting due to its ability to form bright fluorescent nanoclusters, its nontoxicity,[2] and its lower cost than gold and platinum.
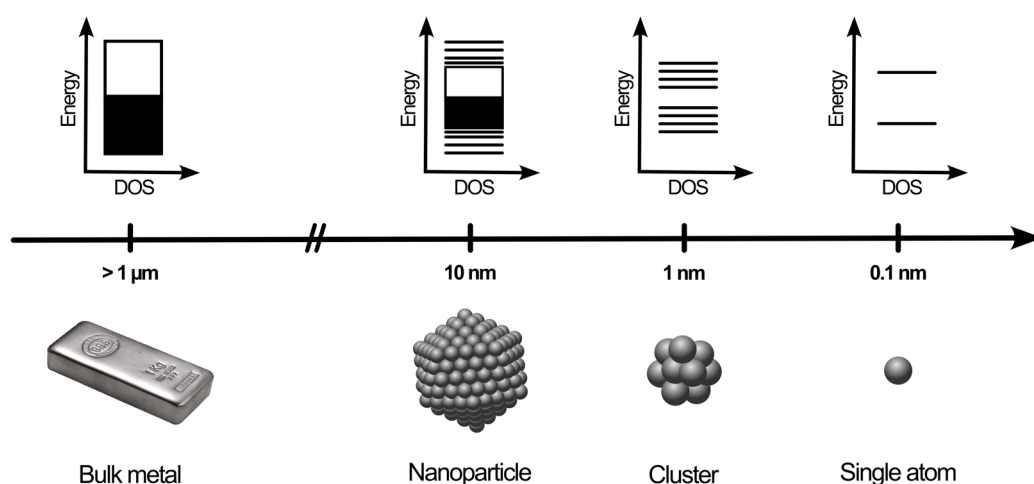
Figure 1: *Energy level diagrams for different sizes of metal – from bulk to single atom. Due to the limited number of metal atoms, discrete energy levels are formed. Nanoclusters therefore behave molecule-like.*

In solution, metal clusters tend to agglomerate, forming larger particles to reduce the surface energy. To avoid this type of aggregation, ligands are required,[9] such as thiols,[10] peptides,[11] and dendrimers.[12] In DNA-AgNCs, the silver cluster is stabilized by a DNA scaffold leading to atomically precise clusters. The special feature of this ligand shell is that it is biocompatible, chemically functionalizable, and water-soluble, which makes it particularly interesting for biological applications.[2]

Furthermore, the use of a DNA scaffold offers programmability, since the DNA sequence determines the properties of the cluster. Based on the four natural nucleobases adenine (A), thymine (T), guanine (G), and cytosine (C), a wide range of combinations are possible.[2] The nucleobases can undergo numerous interactions via the endo- and exocyclic groups (Figure 2). The best-known interaction is the Watson-Crick (WC) base pairing. Hydrogen bonds are formed between A and T and between C and G, leading to the antiparallel double helix structure. Due to this specificity, complex nanostructures such as DNA origami can be formed.[13]
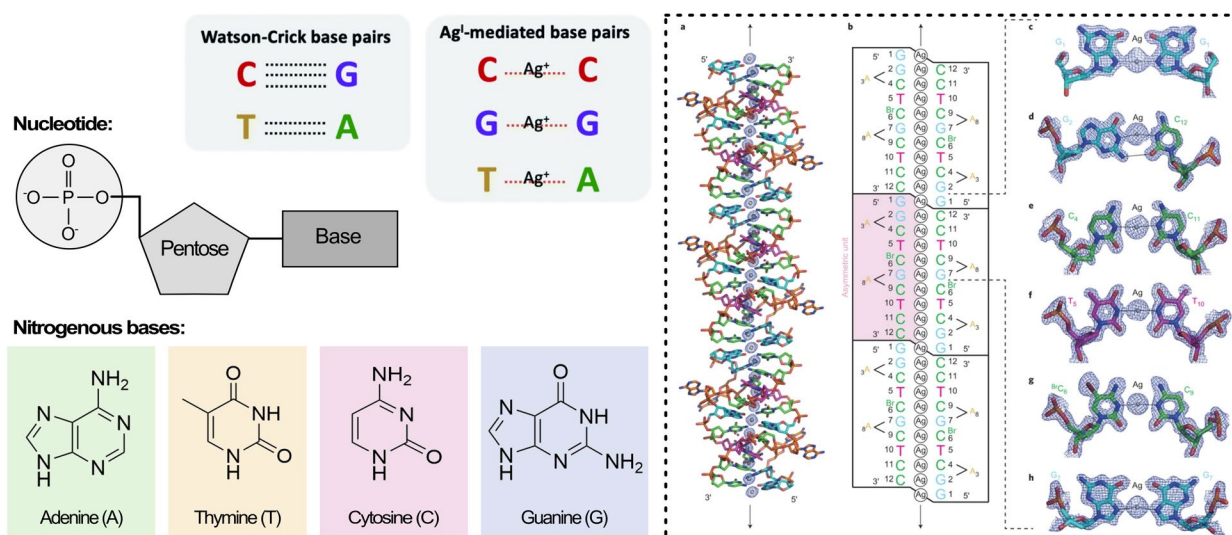
Figure 2: *Schematic representation of nucleotide with nitrogenous bases: Adenine, Thymine, Cytosine, and Guanine. On top illustration of Watson-Crick base pairs and Ag-mediated base pairs, reproduced from Ref.[2] with permission from the Royal Society of Chemistry. Dashed box shows the structure of the metallo-DNA nanowire published by Kondo et al.[14] Reproduced from Ref.[14] with permission from Springer Nature.*

Silver cations (Ag+) form coordinative bonds with the nucleobases and thus compete with WC base pairing. There have been several reports on silver-mediated base pairs.[15-18] It has been observed that the different bases have different affinities for Ag+. The Ag cations interact strongly with cytosine and form highly stable C–Ag+–C base pairs. These C–C mismatches have been observed in double stranded DNA duplexes,[16] whose strand orientation can also be reversed.[17] Guanine also has a strong affinity

for silver, while adenine and thymine have a weaker affinity.[18] The high stability of the planar Ag^+-mediated C–C and G–G homoduplex pairs was confirmed by theoretical calculations.[18] Increased stability was also found for the non-planar heterogeneous pair A–Ag^+–T, which is due to the size difference and stacking behavior of adenine. The X-ray crystal structure of a metallo-DNA nanowire consisting of mixed-base dodecamer duplexes showed G–Ag^+–G, G–Ag^+–C, and T–Ag^+–T base pairing in addition to the C–Ag^+–C,[14] see Figure 2 (dashed box). The metal-mediated base interaction forms an uninterrupted one-dimensional silver ion strand along the DNA helix axis, in which the silver cations interact with each other through argentophilic interactions. Guanine is deprotonated here, which is unusual since it should be protonated at physiological pH.[14]

By screening a large number of DNA sequences, a correlation was found between cluster size and resulting photophysical properties,[2,19,20] see Figure 3. The larger the silver nanocluster, the further it emits in the NIR range. The color of the DNA-AgNCs is determined by the number of reduced silver atoms and not by the total number.[20] The total number includes the neutral (N_0) and cationic (N_+) silver atoms. The composition can be determined by mass spectrometry.[3]
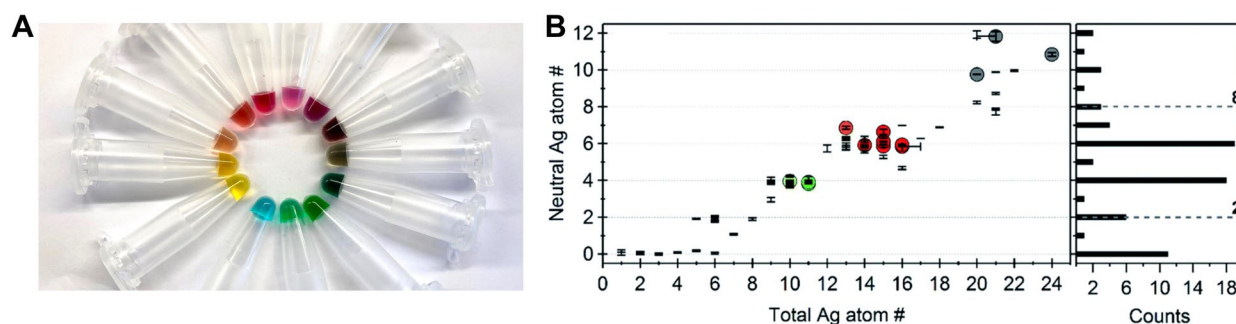
Figure 3: (A) Different DNA-AgNC solutions showing various colors. (B) The number of neutral silver atoms (N_0) plotted against the total number of silver atoms (N_{tot}) of the DNA-AgNCs. The number of reduced silver atoms determines the emission color, bright fluorescent DNA-AgNCs are shown as colored dots. The histogram of the N_0 values shows an increased number of clusters with even N_0, the spherical magic numbers 2 and 8 are less abundant. Reproduced from Ref.[2] with permission from the Royal Society of Chemistry.

A rod-like arrangement of silver atoms encapsulated in DNA oligomers has been proposed by Gwinn et al.,[3] which thus deviates from a spherical cluster geometry. It was shown that a number of neutral silver atoms is dominant: N_0= 4 and 6 for green and red emitters, respectively, and N_0= 10-12 for larger NIR-emitting DNA-AgNCs.[20] These "magic numbers" of neutral silver atoms support the assumption of a rod-like shape and deviate from the magic numbers 2 and 8 normally observed for spherical metal clusters. A "magic color" and thus the fluorescence wavelength can be derived from the magic number of reduced silver atoms.[20]

So far, it is not possible to reliably predict the properties of DNA-AgNCs based on the DNA sequence. It remains a major challenge to decode the relationship between DNA sequence and photophysical properties in order to develop targeted clusters with desired properties. The development of NIR-emitting DNA-AgNCs is of particular interest.

The NIR range ($\approx$ 700-1700 nm)[21] has attracted increasing attention in recent years due to its good light transparency and low autofluorescence compared to the visible range.[22-24] However, there are only a limited number of bright emitters in this range.[25-27] Single-molecule studies have already demonstrated the potential of DNA-AgNCs as suitable NIR fluorophores,[6,28,29] but the number of purified NIR-emitting clusters is still low.

Large-scale high-throughput screening is performed to promote the discovery of NIR-emitting DNA-AgNCs. Copp et al. combine high-throughput experiments with machine learning (ML) to classify DNA sequences based on emission color.[19] The possible combinations are 4^L, where 4 is the number of nucleobases, excluding artificial nucleobases, and L is the length of the sequence. This variety of combinations makes ML attractive to identify patterns and thus elucidate structure-property relationships. In red emitters, for example, "GC" was discovered as a common motif in the sequence.[19] With this and other detected motifs, the machine learning model was trained and further developed. With the help of robot-assisted synthesis and fast parallel fluorimetry in plate readers, a large data set of different DNA sequences correlated with the fluorescence spectra could be created.[19,30] Figure 4 represents the proposed approach to identify DNA sequences for the NIR region.[31]
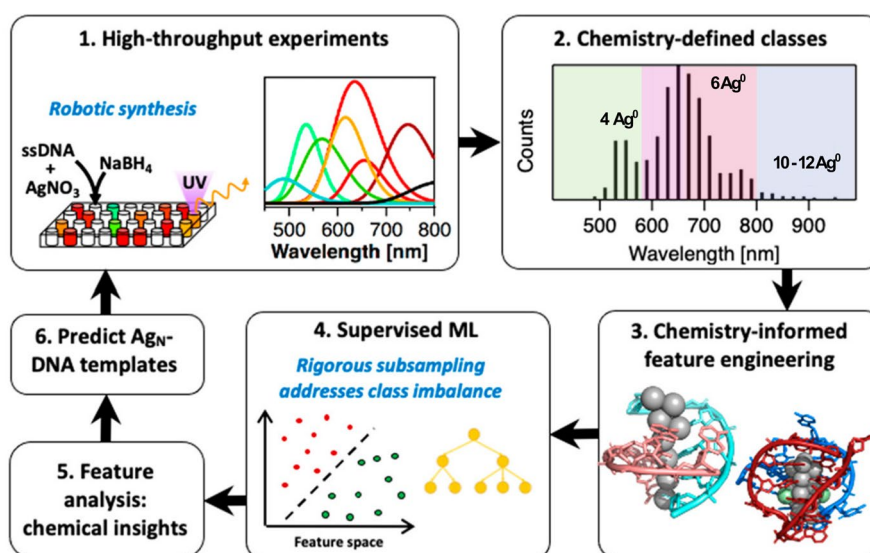
Figure 4: *Schematic representation of ML-supported high-throughput experiment. Adapted from Ref.[31] with permission from the American Chemical Society, Copyright 2022.*

1.2 Motivation

As a biocompatible alternative to organic fluorophores and quantum dots, DNA-AgNCs have several promising properties for various applications. DNA-AgNCs are particularly interesting as sensors and imaging agents due to their brightness, photostability and wavelength tunability.[2] Especially in the NIR range, DNA-AgNCs could play an important role in future biological applications.

To further promote the use of DNA-AgNCs in biological applications, it is important to understand the fundamentals that determine their formation, stability, structure, and optical characteristics.[32] Structure and photophysical properties are correlated. However, how exactly the DNA sequence encodes the properties is not yet fully understood. In order to develop DNA-AgNCs with specific properties such as wavelength, quantum yield, and photostability, it is important to understand this relation.

Elucidating the structure of DNA-AgNCs is key in this regard. So far, the structure of the vast majority of reported DNA-AgNCs are unresolved, with only a very few exceptions.[33-36] A major obstacle is to obtain high-quality crystals. Furthermore, the photophysical mechanisms that control the luminescence of DNA-AgNCs are complex and diverse and only partially understood.[2] In order to unravel this, intensive spectroscopic investigations combined with crystal structure determination are necessary.

It is also important for biological applications to be able to conjugate DNA-AgNCs in a controlled manner. The stabilizing DNA scaffold of DNA-AgNCs can serve as a tool to functionalize them by adding additional groups to the DNA strand or by using the DNA itself. However, the conjugation of purified DNA-AgNCs is not yet well understood. In order to exploit the potential of DNA-AgNCs for life science applications, it is important to develop and investigate further functionalization approaches.

DNA-AgNCs are fascinating emitters. However, there are still numerous scientific challenges that need to be fully elucidated to promote their application in biological systems. Motivated by these aspects, I worked on various projects to improve the fundamental understanding of DNA-AgNCs and to explore conjugation possibilities for bioimaging applications.

2 Workflow of DNA-AgNC Characterization

Different DNA sequences lead to diverse emitters from the visible to the NIR range.[2] To find promising candidates with intriguing properties it is necessary to carry out screening procedures. In this chapter, I will describe the main aspects of the workflow in our research group with a brief theoretical background. An overview of our workflow is shown in Figure 5. The workflow includes the synthesis and purification of the DNA-AgNCs, followed by the spectroscopic and compositional characterization of the purified clusters, as well as the attempt to crystallize the clusters.
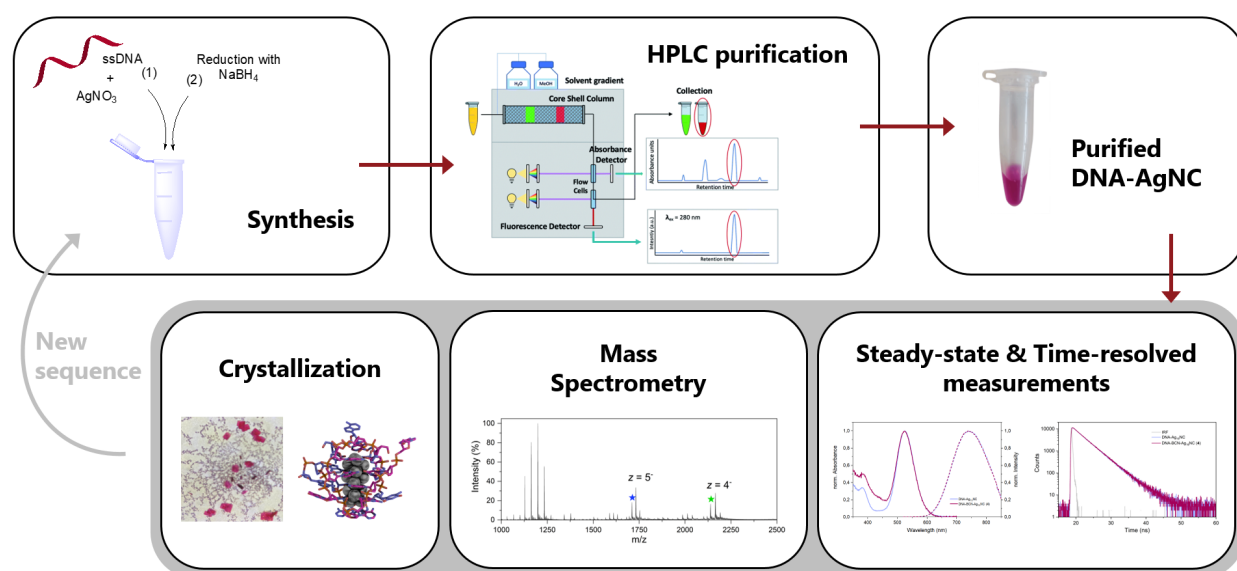
Figure 5: *Overview of our workflow to find promising DNA-AgNCs. The crystallization part can be found in Chapter 3. Adapted from Ref.[2] with permission from the Royal Society of Chemistry. Adapted with permission from Ref.[37] Copyright 2023 American Chemical Society. Adapted with permission from Ref.[34] Copyright 2019 Wiley.*

2.1 Synthesis

The synthesis of DNA-stabilized silver nanoclusters is a one-pot reaction with only two steps. First, hydrated single-stranded oligomers are mixed with silver nitrate ($AgNO_3$) in an aqueous solution containing 10 mM ammonium acetate (NH_4OAc) at neutral pH. After 15 minutes of incubation at room temperature, freshly prepared sodium borohydride ($NaBH_4$) is added to reduce the silver cations. The cluster formation occurs over time while the sample is typically stored at 4 °C.

The stoichiometry between DNA and AgNO$_3$ influences the cluster formation and varies for each nanocluster, depending on the DNA sequence. To determine the optimal ratios, a concentration screening is performed.[38] The first parameter tested is the concentration of AgNO$_3$. For the so-called silver sweep, the concentration of the DNA is kept constant and the ratio of silver nitrate is changed. Typically, the DNA/AgNO$_3$ ratio ranges from 5 to 15 equivalents of Ag$^+$ per DNA strand. Once the optimal AgNO$_3$ ratio is identified, the DNA concentration is adjusted. DNA concentrations are usually between 10-30 µM, and the NaBH$_4$ concentration is always half as high as that of AgNO$_3$. The absorption and fluorescence intensity are monitored over time for all samples to determine the best DNA/AgNO$_3$ ratio.

The formation of DNA-AgNCs is a self-assembly process and can take up to weeks, depending on the kinetics of the cluster formation.[38] This process also yields unwanted side products, including nanoparticles, free DNA, and a mixture of species with varying numbers of silver atoms and DNA-strands.[2] Consequently, purification is essential to isolate the desired DNA-AgNC.

2.2   High-performance Liquid Chromatography

The synthesis of the DNA-AgNC can lead to a highly heterogeneous mixture of products. Fluorescent silver clusters are typically present in low yield relative to the various side products, which makes purification of DNA-AgNCs crucial.[2,39] While DNA-AgNCs have been utilized in some applications without purification, purified samples are essential for a fundamental understanding of the structure and photophysical properties of DNA-AgNC. The most commonly employed purification technique for DNA-AgNCs is reversed-phase high-performance liquid chromatography (HPLC).

A preparative HPLC system from Agilent Technologies is used in our laboratory, which is set up with an Agilent Technologies 1100 Series UV-Vis detector, an Agilent Technologies 1260 infinity fluorescence detector, and a reversed-phase core-shell C18 column (Kinetex, 5 µm, 100 Å, 250 x 4.6 mm) from Phenomenex. The mobile phase is a gradient mixture of 35 mM triethylammonium acetate (TEAA) buffer in Milli-Q water and methanol. TEAA with a pH 7.0 is typically used as an ion-pairing agent to improve the separation. The flow rate is typically 1 mL/min to keep the pressure below the maximum value of 400 mbar.

The desorption of DNA-AgNC from the stationary phase depends on its composition and secondary structure,[32] thus the purification method is specific for each cluster. During purification, aliquots are passed through an absorbance and fluorescence detector. For the configuration of the detectors, absorbance and emission spectra of the unpurified sample are recorded. Typically, the absorption is

monitored at 260 nm for the DNA peak, around 420 nm for the nanoparticles, and one or more specific wavelengths for the DNA-AgNC. The fraction collection is based on the main absorbance peak and fluorescence band of the clusters. Subsequently, a 5-minute wash with 95% TEAA in MeOH is conducted to eliminate any residual sample from the column.

It should be noted that not all DNA-AgNCs survive the purification step and are stable under the applied purification conditions.[40] However, if the cluster has been successfully purified, the purified sample is usually stable for months to years. In our studies, we focus mainly on DNA-AgNCs that have been purified prior to characterization.

2.3   Spectroscopic Characterization

After purification, steady-state and time-resolved fluorescence measurements are carried out to determine the main photophysical properties. With the help of absorption and excitation spectra, the sample's purity can also be determined. I will go into the theoretical background briefly below, based on the textbook by Lakowicz.[41]

2.3.1   Phenomena of Fluorescence

DNA-AgNCs exhibit discrete energy levels that can be investigated using UV-Vis light to probe their electronic states. Absorption occurs when a molecule absorbs a photon, causing a transition from the ground state to an excited state. This process is instantaneous, typically occurring within sub-femtosecond timescales. The absorption can be quantified using the Beer-Lambert law:

$$A = log_{10} \left(\frac{I_0}{I} \right) = \varepsilon \cdot c \cdot l \qquad (1)$$

Where A is the absorbance of the sample, I_0 and I are the intensities of the incident and transmitted radiation, respectively, ε is the molar absorption coefficient, c is the concentration of the sample in solution, and l is the optical path length.

The molar absorption coefficient is the probability that a photon with a certain energy is absorbed by a fluorophore. It is a characteristic property of the fluorophore and is ideally in the range of 10^4-10^5 M^{-1}cm^{-1} indicating a strong light-absorbing ability.
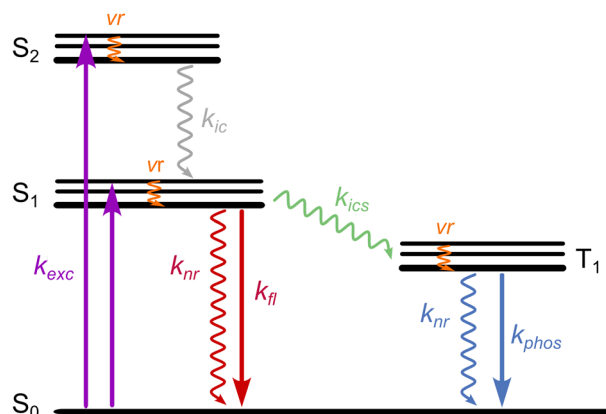
Figure 6: *A typical Jablonski diagram depicting possible processes occurring upon the absorption of a photon. S_0 singlet ground state, S_1 first excited state, S_2 second excited state, T_1 triplet state; k_{exc} excitation rate, k_{ic} internal conversion rate, k_{nr} non-radiative relaxation rate, k_{fl} fluorescence emission rate, k_{isc} intersystem crossing rate, k_{phos} phosphorescence emission rate and vr vibrational relaxation.*

When a photon is absorbed, a molecule is excited from the singlet ground state S_0 to a higher energy state S_n at a rate of k_{exc}. After excitation, the absorbed energy can be released through multiple competing photophysical processes, including both radiative and non-radiative processes. The different possibilities are illustrated in a Jablonski diagram, see Figure 6.

Non-radiative processes include vibrational relaxation, internal conversion, and intersystem crossing. Vibrational relaxation enables the excited molecule to rapidly ($< 10^{-12}$ s) release part of its excess energy by transitioning to the lowest vibrational level of the electronic excited state. Internal conversion is the transition between two electronic states with the same spin multiplicity, for example from S_2 to S_1. The energy gap between the states involved in the radiationless transition determines the rate (k_{ic}). Molecules can also transition between two electronic states with different spin multiplicity via intersystem crossing (k_{isc}). For example, a transition to the first triplet state T_1 can take place through spin inversion of the electron in the excited singlet state.

The molecule in the triplet state T_1 can be deactivated radiatively by phosphorescence, in which the molecule relaxes back to the S_0 state through a spin-forbidden transition ($k_{phos}= 10^{-3}$-10^2 s^{-1}). The other radiative transition back to S_0 occurs from the lowest vibrational level of the first electronic excited singlet state S_1. A photon with a lower energy than the incoming photon is emitted by the excited molecule, which thus returns to the ground state with the rate k_f and is called fluorescence. The transition between two states with the same spin multiplicity is in the order of 10^{-9} to 10^{-7} s. The energy difference between the absorption ($S_{0,v=0} \rightarrow S_{1,v=0}$) and emission ($S_{1,v=0} \rightarrow S_{0,v=0}$) is known as Stokes shift and results in a red shift of the fluorescence band compared to the absorption band.

Radiative decays compete with non-radiative paths for energy dissipation, so the emission of photons is only detectable if it is faster than the competing non-radiative process.

2.3.2 Quantum Yield

The fluorescence quantum yield (QY), along with the fluorescence lifetime, is a key characteristic of a fluorophore.[41] The QY describes the efficiency of the fluorescence process, defined by the number of emitted photons divided by the number of absorbed photons. This corresponds to the ratio between the emissive decay rate (k_f) and the same emissive pathway rate and all competing non-radiative decay rates (k_{nr}). The QY can be calculated using the following equation:

$$QY = \frac{number\ of\ emitted\ photons}{number\ of\ absorbed\ photons} = \frac{k_f}{k_f + k_{nr}} \qquad (2)$$

In comparison with a reference dye of known quantum yield, the fluorescence quantum yield of a fluorophore can be estimated. This relative method[42] can be described by:

$$QY_{Fluo} = \underbrace{\frac{F_{Fluo}}{f_{A,Fluo}}}_{slope_{Fluo}} \cdot \underbrace{\frac{f_{A,Ref}}{F_{Ref}}}_{slope_{Ref}^{-1}} \cdot \frac{n_{Fluo}^2}{n_{Ref}^2} \cdot QY_{Ref} \qquad (3)$$

Where QY represents the fluorescence quantum yield; F is the integrated emission spectrum; f_A is the fraction of absorbed light at the excitation wavelength, which is equal to $1-10^{-A}$ (A is the absorbance at λ_{exc}); and n the refractive index of the solvent. The subscripts *Fluo* and *Ref* refer to the investigated fluorophore (DNA-AgNCs in this thesis) and the reference compound, respectively.

To determine the QY, the integrated emission spectra (F) at different concentrations are plotted against the fraction of absorbed light (f_A) for both the reference dye and the investigated fluorophore. The data are then fitted with a linear function with a zero-intercept and the resulting slopes are used to calculate the quantum yield based on Equation (3).

2.3.3 The Fluorescence Lifetime

The fluorescence lifetime (τ) is another relevant feature of fluorophores,[41] which contains information about the properties and the local environment of the fluorophore. Since fluorescence is

a stochastic process, the fluorescence lifetime or decay time (τ) is the average time spent by a molecule in the excited state S_1 before returning to the ground state. It is defined as the inverse of the sum of the radiative and competing non-radiative decay rates:

$$\tau = \frac{1}{k_f + k_{nr}} \tag{4}$$

Therefore, the decay time is directly proportional to the fluorescence quantum yield:

$$\tau = \frac{QY}{k_f} \tag{5}$$

The fluorescence decay time can be determined by time-correlated single photon counting. By analyzing the decay, the fluorescence lifetime can be obtained. For a single emissive species characterized by a mono-exponential intensity decay, the decay time is equal to the time point at which the initial intensity has dropped to $1/e$ ($\approx 37\%$). In the case of multi-exponential decays, however, the determination of the fluorescence lifetime from the data is more complex. Several factors, such as the presence of a mixture of fluorophores with different lifetimes or the presence of multiple populations of the same fluorophore in different environments, can cause multi-exponential decay. The fluorescence decay can be fitted by the following multi-exponential function:

$$I(t) = \sum_{i=1}^{N} a_i \cdot e^{(-t/\tau_i)} \tag{6}$$

Where t is the time at which the fluorescence decay is measured, a_i is the amplitude/weighting factor of the i-th component and τ_i is the corresponding lifetime.

For an emitter with a multi-exponential decay at a specific wavelength, the lifetime is calculated as the intensity-weighted average fluorescence decay time $<\tau>$:

$$\langle \tau \rangle = \frac{\sum_i a_i \cdot \tau_i^2}{\sum_i a_i \cdot \tau_i} \tag{7}$$

Where $\Sigma_i a_i \tau_i$ corresponds to the steady-state intensity.

The lifetime is often independent of the emission wavelength. However, if the spectral relaxation is on a similar time scale as the fluorescence emission, a change in lifetime is observed across the emission spectrum. Spectral relaxation comprises solvent relaxation and/or other reorganization processes in the local environment of the excited-state fluorophores.[41] Time-resolved emission spectra (TRES) can be used to analyze whether the fluorescence lifetime changes with the emission wavelength. Several j decay processes are measured over the emission range. The average decay time $<\tau_w>$ is calculated as the mean value of $<\tau>_j$ over the emission spectra and weighted with the steady-state intensity ($I_{ss}=\Sigma_j I_j$). If $\Sigma_i a_i \cdot \tau_i = I_j$ is defined, $<\tau_w>$ is given by the following equation:

$$\langle \tau_\omega \rangle = \sum_j \left(\frac{\langle \tau \rangle_j \cdot I_j}{\Sigma_j I_j} \right) \tag{8}$$

In the absence of spectral relaxation on the time scale of the fluorescence emission, $<\tau>$ is equal to $<\tau_w>$. This phenomenon typically appears in the sub-picosecond range and is therefore faster than the instrument response function (IRF). As a result, the lifetime is independent of the emission wavelength. However, if the spectral relaxation occurs on the same time scale as the fluorescence emission, i.e. comparable to or slower than the IRF, the TRES shows a red shift and the mean values deviate from each other. The reason for this is that the observed fluorescence originates from the partially relaxed or non-relaxed excited state and consequently, the average lifetime increases as a function of the emission wavelength, see Figure 7. The fluorescence decay is faster at shorter wavelengths as the excited state is depleted by both emission and spectral relaxation, while it is slower at longer wavelengths as it is only affected by the emission from the relaxed state. Even if there is only a single emitting species in solution, this phenomenon can lead to a multi-exponential fluorescence decay at a fixed emission wavelength.
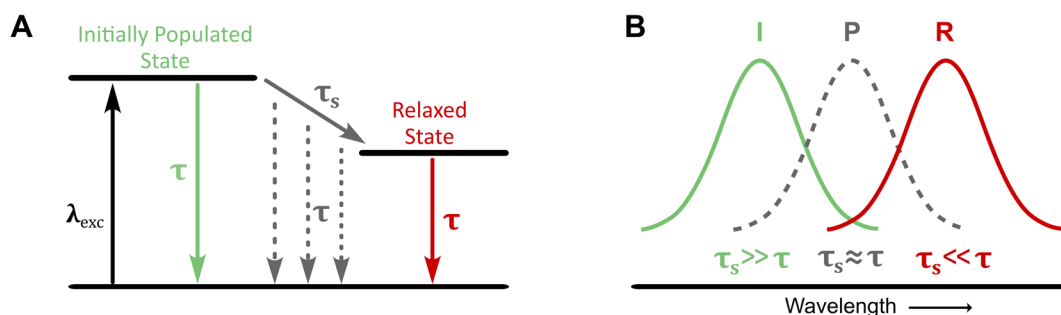
Figure 7: (A) Jablonski diagram and (B) emission spectra for spectral relaxation at different time-scales. **I** represents the initially populated state, **P** the partially relaxed state, and **R** the relaxed state. τ is the lifetime of the fluorophore, whereas τ_s is the spectral relaxation time.[41]

Time-correlated single photon counting

Time-correlated single photon counting (TCSPC) is the most commonly used technique to measure the fluorescence lifetimes of fluorophores. In TCSPC, the photons emitted by a sample are individually detected and their arrival times are recorded relative to an excitation pulse. By repeatedly detecting the time between the excitation pulse and the arrival of a fluorescence photon, a histogram is generated displaying the number of detected photons (counts) as a function of time differences (Δt), see Figure 8. Typically, only one photon or less is recorded per excitation pulse and the histogram represents the decay waveform. The low photon count (1 photon per 100 excitation pulses) is maintained to mitigate the pile-up effect, ensuring equal statistical detection probabilities over the entire time range and preventing distortion of decay shapes towards shorter times. The time resolution is determined by the laser pulse width and detection electronics, both converging into the instrument response function.
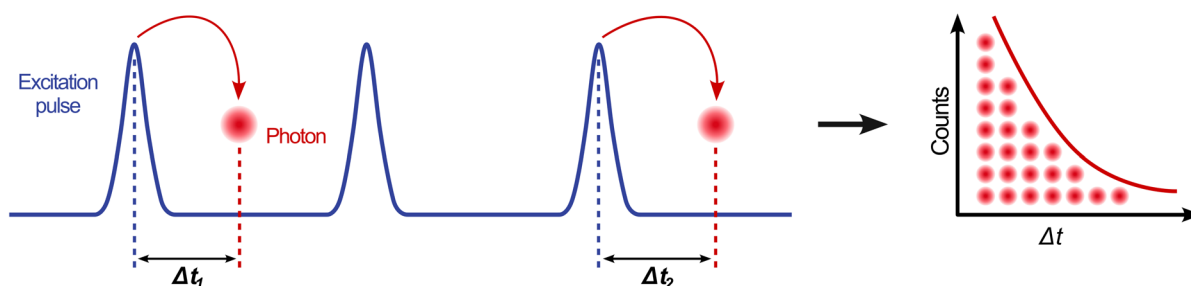
Figure 8: *Principle of time-resolved fluorescence measurements with TCSPC and histogram of detected photons as a function of time bins (Δt).*

2.3.4 Anisotropy

Fluorophores are characterized by their absorption and emission transition dipole moments. Anisotropy measurements are based on the principle of photoselection, where fluorophores are selectively excited by polarized light. Only those molecules with absorption dipole moments aligned parallel to the electrical vector of the polarized light are excited, resulting in a preferentially oriented population of fluorophores that emit polarized fluorescence, assuming that no depolarization processes occur. The emission polarization is quantified as anisotropy (r), defined by:

$$r = \frac{I_{VV} - I_{VH}}{I_{VV} + 2I_{VH}} \tag{9}$$

14

Where I_{VV} and I_{VH} are vertically and horizontally polarized emission intensities, respectively, when the sample is excited by vertically polarized light. Anisotropy is a unitless quantity as the numerator is normalized by the total intensity $I_{VV} + 2I_{VH}$. The anisotropy is an intensity ratiometric measurement and is independent of the fluorophore concentration.[41]

When considering single-photon excitation, the fundamental anisotropy (r_0) is the anisotropy in the absence of depolarization phenomena, like rotational diffusion and/or energy transfer processes. Hence, the value of r_0 is only influenced by the photoselection and the displacement of the absorption and emission dipole moments:

$$r_0 = \frac{2}{5}\left(\frac{3cos^2\beta - 1}{2}\right) \qquad (10)$$

Where β is the angle between the absorption and emission transitions. The maximum theoretical value in solution is reached when the excitation and emission dipoles are parallel ($r_0 = 0.4$). In contrast, a minimum value of -0.2 is obtained when the dipoles are perpendicular to each other. The anisotropy equals zero if β is $54.7°$, called the magic angle. The anisotropy is 0.1, if β is $45°$.

When the rotational rate of the molecules is comparable to the fluorescence lifetime, time-resolved anisotropy measurements can be very useful for determining the rotational correlation time. The rotational correlation time (θ) indicates how fast molecules rotate and is dependent by the size, shape, and flexibility of the molecule. The time-resolved anisotropy, $r(t)$, can be described as a multi-exponential decay:

$$r(t) = r_0 \sum_j g_j \cdot e^{(-t/\theta_j)} \qquad (11)$$

Where r_0 is the limiting anisotropy in the absence of rotational diffusion and g_j the fractional amplitude of θ_j in the anisotropy decay (note that $\Sigma_j g_j = 1$). Rotational correlation times can be related to the hydrodynamic volume (V_{hydro}) of the investigated species by the Perrin equation and is given by:

$$\theta = \frac{\eta \cdot V_{hydro}}{k_B \cdot T} \qquad (12)$$

15

Where η is the dynamic viscosity of the solvent, T is the absolute temperature and k_B is the Boltzmann constant. The hydrodynamic volume of the sample can be determined by measuring *VV* and *VH* intensity decays (time-resolved anisotropy) at specific or multiple temperatures to obtain a better statistical approximation. In the case of several measurements at different temperatures, the rotational correlation time values are then plotted as a function of $\eta/k_B T$, while fixing the intercept at zero. This method implies that the fluorophore has a spherical shape, therefore the value is only an estimate of the actual hydrodynamic volume of the emissive species.

2.4   Determination of Composition via Mass Spectrometry

The size and charge of metal clusters significantly determine their properties. The precise characterization of the composition is an important step to achieve a fundamental understanding.[2] The composition can be determined by mass spectrometry (MS). The principles of MS and the experimental method are described below, as well as how the data are used to determine the mass and oxidation state of DNA-AgNCs. The method used in our laboratory was adapted from Gonzàlez et al.[43]

2.4.1   Introduction to ESI-MS

High-resolution mass spectrometry is a powerful tool for compositional analysis. Electrospray ionization (ESI) is one of the most commonly used ionization techniques in which an aerosol is ionized by applying a high voltage to the dissolved sample. Because of its low fragmentation allowing the detection of the molecular ion, ESI is known as a "soft ionization" technique. Therefore, ESI-MS is well suited for determining the composition of weakly bound, non-covalent nucleic acid complexes, including DNA-AgNCs.[44] The phosphate backbone of the DNA is deprotonated and negatively charged at neutral pH. The use of ESI-MS in negative ion mode is therefore ideal for the mass spectrometry of DNA-encapsulated AgNCs.[2,32]

The used high-resolution mass spectrometer is a quadrupole time-of-flight mass spectrometer from Waters (Xevo G2-XS QTOF). Since this instrument is a hybrid mass spectrometer, and was only operated in full scan MS mode, the setup described here is simplified and reduced to the ionization unit and the time-of-flight (TOF) analyzer. Figure 9 shows the operating sequence of a TOF mass spectrometer. The purified DNA-AgNCs are introduced into the electrospray ionization source by direct injection using a mobile phase solvent mixture of 50 mM ammonium acetate and 20%

methanol.[43] After ionization, the ions are accelerated with the same kinetic energy but have different velocities due to differences in mass and charge. Depending on the ion drift, the ions reach the detector at different times. The detector generates usable signals and records them graphically as a mass spectrum showing the intensity of the signals as a function of their mass-to-charge ratio (m/z). By following the above criteria, it is possible to record mass spectra of DNA-AgNCs with low fragmentation, which allows one to resolve the isotopic pattern.
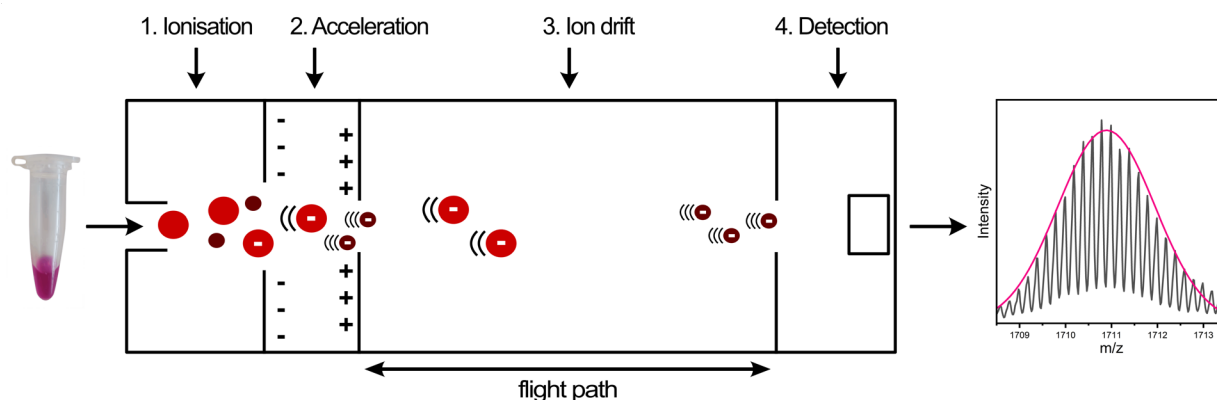
Figure 9: *Schematic representation of the time-of-flight (TOF) mass spectrometer with operating sequence.*

2.4.2   How to Calculate the Cluster Composition

By analyzing the isotopic distribution from the obtained mass spectrum, the total mass and charge of the cluster can be resolved. By comparing the experimental MS spectrum with the theoretical isotope distribution, the number of DNA strands and the total number of silver atoms, differentiated into effective neutral and cationic silver atoms, can be determined. The process of how we obtain this information is described below.[2]

The charge state z- of an m/z peak is determined by the distance between two neighboring peaks of the isotopic pattern. The distance of two peaks is $1/z$, while z is defined as a positive integer. The m/z peak corresponds to the total charge of the complex. The experimentally observed charge $-eZ$ equals the charge of the number of silver cations (eN_+) subtracted by the charge of the number of protons removed from the DNA (en_{pr}):

$$- eZ = eN_+ -\ en_{pr} \tag{13}$$

Since n_{pr} protons have been removed from the DNA-AgNC complex, the experimental total mass m_{tot} (in atomic mass unit, amu) is:

$$m_{tot} = m_{DNA}n_S + m_{Ag}(N_+ + N_0) - n_{pr} \qquad (14)$$

Where m_{DNA} is the mass of the DNA oligomer, n_S is the number of DNA strands stabilizing the DNA-AgNCs, and m_{Ag} is the mass of the silver atom. The mass of a proton is assumed to be 1 amu.

The number of effective valence electrons N_0 in the DNA-AgNC, which determines the electronic properties, can then be calculated by subtracting the charge of the cluster N_+ from the total number, N_{tot}, of silver atoms:

$$N_0 = N_{tot} - N_+ \qquad (15)$$

N_0 and N_+ can be accurately determined from the measured isotope distribution pattern. Theoretical calculations of the isotopic distribution pattern for different N_+ values allow the determination of the charge that best fits the experimental isotopic pattern. An example is given in Figure 10. We used this method to determine the composition and charge of DNA-AgNCs.
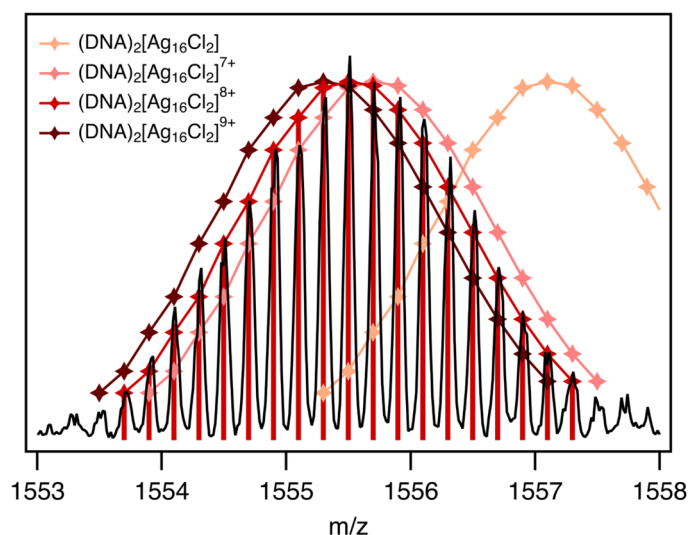
Figure 10: *Example mass spectrum with theoretical isotopic distributions. The experimental isotopic distribution (black curve) of DNA-Ag$_{16}$NC for z = 5- is compared with the theoretical isotopic distributions with different charge states (colored curves). For the calculations, the chemical formula of $C_{192}H_{244}N_{78}O_{112}P_{18}Cl_2Ag_{16}$ is used. The best fit occurs with a charge of 8+. Adapted with permission from Ref.[43] Copyright 2023 American Chemical Society.*

3 Structure-Property Relationship

3.1 Crystal structures

X-ray crystallographic studies are essential to gain insight into the coordination environment of DNA-AgNCs. Over the past few years, there has been a significant advancement in understanding the chemical structure of DNA-AgNCs in relation to their optical properties.[33-36] A breakthrough was achieved in 2019, when the first crystallographic studies on DNA-AgNCs were published; two crystal structures were published more or less at the same time.[33,34] These studies provided crucial insights into the structure of DNA-AgNCs with information about the silver-silver, DNA-silver, and DNA-DNA interactions involved in stabilizing these nanoclusters.

Huard et al. reported the crystal structure of a green-emitting DNA-AgNC comprising 8 silver atoms and stabilized by two 6-base oligomers, 5′-AACCCC-3′.[33] However, the particularity of this cluster is its lack of stability in solution and its formation during the crystallization process, as it requires the crystal construction for stabilization. Consequently, this cluster was not purified before crystallization. The symmetric unit resembles a "Big Dipper" shaped configuration with planar geometry, which can be divided into two parts, the handle (zipper region) and the cluster core.[33]

The zipper is formed by three metal-mediated C−Ag$^+$−C base pairs. In the parallel-oriented DNA strands, each Ag$^+$ interacts with the endocyclic N3 site of cytosine and creates a nearly linear geometry, as reported in non-emissive metallo-DNA nanowire structures (Figures 11A and B).[14] Here, the base-Ag distance measures 2.1 Å.[33]

The zipper region is connected to a trapezoidal Ag$_5$ core, which is encapsulated in a pocket-like manner by the adenine-rich part of the DNA sequence. Here, the Ag-Ag distances are ≈ 2.9 Å, which is comparable to the bond distances in bulk silver.[45] Adenine coordinates with the Ag$_5$ core via the endocyclic N1 and exocyclic N6. Cytosine, on the other hand, interacts with the Ag$_5$ core via the endocyclic N3 and the exocyclic N4 (Figures 11B and C). The exocyclic nitrogens N3 and N4 are deprotonated. As already mentioned, this cluster only exists in the crystalline form, which can possibly be explained by the interaction of a silver atom with the neighboring strand, which could play a role as a stabilization factor.
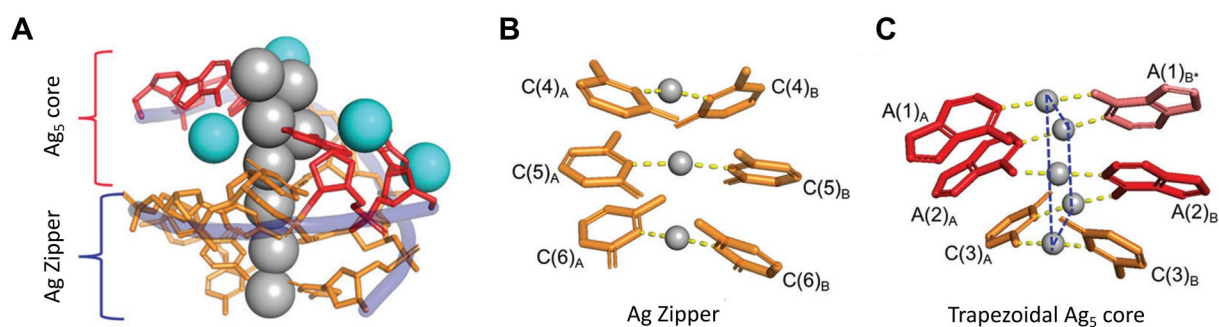
Figure 11: *Crystal structure of the green emissive DNA-AgNC reported by Huard et al.[33] (A) Asymmetric unit. The "BigDipper"-shaped DNA-AgNC is divided into two parts, the Ag Zipper and the Ag_5 core. (B) DNA-silver interactions within the Ag zipper and (C) DNA-silver interactions within the trapezoidal Ag_5 core. Adapted with permission from Ref.[32]*

At the interface of two neighboring DNA-AgNCs, four additional Ag^+ are observed (Figure 11A, cyan silver atoms). Two of them interact with adenines, but the other two are reported as artifacts because their occupancy is considered low. It is assumed that the additional Ag^+ probably promotes crystal packing.[33]

Shortly after the publication of the green emissive DNA-AgNC structure, the first X-ray crystal structure of an HPLC-purified DNA-AgNC was published by Cerretani et al. (Figure 12).[34] This cluster is stabilized by the DNA sequence, 5'-CACCTAGCGA-3' and was previously reported by Copp et al.[19] It has outstanding properties, it emits in the NIR region, has a high quantum yield and exhibits an exceptionally large Stokes shift.[5] The HPLC-purified cluster shows the same spectral properties in the crystalline state as in the solution, therefore the X-ray crystal structure is also of great relevance for the solution phase.[34]

The structure reveals a rod-shaped silver nanocluster core consisting of 16 silver atoms (shown as gray spheres, Figure 12A). Two additional Ag atoms were determined, which, however, only had an occupancy of ~0.3 (shown as cyan spheres, Figure 12A). The distances between silver atoms are between 2.7 and 2.9 Å.[34] This is significantly below the van der Waals radius (3.44 Å) of silver atoms,[46] but is in the range of the metallic radius in bulk material (2.8 Å).[45] In order to determine the charge of the so-called DNA-Ag_{16}NC, additional MS analysis is required, which was not yet published at that time. It is not possible to derive the charge from the distances alone.

The silver core is stabilized by two DNA decamers. It is noticeable that no WC-type base pairs are present in the structure. The cluster is mainly stabilized by silver-mediated and H-bond interactions, resulting in a horseshoe-like winding of the DNA around the Ag core. The AgNC cluster core has a diameter of 7 Å and a height of 15 Å. As in the crystal structure of Huard et al.,[33] cytosine coordinates to the silver with N3 and adenine with N1. Additionally, silver-base interactions of cytosine with O2

and adenine with N7 can be observed. The guanines interact via the positions N7, N1, and O6 (Figure 12B). The Ag-O distances are 2.4-2.9 Å. In comparison, the Ag-N distances are shorter with 2.2-2.5 Å. The shorter bond length indicates that guanine (G9) is deprotonated (2.3-2.4 Å).[34,35]
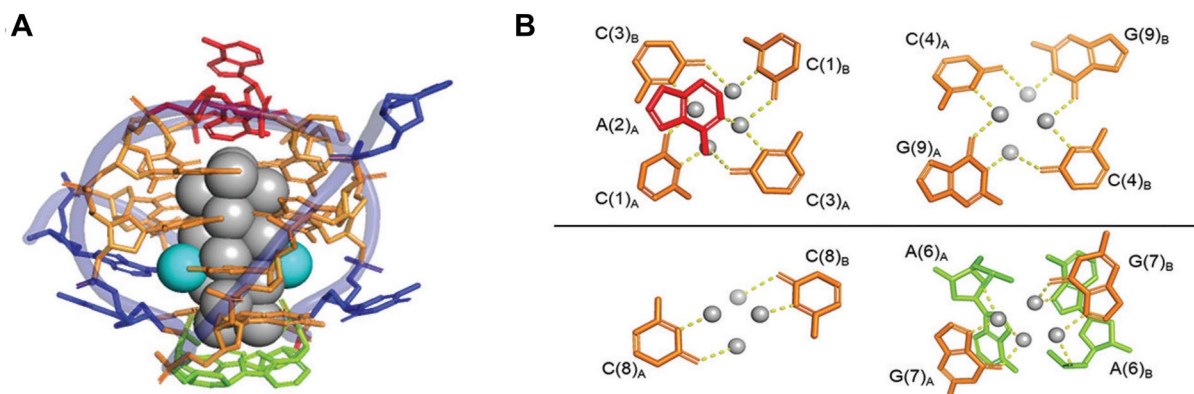
Figure 12: *Crystal structure of the NIR emissive DNA-AgNC reported by Cerretani et al.[34] (A) Asymmetric unit and (B) DNA-silver interactions within the structure showed in a top-view. Adapted with permission from Ref.[32]*

Interactions with the neighboring asymmetric units are also observed in this crystal structure.[34] The terminal adenine, A10, forms a silver-mediated interaction with the A10 of the neighboring unit. In addition, A10 does not interact with the silver core and the removal of this base is found to have no impact on either the crystal structure or the photophysical properties.[35] The thymine at position 5 (T5) also does not interact with the silver core but provides some flexibility to the DNA strand. This finding supports previous observations of low affinity of thymine for Ag$^+$. Both, A10 and T5, are involved in π-stacking interactions that most likely promote crystal packing.[32,35]

To gain a better understanding of the key interactions defining the properties of DNA-AgNCs, the alteration of the DNA sequence is an approach to decode them. Motivated by this, thymine (T5) was mutated to X5 (abasic site), C5 (cytosine), A5 (adenine), and G5 (guanine).[36] The mutation resulted in minimal or no change in the structural and photophysical properties of the DNA-AgNC, implying that the Ag$_{16}$ cluster core was retained. A comparison of the six different crystal structures reveals that two sections of the DNA sequence are important for the formation of the cluster, namely 5'-CACC-3' and 5'-AGCG-3'.[32,36] The mutations at the non-interacting positions 5 and 10 have no influence on the formation of the cluster, but can influence the interactions in the crystal packing. The engineering of the DNA sequence could be an important tool to promote the crystallization of DNA-AgNC in the future.

The role of the additional Ag$^+$ and whether they also exist in the solution state is still not fully understood. However, both structures have additional Ag$^+$, undergoing metal-mediated base pairing and supporting crystal packing but are not involved in the cluster core.[33-36] MS data are required to investigate the existence and role of the additional Ag$^+$ in solution. However, the extent to which these additional Ag$^+$ ions can be detected by ESI-MS is unclear.

In general, ESI-MS provides additional information about the composition of the DNA-AgNC. Recently, ESI-MS was used to solve the mystery of the two low occupancy silver atoms. Gonzàlez-Rosell et al. revealed the presence of chloride ligands in the NIR-emitting DNA-AgNC.[43] Various tests confirmed this observation, although the origin of the chlorides remains unclear. Furthermore, N_0 and N_+ could be determined, leading to the final composition $(DNA)_2[Ag_{16}Cl_2]^{8+}$. With the knowledge of the complete composition and the crystal structure, the first density functional theory (DFT) calculations could be performed.[43,47,48]

The first two crystal structures have already improved our understanding of the structural features of DNA-AgNCs and the main interactions involved in stabilizing DNA-AgNCs. It has been confirmed that DNA-AgNCs have anisotropic rod-like shapes, as proposed by Schultz et al.[3] Furthermore, evidence was found that the interaction with certain bases plays a crucial role in the formation and stabilization of the clusters. The metal-mediated base pairs G–Ag$^+$–G, C–Ag$^+$–C, and A–Ag$^+$–A occurred most frequently, whereas Ag$^+$-mediated thymine base pairs were not observed.[32] Thymine seems to play a more relevant role in the folding of the DNA strand as a flexibility parameter. These findings can help to engineer DNA sequences in the future. In addition to metal-mediated base pairs, non-WC-like H-bond interactions also contribute to the stability of the DNA-AgNC. It was also unraveled that not all nucleotides interact with the nanocluster core. The results of DNA-Ag$_{16}$NC indicate that mutations of non-interacting nucleotides do not affect the formation and properties of DNA-AgNCs.

However, many more DNA-AgNC crystal structures are needed to revolutionize our understanding of the structure-property relationship. It has been shown that the combination of MS and crystallography can be a powerful tool to elucidate the structures of DNA-AgNCs. Only with further resolved structures is the development of applications with these clusters promising.

3.2 Crystallography

The structure determination of macromolecules, including DNA-AgNCs, requires various steps: purification of the target molecule, crystallization, collection of diffraction data, and identification of atomic positions.[49,50] These steps are schematically illustrated in Figure 13. In the following chapter, I will mainly focus on the crystallization part, since the data collection and structure determination are carried out by our collaboration partner Prof. Jiro Kondo.
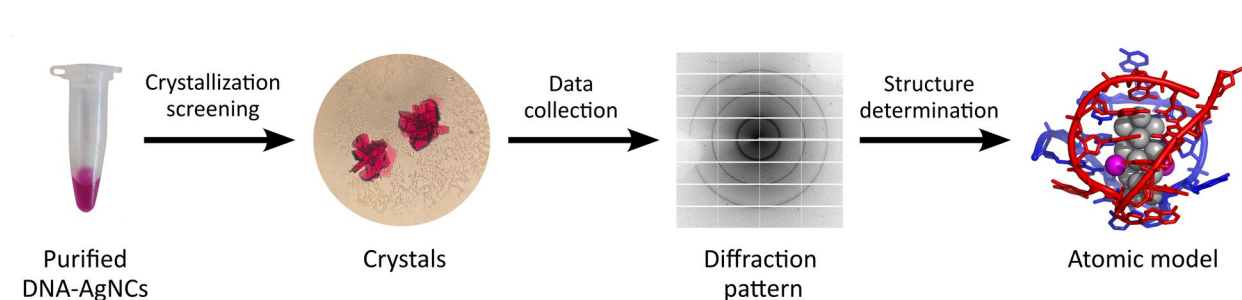
Figure 13: Schematically presentation of steps involved in the structure determination of DNA-AgNCs. Adapted with permission from Ref.[34] Copyright 2019 Wiley.

3.2.1 Crystallization

The first bottleneck in structure determination is obtaining high-quality crystals suitable for single-crystal X-ray diffraction.[49,50] Crystallization is a complex process that is influenced by many parameters. However, finding the right condition is essential as crystals with high diffraction quality are required for successful structure characterization. High diffraction quality refers to the reproducibility and ordering of the crystal in all three spatial dimensions (x, y, and z). Consequently, a high resolution is only achieved when the right crystallization conditions are met. The flexibility of some macromolecules, even DNA-AgNCs can be flexible due to their DNA scaffold, makes the formation of a regular crystal lattice even more difficult. An extensive screening of crystallization conditions is required to find the right parameters for the selected sample. This search can be like looking for a needle in a haystack.[49]

A number of different crystallization techniques have been developed over the past decades.[49-53] Among the most commonly used crystallization methods are vapor diffusion, dialysis, free interface diffusion and batch method. I will mainly focus on the vapor diffusion method, as it is the method employed for the DNA-AgNCs. This method is widely utilized for macromolecules and nucleic acid samples.

The crystallization process can be explained by a phase diagram,[49,53] which illustrates the most stable state, whether liquid, crystalline, or amorphous solid, depending on a variety of crystallization parameters. Typically, the concentration of the macromolecule, in our case DNA-AgNCs, is plotted as a function of a variable, e.g. the precipitant. A schematic representation of a crystallization phase diagram can be found in Figure 14. The impact of parameters such as the concentration of the sample, precipitant(s), additive(s), pH value and temperature on crystal formation can be quantified in this way.
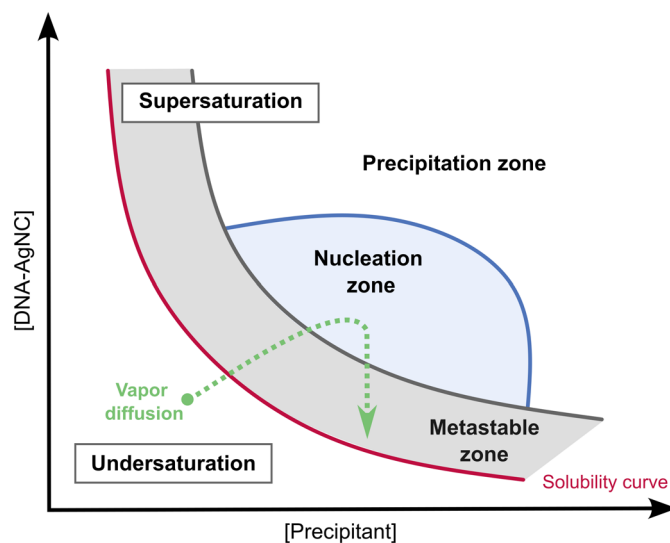
Figure 14: *Representation of crystallization phase diagram. The pathway to the nucleation and metastable zone for the vapor diffusion method is shown (green trace).*

If the concentration of the selected molecule is below the solubility curve (red line, Figure 14), the solution is in the undersaturation area. In this range, the sample is dissolved and no nucleation or crystal growth takes place. If the concentration of the sample is above the solubility limit, the solution is supersaturated. Three zones define the area of supersaturation: Precipitation zone, nucleation zone, and metastable zone. In the precipitation zone, the supersaturation is very high and the formation of amorphous aggregates is favored. If the supersaturation is in the intermediate range, not too high and not too low, both spontaneous nucleation and growth of crystals can occur. For this reason, the area in question is known as the nucleation zone. In direct contact with this zone is the metastable zone. Here, the supersaturation is too low for nucleation, but the growth of the seeded crystals is supported. The crystal growth leads to a reduction in the sample concentration until the solubility limit is again reached. The saturation depends on the concentration of the macromolecule and the precipitating agent. A precipitant is a small molecule that deposits the macromolecule out of the solution.

Hanging drop vapor diffusion method

The hanging drop vapor diffusion method is a popular technique for crystallizing macromolecules.[49,50] A drop composed of sample and crystallization buffer is equilibrated over a liquid reservoir. The drop is located on the downward-facing side of the cap and is sealed. In this closed system, a vapor equilibrium occurs between the droplet and the reservoir. A concentration gradient is achieved since the concentration of precipitant in the reservoir is higher than in the droplet. As a result, water evaporates more quickly from the droplet and is absorbed by the reservoir in order to equilibrate the concentrations. Consequently, the volume of the droplet slowly decreases and the concentration of DNA-AgNCs increases. Since the reservoir volume is considerably larger, the dilution can be neglected. At some point in time, the concentration of the DNA-AgNC will reach a supersaturation level, where nucleation occurs. If all parameters are appropriate, the sample might crystalize. When the crystals nucleate and grow, the sample concentration decreases until the solubility limit is reached. The path of the diffusion method is shown in the phase diagram, see Figure 14. Depending on the sample after a few days or weeks, crystals can be monitored under a microscope. A schematic illustration of the steps is shown in Figure 15.

The benefits of this method are that the crystals are easy to access and multiple drops with a single reservoir can be performed, which is good for large screening. Additionally, it is an easy technique to screen a large number of conditions by varying the crystallization buffer, increasing or decreasing the concentration of the sample, or varying the volume of the drop.
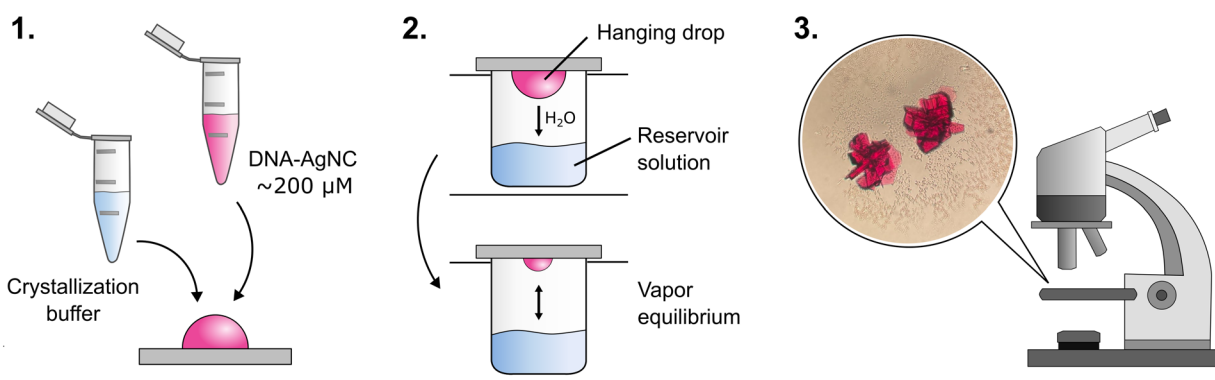
Figure 15: *Illustration of the steps involved in the vapor diffusion method. (1) Crystallization buffer and DNA-AgNC sample are pipetted on the silicon glass surface of the cap. (2) The well containing the reservoir solution is sealed with the cap. The drop hangs from the cap. The droplet reaches supersaturation when the droplet's water vapor equilibrates with the reservoir solution. (3) After a few days or weeks, crystals can be observed under the microscope if all the parameters for crystal growth are appropriate.*

In our crystallization experiments, crystallization plates from NeXtal (EasyXtal 15-well) are used. Different conditions are screened, specifically the crystallization buffer is varied in nitrate salt (Li^+, Na^+, K^+, NH_4^+, Mg^{2+}, Ca^{2+} or Sr^{2+}) and concentration (10, 100, 200, 300, 400 and 500 mM). The crystallization buffer also contains 10 mM spermine, 50 mM 3-(N-morpholino)propanesulfonic acid (MOPS) at pH 7 and is based either on 10% 2-methyl-2,4-pentanediol (MPD) or 10% polyethylene glycol (PEG) 3350. A mixture of 0.5 μL of the crystallization buffer and DNA-AgNC sample with [DNA] ~ 200 μM are equilibrated against 250 μL reservoir solution of 40% PEG or 40% MPD. The crystals are grown at room temperature in the dark.[54]

3.2.2   Data Collection and Structure Determination

Once the first obstacle has been overcome and high-quality crystals are obtained, the structure can be determined by single crystal X-ray diffraction (SC-XRD).[55,56] The X-ray beam interacts with the crystal sample because the wavelength of the radiation matches the interatomic distances. The monochromatic beam is scattered at each crystal plane at a certain angle. This results in a pattern whose intensity is created by interference and represents the atom distribution in the crystal. The X-ray diffraction pattern is essentially a fingerprint of the molecule, showing the structural position of each individual atom.[56]

Based on the position and intensity of the signals in the diffraction pattern, a three-dimensional map can be created. The so-called electron density map is then used to determine the atomic positions and thus solve the molecular structure.[55] The crystallographer uses various tools and programs for the analysis. The solved crystal structure can then be used to determine the molecular packing, bond lengths and non-bonding interactions.

The X-ray data acquisition and structure determination are carried out by our collaboration partner Prof. Jiro Kondo. The X-ray data are collected with synchrotron radiation at the BL-17A beamline at the photon factory in Tsukuba, Japan. The crystals are placed in a nylon loop and the data acquisition is performed under cold nitrogen gas flow to reduce thermal vibrations and radiation damage.

3.3 Publication 1: Structure of a green emissive DNA-AgNC

Vanessa Rück, Vlad A. Neacşu, Mikkel B. Liisberg, Christian B. Mollerup, Park Hee Ju, Tom Vosch, Jiro Kondo, Cecilia Cerretani. Atomic Structure of a DNA-Stabilized Ag_{11} Nanocluster with Four Valence Electrons. *Adv. Optical Mater.* **2024**, *12* (7), 2301928.

3.3.1 Main Findings

So far, only two crystal structures of DNA-AgNCs have been reported. The publication of these crystal structures represents a significant advance but additional crystal structures are necessary to gain a more comprehensive understanding of the structure-property relationship. It has been demonstrated that the combination of MS and single crystal X-ray diffraction of purified DNA-AgNCs is a powerful tool for the determination of the charge, composition, and structure of the encapsulated AgNCs.[43] This information is of significant importance for the development of new DNA-AgNCs with tailored properties, as well as for electronic structure calculations and future functionalization experiments for biological applications.

This work presents the efforts to solve the structure of a green emissive DNA-AgNC. The DNA-AgNC stabilized by the sequence, 5'-TCCACGAGAA-3', called 10Green-AgNC, was previously published by Copp et al.[20] The cluster exhibits 11 silver atoms with four neutral Ag and seven Ag^+ encapsulated by two oligomers. Unfortunately, despite extensive testing of numerous crystallization conditions, no crystals could be obtained.

Based on our previous work, the DNA sequence was extended with adenosines and/or thymidines in order to promote crystal-packing interactions. It was confirmed that nearly identical emitters with comparable properties were stabilized for all modifications. Moreover, the crystallization process was successful, resulting in the formation of crystals. However, the quality of the diffraction pattern was too low for elucidating the structure.

As a new approach, we decided to also test shortening the DNA sequences, given the findings in previous work that adenosines may not interact with the cluster core. The removal of two adenosines at the 3'-end resulted in the stabilization of an emitter with similar properties. For this modification, called 11Green-2end-AgNC, crystals could be obtained whose diffraction data were good enough to resolve the cluster core. An insight into the silver positions could be gained, but unfortunately, the DNA conformation was not successfully resolved. The crystal structure is shown in Figure 16. The single crystal X-ray diffraction data of 11Green-2end-AgNC revealed the presence of 11 silver atoms,

which is consistent with the results of the mass spectrum. The silver atoms are arranged in a potentially very dynamic and flexible rod-like structure.
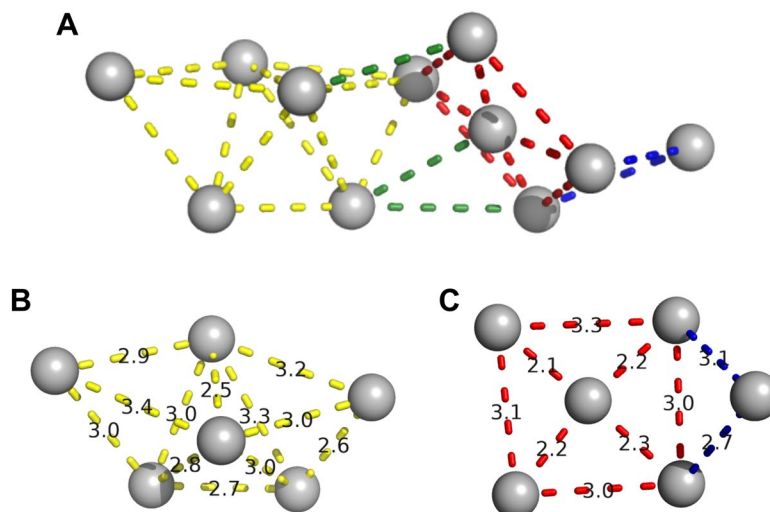
Figure 16: *(A) Subunit of the 11Green-2end AgNC crystal structure. The closest silver distances in the $[Ag_{11}]^{7+}$ nanocluster are indicated by colored dashed lines. (B) View of the tetragon pair with shared bond and edge. (C) Insight into the square planar section with a single atom extension. All distances are in Å. Adapted with permission from Ref.[54] Copyright 2023 Wiley.*

In summary, the work provides a roadmap for improving the crystallization to yield high-quality crystals suitable for SC-XRD. In addition, the study offers valuable insight into the structure-property relationship of a green-emitting DNA-AgNC.

3.3.2 Contribution

In a joint effort with Cecilia Cerretani, I performed the synthesis, HPLC-purification, crystallization, as well as the steady-state and time-resolved spectroscopy characterization of the DNA-AgNC and its mutants. In collaboration with Christian B. Mollerup, I measured the mass spectrum of the DNA-AgNC and its modifications and analyzed the data. I also contributed to the writing of the manuscript.

4 Photophysics of DNA-AgNCs

4.1 Introduction

The absorption spectrum of purified DNA-AgNCs shows a specific anatomy.[32] DNA-AgNCs typically have two dominant peaks: one in the ultraviolet (UV) range and one in the visible to near-infrared (NIR) range, see Figure 17A. The absorption band at approximately 260 nm is associated with the absorption of the nucleobases and is "universal" for all DNA-AgNCs. In addition to the UV band, DNA-AgNCs exhibit a Gaussian-shaped band in the visible to NIR excitation range which is determined by the composition and structure of the cluster core.[2,32] In purified DNA-AgNCs, the absorption spectrum matches the excitation spectrum. If the DNA-AgNC is excited directly in the cluster-specific peak or indirectly via the nucleobase peak, it results in the same emission spectrum (Figure 17B).[57] In addition to the two main features, less intense transitions can also occur at energies between the bands of the nucleobases and the lowest energy transition, which result from the cluster and consequently lead to the same emission maximum when excited.[2,32] The purity of DNA-AgNC samples can be checked by comparing the features observed in absorption and excitation spectra.
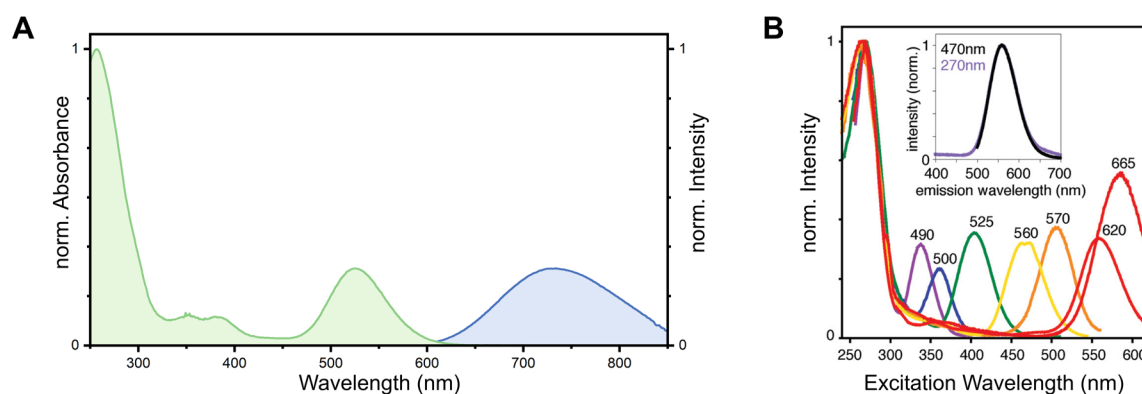
Figure 17: *Exemplary spectra of DNA-AgNCs. (A) Normalized absorption (green) and emission (blue) spectra of DNA-Ag$_{16}$NC. The absorption spectrum shows the typical anatomy with two dominant peaks and additional less intense transitions. The emission spectrum has a Gaussian shape. (B) Excitation spectra of several DNA-AgNCs, normalized in the range of 260-270 nm. The inset shows that the fluorescence spectrum of a DNA-AgNC excited at 270 nm and 470 nm have the same spectral shape and maximum. Adapted with permission from O'Neill et al.[57] Copyright 2011 American Chemical Society.*

Most DNA-AgNCs are characterized by ns-lived fluorescence decay times (1-4 ns) and high quantum yields (> 0.1).[2] Compared to organic fluorophores, DNA-AgNCs do not exhibit vibronic shoulders and their emission spectrum is instead characterized by a Gaussian shape,[58] see Figure 17A. The lack of a

vibronic shoulder can be explained by the comparatively low vibrational energies of the Ag-Ag and Ag-nucleobase bonds.[32] Another difference to common organic fluorophores is the large Stokes shifts of DNA-AgNCs,[59] which may indicate fundamentally distinct excited state dynamics.

Therefore, the Jablonski diagram for organic fluorophores is not adequate to comprehensively describe the fluorescence process of DNA-AgNCs.[32] There are a limited number of experimental studies investigating the ultrafast dynamics of DNA-AgNCs upon excitation. Patel et al. presented the first phenomenological model based on ultrafast transient absorption experiments of three different non-purified red-to-NIR emitting DNA-AgNCs (Figure 18A).[60] An initially Franck-Condon (FC) state is generated upon excitation of the ground state (S_0). After hundreds of femtoseconds, a part of the population returns to the ground state and the other part enters either the emitting state (S_1) or dark state (D_1).[60,61] TCSPC measurements show that the emissive state fluoresces into the ground state on the time scale of a few nanoseconds.[2] The long-lived state (D_1) with µs decay time was detected by transient absorption and single molecule spectroscopy.[6,60] D_1 is formed from the initial FC state and not from the excited state S_1, as for organic fluorophores.[62] Until recently, it was assumed that the long-lived state was dark because no emission was observed.[63,64]

Relatively recent transient absorption studies investigated the ultrafast dynamics of the purified NIR-emitting DNA-Ag$_{16}$NC.[65] Previous studies showed that the DNA-Ag$_{16}$NC has a dual emissive nature.[66] Chen et al. unraveled a relaxation scheme for this particular cluster that differs from the general phenomenological model, see Figure 18B.[65] It was experimentally shown that after excitation to the FC state, the population returns to the S_1 state within a hundred fs. In this case, the long-lived state is formed by $S_1 \rightarrow T_1$. There is no evidence that the long-lived state is formed directly from the FC state. Theoretical calculations confirmed this model.[47] The observation that the relaxation of S_1 occurs via the long-lived state is consistent with the previous findings of Petty et al.[63]
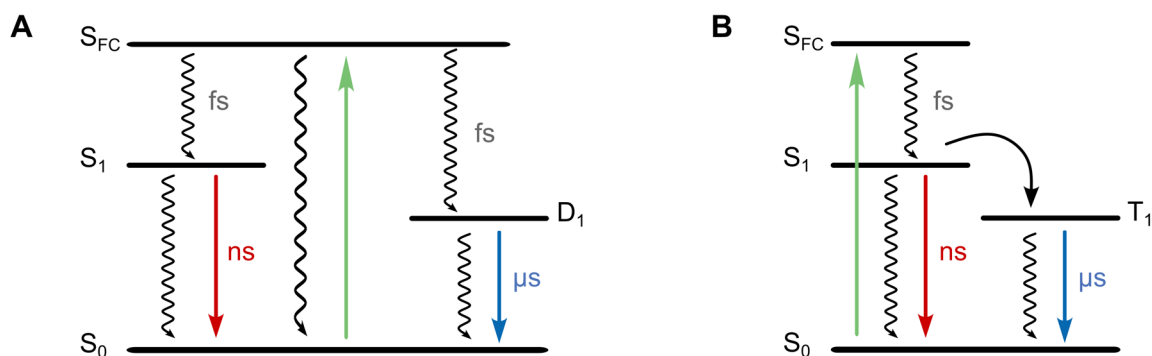
Figure 18: (A) Phenomenological model of DNA-AgNCs with four indicated states: a ground state (S_0), an initially excited Franck-Condon state (S_{FC}), a nanosecond lived emissive state (S_1) and a long-lived dark/emissive state (D_1). (B) Energy diagram of the DNA-Ag$_{16}$NC, showing intersystem crossing from S_1 to the long-lived state (T_1).

Thus, it seems that there is not a single model that describes the excited state dynamics of DNA-AgNCs in general. Which model best describes a particular DNA-AgNC can be investigated using ultrafast time-resolved optical spectroscopy and single-molecule spectroscopy. Further investigations are needed to establish a correlation between DNA-AgNC properties and an appropriate excited state model.

4.1.1 The Short-lived State

The fluorescence-like process from S_1 has a decay time of 1-4 ns.[2] Despite their purity, purified DNA-AgNCs show multiexponential fluorescence decays.[5,67,68] The observed multiexponential behavior can be ascribed to the presence of slow relaxation.[68] While solvent relaxation is typically completed on the picosecond time scale for molecular fluorophores, it occurs on the nanosecond timescale for DNA-AgNCs. The relaxation and fluorescence decay are on the same time scale.[68] The origin of this observation can be attributed to the considerable size of DNA-AgNCs and the length and thus flexibility of the DNA scaffold.[2] DNA templates need much longer to align with the new charge distribution of the clusters in the emissive state. Normalized time-resolved emission spectra (TRES) of DNA-AgNCs demonstrate a continuous shift to longer wavelengths. This redshift is observed on the nanosecond scale and confirms a slow spectral relaxation.

DNA-AgNCs react to environmental changes. When the temperature increases, a red shift of the fluorescence band is observed as the emissive state continues to relax energetically while the absorption remains constant.[68] Increasing the viscosity of the solvent can significantly lengthen the time of the spectral relaxation.[5] The exchange of H_2O against D_2O also affects the photophysical properties of DNA-AgNCs. However, as opposed to e.g. ns-lived organic fluorophores[69] and μs-lived lanthanide complexes,[70] a generally valid statement cannot be made here, because D_2O can lead to an increase in the quantum yield or cause the opposite effect.[66] This shows once again how diverse the photophysics of DNA-AgNCs is.

4.1.2 The Long-lived State

Vosch et al. reported for the first time the presence of a long-lived state in DNA-AgNCs.[6] Through optical activated delayed fluorescence (OADF), it is possible to make the dark state "shine".[71] This process is conceptually similar to thermally activated delayed fluorescence (TADF) but is performed optically. A secondary NIR laser is used to depopulate the long-lived state and pump it into the short-

lived excited state. Regeneration of the short-lived state occurs and consequently, the overall intensity can be increased.[72] Since this delayed fluorescence is caused by the secondary NIR excitation of the μs-based dark state, it can be detected separately in time from the emission generated by the primary excitation.[72] A background-free signal can be created, as the resulting emission is anti-Stokes (see Figure 19).[73,74] OADF is a promising approach to circumvent the autofluorescence of biological substances.[62,73,74]

The long-lived state D_1 has been assumed to be dark, but recently more and more DNA-AgNCs with a luminescent long-lived state have been reported.[63,64,66] Most of these clusters have a dual emissive character, with both a ns-lived and μs-lived state. The long-lived state has been investigated in various studies,[63,72,75] but it has not yet been possible to determine the origin of the state. If it is a phosphorescent-like process and thus a triplet state, the removal of molecular oxygen from the environment would generally lead to an increase of the μs decay time.[2] However, the protective DNA scaffold of DNA-AgNCs partially prevents oxygen from getting to the AgNC and thus hinders quenching of the AgNC. The effectiveness of the protective scaffold varies from cluster to cluster, hence some clusters were found to be more or less sensitive to oxygen.[6,63,66] The properties of DNA-AgNCs seem to be very individual and a general statement cannot be made. Overall, these results indicate the diversity of photophysical properties of this class of nanoclusters.[63,64,75]
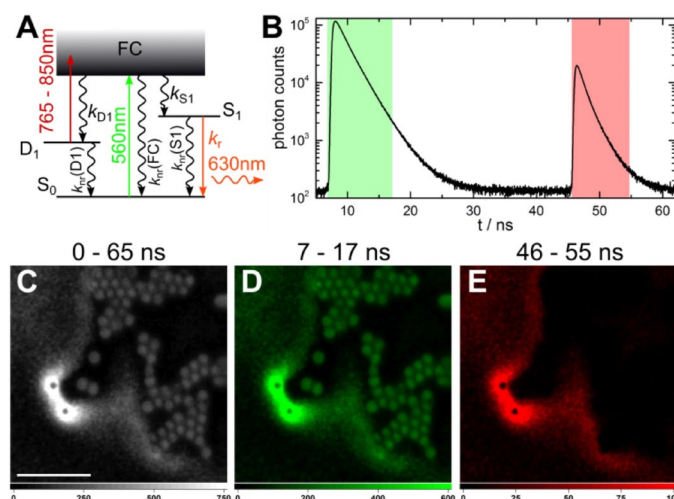
Figure 19: *Optical activated delayed fluorescence (OADF) microscopy. (A) Energy diagram with indicated excitation and deactivation pathways, (B) decay curves under primary excitation (λ_{exc-1}= 560 nm) at 7 ns and secondary excitation (λ_{exc-2}= 765-850 nm) at 46 ns, (C-E) fluorescence images of a heterogeneous sample of DNA-AgNCs within a PVA film and fluorescent microspheres acting as autofluorescence. Images were generated from all detected photons (0-65 ns, C), within the first time gate (7-17 ns, D), and within the OADF time gate (46-55 ns, E). The latter shows only the DNA-AgNCs without background. Adapted from Krause et al.[73] with permission from the Royal Society of Chemistry.*

4.2 Publication 2: An intriguing dual emissive DNA-AgNC

Vanessa Rück, Mikkel B. Liisberg, Christian Brinch Mollerup, Yanmei He, Junsheng Chen, Cecilia Cerretani, Tom Vosch. A DNA-Stabilized Ag_{18}^{12+} Cluster with Excitation-Intensity-Dependent Dual Emission. *Angew. Chem. Int. Ed.* **2023**, *62* (39), e20230976.

4.2.1 Findings

The demand for NIR emitters is high. However, the large variety of DNA sequence combinations poses a challenge for developing NIR-emitting DNA-AgNCs. ML-assisted high-throughput screening helps to correlate color (green/red/NIR) and DNA sequence. Mastracco et al. presented a machine learning model showing a higher design success rate for NIR emissive DNA-AgNC.[31] From the published list of predicted sequences stabilizing NIR emitters, we have selected a few to perform a more detailed photophysical characterization.

One of the selected DNA sequences, 5′-TGGACGGCGG-3′, stabilizes a green absorbing DNA-AgNC with dual emission in the red and near-infrared region, see Figure 20A. The composition and charge of the cluster were determined by MS. It was found that 18 silver atoms are stabilized by two DNA strands with a nanocluster charge of 12+, therefore the cluster is referred to as $DNA_2[Ag_{18}]^{12+}$. Steady-state and time-resolved measurements were used to investigate the dual emissive behavior, which exhibits IRF-limited red fluorescence and microsecond-long NIR luminescence. In addition to the temperature- and solvent dependency, the ratio between luminescence and fluorescence exhibited an excitation-intensity dependency. This behavior is unusual for molecular-like emitters. The ratiometric response to excitation intensity could be the result of optically activated delayed fluorescence.

This special behavior makes the cluster particularly interesting for applications as a nanoscale light intensity meter. In the study, three different approaches for generating calibration curves based on steady-state or time-resolved emission measurements are presented to enable using the cluster as a ratiometric excitation intensity probe. One exemplary way of generating a calibration curve is shown in Figure 20B.
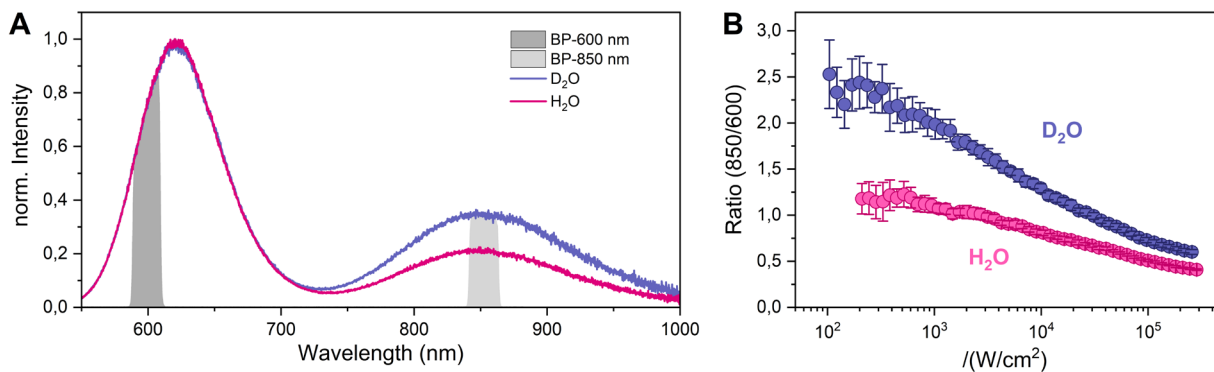
Figure 20: *Excitation intensity studies of the dual emissive DNA$_2$[Ag$_{18}$]$^{12+}$ in two different solutions: 10 mM NH$_4$OAc in H$_2$O (pink) or D$_2$O (blue). (A) Normalized spectra of DNA$_2$[Ag$_{18}$]$^{12+}$ measured at room temperature (λ_{exc}= 514 nm). The emission spectrum shows two distinct peaks, one at 624 nm (short-lived state) and a second at 829 nm (long-lived state). The filtered spectral ranges are shown as gray areas. (B) Calibration curves result from the ratios between the filtered 850 nm signal and the filtered 600 nm signal as a function of different excitation intensities. Adapted with permission from ref.[76] Copyright 2023 Wiley.*

4.2.2 Contribution

I screened all selected DNA sequences. I performed the synthesis, purification and spectroscopic characterization of the DNA$_2$[Ag$_{18}$]$^{12+}$. Furthermore, I measured in collaboration with Christian B. Mollerup the ESI-MS of DNA$_2$[Ag$_{18}$]$^{12+}$ and contributed to the writing of the manuscript.

5 Bioimaging Application

5.1 Introduction

A fluorophore must meet certain requirements to be used successfully in bioimaging applications, such as high brightness, photo- and chemical stability, and non-toxicity.[77] DNA-AgNCs, with their special properties, are promising candidates.[2] The tunable emitters can exhibit high quantum yields, high extinction coefficients, biocompatibility due to their DNA scaffold, and high photostability.[2,32] Moreover, initial studies have demonstrated that DNA-AgNCs are non-toxic to mammalian organisms.[78] Nevertheless, further studies are required to investigate the stability of DNA-AgNCs in the cellular environment and their degradation in the body to obtain a comprehensive understanding of their cytotoxicity.

There is a high demand for fluorophores in the near-infrared region since biological tissue is relatively transparent in the wavelength range of 700-1700 nm, known as the NIR tissue transparency window.[79] Only a few bright fluorophores exist in this range; NIR-emitting organic fluorophores often have low quantum yields.[79] The Nobel Prize-awarded quantum dots fulfill many of the mentioned characteristics but are often toxic and usually larger than organic fluorophores.

Due to their tunable nature and favorable near-infrared emissive properties, DNA-AgNCs are promising for imaging applications in the NIR tissue transparency window.[32] Several NIR-emitting DNA-AgNCs have been reported and are partly characterized by high quantum yields.[3,4] Moreover, some examples are bright enough to be detected at the single-molecule level.[28] The discovery of new NIR emissive DNA-AgNCs is advanced by machine learning-assisted high-throughput screening.[31] Even though developing bright and stable DNA-AgNCs is challenging, their photophysical properties encourage their use in bioimaging studies.

Furthermore, it has been found that many DNA-AgNCs exhibit a microsecond-lived state in addition to the fluorescent state, which can be either dark or luminescent. The presence of the long-lived state gives the possibility of optically activated delayed fluorescence and upconversion fluorescence, which allows background-free imaging due to emission on the anti-Stokes side.[72,73]

Several applications of DNA-AgNCs have been reported over the last few years.[2] However, only a limited number of studies have been performed on purified DNA-AgNCs. In the following, I will address two reported applications of purified DNA-AgNCs, that use either hybridization or encapsulation strategies for imaging with DNA-AgNCs.

The first publication combines DNA-AgNCs with DNA nanotechnology.[80] Nanostructures are formed by the predictable and programmable base-pairing properties of DNA via hybridization. Self-assembly allows the generation of complex 2D and 3D structures, such as DNA origami.[81] This property also enables the precise arrangement of components at the nanoscale to form predetermined architectures. The functionalization of nanostructures with fluorophores[82] or other molecules of interest enables their use in various applications, such as biosensors, imaging, and drug delivery.[13] The decoration of nanostructures is typically achieved through hybridization, which requires the targeted molecules to be functionalized with a single-stranded DNA strand that is complementary to a specific position on the nanostructure. Due to the DNA scaffold of DNA-AgNCs, it seems obvious to combine them with DNA nanotechnology.

In order to decorate nanostructures with DNA-AgNCs, it is necessary to functionalize the DNA scaffold with a linker tail. Although the extension of the DNA template may appear simple at first glance, the design of a bifunctional DNA strand that stabilizes the DNA-AgNC and possesses a tail for WC pairing is not a trivial task. Copp et al. presented a strategy for engineering DNA sequences of DNA-AgNCs to decorate DNA nanotubes.[80] Sequences are selected for the tail region of the bifunctional DNA strand that are known not to stabilize the AgNC and can thus serve as linker sequences. This linker sequence is then combined with the DNA template of a DNA-AgNC. It was demonstrated that the engineered DNA-AgNCs with a tail have the same photophysical properties as the original DNA-AgNCs after HPLC purification. Confocal microscopy confirmed that the programmed positions on the DNA nanotube were successfully decorated with DNA-AgNCs and the photophysical properties remained unchanged,[80] see Figure 21A.

Wang et al. developed a strategy to encapsulate the NIR-I emissive DNA-Ag$_{16}$NC in liposomes for measuring cerebral blood flow velocity in living mice using two-photon fluorescence correlation spectroscopy (FCS),[83] see Figure 21B. The DNA-Ag$_{16}$NCs were encapsulated in 100 nm liposomes to increase the cluster concentration, which additionally shields the DNA-AgNCs from the degrading cellular environment. The encapsulation did not affect the photophysical properties, and resulted in highly emissive liposomes required for two-photon FCS,[83] making the encapsulation approach particularly interesting. Due to the NIR-I emission of DNA-Ag$_{16}$NC, the two-photon excitation is in the NIR-II window, a region where tissue autofluorescence is reduced. This represents an advancement for applying DNA-AgNCs in *in-vivo* measurements.
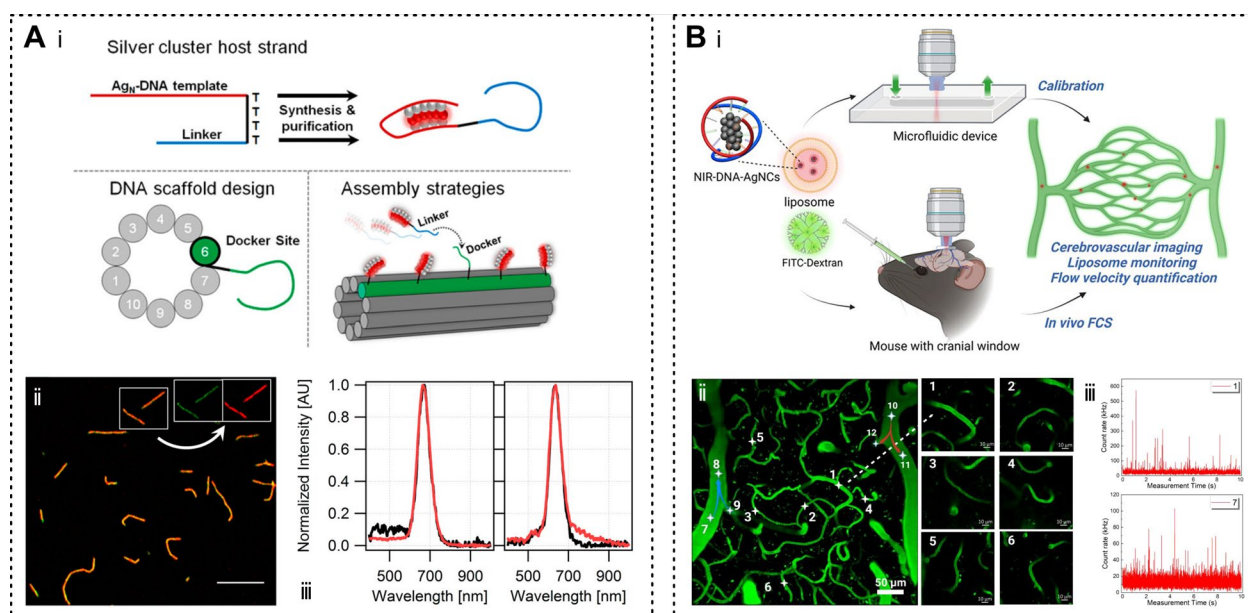
Figure 21: (A) Decoration of DNA nanostructure with DNA-AgNCs: (i) scheme of the assembly strategy DNA-AgNCs on DNA nanotubes; (ii) confocal image of decorated nanotubes and (iii) overlayed emission spectra of DNA-AgNCs with and without linker. Adapted with permission from ref.[80] Copyright 2015 American Chemical Society. (B) Encapsulation of DNA-AgNCs in liposomes for two-photon FCS: (i) workflow scheme for encapsulating the DNA-Ag$_{16}$NC in liposomes and recording the cerebral blood flow of living mice in a flow chamber; (ii) in-vivo images of the mouse's cerebral vasculature with enlarged capillary images and (iii) corresponding FCS traces. Adapted with permission from ref.[83] Copyright 2023 American Chemical Society.

The two presented approaches represent examples of imaging applications of DNA-AgNCs that have been realized through two different strategies: hybridization and encapsulation. In order to further enhance the potential of DNA-AgNCs, additional strategies for functionalizing DNA-AgNCs are required.

5.2 Click Chemistry

In 2001, Sharpless introduced the term "click chemistry" to define a series of reactions in which molecular building blocks are assembled rapidly, selectively, and irreversibly.[84] The Huisgen cycloaddition meets these criteria and consists of the reaction between organic azides and alkyne groups to form 1,2,3-triazole products.[85] The functional groups are bioorthogonal, but the reactions require high temperatures and long reaction times, which limits the use of this reaction.[86]

Meldal[87] and Sharpless[88] simultaneously introduced a copper(I) catalyst to significantly accelerate the Huisgen cycloaddition, see Figure 22A. It is stereospecific, has a high yield and produces little to no by-products. This reaction is known as copper-catalyzed azide-alkyne cycloaddition (CuAAC) and has found wide use in biology, biochemistry, and biotechnology due to its mild reaction conditions.[86]

However, the bottleneck of this reaction is that the copper(I) catalyst is cytotoxic and therefore cannot be used for *in-vivo* applications.[86] To eliminate the metal catalyst and establish the reaction in biological systems, Bertozzi developed the strain-promoted azide-alkyne cycloaddition (SPAAC),[89] see Figure 22B. The SPAAC reaction involves the cycloaddition between an activated alkyne, in particular the strained cyclooctyne, and an organic azide. The bond angle of the sp-hybridized carbons in the ring structure of cyclooctyne is bent from 180° to ~160°, enabling the cycloaddition reaction to occur without a catalyst.[86]
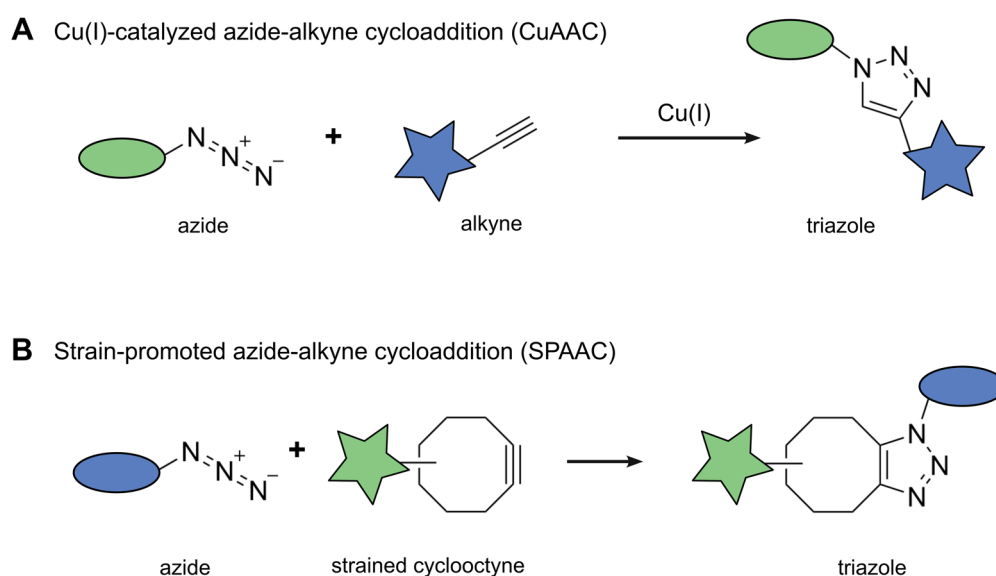
Figure 22: *Schematic illustration of the principles of Cu(I)-catalyzed azide-alkyne cycloaddition (A) and strain-promoted azide-alkyne cycloaddition (B).*

Click chemistry provides a simple approach to selectively link or label complex samples.[86] The reaction can be performed under physiological conditions with high efficiency. Purification is not necessary due to the typically high yields. Another advantage of click chemistry is the small size of the reactants, which usually do not affect the conjugated biomolecules, such as proteins.

In 2022, Sharpless, Meldal, and Bertozzi were awarded the Nobel Prize in Chemistry in recognition of click chemistry as a powerful tool for researching molecular systems, which has since found many applications, such as fluorescence labeling.

5.3 Publication 3: Conjugation of a NIR-emitting DNA-AgNC

Vanessa Rück, Narendra K. Mishra, Kasper K. Sørensen, Mikkel B. Liisberg, Ane B. Sloth, Cecilia Cerretani, Christian B. Mollerup, Andreas Kjaer, Chenguang Lou, Knud J. Jensen, Tom Vosch.

5.3.1 Motivation and Findings

DNA-AgNCs are promising candidates for bioimaging applications due to their intriguing properties. However, until now, little work has been done on conjugating the DNA scaffold of DNA-AgNCs with functional groups. The conjugation, and thus the potential to specifically label targets, is key to unlocking the potential of DNA-AgNCs as fluorophores for bioimaging applications. A potential problem, however, is that the functional group may affect the interaction of the nucleobases with the silver core, causing changes of the spectroscopic properties or a decrease in stability.

In this work, we introduce a rational design approach that overcomes this problem. We present the conjugation of a NIR-emitting DNA-AgNC to three different peptides and a small protein by copper-free click chemistry achieved by SPAAC. The need for a copper catalyst is eliminated by the spontaneous addition of a reactive, ring-strained alkyne to an azido group.[90] Our rational design is based on the known crystal structure of the DNA-Ag$_{16}$NC,[34-36] see Chapter 3. It has been shown that A10 at the 3'-end does not interact with the silver core and its removal does not influence the optical properties.[35] Therefore, the 3'-end was chosen for the addition of the functional group, bicyclononyne (BCN).

The first step consisted of preparing the DNA-Ag$_{16}$NC with the BCN group. After the single-stranded DNA oligomer was modified with the BCN group, the cluster synthesis and HPLC purification were performed. The presence of the linker showed no influence on the formation and photophysical properties of the DNA-Ag$_{16}$NC, verified by ESI-MS and spectroscopic characterization. In the next step, the actual click reaction was carried out. Three peptides of different sizes and a small protein, human insulin, were successfully conjugated to the DNA-Ag$_{16}$NC. This was confirmed by MS, HPLC and spectroscopic characterization, including time-resolved anisotropy measurements.

Subsequently, bioimaging studies were conducted on Chinese hamster ovary (CHO) cells that overexpress human insulin receptor B (hIR-B) on the membranes, see Figure 23. Confocal fluorescence microscopy and fluorescence lifetime imaging microscopy (FLIM) were used to

visualize hIR-B on the membrane. A good and specific staining of the membrane with DNA-Ag$_{16}$NC was observed. The spectroscopic properties of DNA-Ag$_{16}$NCs remained almost unaffected by the cellular environment.
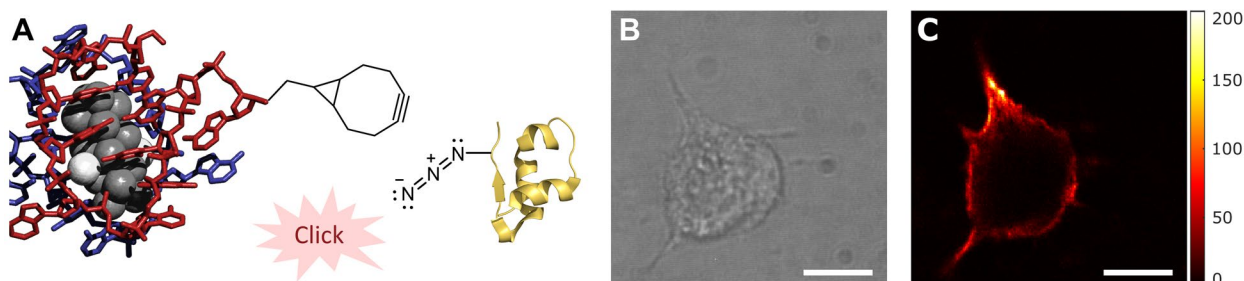
Figure 23: Bioconjugation of a NIR emissive DNA-AgNC to peptides and a small protein. (A) Schematic representation of the SPAAC reaction between the DNA-Ag$_{16}$NC functionalized with a BCN group and human insulin functionalized with an azide group. (B) Bright-field image and (C) confocal microscopy image of stained CHO cells with the DNA-Ag$_{16}$NC insulin conjugate. Scale bars: 10 µm. Adapted with permission from ref.[37] Copyright 2023 American Chemical Society.

We successfully demonstrated the conjugation of biomolecules to a purified DNA-AgNC using SPAAC. The potential of this emitter class was also revealed in bioimaging studies. The presented rational design eliminates the time-consuming testing of different DNA sequence positions to find a suitable position for conjugation. Our approach requires at least one nucleobase that does not interact with the AgNC core while retaining the original photophysical properties. The bottleneck of this approach is that the crystal structure must be solved and so far only a few crystal structures are known.[33-36] Nevertheless, this strategy opens up new application possibilities for DNA-AgNCs.

5.3.2 Contribution

After our collaboration partner modified the DNA strand, I synthesized and purified the functionalized DNA-AgNC. I performed the spectroscopic characterization of the DNA-AgNC and all conjugates. Additionally, I measured in collaboration with Christian B. Mollerup the ESI-MS of the DNA-Ag$_{16}$NC and DNA-BCN-Ag$_{16}$NC. I was also involved in the bioimaging studies on CHO cells and contributed to the writing of the manuscript.

5.4   Publication 4: Effect of single-stranded DNA on DNA-AgNC

Vanessa Rück, Cecilia Cerretani, Tom Vosch. How Inert is Single-Stranded DNA Towards DNA-Stabilized Silver Nanoclusters? A Case Study. *ChemPhotoChem* **2024**, e202400014.

5.4.1   Motivation and Findings

In DNA nanotechnology, structures are often functionalized and decorated with molecules of interest through hybridization. The idea of adding a DNA tail to the DNA-AgNCs can be easily realized by extending the DNA template and is a commonly utilized concept.[91-93] However, the formation of the cluster can be significantly influenced by the additional part designed for subsequent hybridization. It also leads to the question of how "inert" this hybridization tail is during the synthesis process. It is possible that silver cations may also bind to the hybridization tail region, thus preventing the typical Watson-Crick base pair formation upon hybridization with a complementary DNA strand.

After the successful click chemistry of DNA-Ag$_{16}$NCs to different peptides,[37] the idea of clicking the hybridization tail came up to avoid the low synthesis yield due to the formation of additional by-products and to guarantee WC base pair formation upon hybridization. However, initial click tests showed that the cluster degrades in the process. The question arose as to why this was the case. I undertook further investigation to get to the bottom of this, which was the initial motivation for the next publication.

In this publication, the chemical stability of the NIR-emitting DNA-Ag$_{16}$NC is investigated in the presence of different single-stranded DNA oligomers. The purified DNA-Ag$_{16}$NC exhibits good stability for years in 10 mM NH$_4$OAc as the cluster core is well protected by the DNA scaffold and is also compatible with chloride-containing media. It is therefore even more surprising to observe that additional single-stranded DNA strands in the media have a significant effect on the stability of the DNA-Ag$_{16}$NC. The degree of destruction depends on the particular DNA sequence being used. This indicates that there must be fewer or non-reactive motifs in the DNA sequence.

To protect the DNA-AgNC from degradation, we implemented two protection strategies. The first strategy is based on the hybridization of the bare DNA strands with the corresponding complementary sequences. The pre-hybridization of the strands reduced the destruction of the DNA-Ag$_{16}$NC, resulting in a lower drop in both the absorption and emission spectra. The second strategy showed even stronger protection. The passivation of the DNA strands with Ag$^+$ ions left the cluster almost intact and thus appears to be the best strategy to protect the cluster from destruction.

However, it should be noted that the passivated strand is now more likely to undergo silver-mediated base pairing and less likely to form WC base pairing.

Overall, it was shown that there are more or less reactive motifs whose destructive effect on the cluster can be prevented by the two presented protection strategies. The idea that hybridization tails are inert by default needs to be reconsidered. Besides Watson-Crick base pairing, metal-mediated base pairing should not be disregarded. Furthermore, this work demonstrates that free DNA strands in the solution have a major impact on the stability of DNA-AgNCs. This underlines the need for purification of DNA-AgNCs to remove free DNA strands after synthesis.

5.4.2   Contribution

I carried out the synthesis and purification of the DNA-Ag$_{16}$NC and performed all stabilization tests and data analysis. I also contributed to writing the manuscript.

6 Conclusion and Outlook

DNA-stabilized silver nanoclusters are molecular-like emitters with intriguing properties. In recent years, the understanding of the photophysical and structural properties of DNA-AgNCs has improved. However, some obstacles still need to be overcome to gain a comprehensive fundamental understanding of this class of emitters. A fundamental understanding is essential to make them attractive for biological applications. The work presented in this thesis covers a broad spectrum of the research field, from the investigation of photophysical and structural properties to conjugation strategies for applications.

Unraveling the structure-property relationship is key to correlate the photophysical properties with the structure/sequence. The challenge of obtaining high-quality crystals and high-resolution data was demonstrated in my publication on the 11Green-2end-AgNC. The cluster core and thus the arrangement of the silver atoms could be resolved, and a rod-like structure could be confirmed. Unfortunately, however, it was not possible to resolve the DNA structure encapsulating the cluster. This proves how complex and difficult it is to grow DNA-AgNCs crystals suitable for X-ray imaging. For future structure elucidation, the optimization of crystallization conditions and consideration of alternative crystallography methods such as microcrystal electron diffraction (microED) are important to accelerate progress in structure determination. The structure investigation of DNA-AgNCs remains a challenge.

Furthermore, I showed that DNA-AgNCs have exceptional properties. The dual emissive cluster presented in the second publication has very special properties. We discovered that this cluster can be used as a nanoscale light intensity meter. The dual emissive behavior has been discovered with increasing frequency for DNA-AgNCs. In general, the behavior of the clusters is very diverse and for a classification according to their properties, more purified DNA-AgNCs need to be thoroughly characterized.

Another focus of my PhD work was the conjugation of DNA-AgNCs. In order to demonstrate that DNA-AgNCs are promising candidates for biological applications, a rational conjugation strategy is very important. I implemented the copper-free click reaction to conjugate the well-studied and NIR-emitting DNA-Ag$_{16}$NC to three different peptides and a small protein. It was confirmed that the photophysical properties of DNA-Ag$_{16}$NC are not affected by the chosen conjugation strategy, which is very important for its application. This rational approach requires that the crystal structure of the cluster is known in order to select the conjugation site for functionalization and thus avoid random

testing of the possible conjugation position. The lack of structural information on other DNA-AgNCs is a major challenge, but as soon as more structural information becomes available, this rational conjugation strategy can be applied.

The NIR range is of great interest, especially the NIR-II spectral window, where tissue is relatively transparent to a depth of centimeters. So far, mainly DNA-AgNCs emitting within the visible to NIR-I window have been reported. DNA-AgNCs emitting in the NIR-II window are still rare, but DNA-AgNCs are in general very promising for deep tissue imaging, as demonstrated by the first biomedical imaging applications with NIR-I emitting DNA-AgNCs.

ML-assisted high-throughput screening is a promising approach to detect NIR-II emitting DNA-AgNCs. So far, the model was mainly based on a sequence length of 10 bases. Extending the sequence could be a promising approach to drive the formation of larger clusters. During my stay at Copp's group at the University of California Irvine, we have already performed initial tests with a 16-base sequence length. This approach will now be pursued further in order to find clusters in the NIR-II window.

In summary, DNA-AgNCs are very interesting systems with very special and promising properties. In recent years, the combination of ML-assisted high-throughput screening, detailed spectroscopic characterization, crystallization, compositional analysis, and theoretical calculations has led to significant progress in the development and fundamental understanding of DNA-AgNCs. However, further extensive studies are needed to fully exploit the potential of DNA-AgNCs.

7 References

(1)   J. T. Petty, J. Zheng, N. V. Hud, R. M. Dickson. DNA-Templated Ag Nanocluster Formation. *Journal of the American Chemical Society* **2004**, *126* (16), 5207-5212. DOI: 10.1021/ja031931o.

(2)   A. Gonzàlez-Rosell, C. Cerretani, P. Mastracco, T. Vosch, S. M. Copp. Structure and luminescence of DNA-templated silver clusters. *Nanoscale Advances* **2021**, *3* (5), 1230-1260. DOI: 10.1039/D0NA01005G.

(3)   D. Schultz, K. Gardner, S. S. R. Oemrawsingh, N. Markešević, K. Olsson, M. Debord, D. Bouwmeester, E. Gwinn. Evidence for Rod-Shaped DNA-Stabilized Silver Nanocluster Emitters. *Advanced Materials* **2013**, *25* (20), 2797-2803. DOI: 10.1002/adma.201204624.

(4)   V. A. Neacşu, C. Cerretani, M. B. Liisberg, S. M. Swasey, E. G. Gwinn, S. M. Copp, T. Vosch. Unusually large fluorescence quantum yield for a near-infrared emitting DNA-stabilized silver nanocluster. *Chemical Communications* **2020**, *56* (47), 6384-6387. DOI: 10.1039/D0CC01849J.

(5)   S. A. Bogh, M. R. Carro-Temboury, C. Cerretani, S. M. Swasey, S. M. Copp, E. G. Gwinn, T. Vosch. Unusually large Stokes shift for a near-infrared emitting DNA-stabilized silver nanocluster. *Methods Appl. Fluoresc.* **2018**, *6* (2), 024004. DOI: 10.1088/2050-6120/aaa8bc.

(6)   T. Vosch, Y. Antoku, J. C. Hsiang, C. I. Richards, J. I. Gonzalez, R. M. Dickson. Strongly emissive individual DNA-encapsulated Ag nanoclusters as single-molecule fluorophores. *Proceedings of the National Academy of Sciences* **2007**, *104* (31), 12616-12621. DOI: 10.1073/pnas.0610677104.

(7)   T.-H. Lee, J. I. Gonzalez, J. Zheng, R. M. Dickson. Single-Molecule Optoelectronics. *Accounts of Chemical Research* **2005**, *38* (7), 534-541. DOI: 10.1021/ar040146t.

(8)   T. Pradeep. *Atomically precise metal nanoclusters*; Elsevier, **2023**.

(9)   G. Schmid, M. Baumle, M. Geerkens, Helm, C. Osemann, T. Sawitowski. Current and future applications of nanoclusters. *Chemical Society reviews* **1999**, *28* (3), 179-185. DOI: 10.1039/a801153b.

(10)   N. Cathcart, P. Mistry, C. Makra, B. Pietrobon, N. Coombs, M. Jelokhani-Niaraki, V. Kitaev. Chiral Thiol-Stabilized Silver Nanoclusters with Well-Resolved Optical Transitions Synthesized by a Facile Etching Procedure in Aqueous Solutions. *Langmuir* **2009**, *25* (10), 5840-5846. DOI: 10.1021/la9005967.

(11)   J. Yu, S. A. Patel, R. M. Dickson. In Vitro and Intracellular Production of Peptide-Encapsulated Fluorescent Silver Nanoclusters. *Angewandte Chemie International Edition* **2007**, *46* (12), 2028-2030. DOI: 10.1002/anie.200604253.

(12)   J. Zheng, R. M. Dickson. Individual Water-Soluble Dendrimer-Encapsulated Silver Nanodot Fluorescence. *Journal of the American Chemical Society* **2002**, *124* (47), 13982-13983. DOI: 10.1021/ja028282l.

(13)   S. Dey, C. Fan, K. V. Gothelf, J. Li, C. Lin, L. Liu, N. Liu, M. A. D. Nijenhuis, B. Saccà, F. C. Simmel, et al. DNA origami. *Nature Reviews Methods Primers* **2021**, *1* (1), 13. DOI: 10.1038/s43586-020-00009-8.

(14)   J. Kondo, Y. Tada, T. Dairaku, Y. Hattori, H. Saneyoshi, A. Ono, Y. Tanaka. A metallo-DNA nanowire with uninterrupted one-dimensional silver array. *Nature Chemistry* **2017**, *9* (10), 956-960. DOI: 10.1038/nchem.2808.

(15)   J. Müller. Nucleic acid duplexes with metal-mediated base pairs and their structures. *Coordination Chemistry Reviews* **2019**, *393*, 37-47. DOI: 10.1016/j.ccr.2019.05.007.

(16)   P. Scharf, J. Müller. Nucleic Acids With Metal-Mediated Base Pairs and Their Applications. *ChemPlusChem* **2013**, *78* (1), 20-34. DOI: 10.1002/cplu.201200256.

(17)   S. M. Swasey, F. Rosu, S. M. Copp, V. Gabelica, E. G. Gwinn. Parallel Guanine Duplex and Cytosine Duplex DNA with Uninterrupted Spines of AgI-Mediated Base Pairs. *The Journal of Physical Chemistry Letters* **2018**, *9* (22), 6605-6610. DOI: 10.1021/acs.jpclett.8b02851.

(18)   S. M. Swasey, L. E. Leal, O. Lopez-Acevedo, J. Pavlovich, E. G. Gwinn. Silver (I) as DNA glue: Ag+-mediated guanine pairing revealed by removing Watson-Crick constraints. *Scientific Reports* **2015**, *5* (1), 10163. DOI: 10.1038/srep10163.

(19)   S. M. Copp, A. Gorovits, S. M. Swasey, S. Gudibandi, P. Bogdanov, E. G. Gwinn. Fluorescence Color by Data-Driven Design of Genomic Silver Clusters. *ACS Nano* **2018**, *12* (8), 8240-8247. DOI: 10.1021/acsnano.8b03404.

(20)   S. M. Copp, D. Schultz, S. Swasey, J. Pavlovich, M. Debord, A. Chiu, K. Olsson, E. Gwinn. Magic Numbers in DNA-Stabilized Fluorescent Silver Clusters Lead to Magic Colors. *The Journal of Physical Chemistry Letters* **2014**, *5* (6), 959-963. DOI: 10.1021/jz500146q.

(21)   S. Zhu, B. C. Yung, S. Chandra, G. Niu, A. L. Antaris, X. Chen. Near-Infrared-II (NIR-II) Bioimaging via Off-Peak NIR-I Fluorescence Emission. *Theranostics* **2018**, *8* (15), 4141-4151. DOI: 10.7150/thno.27995.

(22)   S. Zhu, R. Tian, A. L. Antaris, X. Chen, H. Dai. Near-Infrared-II Molecular Dyes for Cancer Imaging and Surgery. *Advanced Materials* **2019**, *31* (24), e1900321-n/a. DOI: 10.1002/adma.201900321.

(23)   J. Cao, B. Zhu, K. Zheng, S. He, L. Meng, J. Song, H. Yang. Recent Progress in NIR-II Contrast Agent for Biological Imaging. *Frontiers in Bioengineering and Biotechnology* **2020**, *7*, 487. DOI: 10.3389/fbioe.2019.00487.

(24)   V. J. Pansare, S. Hejazi, W. J. Faenza, R. K. Prud'homme. Review of Long-Wavelength Optical and NIR Imaging Materials: Contrast Agents, Fluorophores, and Multifunctional Nano Carriers. *Chemistry of materials* **2012**, *24* (5), 812-827. DOI: 10.1021/cm2028367.

(25)   Z. Deutsch, O. Schwartz, R. Tenne, R. Popovitz-Biro, D. Oron. Two-Color Antibunching from Band-Gap Engineered Colloidal Semiconductor Nanocrystals. *Nano Letters* **2012**, *12* (6), 2948-2952. DOI: 10.1021/nl300638t.

(26)   F. Fuchs, B. Stender, M. Trupke, D. Simin, J. Pflaum, V. Dyakonov, G. V. Astakhov. Engineering near-infrared single-photon emitters with optically active spins in ultrapure silicon carbide. *Nat Commun* **2015**, *6* (1), 7578-7578. DOI: 10.1038/ncomms8578.

(27)   M. Fu, P. Tamarat, J.-B. Trebbia, M. I. Bodnarchuk, M. V. Kovalenko, J. Even, B. Lounis. Unraveling exciton–phonon coupling in individual FAPbI3 nanocrystals emitting near-infrared single photons. *Nat Commun* **2018**, *9* (1), 3318. DOI: 10.1038/s41467-018-05876-0.

(28)   M. B. Liisberg, Z. Shakeri Kardar, S. M. Copp, C. Cerretani, T. Vosch. Single-Molecule Detection of DNA-Stabilized Silver Nanoclusters Emitting at the NIR I/II Border. *The Journal of Physical Chemistry Letters* **2021**, *12* (4), 1150-1154. DOI: 10.1021/acs.jpclett.0c03688.

(29)   E. N. Hooley, V. Paolucci, Z. Liao, M. R. Carro Temboury, T. Vosch. Single-Molecule Characterization of Near-Infrared-Emitting Silver Nanoclusters. *Advanced Optical Materials* **2015**, *3* (8), 1109-1115. DOI: 10.1002/adom.201500048.

(30)   S. M. Swasey, S. M. Copp, H. C. Nicholson, A. Gorovits, P. Bogdanov, E. G. Gwinn. High throughput near infrared screening discovers DNA-templated silver clusters with peak fluorescence beyond 950 nm. *Nanoscale* **2018**, *10* (42), 19701-19705. DOI: 10.1039/C8NR05781H.

(31)   P. Mastracco, A. Gonzàlez-Rosell, J. Evans, P. Bogdanov, S. M. Copp. Chemistry-Informed Machine Learning Enables Discovery of DNA-Stabilized Silver Nanoclusters with Near-Infrared Fluorescence. *ACS Nano* **2022**, *16* (10), 16322-16331. DOI: 10.1021/acsnano.2c05390.

(32)   R. Guha, S. M. Copp. Nucleic Acid-Templated Metal Nanoclusters. In *Modern Avenues in Metal-Nucleic Acid Chemistry*, 1 ed.; Vol. 25; CRC Press, **2023**; pp 291-342.

(33)   D. J. E. Huard, A. Demissie, D. Kim, D. Lewis, R. M. Dickson, J. T. Petty, R. L. Lieberman. Atomic Structure of a Fluorescent Ag8 Cluster Templated by a Multistranded DNA Scaffold. *Journal of the American Chemical Society* **2019**, *141* (29), 11465-11470. DOI: 10.1021/jacs.8b12203.

(34)   C. Cerretani, H. Kanazawa, T. Vosch, J. Kondo. Crystal structure of a NIR-Emitting DNA-Stabilized Ag16 Nanocluster. *Angewandte Chemie International Edition* **2019**, *58* (48), 17153-17157. DOI: 10.1002/anie.201906766.

(35)   C. Cerretani, J. Kondo, T. Vosch. Removal of the A10 adenosine in a DNA-stabilized Ag16 nanocluster. *RSC Advances* **2020**, *10* (40), 23854-23860. DOI: 10.1039/D0RA02672G.

(36)   C. Cerretani, J. Kondo, T. Vosch. Mutation of position 5 as a crystal engineering tool for a NIR-emitting DNA-stabilized Ag16 nanocluster. *CrystEngComm* **2020**, *22* (46), 8136-8141. DOI: 10.1039/D0CE01225D.

(37)   V. Rück, N. K. Mishra, K. K. Sørensen, M. B. Liisberg, A. B. Sloth, C. Cerretani, C. B. Mollerup, A. Kjaer, C. Lou, K. J. Jensen, et al. Bioconjugation of a Near-Infrared DNA-Stabilized Silver Nanocluster to Peptides and Human Insulin by Copper-Free Click Chemistry. *Journal of the American Chemical Society* **2023**, *145* (30), 16771-16777. DOI: 10.1021/jacs.3c04768.

(38)   C. Cerretani. Photophysical and structural characterisation of emissive DNA-templated silver nanoclusters. PhD thesis, University of Copenhagen, Copenhagen, **2020**.

(39)   E. Gwinn, D. Schultz, S. M. Copp, S. Swasey. DNA-Protected Silver Clusters for Nanophotonics. *Nanomaterials* **2015**, *5* (1), 180-207. DOI: 10.3390/nano5010180.

(40)   E. Bethur, R. Guha, Z. Zhao, B. B. Katz, P. D. Ashby, H. Zeng, S. M. Copp. Formation and Nanomechanical Properties of Silver-Mediated Guanine DNA Duplexes in Aqueous Solution. *ACS Nano* **2024**, *18* (4), 3002-3010. DOI: 10.1021/acsnano.3c08008.

(41)   J. R. Lakowicz. *Principles of Fluorescence Spectroscopy*; Springer, **2006**. DOI: 10.1007/978-0-387-46312-4.

(42)   A. M. Brouwer. Standards for photoluminescence quantum yield measurements in solution (IUPAC Technical Report). *Pure and Applied Chemistry* **2011**, *83* (12), 2213-2228. DOI: 10.1351/PAC-REP-10-09-31.

(43)   A. Gonzàlez-Rosell, S. Malola, R. Guha, N. R. Arevalos, M. F. Matus, M. E. Goulet, E. Haapaniemi, B. B. Katz, T. Vosch, J. Kondo, et al. Chloride Ligands on DNA-Stabilized Silver Nanoclusters. *Journal of the American Chemical Society* **2023**, *145* (19), 10721-10729. DOI: 10.1021/jacs.3c01366.

(44)   E. Largy, A. König, A. Ghosh, D. Ghosh, S. Benabou, F. Rosu, V. Gabelica. Mass Spectrometry of Nucleic Acid Noncovalent Complexes. *Chemical Reviews* **2022**, *122* (8), 7720-7839. DOI: 10.1021/acs.chemrev.1c00386.

(45)   A. F. Wells. *Structural inorganic chemistry*; Oxford University Press, Clarendon Press, **1984**.

(46)   A. Bondi. van der Waals Volumes and Radii. *The Journal of Physical Chemistry* **1964**, *68* (3), 441-451. DOI: 10.1021/j100785a001.

(47) S. Malola, H. Häkkinen. On transient absorption and dual emission of the atomically precise, DNA-stabilized silver nanocluster Ag16Cl2. *Chemical Communications* **2024**, *60* (24), 3315-3318. DOI: 10.1039/D3CC06085C.

(48) S. Malola, M. F. Matus, H. Häkkinen. Theoretical Analysis of the Electronic Structure and Optical Properties of DNA-Stabilized Silver Cluster Ag16Cl2 in Aqueous Solvent. *The Journal of Physical Chemistry C* **2023**, *127* (33), 16553-16559. DOI: 10.1021/acs.jpcc.3c04103.

(49) N. E. Chayen, E. Saridakis. Protein crystallization: from purified protein to diffraction-quality crystal. *Nature Methods* **2008**, *5* (2), 147-153. DOI: 10.1038/nmeth.f.203.

(50) I. Russo Krauss, A. Merlino, A. Vergara, F. Sica. An Overview of Biological Macromolecule Crystallization. *International Journal of Molecular Sciences* **2013**, *14* (6), 11643-11691. DOI: 10.3390/ijms140611643.

(51) N. E. Chayen, T. J. Boggon, A. Cassetta, A. Deacon, T. Gleichmann, J. Habash, S. J. Harrop, J. R. Helliwell, Y. P. Nieh, M. R. Peterson, et al. Trends and Challenges in Experimental Macromolecular Crystallography. *Quarterly Reviews of Biophysics* **1996**, *29* (3), 227-278. DOI: 10.1017/S0033583500005837.

(52) R. Giegé, A. Ducruix. *Crystallization of nucleic acids and proteins : a practical approach*; Oxford University Press, **1999**.

(53) A. McPherson. *Crystallization of biological macromolecules*; Cold Spring Harbor Laboratory Press, **1999**.

(54) V. Rück, V. A. Neacşu, M. B. Liisberg, C. B. Mollerup, P. H. Ju, T. Vosch, J. Kondo, C. Cerretani. Atomic Structure of a DNA-Stabilized Ag$_{11}$ Nanocluster with Four Valence Electrons. *Advanced Optical Materials* **2024**, *12* (7), 2301928. DOI: 10.1002/adom.202301928.

(55) D. M. Blow. *Outline of crystallography for biologists*; Oxford University Press, **2002**.

(56) A. A. Bunaciu, E. g. Udriştioiu, H. Y. Aboul-Enein. X-Ray Diffraction: Instrumentation and Applications. *Critical Reviews in Analytical Chemistry* **2015**, *45* (4), 289-299. DOI: 10.1080/10408347.2014.949616.

(57) P. R. O'Neill, E. G. Gwinn, D. K. Fygenson. UV Excitation of DNA Stabilized Ag Cluster Fluorescence via the DNA Bases. *The Journal of Physical Chemistry C* **2011**, *115* (49), 24061-24066. DOI: 10.1021/jp206110r.

(58) D. Schultz, S. M. Copp, N. Markešević, K. Gardner, S. S. R. Oemrawsingh, D. Bouwmeester, E. Gwinn. Dual-Color Nanoscale Assemblies of Structurally Stable, Few-Atom Silver Clusters, As Reported by Fluorescence Resonance Energy Transfer. *ACS Nano* **2013**, *7* (11), 9798-9807. DOI: 10.1021/nn4033097.

(59) S. M. Copp, A. Gonzàlez-Rosell. Large-scale investigation of the effects of nucleobase sequence on fluorescence excitation and Stokes shifts of DNA-stabilized silver clusters. *Nanoscale* **2021**, *13* (8), 4602-4613. DOI: 10.1039/D0NR08300C.

(60) S. A. Patel, M. Cozzuol, J. M. Hales, C. I. Richards, M. Sartin, J.-C. Hsiang, T. Vosch, J. W. Perry, R. M. Dickson. Electron Transfer-Induced Blinking in Ag Nanodot Fluorescence. *The Journal of Physical Chemistry C* **2009**, *113* (47), 20264-20270. DOI: 10.1021/jp9079537.

(61) E. Thyrhaug, S. A. Bogh, M. R. Carro-Temboury, C. S. Madsen, T. Vosch, D. Zigmantas. Ultrafast coherence transfer in DNA-templated silver nanoclusters. *Nat Commun* **2017**, *8* (1), 15577. DOI: 10.1038/ncomms15577.

(62) S. Krause, M. R. Carro-Temboury, C. Cerretani, T. Vosch. Probing heterogeneity of NIR induced secondary fluorescence from DNA-stabilized silver nanoclusters at the single molecule level. *Physical Chemistry Chemical Physics* **2018**, *20* (24), 16316-16319. DOI: 10.1039/C8CP02584C.

(63) J. T. Petty, S. Carnahan, D. Kim, D. Lewis. Long-lived Ag106+ luminescence and a split DNA scaffold. *The Journal of Chemical Physics* **2021**, *154* (24). DOI: 10.1063/5.0056214.

(64) V. Rück, C. Cerretani, V. A. Neacșu, M. B. Liisberg, T. Vosch. Observation of microsecond luminescence while studying two DNA-stabilized silver nanoclusters emitting in the 800–900 nm range. *Physical Chemistry Chemical Physics* **2021**, *23* (24), 13483-13489. DOI: 10.1039/D1CP01731D.

(65) J. Chen, A. Kumar, C. Cerretani, T. Vosch, D. Zigmantas, E. Thyrhaug. Excited-State Dynamics in a DNA-Stabilized Ag16 Cluster with Near-Infrared Emission. *The Journal of Physical Chemistry Letters* **2023**, *14* (17), 4078-4083. DOI: 10.1021/acs.jpclett.3c00764.

(66) C. Cerretani, G. Palm-Henriksen, M. B. Liisberg, T. Vosch. The effect of deuterium on the photophysical properties of DNA-stabilized silver nanoclusters. *Chemical Science* **2021**, *12* (48), 16100-16105. DOI: 10.1039/D1SC05079F.

(67) C. Cerretani, T. Vosch. Switchable Dual-Emissive DNA-Stabilized Silver Nanoclusters. *ACS Omega* **2019**, *4* (4), 7895-7902. DOI: 10.1021/acsomega.9b00614.

(68) C. Cerretani, M. R. Carro-Temboury, S. Krause, S. A. Bogh, T. Vosch. Temperature dependent excited state relaxation of a red emitting DNA-templated silver nanocluster. *Chemical Communications* **2017**, *53* (93), 12556-12559. DOI: 10.1039/C7CC06785B.

(69) L. Stryer. Excited-state proton-transfer reactions. A deuterium isotope effect on fluorescence. *Journal of the American Chemical Society* **1966**, *88* (24), 5708-5712.

(70) J. L. Kropp, M. W. Windsor. Enhancement of Fluorescence Yield of Rare-Earth Ions by Heavy Water. *The Journal of Chemical Physics* **1963**, *39* (10), 2769-2770.

(71) C. I. Richards, J.-C. Hsiang, D. Senapati, S. Patel, J. Yu, T. Vosch, R. M. Dickson. Optically Modulated Fluorophores for Selective Fluorescence Signal Recovery. *Journal of the American Chemical Society* **2009**, *131* (13), 4619-4621. DOI: 10.1021/ja809785s.

(72) B. C. Fleischer, J. T. Petty, J.-C. Hsiang, R. M. Dickson. Optically Activated Delayed Fluorescence. *The Journal of Physical Chemistry Letters* **2017**, *8* (15), 3536-3543. DOI: 10.1021/acs.jpclett.7b01215.

(73) S. Krause, M. R. Carro-Temboury, C. Cerretani, T. Vosch. Anti-Stokes fluorescence microscopy using direct and indirect dark state formation. *Chemical Communications* **2018**, *54* (36), 4569-4572. DOI: 10.1039/C8CC01521J.

(74) S. Krause, C. Cerretani, T. Vosch. Disentangling optically activated delayed fluorescence and upconversion fluorescence in DNA stabilized silver nanoclusters. *Chemical Science* **2019**, *10* (20), 5326-5331. DOI: 10.1039/C9SC00865A.

(75) M. B. Liisberg, S. Krause, C. Cerretani, T. Vosch. Probing emission of a DNA-stabilized silver nanocluster from the sub-nanosecond to millisecond timescale in a single measurement. *Chemical Science* **2022**, *13* (19), 5582-5587. DOI: 10.1039/D2SC01137A.

(76) V. Rück, M. B. Liisberg, C. B. Mollerup, Y. He, J. Chen, C. Cerretani, T. Vosch. A DNA-Stabilized Ag_{18}^{12+} Cluster with Excitation-Intensity-Dependent Dual Emission. *Angewandte Chemie International Edition* **2023**, *62* (39), e202309760. DOI: 10.1002/anie.202309760.

(77) P. Reineck, B. C. Gibson. Near-Infrared Fluorescent Nanomaterials for Bioimaging and Sensing. *Advanced Optical Materials* **2017**, *5* (2), 1600446. DOI: 10.1002/adom.201600446.

(78) L. Rolband, L. Yourston, M. Chandler, D. Beasock, L. Danai, S. Kozlov, N. Marshall, O. Shevchenko, A. V. Krasnoslobodtsev, K. A. Afonin. DNA-Templated Fluorescent Silver Nanoclusters Inhibit Bacterial Growth While Being Non-Toxic to Mammalian Cells. *Molecules* **2021**, *26* (13), 4045. DOI: 10.3390/molecules26134045.

(79) G. Hong, A. L. Antaris, H. Dai. Near-infrared fluorophores for biomedical imaging. *Nature Biomedical Engineering* **2017**, *1* (1), 0010. DOI: 10.1038/s41551-016-0010.

(80) S. M. Copp, D. E. Schultz, S. Swasey, E. G. Gwinn. Atomically Precise Arrays of Fluorescent Silver Clusters: A Modular Approach for Metal Cluster Photonics on DNA Nanostructures. *ACS Nano* **2015**, *9* (3), 2303-2310. DOI: 10.1021/nn506322q.

(81) P. W. K. Rothemund. Folding DNA to create nanoscale shapes and patterns. *Nature* **2006**, *440* (7082), 297-302. DOI: 10.1038/nature04586.

(82) R. Schreiber, J. Do, E.-M. Roller, T. Zhang, V. J. Schüller, P. C. Nickels, J. Feldmann, T. Liedl. Hierarchical assembly of metal nanoparticles, quantum dots and organic dyes using DNA origami scaffolds. *Nature Nanotechnology* **2014**, *9* (1), 74-78. DOI: 10.1038/nnano.2013.253.

(83) X. Wang, M. B. Liisberg, G. L. Nolt, X. Fu, C. Cerretani, L. Li, L. A. Johnson, T. Vosch, C. I. Richards. DNA-AgNC Loaded Liposomes for Measuring Cerebral Blood Flow Using Two-Photon Fluorescence Correlation Spectroscopy. *ACS Nano* **2023**, *17* (13), 12862-12874. DOI: 10.1021/acsnano.3c04489.

(84) H. C. Kolb, M. G. Finn, K. B. Sharpless. Click Chemistry: Diverse Chemical Function from a Few Good Reactions. *Angewandte Chemie International Edition* **2001**, *40* (11), 2004-2021. DOI: 10.1002/1521-3773(20010601)40:11<2004::AID-ANIE2004>3.0.CO;2-5.

(85) R. Huisgen. 1,3-Dipolar Cycloadditions. Past and Future. *Angewandte Chemie International Edition* **1963**, *2* (10), 565-598. DOI: 10.1002/anie.196305651.

(86) N. Z. Fantoni, A. H. El-Sagheer, T. Brown. A Hitchhiker's Guide to Click-Chemistry with Nucleic Acids. *Chemical Reviews* **2021**, *121* (12), 7122-7154. DOI: 10.1021/acs.chemrev.0c00928.

(87) C. W. Tornøe, C. Christensen, M. Meldal. Peptidotriazoles on Solid Phase: [1,2,3]-Triazoles by Regiospecific Copper(I)-Catalyzed 1,3-Dipolar Cycloadditions of Terminal Alkynes to Azides. *The Journal of Organic Chemistry* **2002**, *67* (9), 3057-3064. DOI: 10.1021/jo011148j.

(88) V. V. Rostovtsev, L. G. Green, V. V. Fokin, K. B. Sharpless. A Stepwise Huisgen Cycloaddition Process: Copper(I)-Catalyzed Regioselective "Ligation" of Azides and Terminal Alkynes. *Angewandte Chemie International Edition* **2002**, *41* (14), 2596-2599. DOI: 10.1002/1521-3773(20020715)41:14<2596::AID-ANIE2596>3.0.CO;2-4.

(89) N. J. Agard, J. A. Prescher, C. R. Bertozzi. A Strain-Promoted [3 + 2] Azide–Alkyne Cycloaddition for Covalent Modification of Biomolecules in Living Systems. *Journal of the American Chemical Society* **2004**, *126* (46), 15046-15047. DOI: 10.1021/ja044996f.

(90) E. Kim, H. Koo. Biomedical applications of copper-free click chemistry: in vitro, in vivo, and ex vivo. *Chemical Science* **2019**, *10* (34), 7835-7851. DOI: 10.1039/C9SC03368H.

(91) H.-C. Yeh, J. Sharma, J. J. Han, J. S. Martinez, J. H. Werner. A DNA–Silver Nanocluster Probe That Fluoresces upon Hybridization. *Nano Letters* **2010**, *10* (8), 3106-3110. DOI: 10.1021/nl101773c.

(92) P. Shah, A. Rørvig-Lund, S. B. Chaabane, P. W. Thulstrup, H. G. Kjaergaard, E. Fron, J. Hofkens, S. W. Yang, T. Vosch. Design Aspects of Bright Red Emissive Silver Nanoclusters/DNA Probes for MicroRNA Detection. *ACS Nano* **2012**, *6* (10), 8803-8814. DOI: 10.1021/nn302633q.

(93) J. T. Petty, S. P. Story, S. Juarez, S. S. Votto, A. G. Herbst, N. N. Degtyareva, B. Sengupta. Optical Sensing by Transforming Chromophoric Silver Clusters in DNA Nanoreactors. *Analytical Chemistry* **2012**, *84* (1), 356-364. DOI: 10.1021/ac202697d.

8 Appended Publications

Publication 1:

Vanessa Rück, Vlad A. Neacşu, Mikkel B. Liisberg, Christian B. Mollerup, Park Hee Ju, Tom Vosch, Jiro Kondo, Cecilia Cerretani. Atomic Structure of a DNA-Stabilized Ag_{11} Nanocluster with Four Valence Electrons. *Adv. Optical Mater.* **2024**, *12* (7), 2301928.

Publication 2:

Vanessa Rück, Mikkel B. Liisberg, Christian Brinch Mollerup, Yanmei He, Junsheng Chen, Cecilia Cerretani, Tom Vosch. A DNA-Stabilized Ag_{18}^{12+} Cluster with Excitation-Intensity-Dependent Dual Emission. *Angew. Chem. Int. Ed.* **2023**, *62* (39), e20230976

Publication 3:

Vanessa Rück, Narendra K. Mishra, Kasper K. Sørensen, Mikkel B. Liisberg, Ane B. Sloth, Cecilia Cerretani, Christian B. Mollerup, Andreas Kjaer, Chenguang Lou, Knud J. Jensen, Tom Vosch. Bioconjugation of a Near-Infrared DNA-Stabilized Silver Nanocluster to Peptides and Human Insulin by Copper-Free Click Chemistry. *J. Am. Chem. Soc.* **2023**, *145* (30), 16771–16777.

Publication 4:

Vanessa Rück, Cecilia Cerretani, Tom Vosch. How Inert is Single-Stranded DNA Towards DNA-Stabilized Silver Nanoclusters? A Case Study. *ChemPhotoChem* **2024**, e202400014.

Publication 1

Atomic Structure of a DNA-Stabilized Ag$_{11}$ Nanocluster with Four Valence Electrons

Vanessa Rück, Vlad A. Neacşu, Mikkel B. Liisberg, Christian B. Mollerup, Park Hee Ju, Tom Vosch, Jiro Kondo, Cecilia Cerretani.
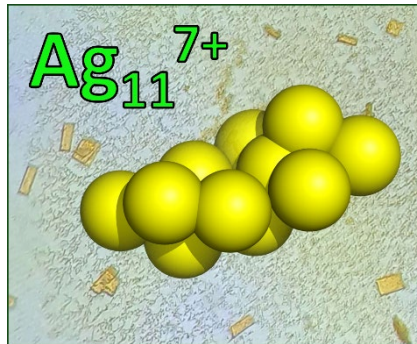
Atomic Structure of a DNA-Stabilized Ag$_{11}$ Nanocluster with Four Valence Electrons

Vanessa Rück, Vlad A. Neacşu, Mikkel B. Liisberg, Christian B. Mollerup, Park Hee Ju, Tom Vosch,* Jiro Kondo,* and Cecilia Cerretani*

The combination of mass spectrometry and single crystal X-ray diffraction of HPLC-purified DNA-stabilized silver nanoclusters (DNA-AgNCs) is a powerful tool to determine the charge and structure of the encapsulated AgNC. Such information is not only relevant to design new DNA-AgNCs with tailored properties, but it is also important for bio-conjugation experiments and is essential for electronic structure calculations. Here, the efforts to determine the structure of a HPLC-purified green emissive DNA-AgNC are presented. Unfortunately, the original DNA-AgNC, known to have four valence electrons, could not be crystallized. By modifying the stabilizing DNA sequence, while maintaining the original spectroscopic properties, several mutants could be successfully crystallized, and for one of them, single crystal X-ray diffraction data provided insight into the silver positions. While the DNA conformation is not resolved, the described approach provides valuable insight into the class of green and dual emissive DNA-AgNCs with four valence electrons. These results constitute a roadmap on how to improve crystallization and crystal quality for X-ray diffraction measurements.

V. Rück, V. A. Neacşu, M. B. Liisberg, T. Vosch, C. Cerretani
Department of Chemistry
University of Copenhagen
Universitetsparken 5, Copenhagen 2100, Denmark
E-mail: tom@chem.ku.dk; cece@chem.ku.dk

V. A. Neacşu
Department of Chemistry
City University of Hong Kong
83 Tat Chee Avenue, Kowloon Tong, Hong Kong 999077, China

C. B. Mollerup
Department of Forensic Medicine
University of Copenhagen
Frederik V's Vej 11, Copenhagen 2100, Denmark

P. H. Ju, J. Kondo
Department of Materials and Life Sciences
Sophia University
7-1 Kioi-cho, Chiyoda-ku, Tokyo 102-8554, Japan
E-mail: j.kondo@sophia.ac.jp

1. Introduction

DNA-stabilized silver nanoclusters (DNA-AgNCs) are water-soluble emitters formed by cationic and neutral silver atoms embedded in short DNA oligomers (10-30 bases).[1] Insight into the relationship between the DNA scaffold and the stabilized AgNCs has been achieved by the availability of large screening libraries and machine-learning-assisted predictions.[2] Additionally, purification methods such as size-exclusion chromatography (SEC)[3] and high-performance liquid chromatography (HPLC),[3b,4] have been paramount in isolating atomically-precise DNA-AgNCs. This has not only facilitated detailed photophysical characterization but also size and charge determination by mass spectrometry, which demonstrated the relation between the number of neutral Ag atoms (5s^1 valence electrons) and the emission color.[5] However, single crystal X-ray diffraction measurements are still needed to gain insight into the atomic arrangement of the silver atoms, the coordinate bonds to the DNA and the overall DNA conformation. In 2019, Huard et al. reported the structure of a green-emitting (DNA)$_2$Ag$_8$NC,[6] while consecutive manuscripts by Cerretani et al. have described the structure of a NIR emissive Ag$_{16}$NC and seven mutations thereof.[7] When the crystal structure of this NIR emitter was published,[7d] no mass spectrum was available and some electron density was assigned to two additional silver atoms with low occupancy (≈0.3). However, Gonzàlez-Rosell et al. recently combined mass spectrometry with a re-evaluation of the X-ray data to demonstrate the presence of two chloride ligands in the DNA-Ag$_{16}$NC structure.[8] The electron density of a chloride ion is indeed approximately one-third of that of silver, and the experimental mass data was consistent with the theoretical isotopic distribution of (DNA)$_2$[Ag$_{16}$Cl$_2$]$^{8+}$. These results highlight the importance of combining mass spectrometry with single crystal X-ray diffraction measurements to unravel the overall structure of this class of complex emitters.

While structure determination from crystallized DNA-AgNCs together with mass spectrometry provides a wealth of information, each individual step is neither trivial nor guaranteed to succeed. In this article, we have summarized our strategies to crystallize and solve the atomic structure of a recurring type of green emissive DNA-AgNC, the 4-valence-electron

**ADVANCED
SCIENCE NEWS**
www.advancedsciencenews.com

**ADVANCED
OPTICAL
MATERIALS**
www.advopticalmat.de

Table 1. Overview of the steady-state and time-resolved solution data of 10Green-AgNC and derived mutants.

Sample	DNA sequence	λ_{abs} [nm]	λ_{em} [nm]	$<\tau>$ [ns]	Q
10Green-AgNC	TCC ACG AGA A	472	535	0.65	0.11[a]
11Green-AgNC	**A** TCC ACG AGA A	472	535	0.88	0.14[a]
5A-11Green-AgNC	**AA** TCC ACG AGA A	472	536	0.70	0.09[a] /0.10[b]
5AA-11Green-AgNC	**AAA** TCC ACG AGA A	472	536	0.70	0.10[b]
5TA-11Green-AgNC	**TAA** TCC ACG AGA A	473	537	0.73	0.13[b]
5T-11Green-AgNC	**TA** TCC ACG AGA A	472	536	0.77	0.10[b]
5T-3T-11Green-AgNC	**TA** TCC ACG AGA A**T**	470	535	0.69	0.09[b]
3T-11Green-AgNC	**A** TCC ACG AGA A**T**	473	535	0.80	0.13[b]
3A-11Green-AgNC	**A** TCC ACG AGA A**A**	472	536	0.80	0.13[b]
BrC3-11Green-AgNC	**A TC(Br)**C ACG AGA A	471	537	0.60	0.07[b]
11Green-2end-AgNC	**A** TCC ACG AG	470	534	0.42	0.04[a]
5A-11Green-2end-AgNC	**AA** TCC ACG AG	471	536	0.37	0.07[b]

λ_{abs} and λ_{em} are, respectively, the absorption and emission (λ_{exc} = 469.5 nm) maxima measured at room temperature in 10 mM NH$_4$OAc. $<\tau>$ is the intensity-weighted average decay time monitored at 535 nm, exciting at 469.5 nm. Q is the fluorescence quantum yield measured at room temperature (λ_{exc} = 445.4 nm). [a] Q determined with a relative method, using Fluorescein in 0.1 M NaOH as reference dye.[12] [b] Q estimated using a single measurement for the fraction of absorbed light and a single measurement of the integrated emission. As shown for 5A-11Green-AgNC, the two methods give comparable Q values. See Supporting Information for more details.

[Ag$_{11}$]$^{7+}$/[Ag$_{10}$]$^{6+}$ system. For this purpose, we chose the (DNA)$_2$-[Ag$_{11}$]$^{7+}$ NC, further defined as 10Green-AgNC, previously reported by Copp et al.[5] The aim was to combine mass spectrometry results with structural information from single crystal X-ray diffraction data. Since the original DNA-AgNC could not be crystallized, the stabilizing DNA sequence was modified in several ways, while retaining the spectroscopic properties of the embedded cluster. X-ray diffraction data of one of the mutants provided insight into the arrangement of the silver atoms.

Our path to obtain well-diffracting DNA-AgNC crystals, combined with mass spectrometry and photophysical characterization, can be a roadmap for unraveling the structure/spectroscopic property relationship of other types of DNA-AgNCs.

2. Results and Discussion

2.1. Modification of 10Green-AgNC for Crystallization

The original mass spectrometry data of 10Green-AgNC was published in 2014 by Copp et al.[5] The green emissive
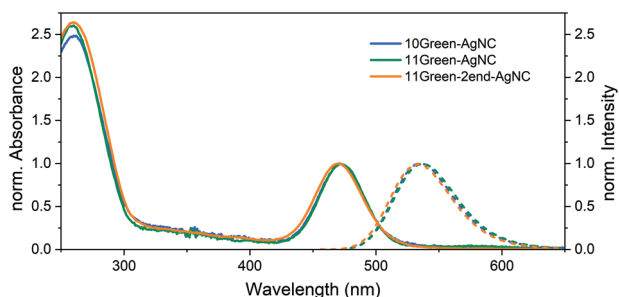
Figure 1. Overlay of normalized absorption (solid lines) and emission spectra (dashed lines) of 10Green-AgNC, 11Green-AgNC and 11Green-2end-AgNC in 10 mM ammonium acetate (NH$_4$OAc) at room temperature. The emission spectra were recorded exciting at 469.5 nm.

10Green-AgNC is composed by two 10-base DNA stands, 5'-TCCACGAGAA-3', wrapped around eleven silver atoms, of which four are neutral and the remaining seven are cationic ([Ag$_{11}$]$^{7+}$).[5] Recently, a similar 4-valence-electron [Ag$_{11}$]$^{7+}$ NC has been described by Petty et al. to be formed when using 5'-CCCCAACCCCT-3' as the stabilizing scaffold. The closely related [Ag$_{10}$]$^{6+}$ core has also been reported several times by Petty and co-workers.[9] Hence, the combination of structural information with knowledge of the charge from mass spectrometry would allow one to compute the electronic structure[8,10] of what seems to be a recurring type of green emissive AgNC. **Figure 1** shows that 10Green-AgNC has an absorption and emission maximum at 472 and 535 nm, respectively. The intensity-weighted average decay time, $<\tau>$, was determined to be 0.65 ns and the fluorescence quantum yield (Q) was estimated to be 0.11 (**Table 1**).

Our first attempt to crystallize 10Green-AgNC consisted of screening a large number of commonly used crystallization conditions (see Supporting Information), utilizing the hanging-drop vapor diffusion method. Even though this approach was successful for a series of NIR emissive DNA-Ag$_{16}$NCs,[7d] it did not yield any crystals for 10Green-AgNC. Based on our previous work,[7c,d] we modified the original sequence by adding one adenosine at the 5'-end, as we noticed for DNA-Ag$_{16}$NC that the terminal adenosine did not affect the photophysical properties but could promote or alter the crystal packing interactions.

The additional base was attached to the 5'- and not the 3'-terminus because the 3'-end of the DNA strand was already rich in adenosines. Moreover, the introduction of the 5' overhang to enhance crystal packing interactions has been routinely used in RNA crystallography.[11] The new DNA sequence, 5'-ATCCACGAGAA-3', indeed stabilized a nearly identical green emitter (further referred to as 11Green-AgNC), as illustrated by the spectra in Figure 1 and the data in Table 1. Both 10Green-AgNC and 11Green-AgNC were HPLC purified prior

**ADVANCED
SCIENCE NEWS**

www.advancedsciencenews.com

**ADVANCED
OPTICAL
MATERIALS**

www.advopticalmat.de
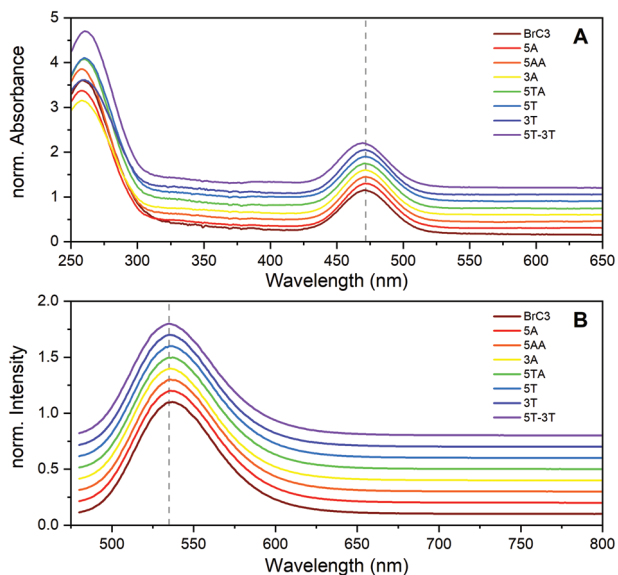
Figure 2. A) Normalized absorption and B) emission spectra of all 11Green-AgNC mutations with additional adenosines and thymidines, as well as brominated C3 (BrC3), in 10 mM NH_4OAc at room temperature. The emission spectra were recorded exciting at 469.5 nm. The spectra are plotted with an offset for displaying purposes. The dashed lines in A) and B) correspond, respectively, to 472 and 535 nm, which are the absorption and emission maxima of 11Green-AgNC.

to crystallization attempts (the chromatograms are reported in Figures S1 and S2, Supporting Information). The addition of the extra adenosine at the 5′-terminus enabled the crystallization of 11Green-AgNC (Figures S29 and S30, Supporting Information).

While the first obstacle was overcome, the quality of the collected single crystal X-ray diffraction data was too poor to attempt structure determination (Table S1, Supporting Information). The next step was to further extend the 3′- and 5′-ends with even more adenosines and/or thymidines, since the latter are known to be the least favorable to coordinate silver atoms. **Figure 2** and Table 1 show that the seven new HPLC-purified mutants displayed no significant alterations of the photophysical properties in solution. Minor concurrent changes in the fluorescence decay time and fluorescence quantum yield are most likely due to mutant-specific changes in the non-radiative decay rate.

For this series, the best X-ray diffraction results were achieved for 5A-11Green-AgNC, when using a 2 Å X-ray beam. The 5A-11Green-AgNC crystals diffracted with a resolution of 2.6 Å (Table S1, Supporting Information), which allowed us to narrow down the space group to two different possibilities: $P6_222$ or $P6_422$ (hexagonal) with unit cell dimensions of $a = b = 28.7$ Å and $c = 193.7$ Å. However, the phase determination using the single-wavelength anomalous dispersion (SAD) method failed. While it is unclear why this approach did not work, it could be that the silver atoms encapsulated in the DNA scaffold are disordered.

Crystals were also obtained for 3T-11Green-AgNC and 3A-11Green-AgNC, but the quality of the diffraction data was again poor (Table S1, Supporting Information). Since the SAD method using silver was unsuccessful, we tried to incorporate bromine in the structure and use the corresponding anomalous signal to solve the phase. For 11Green-AgNC, the third base in the DNA

sequence was exchanged with a brominated cytosine, where the bromine is covalently bound to the fift carbon of the pyrimidine ring. The modification is further defined as BrC3-11Green-AgNC.

The solution properties of BrC3-11Green-AgNC are once more alike (see Table 1 and Figure 2) to 10Green-AgNC. BrC3-11Green-AgNC yielded large single crystals, and good diffraction data with resolutions of 2.3 and 2.5 Å was obtained, when utilizing 2 Å and 0.915 Å X-ray beams, respectively (Table S1, Supporting Information). The BrC3-11Green-AgNC crystal was found to be isomorphous with the 5A-11Green-AgNC crystal (space group: $P6_222$ or $P6_422$, unit cell dimensions: $a = b = 28.4$ Å and $c = 194.1$ Å). Unfortunately, the anomalous signal from bromine did not help to solve the phase, and thus the atomic structure could not be determined.

Extending the DNA sequence with adenosines and thymidines to promote crystal packing interactions and/or brominating one of the bases was successful in obtaining crystals, but the quality of the diffraction data was not good enough to solve the structure.

Therefore, we decided to shorten the DNA scaffold, even though the additional nucleobases seemed to help promote crystal packing interactions. This rationale was based on the idea that terminal adenosines might not interact with the silver core, as observed for DNA-A10-Ag_{16}NC, and hence a similar emitter could be formed in a shortened sequence.[7c] Moreover, the presence of additional nucleobases meant that there were significantly more nucleotides than silver atoms.

Removing two bases from the 3′-end of 11Green-AgNC and 5A-11Green-AgNC yielded two new DNA-AgNCs, namely 11Green-2end-AgNC and 5A-11Green-2end-AgNC, respectively (see Table 1). Both modifications showed similar photophysical properties as the original green emitter (Figure 1; Figures S16 and S17, Supporting Information), and were successfully crystallized. Single crystal X-ray diffraction data of 11Green-2end-AgNC provided insight into the position of the silver atoms. Hence, a detailed spectroscopic, structural and compositional analysis of this mutant was undertaken.

2.2. 11Green-2end-AgNC

As briefly mentioned in the previous section, spectroscopic characterization revealed that 11Green-2end-AgNC has the same steady-state properties as the original 10Green-AgNC, but with a small drop in the fluorescence decay time and hence quantum yield (Figure 1 and Table 1). The mass spectrum of 11Green-2end-AgNC (**Figure 3**) shows a molecular ion peak centered at 1647.79 m/z with a $z = 4^-$ charge state. The experimental mass data is consistent with the theoretical isotopic distribution of a compound comprising two DNA strands and 11 silver atoms with an overall charge of 7+. This confirms that the silver nanocluster in 11Green-2end-AgNC is compositionally the same as the 4-valence-electron $(DNA)_2$-$[Ag_{11}]^{7+}$ NC (10Green-AgNC) reported by Copp et al.[5] While the spectroscopic data indicates that all DNA modifications formed alike emitters, mass spectrometry measurements were also performed on two other mutants to further prove the similarities. Both the 11Green-AgNC and the 5A-11Green-AgNC gave molecular ion peaks corresponding to a

**ADVANCED
SCIENCE NEWS**

www.advancedsciencenews.com

**ADVANCED
OPTICAL
MATERIALS**

www.advopticalmat.de
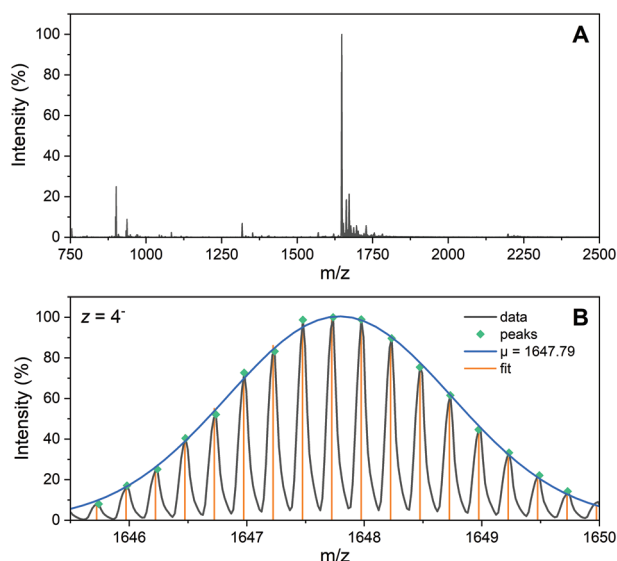
Figure 3. A) Mass spectrum of DNA$_2$[Ag$_{11}$]$^{7+}$ system (11Green-2end-AgNC). The sum formula is C$_{174}$H$_{220}$N$_{72}$O$_{100}$P$_{16}$[Ag$_{11}$]$^{7+}$, which corresponds to a molecular mass of 6602.21 g mol^{-1}. B) Zoomed-in view of the molecular ion peak with $z = 4^-$ charge state. The experimental isotopic distribution is reported with the corresponding Gaussian fit (blue) and the theoretical isotopic distribution (orange). The calculated average mass is 1647.79 m/z. Additional zoomed-in views can be found in the Supporting Information.

(DNA)$_2$-[Ag$_{11}$]$^{7+}$ compound (see Figures S22, S23, and S25, Supporting Information).

Unlike 11Green-AgNC and 5A-11Green-AgNC, 11Green-2end-AgNC crystals diffracted with a resolution of 2.0 Å, using a 2 Å X-ray beam (Table S1, Supporting Information). The space group of the crystal was found to be P1 (triclinic), with asymmetric units formed by two DNA-AgNCs. In contrast to DNA-Ag$_{16}$NC, the geometry of this AgNC looks less defined. **Figure 4**A shows the electron density of 11 silver atoms belonging to one of the (DNA)$_2$[Ag$_{11}$]$^{7+}$ systems in the crystallographic unit.

The silver atoms are arranged in an overall rod-like shape (Figure 4A,B), where six of them resemble a tetragon pair with a shared bond and edge[13] (yellow dashed lines, "boat") and the other five assume a square planar arrangement with a single atom extension (red and blue dashed lines, "lounge chair"). The Ag-Ag distances within the "boat" subsection seem in line with previously reported distances, ranging from 2.5 to 3.4 Å.[6,7d] This indicates that some Ag-Ag distances are below the bulk silver distance (2.88 Å)[14] and some approach the Van der Waals distance (3.44 Å).[15] With regard to the "lounge chair", the distances connecting the central atom in the square planar structure appear to be unrealistically short (2.1–2.3 Å). It is worth noticing that the silver atoms in the "lounge chair" section of the second DNA-AgNC in the asymmetric unit (Figure S26, Supporting Information) are arranged in a square pyramidal geometry instead, and the interatomic distances display more realistic values of 2.8–3.0 Å, with the exception of very short (2.4 Å) and very long distances (3.9 and 4.8 Å) at the base of the pyramid.

We thus speculate that the real arrangement of the silver atoms lies somewhere in between both (Figure 4D; Figure S26, Supporting Information) and it might indicate large flexibility in this

part of the AgNC. Unfortunately, the "boat" section of the second DNA-AgNC in the asymmetric unit (Figure S26, Supporting Information) could not be fully resolved, meaning that only 9 silver positions in total were assigned with certainty. It is reasonable to assume that this second DNA-AgNC should also contain 11 silver atoms, given the single emissive species found in the solution and the single mass peak corresponding to (DNA)$_2$-[Ag$_{11}$]$^{7+}$ NC. The difficulty in pinpointing the two silver atoms in the "boat" part of the second DNA-AgNC, along with the range of too small and too large distances for the "lounge chair" section, indicate that [Ag$_{11}$]$^{7+}$ might be intrinsically very dynamic. This also implies that obtaining a meaningful snapshot of the interatomic distances could be hard to achieve. Finally, the two sections ("boat" and "lounge chair") interact with each other (green dashed lines in Figure 4B) with interatomic distances ranging between 3.1 and 3.4 Å.

The structure presented in Figure 4 shows similarities with the geometrically optimized model of Ag$_{10}$NC@hpC$_{12}$ reported by Gupta et al.[16] This computed 10-silver nanocluster embedded in a C12 hairpin is also formed by two parts: a similar distorted square planar section with a single extending atom ("lounge chair" part) and a pseudo-trapezoidal Ag$_5$ section that shows a resemblance to our "boat" arrangement.

While some rough outlines of electron density corresponding to the DNA bases could be observed, the quality was not good enough to build a DNA model or assign nucleotide residues. Nevertheless, thanks to mass spectrometry data, we can confidently state that each [Ag$_{11}$]$^{7+}$ cluster is embedded in two DNA strands.

Next, we investigated the spectroscopic properties of 11Green-2end-AgNC in the crystalline state. **Figure 5**A,B shows bright-field and wide-field fluorescence images of 11Green-2end-AgNC crystals. Interestingly, emission spectra of individual crystals, recorded with a home-built confocal microscope (Figure 5C),[17] display two emission bands. Besides the green emission peak, which is slightly red-shifted with respect to the solution data, a second band centered at around 675 nm is present. This indicates that, while only showing a nanosecond-lived fluorescence band in solution (Table 1), 11Green-2end-AgNC behaves as a dual emitter in the crystalline state. Consistent with previously reported dual emissive DNA-AgNCs,[9a,f,g,18] the additional red-shifted band of 11Green-2end-AgNC is characterized by a microsecond decay time. More precisely, the green emissive state has a lifetime of 0.50 ns (Figure S27, Supporting Information), similar to the solution state value, whereas the red emissive band shows an average decay time of 167 μs (Figure S28, Supporting Information). It is still an open question whether the red-shifted "phosphorescence-like" emission is due to an actual spin change to a triplet state or not. Our findings indicate that (DNA)$_2$-[Ag$_{11}$]$^{7+}$ NC can change from being a single emitter in solution to a dual emitter in the solid state. This means that crystal packing interactions most likely affect the geometry of the [Ag$_{11}$]$^{7+}$ NC, and hence modify the photophysical parameters observed in solution.

Emission spectra and decay times of 11Green-AgNC and 5A-11Green-AgNC crystals were additionally acquired to confirm the homogeneity of the spectroscopic properties among different mutants (Figures S30–S33, Supporting Information). While the emission spectra of 11Green-AgNC crystals were very alike to those of 11Green-2end-AgNC, the ratio of the red-to-green band was significantly higher for the 5A-11Green-

ADVANCED
SCIENCE NEWS

www.advancedsciencenews.com

ADVANCED
OPTICAL
MATERIALS

www.advopticalmat.de
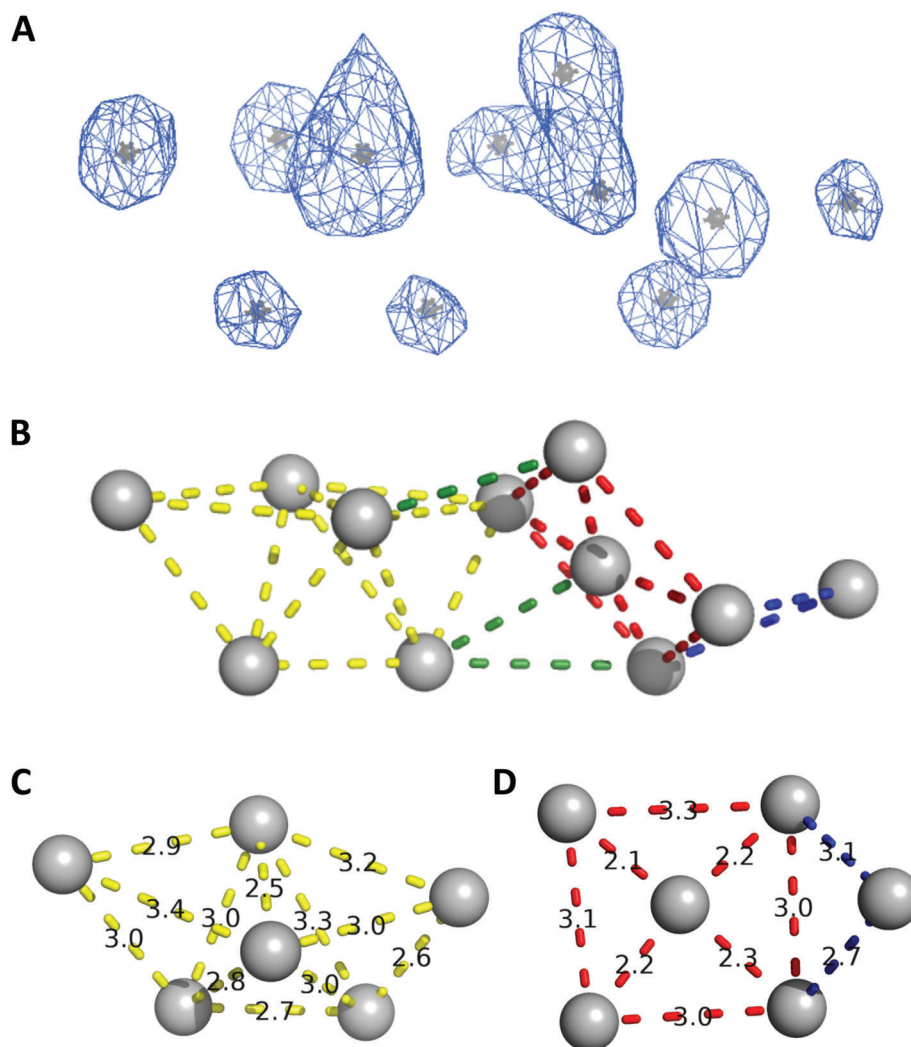
Figure 4. Structure of one subunit of 11Green-2end-AgNC crystal. A) Density-modified electron density map of silver atoms obtained by the SAD phasing, contoured at 5σ level. B) Nearest inter-silver distances (up to 3.4 Å) represented by colored dashed lines to highlight the subsections of the $[Ag_{11}]^{7+}$ nanocluster. Detailed views of C) the tetragon pair with shared bond and edge, and D) the square planar section with a single atom extension. All distances are given in Å.

AgNC crystals. These crystals were however 2 years old, hence the crystallization buffer had completely evaporated. The addition of 40% PEG 3350 to the 5A-11Green-AgNC crystals made the photophysical features more in line with those measured for the freshly prepared 11Green-2end-AgNC (3 weeks old) and 11Green-AgNC crystals (7 days old), even though the mean fluorescence decay time remained longer (Figure S34, Supporting Information). This clearly indicates that the hydration level plays also a critical role in the observed red-to-green band ratio. To further test this idea and exclude age-related causes, the reversibility of these changes was checked by measuring a droplet of 11Green-2end-AgNC in 10 mM NH_4OAc on the microscope and recording a series of emission spectra before and after the evaporation of the solvent. As shown in Figure S35 (Supporting Information), when the droplet dries out, the emission spectra display two bands, with the second 675 nm band even more pronounced than in the crystalline state. Upon rehydration, 11Green-2end-AgNC

again behaves as a green emitter with a single emission band. The three cycles illustrate that the effect is fully reversible and the long-lived emission band is only present in the solid state. Additionally, given the much less intense red band in the hydrated crystalline state, it is also fair to assume that the determined structure is closer to that in solution compared to the dehydrated state. To the best of our knowledge, this is the first time that hydration-dependent emission properties have been demonstrated for DNA-AgNCs in the solid state, while this effect is commonly observed for zeolite-stabilized AgNCs.[19]

3. Conclusion

We described a series of mutants of 10Green-AgNC, which was known to be a green emissive $(DNA)_2$-$[Ag_{11}]^{7+}$ NC with four valence electrons. Modifications of the DNA sequence of the original emitter were introduced to promote crystallization without

**ADVANCED
SCIENCE NEWS**

www.advancedsciencenews.com

**ADVANCED
OPTICAL
MATERIALS**

www.advopticalmat.de
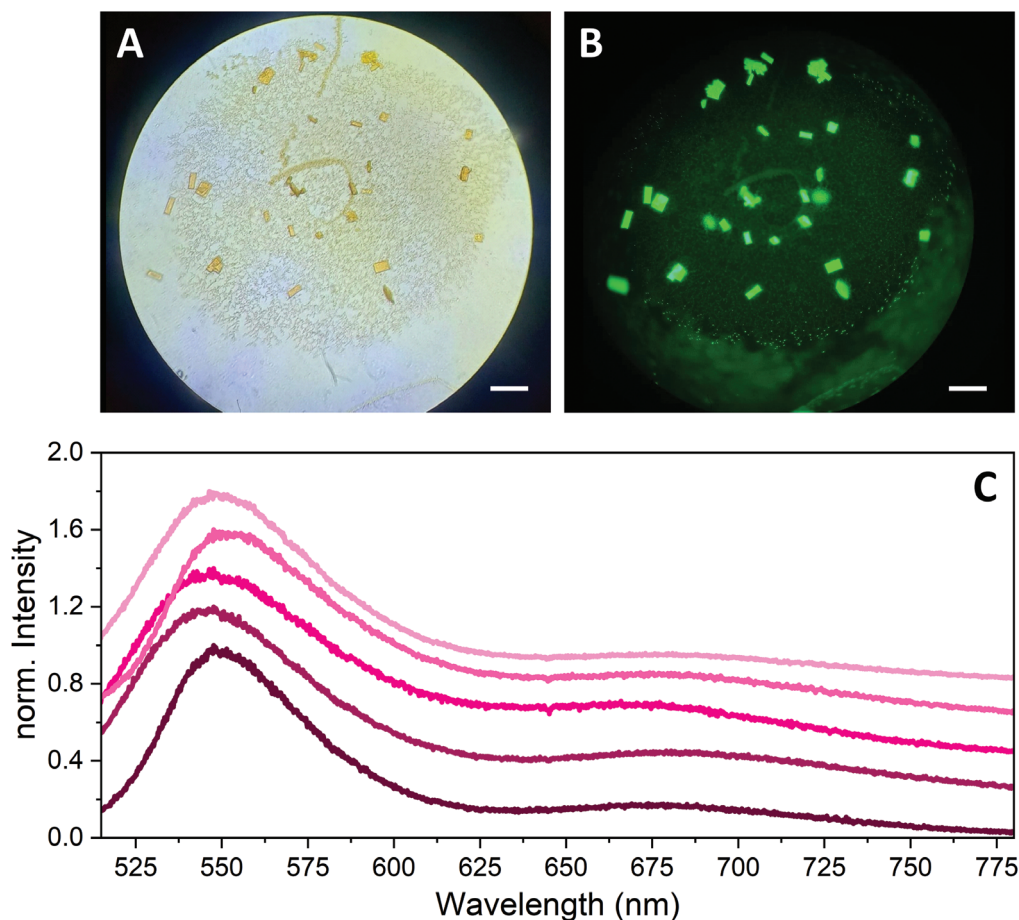
Figure 5. A) Bright-field and B) fluorescence images (λ_{exc} = 470–495 nm, λ_{em} = 510–550 nm) of 11Green-2end-AgNC crystals grown in 10% MPD, 10 mM spermine, 10 mM Ca(NO$_3$)$_2$ and 50 mM MOPS at pH 7. The scale bar corresponds to 50 µm. C) Emission spectra of different crystals, recorded with a confocal microscope exciting at 458 nm. The spectra are normalized to the emission maximum and have a constant 0.2 offset for displaying purposes.

major changes in the emissive properties. Addition of adenosines and/or thymidines at the 3′- and 5′-ends did not affect the photophysical properties, but enabled crystallization. Bromination of the DNA strand also preserved the spectroscopic characteristics of the original green emitter. Despite being able to grow well-diffracting crystals for 5A-11Green-AgNC and BrC3-11Green-AgNC, the SAD methods using the anomalous signals of silver and bromine were not successful in determining the structure. On the other hand, removing two adenosines from the 3′-end of the 11-base DNA strand, 5′-ATCCACGAG*AA*-3′, promoted the formation of the same green emissive species with the benefit of obtaining crystals that gave insight into the silver positions. In agreement with the mass spectrum, single crystal X-ray diffraction data of 11Green-2end-AgNC unveiled the presence of 11 silver atoms in a potentially very dynamic and flexible rod-like structure. This flexibility of silver atoms within the nanocluster might also be the reason for the reversible appearance of a microsecond-lived red-shifted band in the crystalline and dried states. In addition, we demonstrated for the first time that the degree of hydration plays a crucial role in the observed photophysical properties. The combination of mass spectrometry data and single crystal X-ray diffraction measurements has thus provided the first insight

in the structure/property relationship of HPLC-purified green-emissive DNA-stabilized [Ag$_{11}$]$^{7+}$/[Ag$_{10}$]$^{6+}$ NC systems.

Supporting Information

Supporting Information is available from the Wiley Online Library or from the author.

Acknowledgements

Conflict of Interest

The authors declare no conflict of interest.

Data Availability Statement

The data that support the findings of this study are available in the supplementary material of this article.

Keywords

fluorescence, HPLC purification, mass spectrometry, silver nanoclusters, X-ray diffraction

[1] A. Gonzàlez-Rosell, C. Cerretani, P. Mastracco, T. Vosch, S. M. Copp, *Nanoscale Adv.* **2021**, *3*, 1230.

[2] a) S. M. Copp, P. Bogdanov, M. Debord, A. Singh, E. Gwinn, *Adv. Mater.* **2014**, *26*, 5839; b) S. M. Copp, A. Gorovits, S. M. Swasey, S. Gudibandi, P. Bogdanov, E. G. Gwinn, *ACS Nano* **2018**, *12*, 8240; c) S. M. Swasey, S. M. Copp, H. C. Nicholson, A. Gorovits, P. Bogdanov, E. G. Gwinn, *Nanoscale* **2018**, *10*, 19701.

[3] a) B. Sengupta, K. Springer, J. G. Buckman, S. P. Story, O. H. Abe, Z. W. Hasan, Z. D. Prudowsky, S. E. Rudisill, N. N. Degtyareva, J. T. Petty, *J. Phys. Chem. C* **2009**, *113*, 19518; b) J. T. Petty, O. O. Sergev, D. A. Nicholson, P. M. Goodwin, B. Giri, D. R. McMullan, *Anal. Chem.* **2013**, *85*, 9868.

[4] D. Schultz, E. G. Gwinn, *Chem. Commun.* **2012**, *48*, 5748.

[5] S. M. Copp, D. Schultz, S. Swasey, J. Pavlovich, M. Debord, A. Chiu, K. Olsson, E. Gwinn, *J. Phys. Chem. Lett.* **2014**, *5*, 959.

[6] D. J. E. Huard, A. Demissie, D. Kim, D. Lewis, R. M. Dickson, J. T. Petty, R. L. Lieberman, *J. Am. Chem. Soc.* **2019**, *141*, 11465.

[7] a) C. Cerretani, M. Liisberg, V. Rück, J. Kondo, T. Vosch, *Nanoscale Adv.* **2022**, *4*, 3212; b) C. Cerretani, J. Kondo, T. Vosch, *CrystEngComm* **2020**, *22*, 8136; c) C. Cerretani, J. Kondo, T. Vosch, *RSC Adv.* **2020**,
10, 23854; d) C. Cerretani, H. Kanazawa, T. Vosch, J. Kondo, *Angew. Chem., Int. Ed.* **2019**, *58*, 17153.

[8] A. Gonzàlez-Rosell, S. Malola, R. Guha, N. R. Arevalos, M. Rafik, M. F. Matus, M. E. Goulet, E. Haapaniemi, B. B. Katz, T. Vosch, J. Kondo, H. Häkkinen, S. M. Copp, *J. Am. Chem. Soc.* **2023**, *145*, 10721.

[9] a) J. T. Petty, S. Carnahan, D. Kim, D. Lewis, *J. Chem. Phys.* **2021**, *154*, 244302; b) Y. Zhang, C. He, J. T. Petty, B. Kohler, *J. Phys. Chem. Lett.* **2020**, *11*, 8958; c) J. T. Petty, M. Ganguly, A. I. Yunus, C. He, P. M. Goodwin, Y.-H. Lu, R. M. Dickson, *J. Phys. Chem. C* **2018**, *122*, 28382; d) J. T. Petty, O. O. Sergev, M. Ganguly, I. J. Rankine, D. M. Chevrier, P. Zhang, *J. Am. Chem. Soc.* **2016**, *138*, 3469; e) C. He, P. M. Goodwin, A. I. Yunus, R. M. Dickson, J. T. Petty, *J. Phys. Chem. C* **2019**, *123*, 17588; f) Y. Zhang, C. He, K. d. L. Harpe, P. M. Goodwin, J. T. Petty, B. Kohler, *J. Chem. Phys.* **2021**, *155*, 094305; g) D. Lewis, C. Setzler, P. M. Goodwin, K. Thomas, M. Branham, C. A. Arrington, J. T. Petty, *J. Phys. Chem. C* **2023**, *127*, 10574.

[10] S. Malola, M. F. Matus, H. Häkkinen, *J. Phys. Chem. C* **2023**, *127*, 16553.

[11] J. Kondo, *Nucleic Acid Crystallogr.* **2016**, 315.

[12] A. M. Brouwer, *Pure Appl. Chem.* **2011**, *83*, 2213.

[13] T. Yumura, M. Kumondai, Y. Kuroda, T. Wakasugi, H. Kobayashi, *RSC Adv.* **2017**, *7*, 4950.

[14] A. F. Wells, *Structural Inorganic Chemistry*, 5th ed., Oxford University Press, Oxford, **1984**.

[15] A. Bondi, *J. Phys. Chem.* **1964**, *68*, 441.

[16] A. K. Gupta, N. Marshall, L. Yourston, L. Rolband, D. Beasock, L. Danai, E. Skelly, K. A. Afonin, A. V. Krasnoslobodtsev, *Nanoscale Adv.* **2023**, *5*, 3500.

[17] M. B. Liisberg, Z. Shakeri Kardar, S. M. Copp, C. Cerretani, T. Vosch, *J. Phys. Chem. Lett.* **2021**, *12*, 1150.

[18] a) V. Rück, C. Cerretani, V. A. Neacşu, M. B. Liisberg, T. Vosch, *Phys. Chem. Chem. Phys.* **2021**, *23*, 13483; b) C. Cerretani, G. Palm-Henriksen, M. B. Liisberg, T. Vosch, *Chem. Sci.* **2021**, *12*, 16100.

[19] a) E. Coutino-Gonzalez, W. Baekelant, D. Grandjean, M. B. J. Roeffaers, E. Fron, M. S. Aghakhani, N. Bovet, M. Van der Auweraer, P. Lievens, T. Vosch, B. Sels, J. Hofkens, *J. Mater. Chem. C* **2015**, *3*, 11857. b) H. Lin, K. Imakita, M. Fujii, *Appl. Phys. Lett.* **2014**, *105*, 211903.

Supporting Information

Atomic Structure of a DNA-stabilized Ag_{11} Nanocluster with Four Valence Electrons

Vanessa Rück,[a] Vlad A. Neacșu,[a, b] Mikkel B. Liisberg,[a] Christian B. Mollerup,[c]

Park Hee Ju,[d] Tom Vosch,*[a] Jiro Kondo,*[d] Cecilia Cerretani*[a]

E-mail: tom@chem.ku.dk

E-mail: j.kondo@sophia.ac.jp

E-mail: cece@chem.ku.dk

[a]   Department of Chemistry, University of Copenhagen, Universitetsparken 5, 2100 Copenhagen, Denmark.
[b]   Department of Chemistry, City University of Hong Kong, 83 Tat Chee Avenue, Kowloon Tong, 999077 Hong Kong, China.
[c]   Department of Forensic Medicine, University of Copenhagen, Frederik V's Vej 11, 2100 Copenhagen, Denmark.
[d]   Department of Materials and Life Sciences, Sophia University, 7-1 Kioi-cho, Chiyoda-ku, 102-8554 Tokyo, Japan.

MATERIALS AND METHODS

Synthesis of DNA-AgNCs.

The oligonucleotides and the nuclease-free water were purchased from Integrated DNA Technologies (IDT), while the brominated modifications were bought from GeneDesign. All DNA sequences are listed below together with their corresponding names. $AgNO_3$ (≥ 99.998%), $NaBH_4$ (≥ 99.99%) and ammonium acetate (NH_4OAc, ≥ 98%) were purchased from Sigma Aldrich. All chemicals were used as received and dissolved in nuclease-free H_2O.

All DNA-AgNCs were synthesized by mixing the hydrated DNA with $AgNO_3$ in a 10 mM NH_4OAc solution (pH 7). After 15 min, the reaction mixture was reduced with $NaBH_4$. The final ratio of the components was [DNA]:[Ag$^+$]:[BH$_4^-$] = 30 µM: 150 µM: 75 µM. The samples were stored in the fridge for 4 days before purification.

DNA sequences:

- 10Green: 5'-TCCACGAGAA-3'
- 11Green: 5'-**A**TCCACGAGAA-3'
- 5A-11Green: 5'-**AA**TCCACGAGAA-3'
- 5AA-11Green: 5'-**AAA**TCCACGAGAA-3'
- 3A-11Green: 5'-**A**TCCACGAGAA**A**-3'
- 5TA-11Green: 5'-**TAA**TCCACGAGAA-3'
- 5T-11Green: 5'-**TA**TCCACGAGAA-3'
- 3T-11Green: 5'-**A**TCCACGAGAA**T**-3'
- 5T-3T-11Green: 5'-**TA**TCCACGAGAA**T**-3'
- BrC3-11Green: 5'-**ATC(Br)**CACGAGAA-3'
- 11Green-2end: 5'-**A**TCCACGAG-3'
- 5A-11Green-2end: 5'-**AA**TCCACGAG-3'

HPLC purification.

The HPLC purification was performed using a preparative HPLC system from Agilent Technologies with an Agilent Technologies 1260 Infinity fluorescence detector, an Agilent Technologies 1100 Series UV-Vis detector, and a Kinetex C18 column (5 µm, 100 Å, 250 × 4.6 mm; Phenomenex), equipped with a fraction collector. The mobile phase was a gradient mixture of 35 mM triethylammonium acetate (TEAA) buffer in water (A) and methanol (B). All DNA-AgNC modifications, but 11Green-2end-AgNC and 5A-11Green-2end-AgNC, were purified with the same method. The gradient was kept constant at 15% B for the first 2 min, then varied from 15% to 35% B in 20 min, and finally, in the 22-25 min range, it was rapidly increased to 95% B. The run was followed by 5 min of washing with 95% B to ensure the elution of any remaining sample from the column. The flow rate was set to 1 mL/min. The HPLC chromatograms are shown in Figures S1-S10.

For the two shortened modifications, 11Green-2end-AgNC and 5A-11Green-2end-AgNC, the HPLC method was extended by 5 min. More precisely, after the first 2 min at 15% B, the elution gradient was increased up to 40 % B in 25 min, then varied to 95% B as described above. The corresponding HPLC chromatograms are reported in Figures S11-S12.

In all cases, the purified fractions were collected based on the absorbance signal at 470 nm. The retention time varied for each modification and the specific times are reported in the captions of the corresponding chromatograms.

After purification, the solvent was exchanged to 10 mM NH₄OAc by spin-filtration, using 3 kDa cut-off membrane filters (Amicon Ultra Centrifugal Filter Unit, Ultracel-3, Merck).

SPECTROSCOPIC MEASUREMENTS

Absorption measurements.

All absorption measurements were carried out on a Cary 300 UV-Vis spectrophotometer from Agilent Technologies using a deuterium lamp for ultraviolet radiation and a halogen lamp for visible and near-infrared radiation. The measurements were performed in a single-beam configuration with a 0/100% transmittance baseline correction. Every spectrum was subtracted by the corresponding blank absorption spectrum.

Steady-state emission and excitation measurements.

Steady-state fluorescence measurements were performed using a FluoTime300 instrument from PicoQuant. Emission spectra were carried out exciting with picosecond-pulsed lasers from Picoquant: 445.4 nm (LDH-PC-450B) and 469.5 nm (LDH-P-C-470).

The excitation spectra and 2D emission *vs* excitation plots were measured using a QuantaMaster400 from PTI/HORIBA with a xenon arc lamp as excitation source.

All spectra were corrected for the wavelength dependency of the detector and the excitation spectra were additionally corrected for the lamp power. The 2D plots were recorded exciting from 420 to 530 nm, in steps of 5 or 10 nm. For all fluorescence measurements, the absorbance of the investigated compound was kept below 0.1 at the excitation wavelength in order to avoid inner filter effects.

Fluorescence quantum yield determination.

The fluorescence quantum yield of all DNA-AgNCs (Q_{NC}) was determined through a relative method, using Fluorescein in 0.1 M NaOH (Q_{ref} = 0.91) as a reference dye.[1] For 10Green-AgNC, 11Green-AgNC, 5A-11Green-AgNC and 11Green-2end-AgNC, the absorption and emission spectra (λ_{exc}= 445.4 nm) were recorded in 10 mM NH₄OAc solution at 25 ˚C for 5 different concentrations of the samples and the reference, whereas all other modifications were measured only at one concentration. The integrated emission spectra (**F**) were plotted against the fraction of absorbed light (**f_A** = 1 − 10^{-A}) at the excitation wavelength, and the data were linearly fitted while fixing the y-intercept at zero. The resulting slopes were then used to calculate the quantum yield according to the following formula:[1]

$$Q_{NC} = \frac{F_{NC}}{f_{A,NC}} \cdot \frac{f_{A,ref}}{F_{ref}} \cdot \frac{n_{NC}^2}{n_{ref}^2} \cdot Q_{ref}$$

where the subscripts **NC** and **ref** represent the DNA-AgNC and the reference dye, respectively, and **n** is the refractive index of the medium in which the compound is dissolved.

For one-point measurements, no plots were constructed, and the QY was calculated from single values of the integrated emission spectrum and fraction of absorbed light for both DNA-AgNCs and Fluorescein.

Time-correlated single-photon counting (TCSPC).
Time-resolved fluorescence measurements were performed using a Fluotime300 instrument from PicoQuant with a 469.5 nm picosecond-pulsed laser (LDH-P-C-470) as excitation source for all DNA-AgNCs. The intensity decays were monitored at 535 nm. The integration time was chosen to be 2 s and the repetition rate was set to 40 MHz in order to reach at least 10,000 counts in the maximum. The data were analyzed using Fluofit v.4.6 software from PicoQuant. The decay curves were fitted with a multi-exponential reconvolution model including the instrument response function (IRF). The obtained amplitude (α_i) and decay time (τ_i) components were used to calculate the intensity-weighted average decay time <τ> at the selected emission wavelength.[2]

MASS SPECTROMETRY

Electrospray ionization-mass spectrometry (ESI-MS) measurements were performed with a Xevo G2-XS QTof (Waters Corporation, Milford, MA, USA), using negative ion mode with a 2 kV capillary voltage, 30 V cone voltage and no collision energy. Spectra were collected from 750 to 4000 m/z, and with a scan time of 1 s. Source temperature was 80 °C with a cone gas flow of 45 L/h, and the desolvation temperature and gas flow were 150 °C and 450 L/h, respectively. The QTOF was calibrated using ESI-L Low Tune Mix (Agilent Technologies, Santa Clara, CA, USA), which contained compounds in the mass range of 1034 to 2834 m/z. All samples were injected using an Acquity I-Class Plus system (Waters) with a flow-through needle autosampler, with a flow of 0.1 mL/min 50 mM NH_4Oac buffer at pH 7 – MeOH (80:20) and using 5 µL injection volume. The system was operated using UNIFI v.1.9.4 (Waters), and the final spectra were generated by averaging multiple spectra surrounding the apex of the observed peak.
The recorded data were analyzed and fitted with the open-source software EnviPat Web[3] (https://www.envipat.eawag.ch/index.php).

CRYSTALLIZATION

Crystal growth.
Crystals were grown in an incubator at 293 K by the hanging-drop vapor-diffusion method. 0.2-1 µL of DNA-AgNC solution, with [DNA] ≥ 200 µM, were mixed with 0.2-1 µL of crystallization buffer and equilibrated against 250 µL of a reservoir solution, either 40% 2-methyl-2,4-pentanediol (MPD) or 40% polyethylene glycol (PEG) 3350. The crystallization buffer contains either 10% MPD or 10% PEG 3350, a nitrate salt (Li^+, Na^+, K^+, NH_4^+, Mg^{2+}, Ca^{2+} or Sr^{2+}) with different concentrations (10, 100, 200, 300, 400 and 500 mM), 10 mM spermine and 50 mM 3-(N-morpholino)propanesulfonic acid (MOPS) at pH 7. Crystals were obtained with various conditions between 1 and 4 weeks after starting the crystallization.
For BrC3-11Green-AgNC, crystallization buffers containing hexaamminecobalt(III), instead of spermine, were also used.

X-ray data collection.
X-ray data was collected at 100 K with synchrotron radiation at the BL-17A beamline at the Photon Factory (Tsukuba, Japan). In order to obtain a strong anomalous signal from the silver atoms, an X-ray beam with 2.0 Å wavelength (the longest available in the beamline) was chosen for the data collection of all modifications. For the bromine derivative, BrC3-11Green-AgNC, an X-ray beam with 0.915 Å wavelength

(K absorption edge of bromine) was instead chosen. Diffraction data were taken using 0.1-1° oscillation with 0.1-0.2 s exposure per frame.

Structure determination and refinement.
The data set was processed by the program XDS.[4] We tried to determine the initial phases using the program AutoSol of the Phenix suite.[5] Although all phase determination trials failed, the dataset of 11Green-2end-AgNC with the highest maximum resolution (2.0 Å) provided reasonable heavy metal positions. Details on the resolution, space group and unit cell dimensions are summarized in Table S1.

Table S1. Overview of crystallization conditions, data collection and analysis.

Name & DNA sequence	Crystal	Crystallization condition	Data collection (BL17A-Photon Factory)	Resolution & Space group
10Green-AgNC	No	-	-	-
11Green-AgNC		10% MPD, 10 mM spermine, 50 mM MOPS and 400 mM Sr(NO$_3$)$_2$	2 Å	Poor diffraction
5A-11Green-AgNC		10% MPD, 10 mM spermine, 50 mM MOPS and 200 mM NaNO$_3$	2 Å	2.6 Å $P6_2$22 or $P6_4$22 ($a = b$ = 28.7 Å c = 193.7 Å)
5AA-11Green-AgNC	No			
5TA-11Green-AgNC	No			
5T-11Green-AgNC	No			
5T-3T-11Green-AgNC	No			
3T-11Green-AgNC		10% MPD, 10 mM spermine, 50 mM MOPS and 10 mM LiNO$_3$	2 Å	Poor diffraction
3A-11Green-AgNC		10% MPD, 10 mM spermine, 50 mM MOPS and 400 mM KNO$_3$	2 Å	Poor diffraction
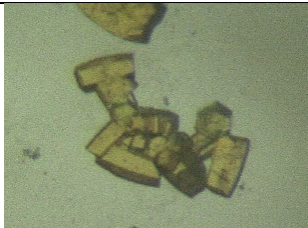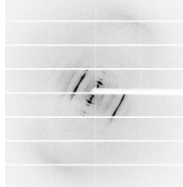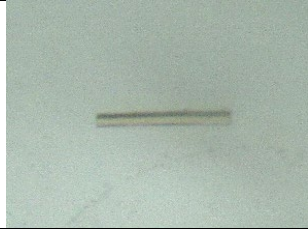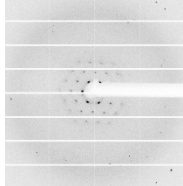
BrC3-11Green-AgNC		10% MPD, 10 mM spermine, 50 mM MOPS and 300 mM NaNO$_3$	 2 Å	2.3 Å $P6_2$22 or $P6_4$22 ($a = b$ = 28.4 Å c = 194.1 Å)
BrC3-11Green-AgNC		10% MPD, 10 mM [Co(NH$_3$)$_6$]$^{3+}$, 50 mM MOPS and 300 mM KNO$_3$	 0.915 Å	2.6 Å $P6_2$22 or $P6_4$22 ($a = b$ = 28.5 Å c = 194.1 Å)
11Green-2end-AgNC		10% MPD, 10 mM spermine, 50 mM MOPS and 200 mM LiNO$_3$	 2 Å	2.0 Å $P1$ (a = 19.0 Å b = 27.8 Å c = 41.5, α = 102.7°, β = 98.3° γ = 108.8°)
5A-11Green-2end-AgNC		10% MPD, 10 mM spermine, 50 mM MOPS and 400 mM KNO$_3$	 2 Å	3.1 Å $P6_3$22 ($a = b$ = 28.3 Å c = 209.5 Å)
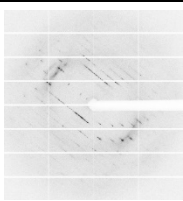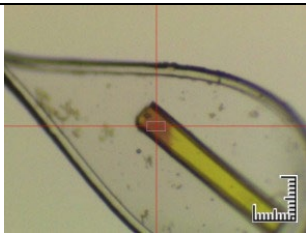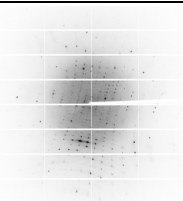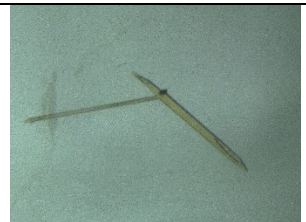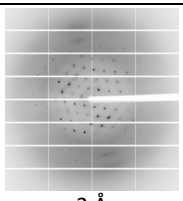
Spectroscopic characterization.

Bright-field and fluorescence images were recorded on an inverted Olympus IX71 microscope, with a 10x or 20x air objective (CPlanFL N 10x, NA = 0.3, Olympus and LCAch N 20x PhC, NA = 0.3, Olympus). For the bright-field images, white light was used. For the fluorescence images, an X-Cite Series 120Q light source was utilized in combination with an Olympus U-MNIBA3 filter cube. All images (Figures 5 and S29-S31) were recorded with the camera of an iPhone SE.

For the recording of spectra and decays of individual crystals, we used a home-built microscope. In this setup, we used a pulsed fiber coupled (NKT Photonics, FD7-PM) supercontinuum white-light laser (NKT Photonics, SuperK EXTREME EXB-6) with a repetition rate of 13 MHz. This delivered a wavelength of 458 nm by sending the continuum output through an acousto-optic tunable filter (NKT Photonics, SuperK SELECT). The output of the fiber was expanded by a telecentric lens system and cleaned up by a 458 nm band-pass filter (LL01-458-25, Semrock) before it was reflected by a 30:70 beam splitter (XF122, Omega Optical) and sent through an air objective (CPlanFL N 10x, NA = 0.3, Olympus), which focused the laser onto the sample and collected the emission. The laser light was blocked by a 458 nm long-pass filter (BLP01-458R-25, Semrock) and out-of-focus light was blocked by a 100 µm pinhole. The luminescence was sent through a spectrograph (Acton Research, SP 2356 spectrometer, 300 grooves/mm) onto a nitrogen cooled CCD camera (Princeton Instruments, SPEC-10:100B/LN-eXcelon) to record the spectra. As previously reported, the emission spectra were wavelength- and intensity-corrected using calibrated light

sources.[6] Fluorescence decays were recorded by redirecting the emission onto an avalanche photodiode (CD3226, PerkinElmer) connected to a single photon counting board (SPC-830, Becker & Hickl). All fluorescence decays were fitted with FluoFit v. 4.6 software (PicoQuant) by using a multi-exponential reconvolution model, including the IRF.

In order to measure the equilibration and decay of the additional long-lived emission band, a burst mode excitation scheme was utilized as described in detail by Liisberg *et al.*[7] Here we adjusted our supercontinuum excitation source to have a burst mode excitation profile with on and off periods of 2 ms each. In this approach, we are able to simultaneously capture the short-lived (ns, Figure S27) fluorescence and long-lived (µs, Figure S28) luminescence in a single measurement.

For recording emission spectra of a 10 µL droplet of 11Green-2end-AgNC before and after evaporation of the solvent (3 cycles), the same home-built microscope described above was used, with the exception of a 100x oil immersion objective (UPlanSApo 100x, NA = 1.4, Olympus) and an additional filter in the excitation path, a short-pass 561 nm filter (SP01-561RU-25, Semrock), to reduce the increased scattering in the dried drop. The power of the laser on top of the microscope was 60 nW. The recorded spectra for all three cycles are reported in Figure S35.

References

[1] A. M. Brouwer, *Pure Appl. Chem.*, **2011**, *83* , 2213.

[2] J. R. Lakowicz, *Principles of Fluorescence Spectroscopy*, **2006**.

[3] M. Loos, C. Gerber, F. Corona, J. Hollender, H. Singer *Anal. Chem.*, **2015**, *87*, 5738-5744.

[4] W. Kabsch, Acta Crystallogr., *Sect D: Biol. Crystallogr.*, **2010**, *66*, 133-144.

[5] a) P. D. Adams, P. V. Afonine, G. Bunkóczi, V. B. Chen, I. W. Davis, N. Echols, J. J. Headd, L. W. Hung, G. J. Kapral, R. W. Grosse-Kunstleve, A. J. McCoy, N. W. Moriarty, R. Oeffner, R. J. Read, D. C. Richardson, J. S. Richardson, T. C. Terwilliger, P. H. Zwart, *Acta Crystallogr., Sect D: Biol. Crystallogr.*, **2010**, *66*, 213-221; b) R. W. Grosse-Kunstleve, P. D. Adams, *Acta Crystallogr., Sect D: Biol. Crystallogr.*, **2003**, *59*, 1966-1973; c) T. C. Terwilliger, P. D. Adams, R. J. Read, A. J. McCoy, N. W. Moriarty, R. W. Grosse-Kunstleve, P. V. Afonine, P. H. Zwart, L. W. Hung, *Acta Crystallogr., Sect D: Biol. Crystallogr.*, **2009**, *65*, 582-601.

[6] M. B. Liisberg, Z. S. Kardar, S. M. Copp, C. Cerretani, T. Vosch *J. Phys. Chem. Lett.*, **2021**, *12*, 1150–1154.

[7] M. B. Liisberg, S. Krause, C. Cerretani, T. Vosch *Chem. Sci.*, **2022**,*13*, 5582-5587.
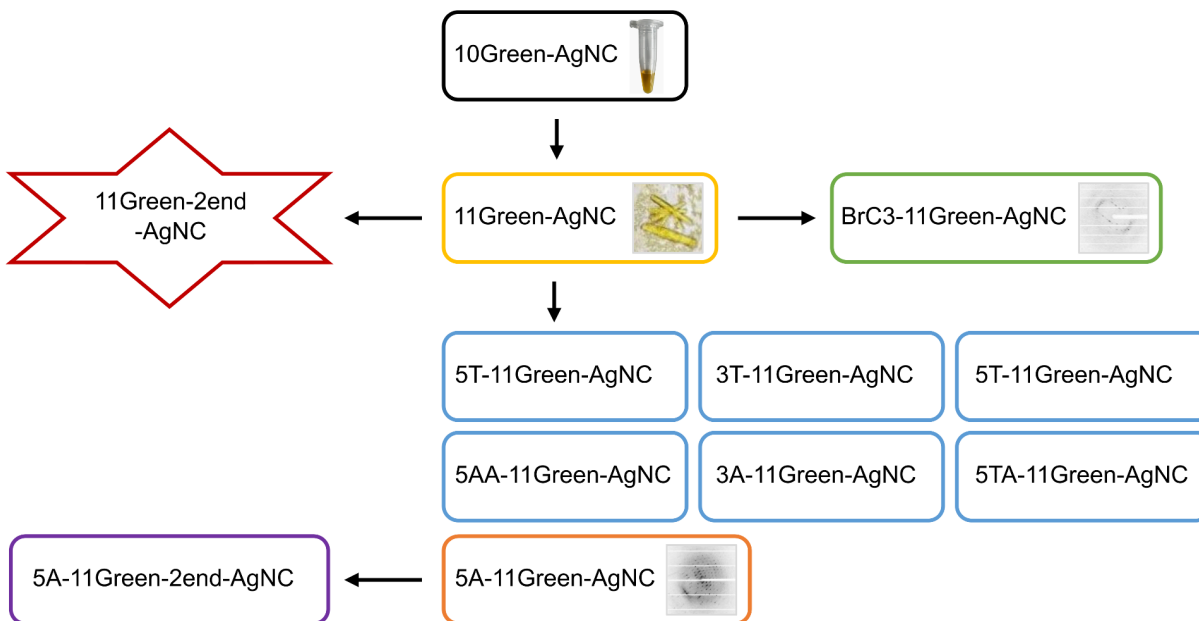
Scheme 1. Applied strategies for crystallizing 10Green-AgNC and solving the structure by single crystal X-ray diffraction measurements. First, one adenosine was added to the 5'-terminus of 10Green-AgNC. Then, additional adenosines and/or thymidines were appended at the 3'- and 5'-ends of 11Green-AgNC. Afterwards, a brominated version of 11Green-AgNC was synthesized. Most modifications yielded crystals, but poor diffraction data. In the end, the DNA scaffold was shortened. Removing two bases from the 3'-end of 11Green-AgNC and 5A-11Green-AgNC resulted in two new DNA-AgNCs, namely 11Green-2end-AgNC and 5A-11Green-2end-AgNC, respectively. The collection of X-ray data for 11Green-2end-AgNC crystals was successful, and the arrangement of silver atoms was unraveled.

HPLC Chromatograms
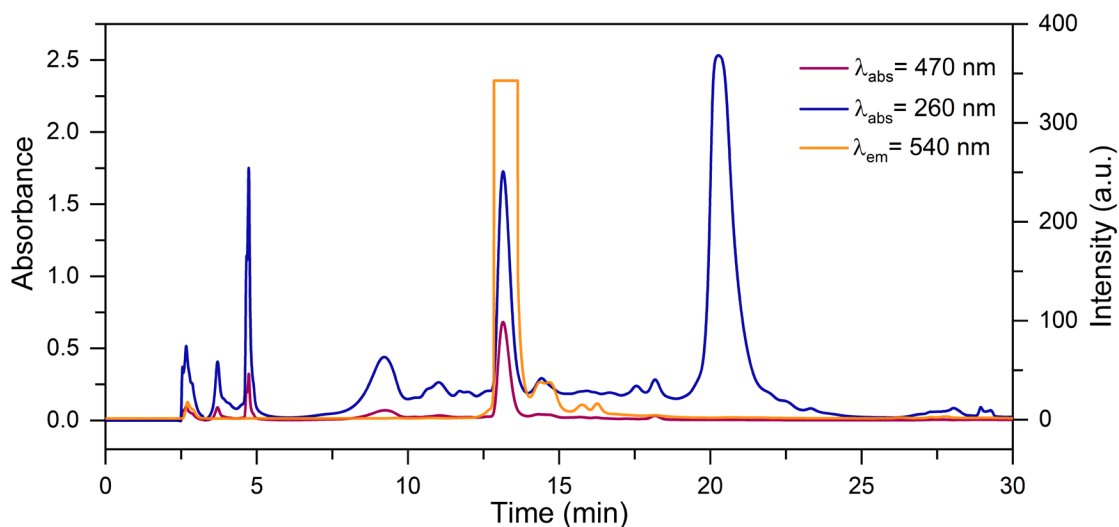
Figure S1. HPLC chromatograms of 10Green-AgNCs monitoring the absorption at 470 nm and 260 nm, and the fluorescence signal at 540 nm (exciting at 470 nm). The plateau of the peak in the fluorescence chromatogram is due to detector saturation. The fraction was collected at $t_R \approx$ 13 min ($\approx$ 26% B).
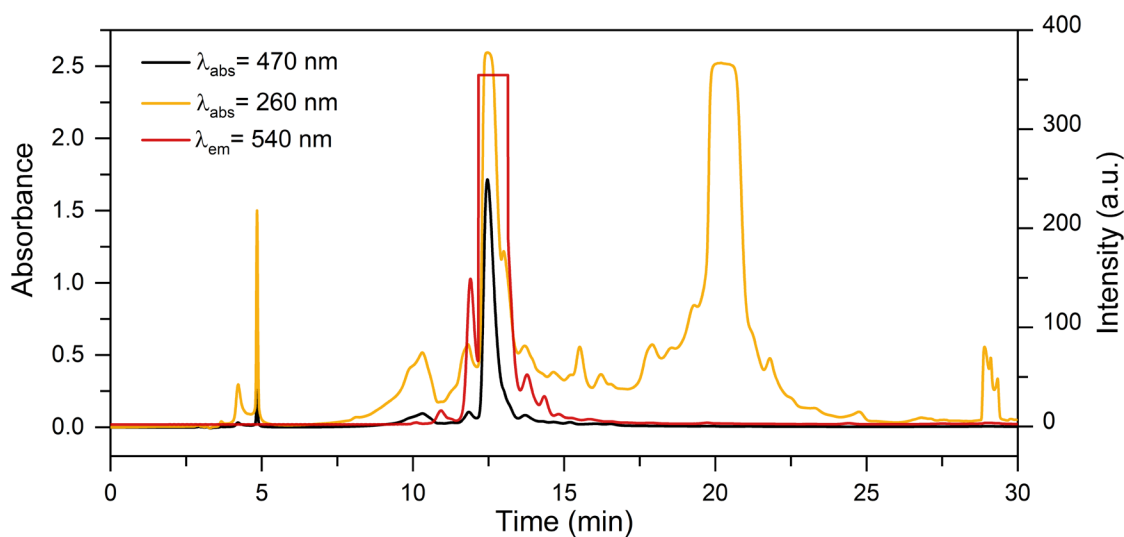
Figure S2. HPLC chromatograms of 11Green-AgNCs monitoring the absorption at 470 nm and 260 nm, and the fluorescence signal at 540 nm (exciting at 470 nm). The plateau of the 260 nm absorption and fluorescence signals is due to detector saturation. The fraction was collected at $t_R \approx$ 12 min ($\approx$ 25% B).
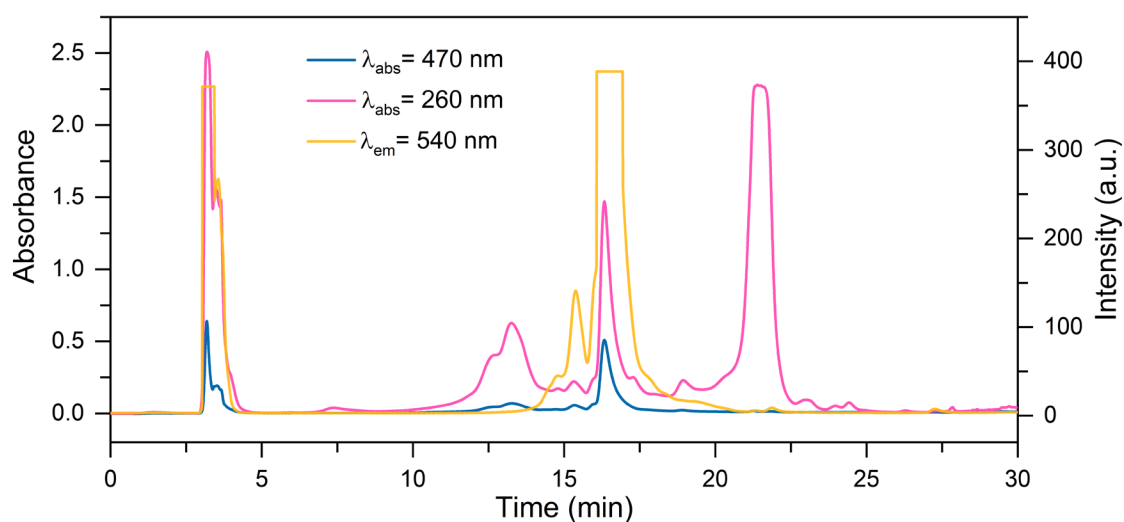
Figure S3. HPLC chromatograms of 5A-11Green-AgNCs monitoring the absorption at 470 nm and 260 nm, and the fluorescence signal at 540 nm (λ_{exc}= 470 nm). The plateau of the peaks in the 260 nm absorption and fluorescence chromatograms is due to detector saturation. The fraction was collected between 16 and 17 min (29-30% B).
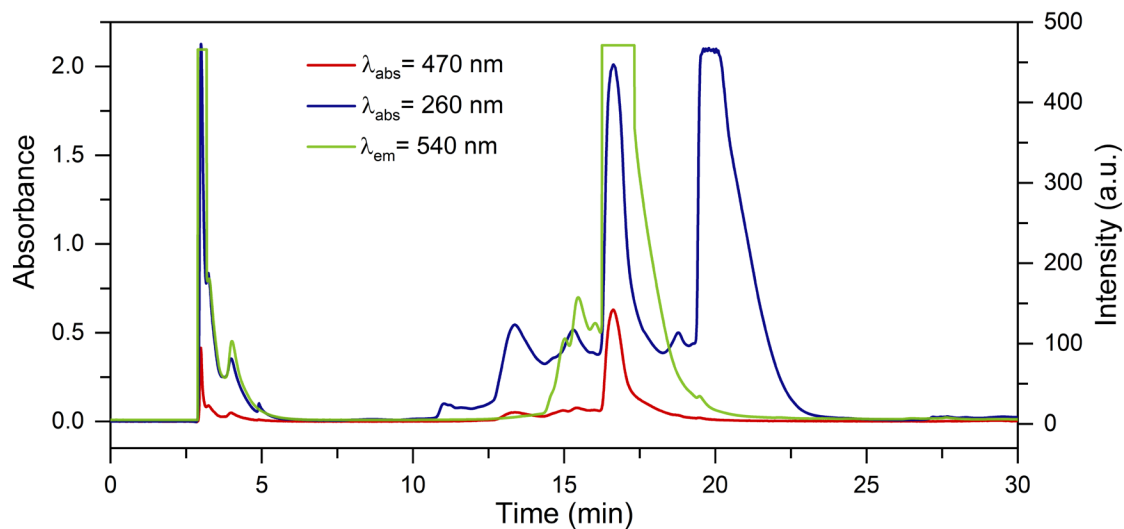
Figure S4. HPLC chromatograms of 5AA-11Green-AgNCs monitoring the absorption at 470 nm and 260 nm, and the fluorescence signal at 540 nm (λ_{exc}= 470 nm). The plateau in the 260 nm absorption and fluorescence signals is due to detector saturation. The fraction was collected at t_R≈ 16.2-18 min (≈ 29-31% B).
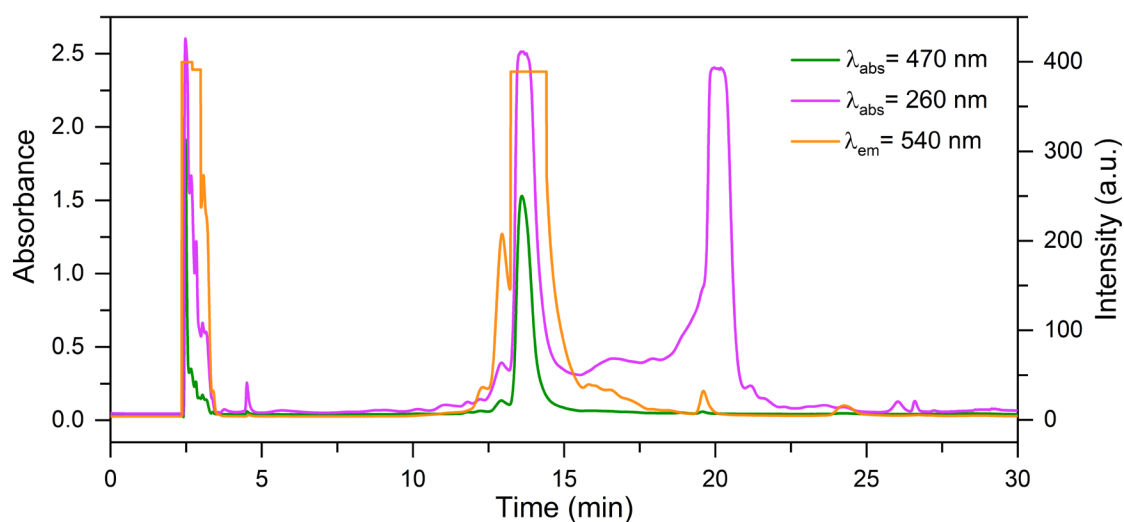
Figure S5. HPLC chromatograms of 3A-11Green-AgNCs monitoring the absorption at 470 nm and 260 nm, and the fluorescence signal at 540 nm (exciting at 470 nm). The plateau of the peaks in the 260 nm absorption and fluorescence chromatograms is due to detector saturation. The fraction was collected around 13.2-15 min (≈ 26-28% B).
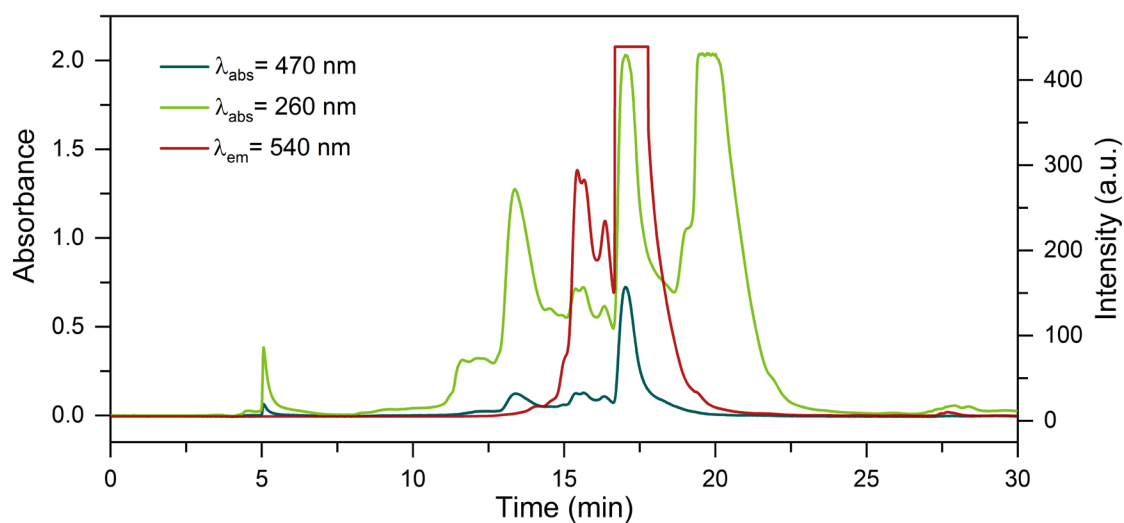
Figure S6. HPLC chromatograms of 5TA-11Green-AgNCs monitoring the absorption at 470 nm and 260 nm, and the fluorescence signal at 540 nm (exciting at 470 nm). The plateau of the peaks in the 260 nm absorption and fluorescence chromatograms is due to detector saturation. The fraction was collected at 17-18 min (≈ 30-31% B).
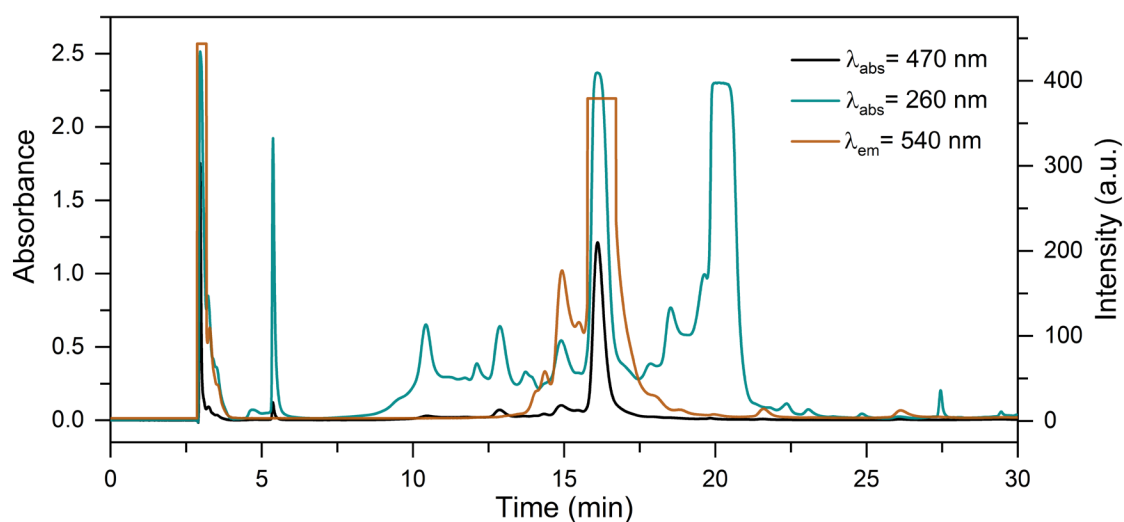
Figure S7. HPLC chromatograms of 5T-11Green-AgNCs monitoring the absorption at 470 nm and 260 nm, and the fluorescence signal at 540 nm (exciting at 470 nm). The plateau of the 260 nm absorption and fluorescence signals is due to detector saturation. The fraction was collected at $t_R \approx$ 16-17 min ($\approx$ 29-30% B).
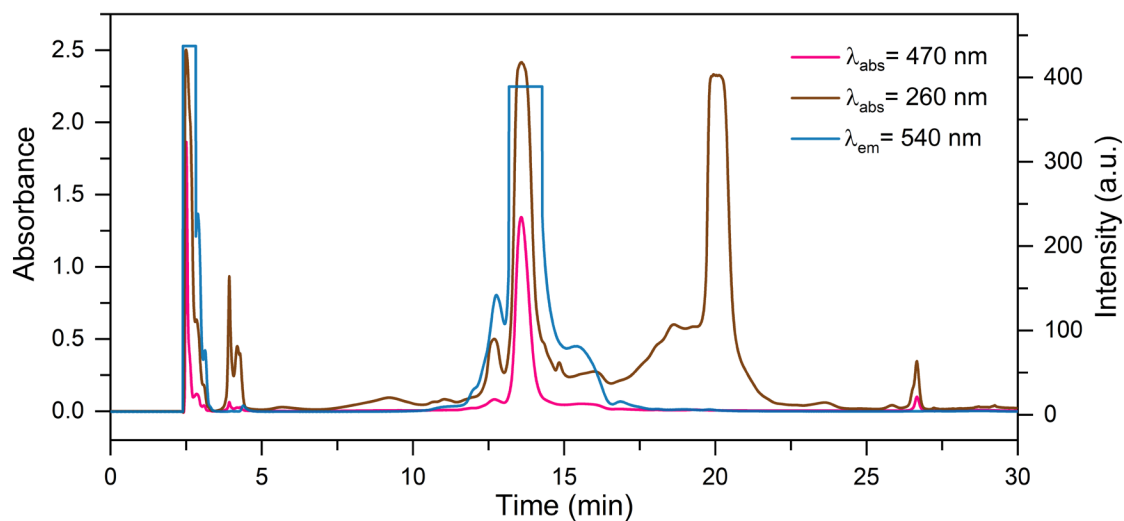
Figure S8. HPLC chromatograms of 3T-11Green-AgNCs monitoring the absorption at 470 nm and 260 nm, and the fluorescence signal at 540 nm (exciting at 470 nm). The plateau of the peaks in the 260 nm absorption and fluorescence chromatograms is due to detector saturation. The fraction was collected at $t_R \approx$ 13.6 min (between 26-27% B).
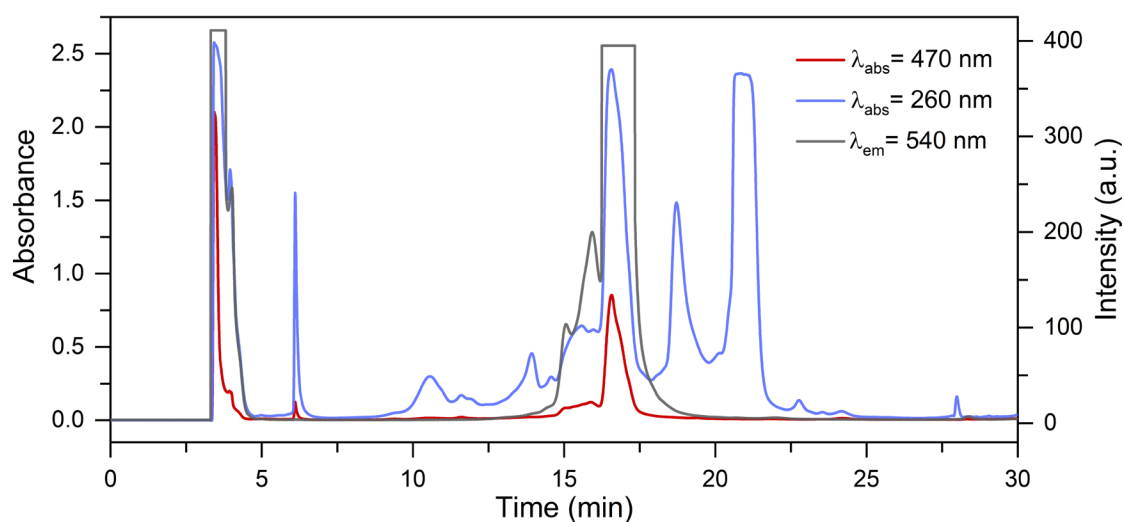
Figure S9. HPLC chromatograms of 5T-3T-11Green-AgNCs monitoring the absorption at 470 nm and 260 nm, and the fluorescence signal at 540 nm (exciting at 470 nm). The plateau of the 260 nm absorption and fluorescence signals is due to detector saturation. The fraction was collected around 16.2-17.5 min (≈ 29-31% B).
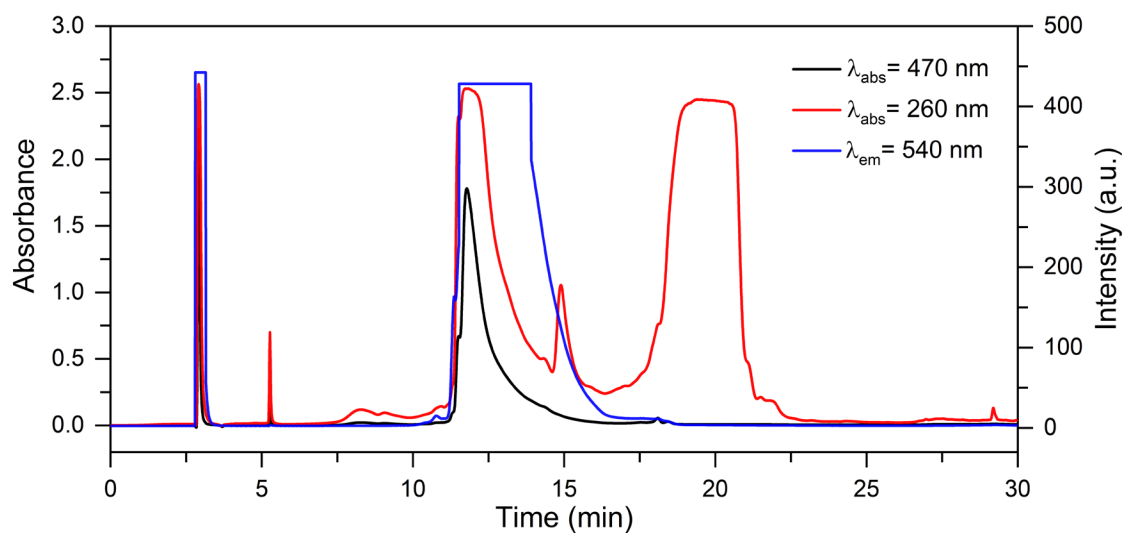
Figure S10. HPLC chromatograms of BrC3-11Green-AgNCs monitoring the absorption at 470 nm and 260 nm, and the fluorescence signal at 540 nm (exciting at 470 nm). The plateau in both the 260 nm absorption and fluorescence chromatograms is due to detector saturation. The fraction described in the manuscript was collected at t_R ≈ 13-15 min (≈ 26-28% B). This retention time corresponds to the tail of the 470 nm peak.
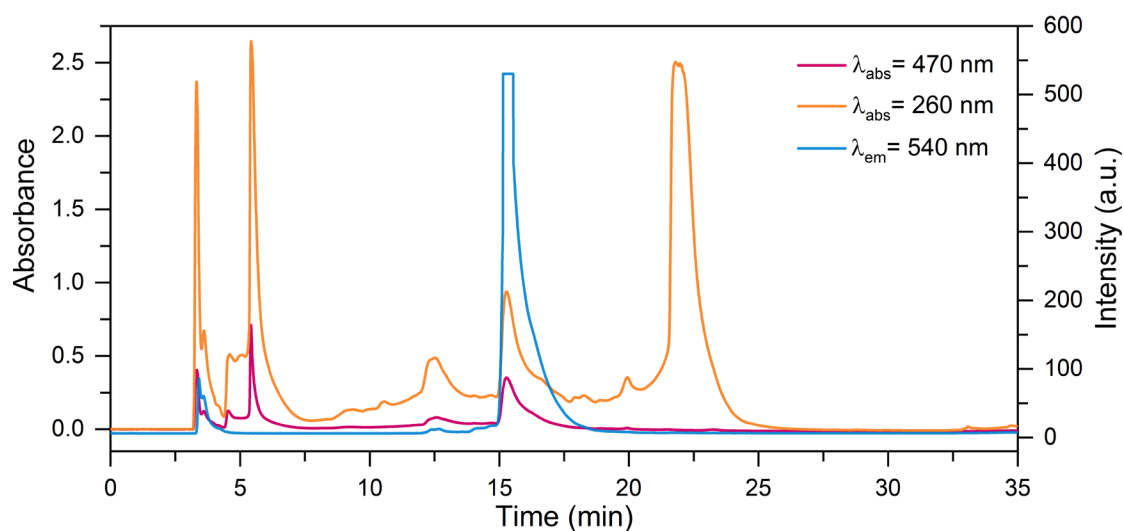
Figure S11. HPLC chromatograms of 11Green-2end-AgNCs monitoring the absorption at 470 nm and 260 nm, and the fluorescence signal at 540 nm (exciting at 470 nm). The plateau in both the 260 nm absorption and fluorescence chromatograms is due to detector saturation. The fraction described in the manuscript was collected at $t_R \approx$ 15-18 min ($\approx$ 28-31% B).
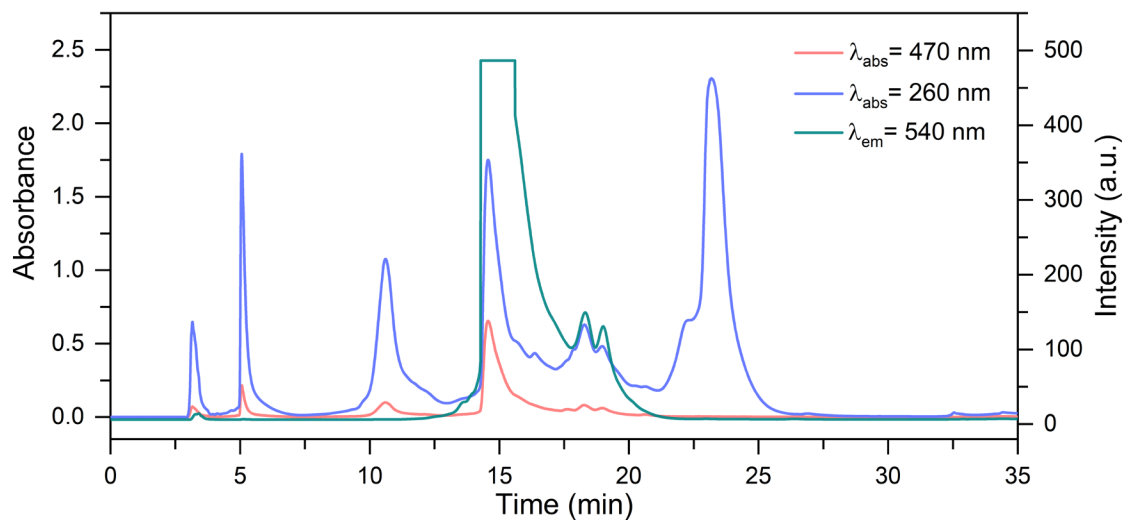
Figure S12. HPLC chromatograms of 5A-11Green-2end-AgNCs monitoring the absorption at 470 nm and 260 nm, and the fluorescence signal at 540 nm (exciting at 470 nm). The plateau in the fluorescence chromatogram is due to detector saturation. The fraction described in the manuscript was collected at $t_R \approx$ 14-16 min ($\approx$ 27-29% B).

14

Solution state
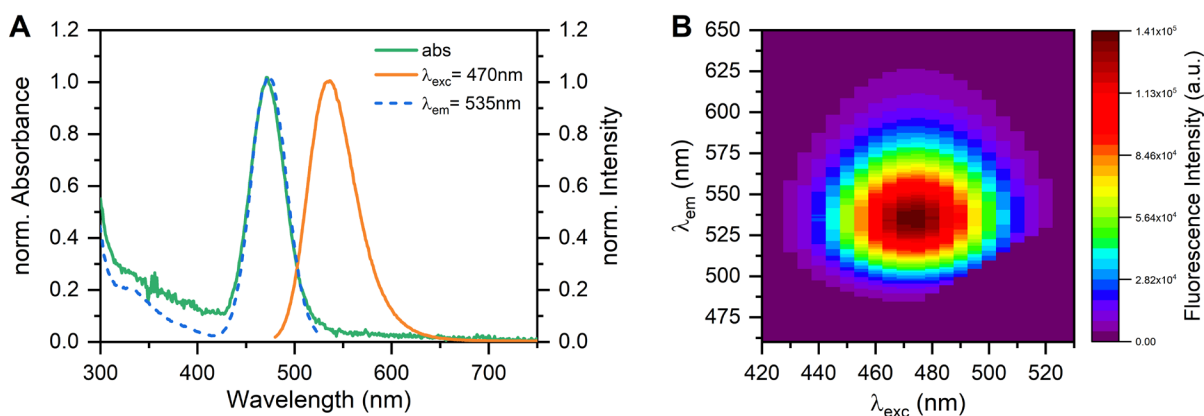
Figure S13. 10Green-AgNCs in 10 mM NH$_4$OAc at 25 ˚C. (A) Normalized absorption (green), emission (orange) and excitation (dashed blue) spectra. The emission spectrum was recorded exciting at 470 nm, while the excitation spectrum was monitored at 535 nm. (B) 2D emission *vs* excitation plot measured in steps of 5 nm.
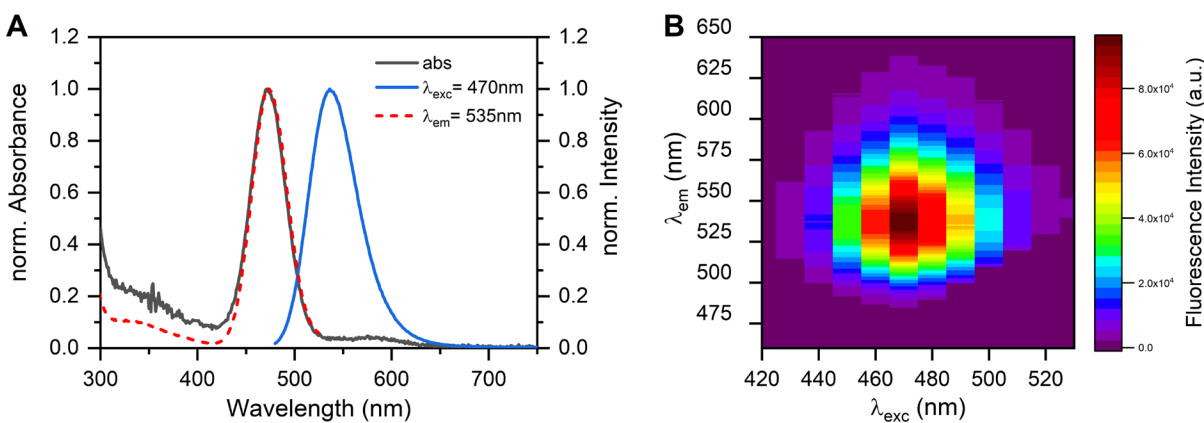
Figure S14. 11Green-AgNCs in 10 mM NH$_4$OAc at 25 ˚C. (A) Normalized absorption (gray), emission (blue) and excitation (dashed red) spectra. The emission spectrum was acquired exciting at 470 nm, whereas the excitation spectrum was monitored at 535 nm. (B) 2D emission *vs* excitation plot recorded in steps of 10 nm.
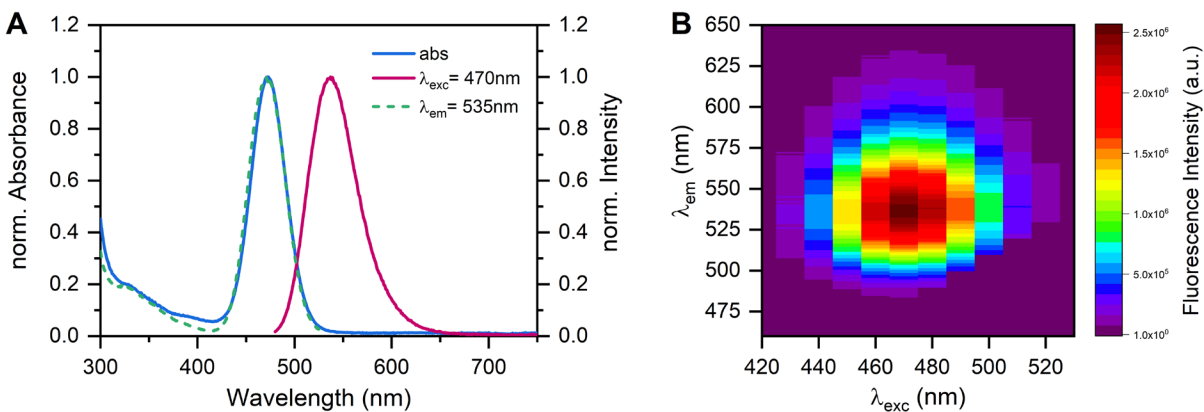
Figure S15. 5A-11Green-AgNCs in 10 mM NH_4OAc at 25 ˚C. (A) Normalized absorption (blue), emission (mauve) and excitation (dashed green) spectra. The emission spectrum was acquired exciting at 470 nm, while the excitation spectrum was monitored at 535 nm. (B) 2D emission *vs* excitation plot measured in steps of 10 nm.
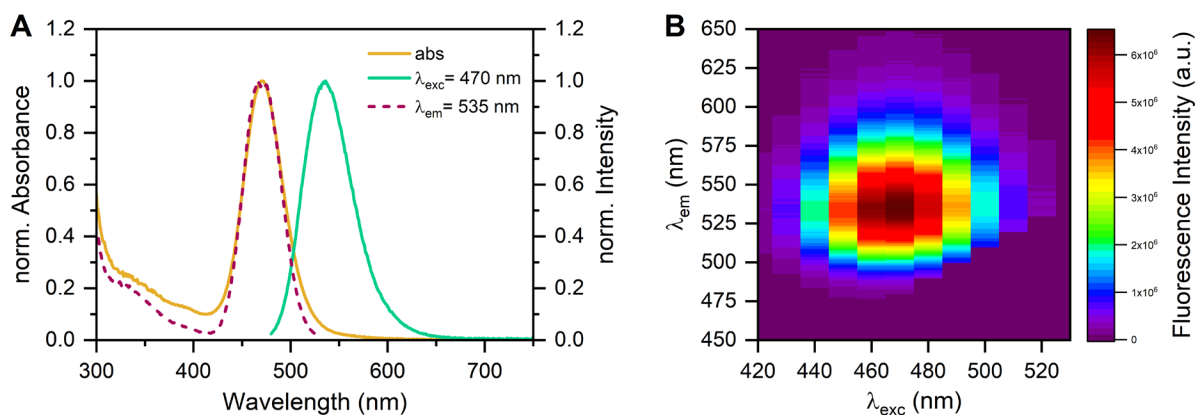
Figure S16. 11Green-2end-AgNCs in 10 mM NH_4OAc at 25 ˚C. (A) Normalized absorption (pink), emission (blue) and excitation (dashed purple) spectra. The emission spectrum was acquired exciting at 470 nm, whereas the excitation spectrum was monitored at 535 nm. (B) 2D emission *vs* excitation plot recorded in steps of 10 nm.
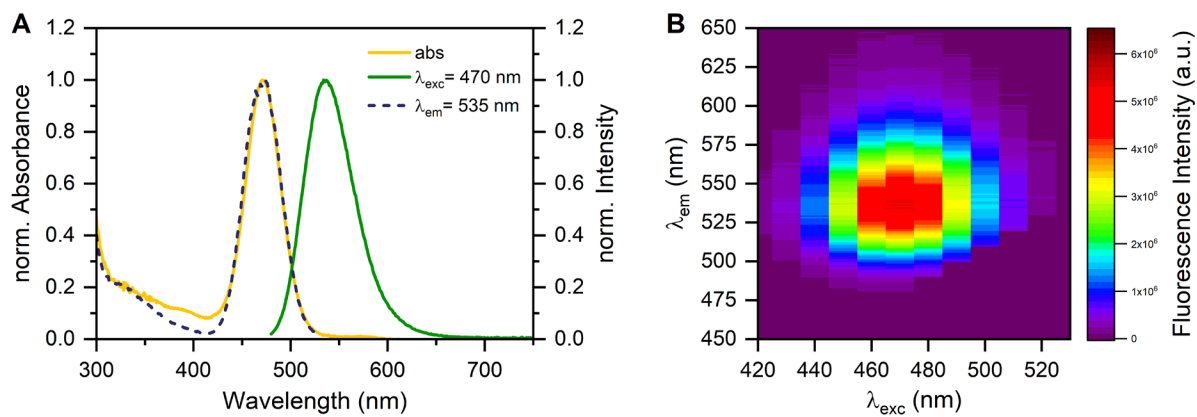
Figure S17. 5A-11Green-2end-AgNCs in 10 mM NH₄OAc at 25 ˚C. (A) Normalized absorption (pink), emission (blue) and excitation (dashed purple) spectra. The emission spectrum was acquired exciting at 470 nm, whereas the excitation spectrum was monitored at 535 nm. (B) 2D emission *vs* excitation plot recorded in steps of 10 nm.
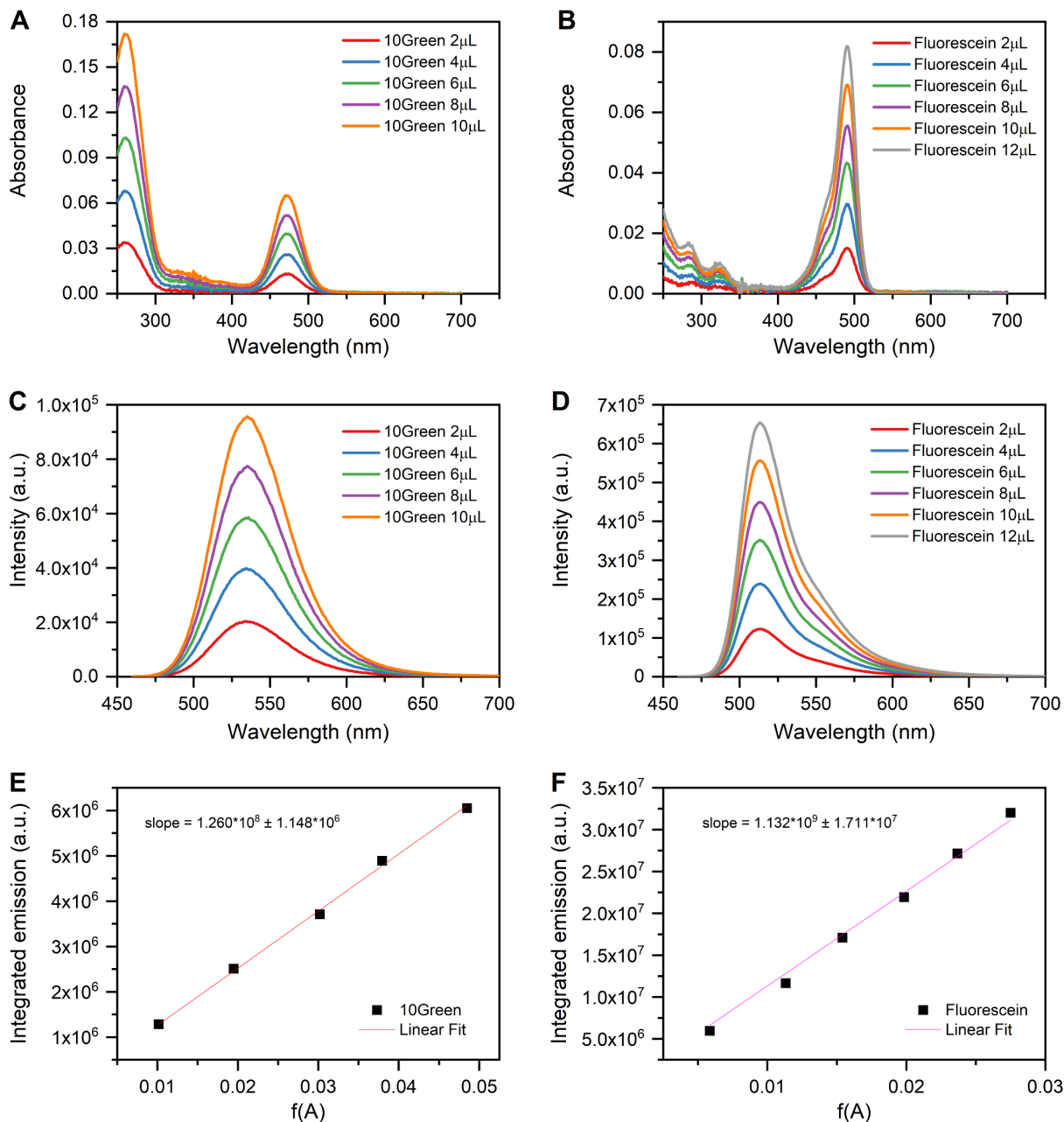
Figure S18. 10Green-AgNC quantum yield determination. (A) Absorption and (C) emission spectra (λ_{exc}= 445.4 nm) of 10Green-AgNCs in 10 mM NH$_4$OAc at 25 ˚C. (B) Absorption and (D) emission spectra (λ_{exc}= 445.4 nm) of Fluorescein in 0.1 M NaOH. (E) and (F) Zero-intercept linear fits of the integrated fluorescence vs. the fraction of absorbed light for 10Green-AgNCs and Fluorescein, respectively. The slopes were used to calculate the Q of the sample.
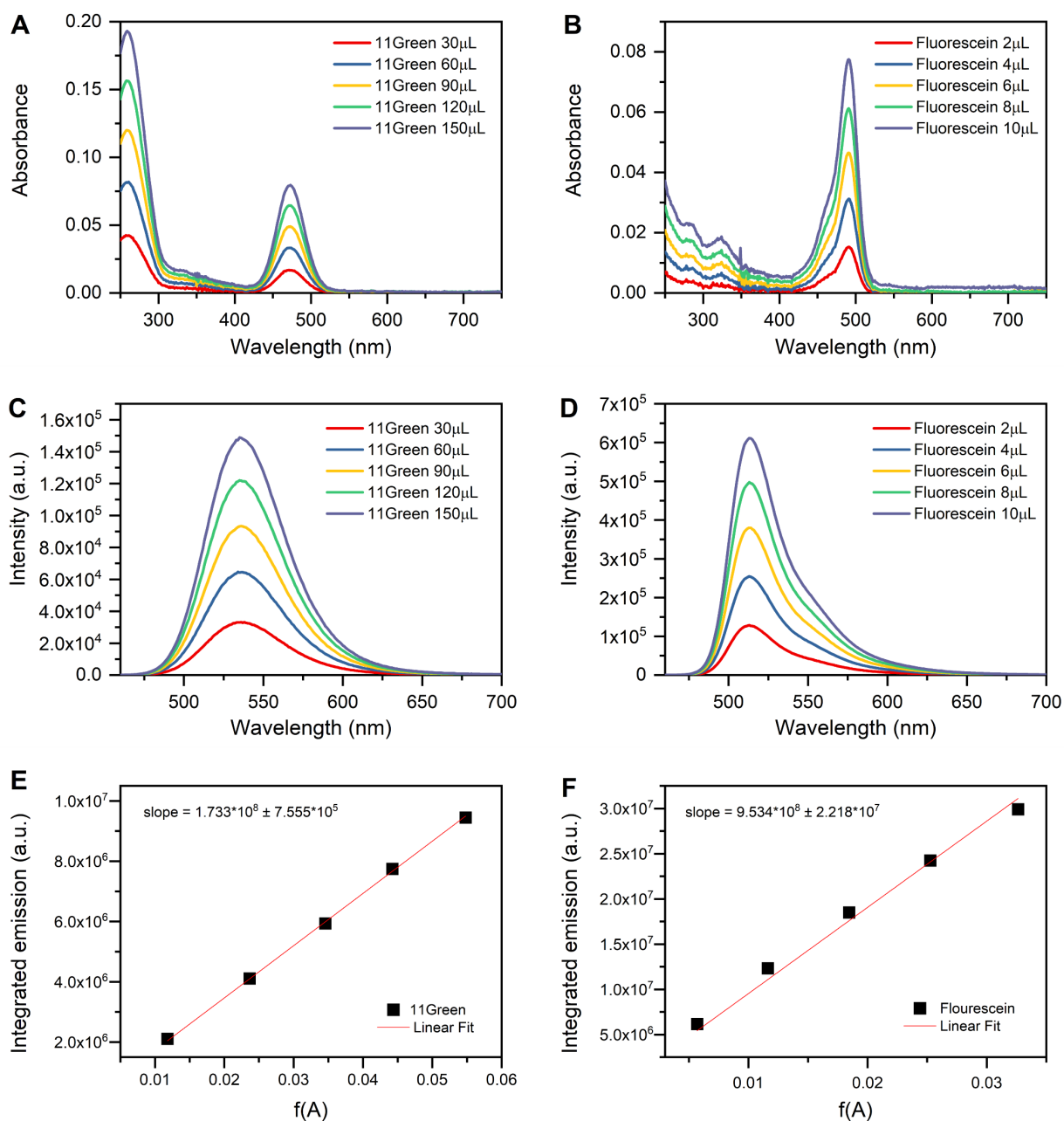
Figure S19. 11Green-AgNC quantum yield determination. (A) Absorption and (C) emission spectra (λ_{exc}= 445.4 nm) of 11Green-AgNCs in 10 mM NH_4OAc at 25 ˚C. (B) Absorption and (D) emission spectra (λ_{exc}= 445.4 nm) of Fluorescein in 0.1 M NaOH. (E) and (F) Linear fits with zero-intercept of the integrated fluorescence vs. the fraction of absorbed light for 11Green-AgNCs and Fluorescein, respectively. The slopes were used to calculate the Q of the sample.
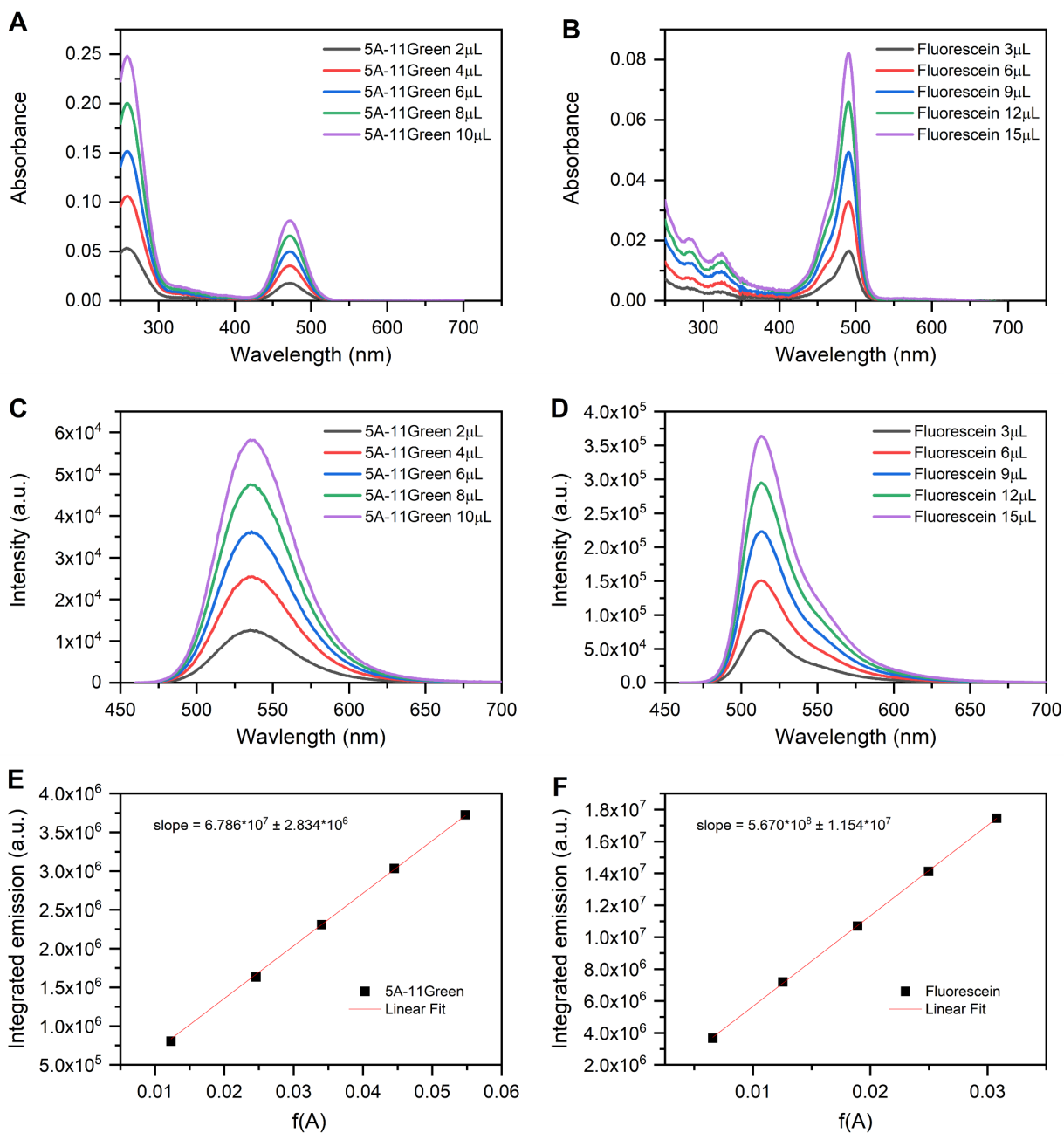
Figure S20. 5A-11Green-AgNC quantum yield determination. (A) Absorption and (C) emission spectra (λ_{exc}= 445.4 nm) of 5A-11Green-AgNCs in 10 mM NH_4OAc at 25 ˚C. (B) Absorption and (D) emission spectra (λ_{exc}= 445.4 nm) of Fluorescein in 0.1M NaOH. (E) and (F) Zero-intercept linear fit of the integrated fluorescence vs. the fraction of absorbed light for 5A-11Green-AgNCs and Fluorescein, respectively. The slopes were used to calculate the Q of the sample.
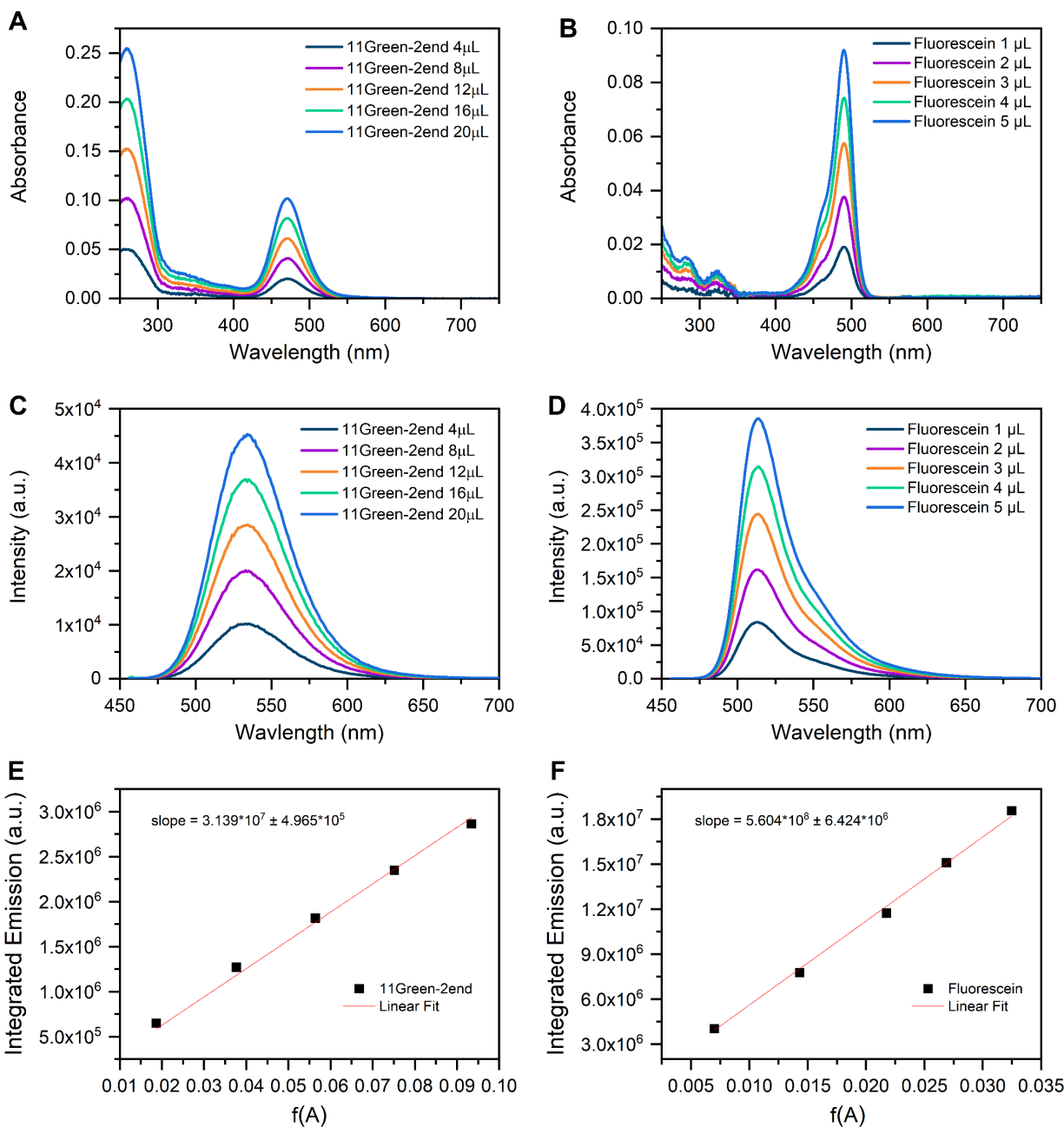
Figure S21. 11Green-2end-AgNC quantum yield determination. (A) Absorption and (C) emission spectra (λ_{exc}= 445.4 nm) of 11Green-2end-AgNCs in 10 mM NH_4OAc at 25 ˚C. (B) Absorption and (D) emission spectra (λ_{exc}= 445.4 nm) of Fluorescein in 0.1M NaOH. (E) and (F) Zero-intercept linear fit of the integrated fluorescence vs. the fraction of absorbed light for 11Green-2end-AgNCs and Fluorescein, respectively. The slopes were used to calculate the Q of the sample.

Mass spectrometry
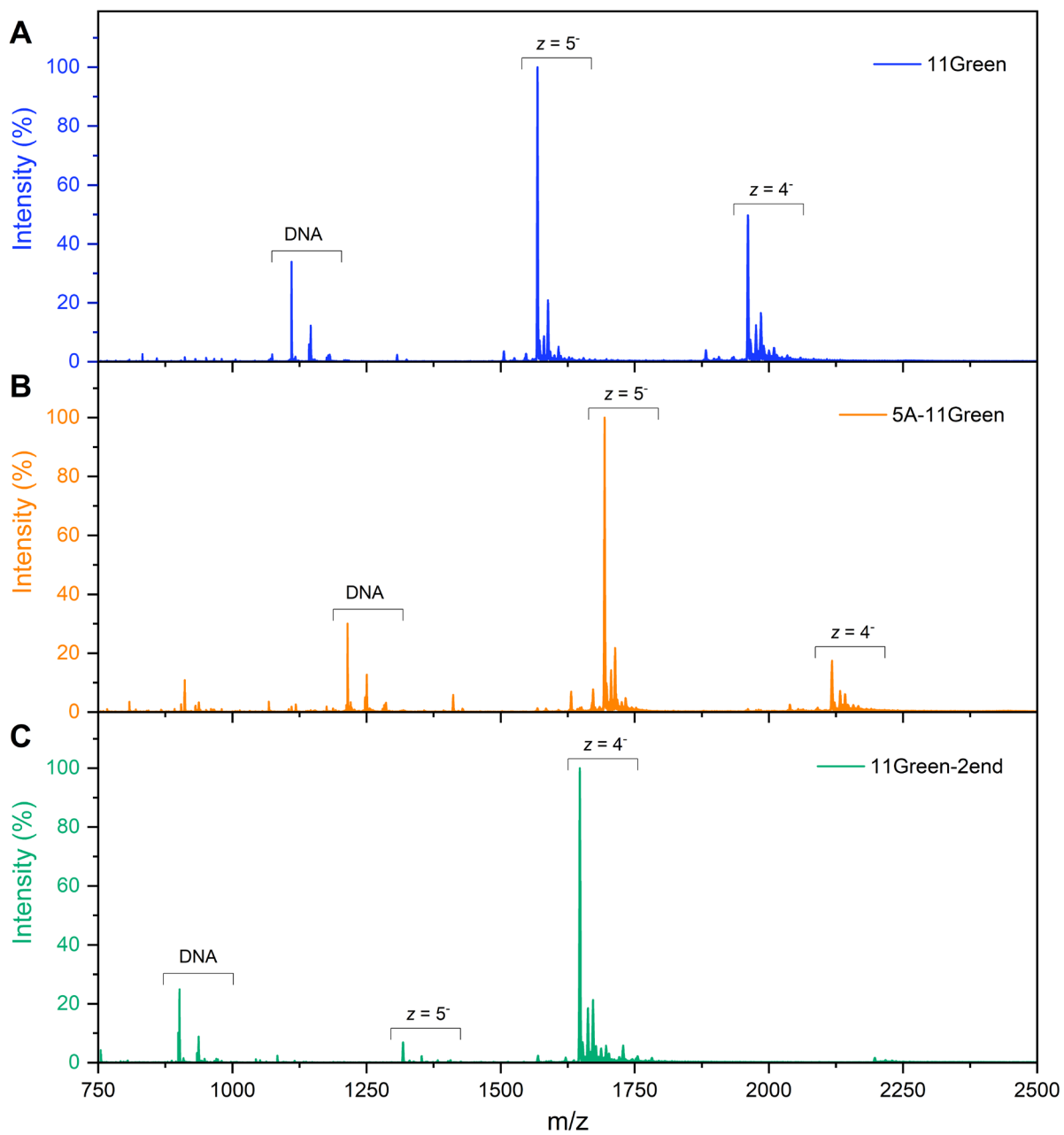
Figure S22. Mass spectrometry data of (A) 11Green-AgNC, (B) 5A-Green-AgNC and (C) 11Green-2end-AgNC. Spectra were collected from 750 to 4000 m/z, but no signals are observed above 2500 m/z.
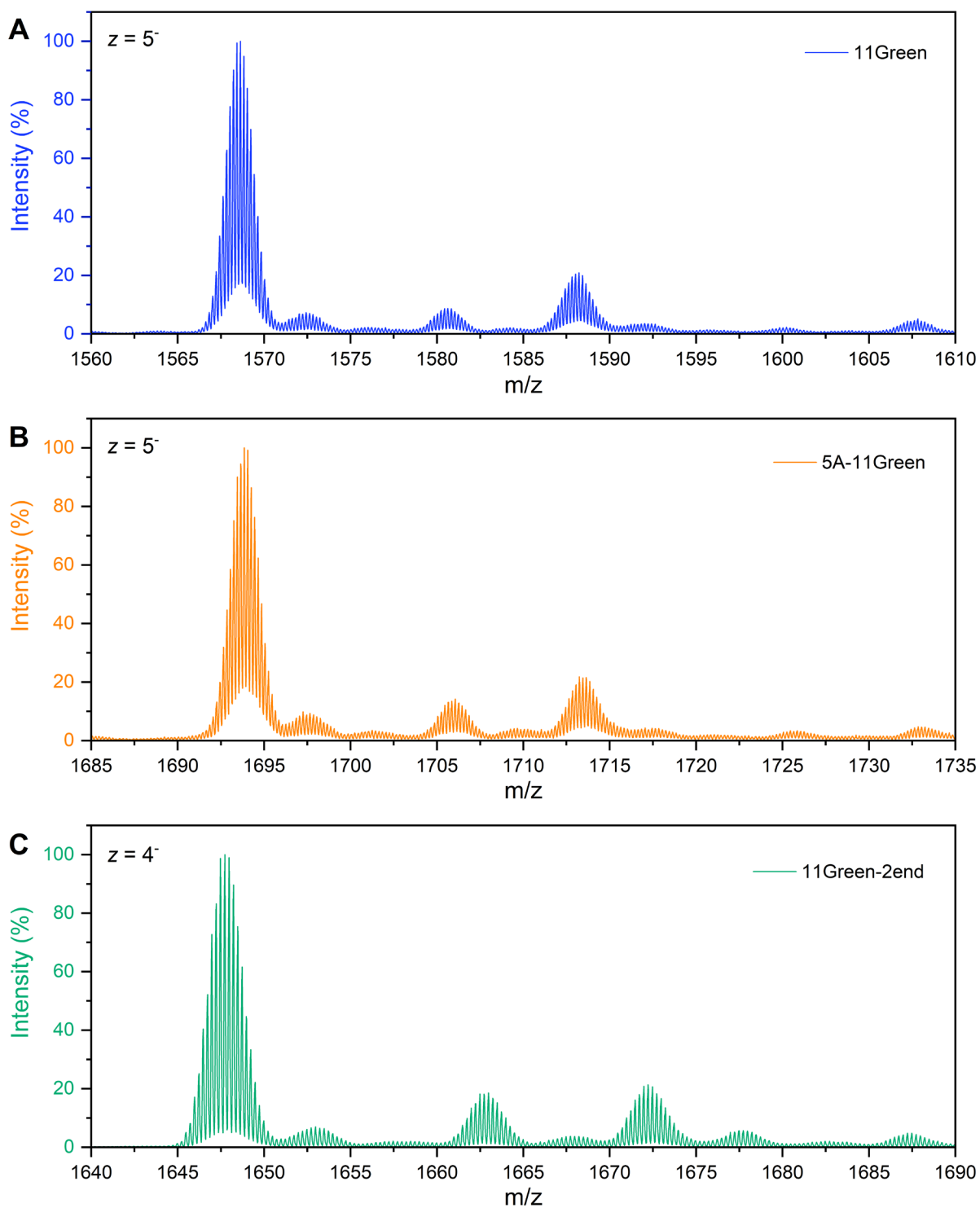
Figure S23. Zoom-in of the main peaks in the mass spectra shown in Figure S22. All three samples are characterized by the same experimental isotopic pattern. The analysis of spectrum C is reported in Figure S24.
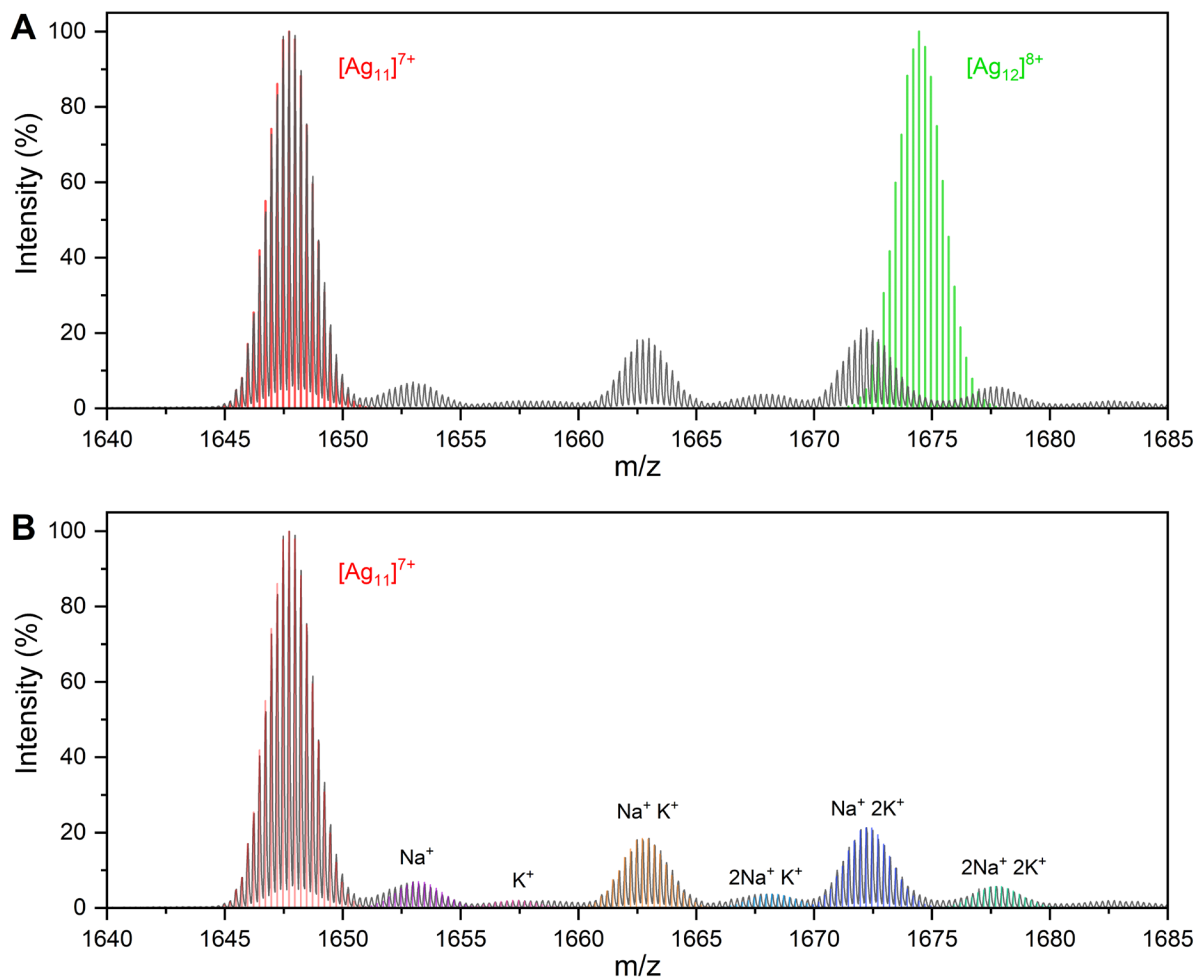
Figure S24. (A) Mass spectrum (gray) of 11Green-2end-AgNC with calculated isotopic distributions for Ag_{11}^{7+} (red) and Ag_{12}^{8+} (green) at $z= 4^-$. The most intense peak corresponds to (DNA)$_2$-[Ag$_{11}$]$^{7+}$ NC, indicated as Ag_{11}^{7+}, while no peak matches the theoretical distribution of a 12-silver-atom nanocluster (Ag_{12}^{8+}). (B) Mass spectrum (gray) of the main product, Ag_{11}^{7+}, and Na$^+$ and/or K$^+$ adducts at $z= 4^-$. The colored lines correspond to the theoretical distributions and each adduct is reported on top of the related peak. The total charge of the nanocluster is unaltered.
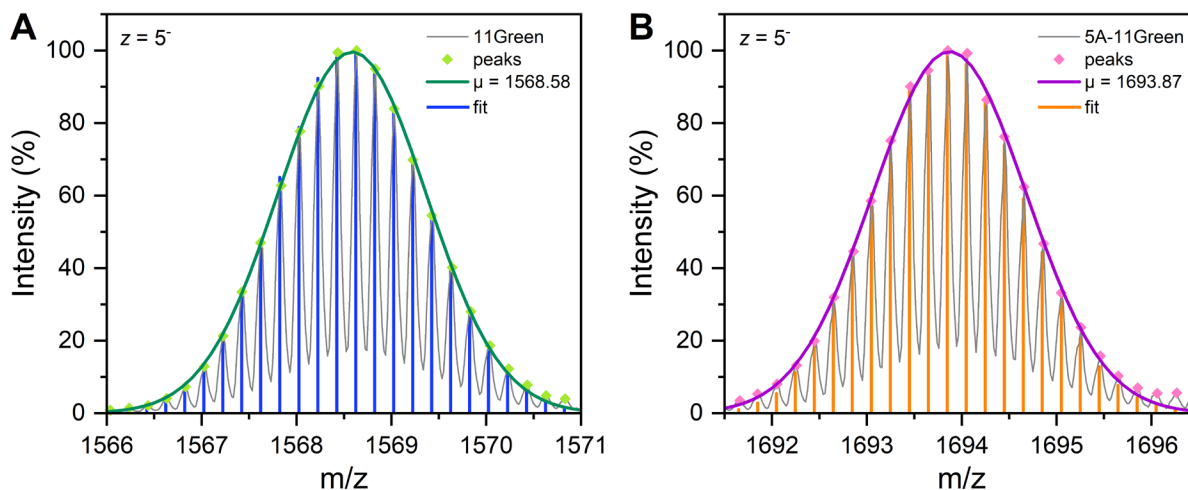
Figure S25. (A) Zoomed-in view of the molecular ion peak of 11Green-AgNC with *z*= 5⁻ charge state. The experimental isotopic distribution is reported with the corresponding Gaussian fit (dark green) and the theoretical isotopic distribution (blue). The calculated average mass is 1568.586 m/z and is consistent with the molecular mass of 7855.05 g/mol. The sum formula is $C_{214}H_{268}N_{92}O_{120}P_{20}[Ag_{11}]^{7+}$. (B) Zoomed-in view of the molecular ion peak of 5A-11Green-AgNC with *z*= 5⁻ charge state. The experimental isotopic distribution is reported with the corresponding Gaussian fit (purple) and the theoretical isotopic distribution (orange). The sum formula is $C_{234}H_{292}N_{102}O_{130}P_{22}[Ag_{11}]^{7+}$, which corresponds to a molecular mass of 8481.47 g/mol. The calculated average mass of 1568.586 m/z matches the molecular mass.

Crystalline state

Figure S26. (A) Density-modified electron density map of silver atoms obtained by the SAD phasing, contoured at 4σ level. (B) Structure of the 9-silver subunit of 11Green-2end-AgNC crystal with nearest inter-silver distances represented by colored dashed lines to highlight the subsections of the cluster.

Figure S27. Fluorescence decay curves of 11Green-2end-AgNC crystals, exciting at 458 nm. The decays are normalized to the emission maximum and have a constant 0.2 offset for displaying purposes. The IRF is the dashed gray line. The crystals were grown with 10% MPD, 10 mM spermine, 50 mM MOPS and 10 mM $Ca(NO_3)_2$. Each decay was fitted with a 3- or 4-exponential reconvolution function including the IRF. The resulting intensity-weighted average decay times, <τ>, (0.43, 0.61, 0.57, 0.52 and 0.36 ns) were then used to calculate the mean decay time value, τ_{av}, of 0.50 ns.

Figure S28. Long-lived luminescence from the red-shifted band of 11Green-2end-AgNC crystals, recorded with a confocal microscope in burst mode, exciting at 458 nm. The traces are normalized to the emission maximum and have a constant 0.2 offset for displaying purposes. The IRF is the dashed gray line. The crystals were grown with 10% MPD, 10 mM spermine, 50 mM MOPS and 10 mM $Ca(NO_3)_2$. Every decay (after the laser is turned off) was tail-fitted with a bi-exponential function, and the resulting intensity-weighted average decay times, $<\tau_{\mu s}>$, (170, 171, 160, 165 and 169 µs) were used to calculate the mean decay time value, $<\tau_{\mu s}>_{av}$, of 167 µs reported in the manuscript.
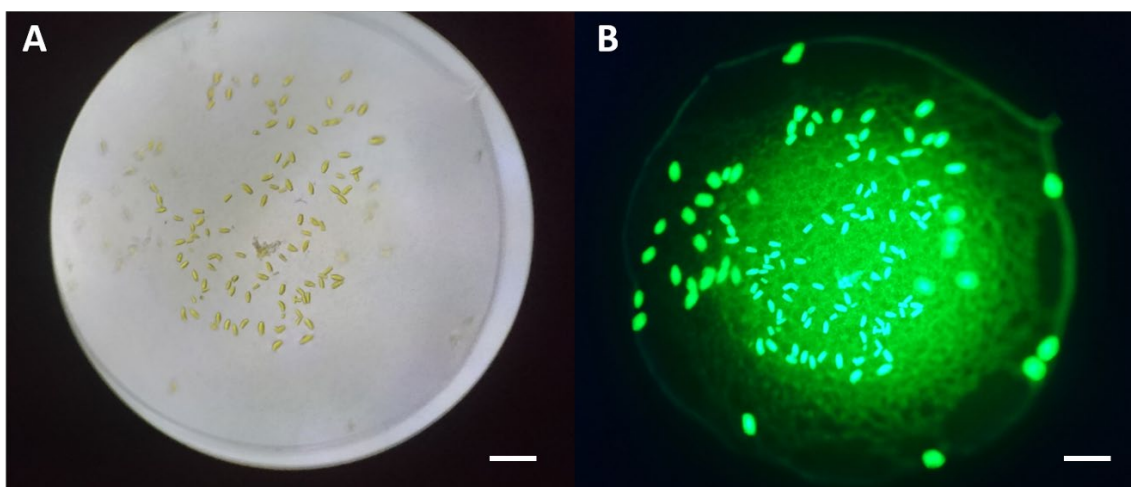
Figure S29. (A) Bright field and (B) fluorescence images (λ_{exc}= 470-495 nm – λ_{em}= 510-550 nm) of 11Green-AgNC crystals grown in 10 % MPD, 10 mM spermine, 10 mM NH_4NO_3 and 50 mM MOPS at pH 7. The crystals were 3 weeks old. The scale bar corresponds to 100 µm.
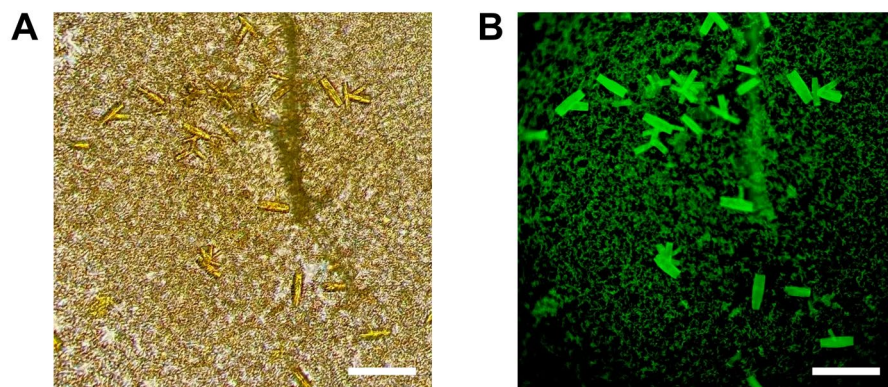
Figure S30. (A) Bright-field and (B) fluorescence images (λ_{exc}= 470-495 nm – λ_{em}= 510-550 nm) of 11Green-AgNC crystals grown in 10 % MPD, 10 mM spermine, 100 mM NH_4NO_3 and 50 mM MOPS at pH 7. The crystals were 7 days old. The scale bar corresponds to 100 µm.
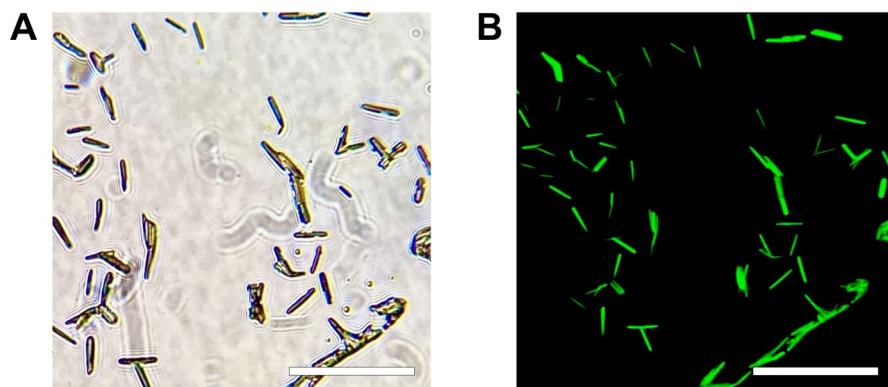
Figure S31. (A) Bright-field and (B) fluorescence images (λ_{exc}= 470-495 nm – λ_{em}= 510-550 nm) of 5A-11Green-AgNC crystals grown in 10 % PEG, 10 mM spermine, 10 mM $LiNO_3$ and 50 mM MOPS at pH 7. The crystals were two years old. The scale bar corresponds to 100 µm.
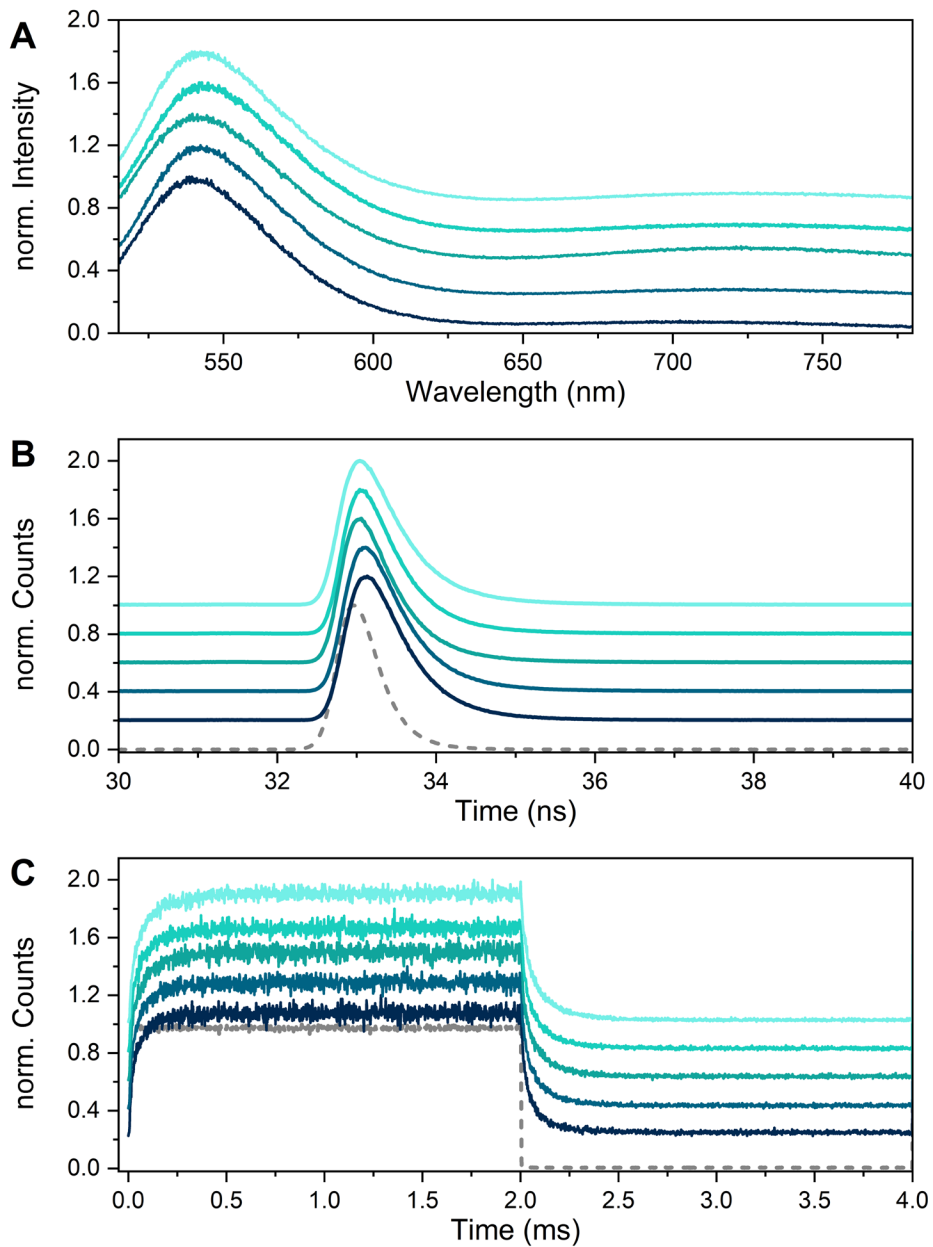
Figure S32. (A) Emission spectra, (B) fluorescence decays and (C) long-lived luminescence traces of 11Green-AgNC crystals, shown in Figure S30, recorded with a confocal microscope, exciting at 458 nm. The traces are normalized and have a constant 0.2 offset for displaying purposes. The IRFs are the dashed gray lines. (B) Each fluorescence decay was fitted with a bi-exponential reconvolution function including the IRF. The resulting intensity-weighted average decay times, $\langle\tau\rangle$, (0.44, 0.46, 0.46, 0.47 and 0.48 ns) were then used to calculate the mean decay time value, τ_{av}, of 0.46 ns. (C) Every luminescence decay (from 2.0 ms) was tail-fitted with a bi-exponential function. The mean decay time value, $\langle\tau_{\mu s}\rangle_{av}$, of 88 µs was calculated from the intensity-weighted average decay times, $\langle\tau_{\mu s}\rangle$ (78, 84, 87, 89 and 103 µs).
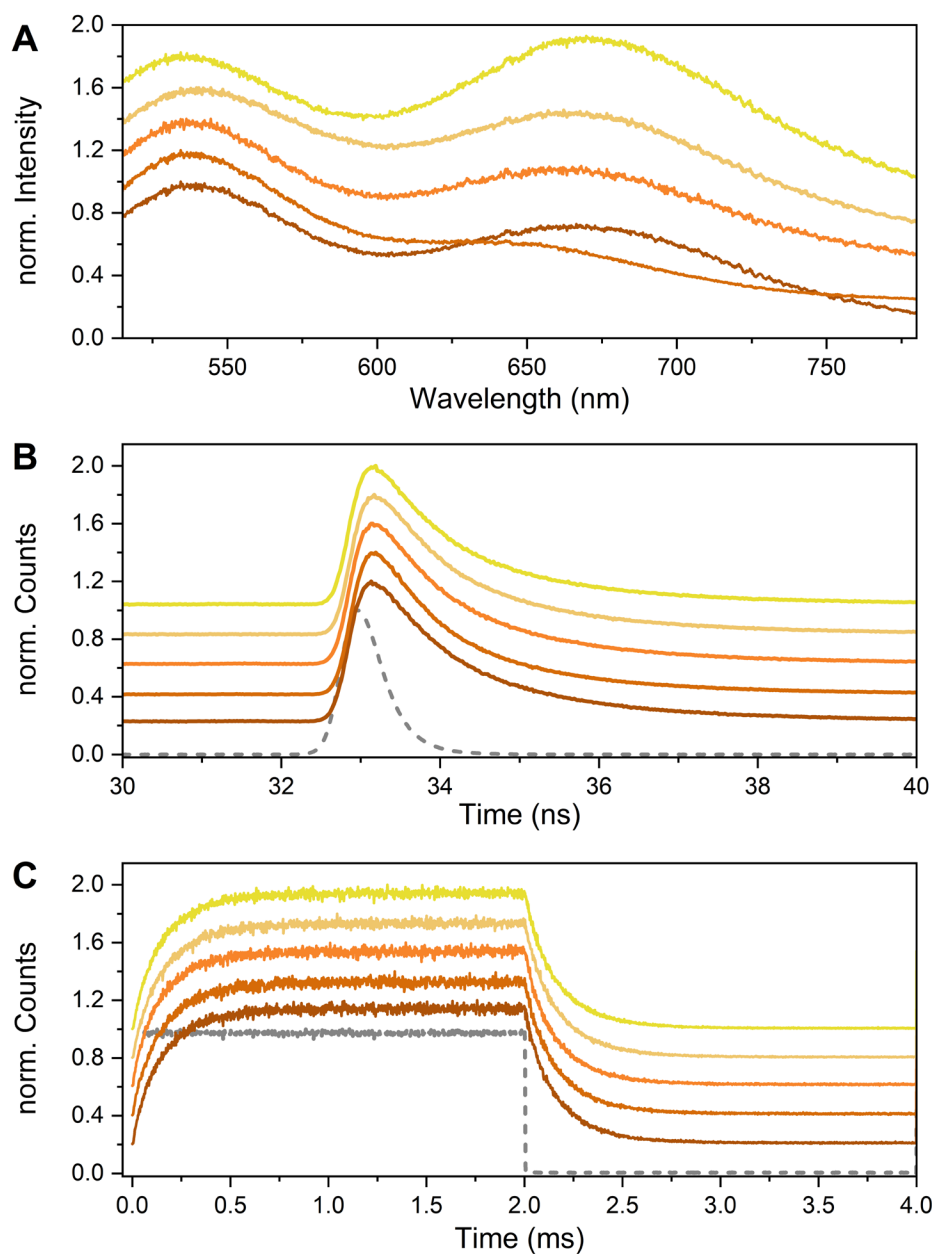
Figure S33. (A) Emission spectra, (B) fluorescence decays and (C) long-lived luminescence traces of 5A-11Green-AgNC crystals, shown in Figure S31, recorded with a confocal microscope, exciting at 458 nm. The traces are normalized and have a constant 0.2 offset for displaying purposes. The IRFs are the dashed gray lines. (B) Each fluorescence decay was fitted with a bi-exponential reconvolution function including the IRF. The resulting intensity-weighted average decay times, $<\tau>$, (1.48, 1.47, 1.58, 1.57 and 1.56 ns) were then used to calculate the mean decay time value, τ_{av}, of 1.53 ns. (C) Every luminescence decay (from 2.0 ms) was tail-fitted with a bi-exponential function. The mean decay time value, $<\tau_{\mu s}>_{av}$, of 172 µs was calculated from the intensity-weighted average decay times, $<\tau_{\mu s}>$ (170, 170, 169, 178 and 174 µs).
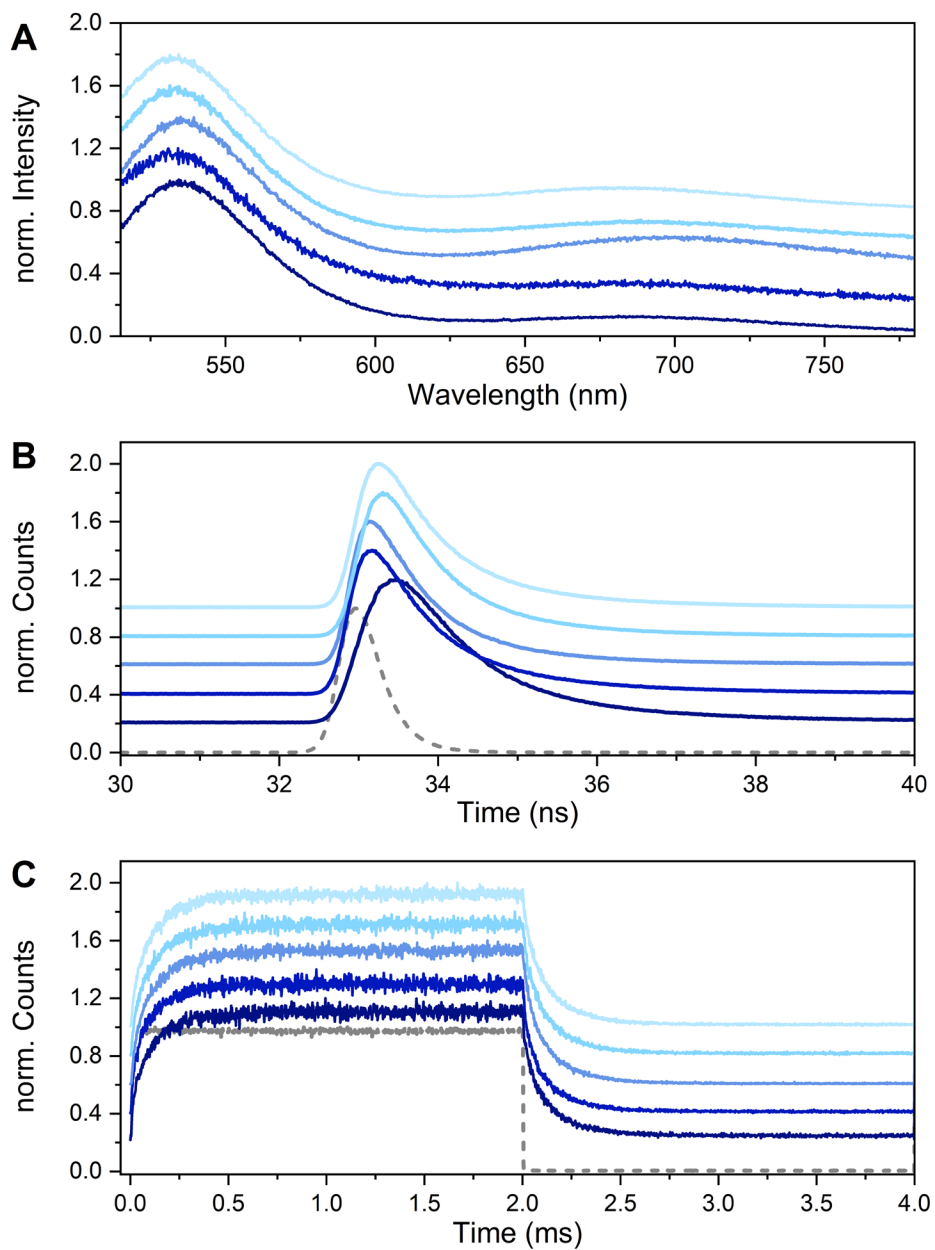
Figure S34. Rehydrated 5A-11Green-AgNC crystals. 40% PEG 3350 was added to the two-year-old crystals, shown in Figure S31. (A) Emission spectra, (B) fluorescence decays and (C) long-lived luminescence, recorded with a confocal microscope, exciting at 458 nm. The normalized traces have a constant 0.2 offset for displaying purposes. The IRFs are the dashed gray lines. (B) Each fluorescence decay was fitted with a tri-exponential reconvolution function including the IRF. The resulting intensity-weighted average decay times, $\langle\tau\rangle$, (1.72, 1.34, 0.97, 1.03 and 1.12 ns) were then used to calculate the mean decay time value, τ_{av}, of 1.24 ns. (C) Every luminescence decay (from 2.0 ms) was tail-fitted with a bi-exponential function. The mean decay time value, $\langle\tau_{\mu s}\rangle_{av}$, of 132 μs was calculated from the intensity-weighted average decay times, $\langle\tau_{\mu s}\rangle$ (132, 125, 136, 129 and 137 μs).

Droplet experiment
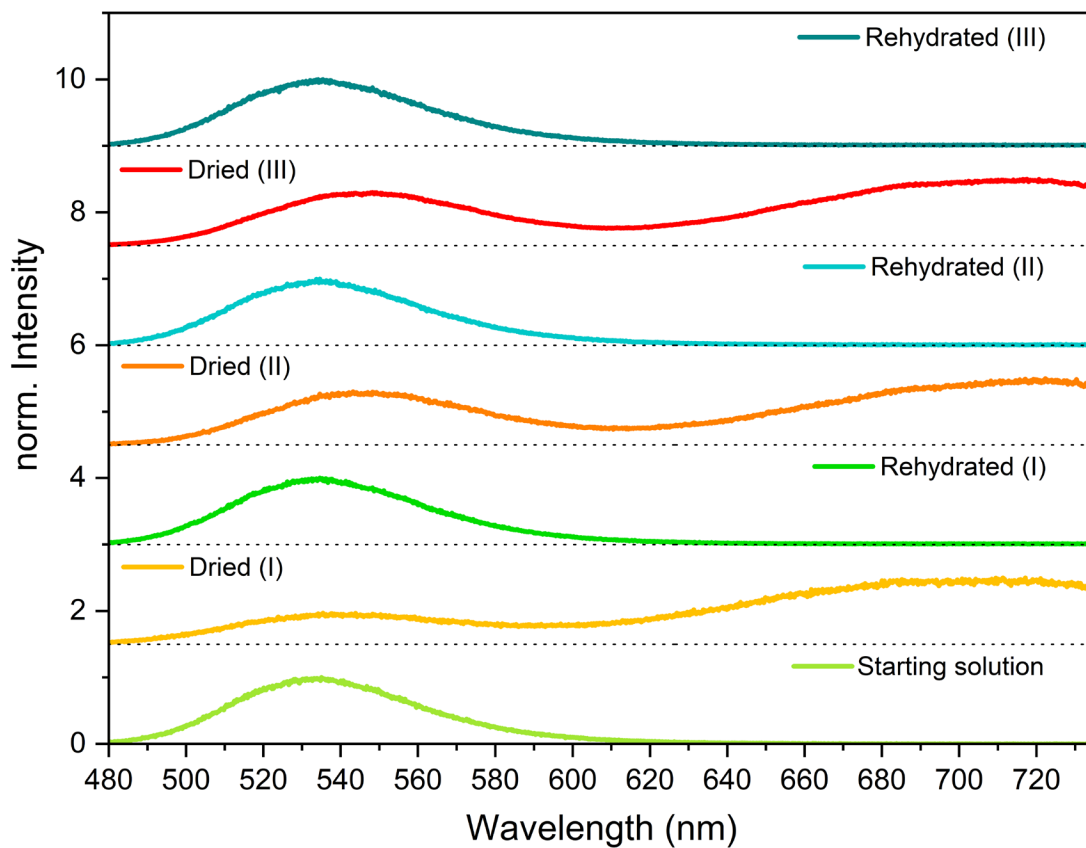
Figure S35. Normalized emission spectra of a 10 μL droplet of 11Green-2end-AgNC measured in 10 mM NH₄OAc before and after evaporation of the solvent (3 cycles). The spectra were acquired by exciting at 458 nm.

Publication 2

A DNA-Stabilized Ag_{18}^{12+} Cluster with Excitation-Intensity-Dependent Dual Emission

Vanessa Rück, Mikkel B. Liisberg, Christian Brinch Mollerup, Yanmei He, Junsheng Chen, Cecilia Cerretani, Tom Vosch.

GDCh

Research Articles

Angewandte
Chemie
International Edition
www.angewandte.org

Nanoclusters Hot Paper
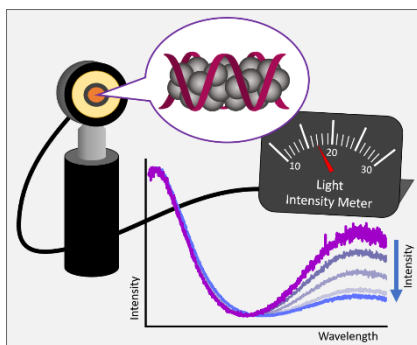
A DNA-Stabilized Ag_{18}^{12+} Cluster with Excitation-Intensity-Dependent Dual Emission

Vanessa Rück, Mikkel B. Liisberg, Christian Brinch Mollerup, Yanmei He, Junsheng Chen, Cecilia Cerretani,* and Tom Vosch*

Abstract: DNA-stabilized silver nanoclusters (DNA-AgNCs) are easily tunable emitters with intriguing photophysical properties. Here, a DNA-AgNC with dual emission in the red and near-infrared (NIR) regions is presented. Mass spectrometry data showed that two DNA strands stabilize 18 silver atoms with a nanocluster charge of 12+. Besides determining the composition and charge of $DNA_2[Ag_{18}]^{12+}$, steady-state and time-resolved methods were applied to characterize the picosecond red fluorescence and the relatively intense microsecond-lived NIR luminescence. During this process, the luminescence-to-fluorescence ratio was found to be excitation-intensity-dependent. This peculiar feature is very rare for molecular emitters and allows the use of $DNA_2[Ag_{18}]^{12+}$ as a nanoscale excitation intensity probe. For this purpose, calibration curves were constructed using three different approaches based either on steady-state or time-resolved emission measurements. The results showed that processes like thermally activated delayed fluorescence (TADF) or photon upconversion through triplet-triplet annihilation (TTA) could be excluded for $DNA_2[Ag_{18}]^{12+}$. We, therefore, speculate that the ratiometric excitation intensity response could be the result of optically activated delayed fluorescence.

Introduction

DNA-stabilized silver nanoclusters (DNA-AgNCs) were first reported in 2004[1] and are, in many aspects, a unique class of emitters. Due to the encoding nature of the stabilizing nucleobase sequence, a myriad of atomically-precise AgNCs with different numbers of atoms, geometries and charge states can be obtained.[2]

Given the vast chemical space, high-throughput screening along with machine learning algorithms have been applied to relate emission colors to DNA sequences.[3] This correlation has been based on the assumption that every DNA-AgNC produces a single emission band. However, dual emission has recently been reported for some DNA-AgNCs,[4] and might be more prevalent than previously assumed. Such dual emission typically consists of a nanosecond-lived fluorescence band with an additional red-

shifted microsecond-lived luminescence band. The latter is the result of a less-allowed transition that might involve a change in spin multiplicity, but so far this has not been demonstrated with absolute certainty.

Here, we present an atomically-precise DNA-AgNC that has a dominant absorption feature in the green range and dual emission in the red and NIR regions. In addition to the rather pronounced microsecond-lived luminescence band, the ratio between the picosecond-lived fluorescence and the microsecond-lived luminescence is excitation-intensity-dependent, which is rather unusual for molecule-like emitters. Excitation wavelength-dependent emission spectra[5] or excitation intensity-dependent fluorescence quantum yields have been previously reported,[6] but it is rare to find examples of excitation-intensity-dependent ratiometric spectral changes for molecular emitters. Such features are usually more common in systems that support multiple consecutive excitations like lanthanide upconversion nanoparticles.[7] A ratiometric, excitation-intensity-dependent molecular probe, like $DNA_2[Ag_{18}]^{12+}$ investigated here, would be an ideal nanoscale light intensity meter. It could be applied in microscopy settings to better estimate the excitation intensity in the irradiated area with appropriate calibration curves. To demonstrate this possibility, three different approaches for constructing excitation intensity calibration curves are presented, by either measuring emission spectra on a spectrometer, recording intensities on two detectors with two band-pass filters, or by performing time-correlated single photon counting (TCSPC) experiments with one detector.

[*] V. Rück, M. B. Liisberg, J. Chen, C. Cerretani, T. Vosch
Department of Chemistry, University of Copenhagen
Universitetsparken 5, 2100 Copenhagen (Denmark)
E-mail: cece@chem.ku.dk
        tom@chem.ku.dk

C. B. Mollerup
Department of Forensic Medicine, University of Copenhagen
Frederik V's Vej 11, 2100 Copenhagen (Denmark)

Y. He
Division of Chemical Physics and NanoLund, Lund University
P.O. Box 124, 22100 Lund (Sweden)

Results and Discussion

Photophysical characterization

The DNA-AgNC investigated in this paper, further defined as $DNA_2[Ag_{18}]^{12+}$, was synthesized using 5′-TGGACGGCGG-3′ as template (see "Compositional analysis" section below). This DNA sequence was predicted by a machine learning algorithm to emit in the NIR range, with an emission maximum between 800 and 1000 nm.[3a] Screening of the unpurified compound by Mastracco et al. showed emission maxima at 609, 644 and 897 nm, upon direct excitation of the DNA band.[3a] Intrigued by the potential of a new NIR emissive DNA-AgNC, we decided to synthesize, purify and study the photophysical properties of $DNA_2[Ag_{18}]^{12+}$, as well as characterize its composition by mass spectrometry.
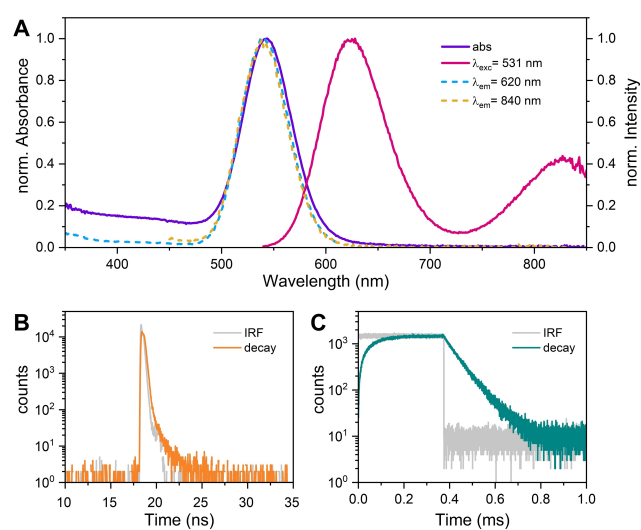
Figure 1. Steady-state and time-resolved data of $DNA_2[Ag_{18}]^{12+}$ measured in 10 mM NH$_4$OAc aqueous solution at 25 °C. (A) Overlay of the normalized steady-state absorption, excitation and emission spectra. The emission spectrum was recorded exciting at 531 nm, whereas the excitation spectra were acquired monitoring at 620 and 840 nm. (B) Fluorescence decay (orange) measured at 625 nm, exciting at 531 nm, together with the IRF (gray). (C) Luminescence intensity recorded at 840 nm in burst mode[8] (dark green), exciting at 531 nm, along with the IRF (gray).

Details on the synthesis and high-performance liquid chromatography (HPLC) purification can be found in the Supporting Information and Figure S1. Figure 1A shows the absorption, excitation and emission spectra of DNA_2-$[Ag_{18}]^{12+}$ in 10 mM ammonium acetate (NH$_4$OAc) aqueous solution at 25 °C. The absorption spectrum features a well-defined AgNC-related band at 543 nm. Exciting at 531 nm yields an emission spectrum with two distinct peaks, one centered at 624 nm and another one around 829 nm. Excitation spectra monitoring the emission at 620 and 840 nm show spectra that nicely resemble the absorption spectrum.

This similarity between the absorption and the two excitation spectra proves that both emission features originate from the same emitter. The fluorescence quantum yield (625 nm band) was determined to be 0.02, using Cresyl violet as a reference dye (see Supporting Information and Figure S2 for details). TCSPC experiments revealed that the emission measured at 625 nm is from a fluorescent state, while the band centered at 829 nm arises from a less-allowed transition (Figures S3–S6). When $DNA_2[Ag_{18}]^{12+}$ is measured in 10 mM NH$_4$OAc aqueous solution at 25 °C (Figure 1C), the decay time at 840 nm is 66.1 μs, whereas the fluorescence decay is too short to be determined accurately by TCSPC (Figure 1B), since it is only slightly broader than the instrument response function (IRF). However, when $DNA_2[Ag_{18}]^{12+}$ is measured at −196 °C, the fluorescence decay time is significantly longer and the luminescence-to-fluorescence ratio (I_{Lu}/I_{Fl}) is considerably lower than at room temperature (see Table 1 and Figure S3). In order to determine the limiting anisotropy, $DNA_2[Ag_{18}]^{12+}$ was measured in 95 % glycerol at 5 and 25 °C (Figures S4–S6). Interestingly, the fluorescence decay times were in both cases a factor of 10 longer than in the 10 mM NH$_4$OAc aqueous solution (Table 1), whereas the luminescence decay times were longer than the aqueous solution value. This shows that not only lowering the temperature, but also increasing the viscosity influences the I_{Lu}/I_{Fl} ratio. Figure S4 shows that the fundamental anisotropy at 610 nm is close to 0.4, which indicates that the absorption and fluorescence transition dipole moments are parallel and that the AgNC is potentially rod-like in nature.[9] An anisotropy value close to zero was instead observed for the emission band at 820 nm. Unlike for the picosecond fluorescence, the assumption that

Table 1: Overview of steady-state and time-resolved properties of $DNA_2[Ag_{18}]^{12+}$ in 10 mM NH$_4$OAc aqueous and deuterated solutions, indicated as H$_2$O and D$_2$O, respectively, and in 95 % glycerol and 5 % 10 mM NH$_4$OAc H$_2$O solution (95 % Glycerol).

Condition	λ_{Abs} [nm]	λ_{Fl} [nm]	$\langle\tau_{Fl}\rangle$ [ns]	λ_{Lu} [nm]	$\langle\tau_{Lu}\rangle$ [μs]	Ratio I_{Lu}/I_{Fl}
H$_2$O, 25 °C	543	624	IRF[a,b]	829	66.1[d]	0.44
H$_2$O, −196 °C	–	597	2.38[b]	782	242[e]	0.036
D$_2$O, 25 °C	543	624	IRF[a,b]	828	151[d]	0.94
D$_2$O, −196 °C	–	596	2.47[b]	781	413[e]	0.030
95 % Glycerol, 25 °C	545	618	0.98[c]	839	82.4[f]	0.096
95 % Glycerol, 5 °C	544	613	1.38[c]	837	103[f]	0.093

λ_{Abs}, λ_{Fl} and λ_{Lu} are the absorption, fluorescence and luminescence maxima, respectively. The steady-state emission spectra were recorded with a FluoTime300 instrument (PicoQuant), exciting at 531 nm. $<\tau_{Fl}>$ and $<\tau_{Lu}>$ are the fluorescence and luminescence intensity-weighted average decay times, respectively, obtained by exciting at 531 nm and monitoring the emission at [b] 625 nm, [c] 595 nm, [d] 840 nm, [e] 785 nm, and [f] 820 nm. [a] indicates that the fluorescence decay time is IRF-limited. I_{Lu}/I_{Fl} is the luminescence-to-fluorescence ratio between the two maxima.

$DNA_2[Ag_{18}]^{12+}$ does not rotate on the microsecond time-scale is probably not valid.

Hence, the anisotropy value of zero most likely reflects the randomization of the luminescence transition dipole moment by rotation, even in a highly viscous solvent like 95 % glycerol. The dual emissive behavior of $DNA_2[Ag_{18}]^{12+}$ was also investigated in 10 mM NH_4OAc D_2O solution (Figures S7–S8), given the rather unusual effect of D_2O on a previously reported $DNA-Ag_{16}NC$.[4d] For $DNA_2[Ag_{18}]^{12+}$, the fluorescence decay time was IRF-limited in both H_2O and D_2O at 25 °C, therefore no conclusions could be drawn on the potential increase of the fluorescence decay time going from H_2O to D_2O. On the other hand, the luminescence decay time lengthened by a factor of ≈ 2, as would be expected from reduced coupling to vibrational overtones of the O–D vs O–H stretching modes.[10] A similar increase was also observed for the luminescence decay time at −196 °C, while the fluorescence decay time did not change significantly (see Table 1).

In order to accurately measure the fluorescence decay time and investigate the dual emission of $DNA_2[Ag_{18}]^{12+}$, femtosecond transient absorption (fs-TA) measurements were performed. Figure 2 shows fs-TA spectra probed at different time delays after excitation at 515 nm. Recognizable features are the ground state bleach (GSB) around 545 nm, stimulated emission (SE) of the fluorescent state around 625 nm and the excited state absorption (ESA) peaking at 700 nm. Plotting the kinetic traces at the aforementioned wavelengths (Figure 2) leads to a similar time constant of 91 ps for the ground state recovery and disappearance of both the stimulated emission and the

excited state absorption at 700 nm. We can therefore confidently assign the 91 ps to the decay time of the fluorescence state, which is in line with the IRF-limited fluorescence decay recorded with TCSPC measurements.

From the fs-TA data one can also conclude that the ESA feature at 700 nm can be associated with the fluorescent state. Furthermore, in agreement with the microsecond decay time of the luminescence, the GSB at 545 nm does not fully recover to zero, even after 8 ns, indicating the presence of a long-lived population. The fs-TA spectrum after 8 ns shows only a broad, positive and nearly flat continuum signal covering the probed wavelength range that can be assigned to the ESA of the luminescent state. However, due to the absence of pronounced, spectrally isolated ESA features of the luminescent state, it is hard to conclude whether the luminescent state is formed from the fluorescent state, as was reported for $DNA-Ag_{16}NC$,[11] or directly from the Franck-Condon state.[12] No clear ESA features that rise with a 91 ps time constant could be observed in the measured wavelength region. The full range of the fs-TA spectrum that was measured can be found in Figure S9.

Compositional analysis

For determining the composition and charge state of $DNA_2-[Ag_{18}]^{12+}$, a HPLC-purified fraction in 10 mM NH_4OAc aqueous solution was directly injected into a Xevo G2-XS QTof mass spectrometer and negative ion mode electrospray ionization measurements were performed.[13] The results can be seen in the mass spectrum reported in Figure 3. The two molecular ion peaks centered at 1628.53 and 2035.95 m/z correspond to the charge states z = 5- and

Figure 2. (A) Femtosecond transient absorption (fs-TA) spectra at different time delays of $DNA_2[Ag_{18}]^{12+}$ in 10 mM NH_4OAc aqueous solution. (B) Kinetic traces at 549, 624 and 698 nm, extracted from the fs-TA experiment (Figures 2A and S9). The solid lines represent the global bi-exponential fit. The first time constant is 91 ps, while the second time constant was added to represent the long-lived state, since the signals did not recover to zero.

Figure 3. (A) Mass spectrum of $DNA_2[Ag_{18}]^{12+}$ with highlighted molecular ion peaks. The sum formula is $C_{196}H_{244}N_{86}O_{116}P_{18}[Ag_{18}]^{12+}$, which corresponds to a molecular mass of 8159.75 g/mol. (B) Zoomed-in views of highlighted peaks in the mass spectrum for z = 5- and 4-charge states, along with theoretical isotopic distributions (orange and pink) and the corresponding Gaussian fits (blue) of the experimental isotopic distributions with average molecular masses.

z=4-, respectively. The experimental mass data is consistent with the theoretical isotopic distribution of a compound comprising two 10-base DNA strands and 18 silvers with an overall nanocluster charge of 12+. Hence, the Ag_{18}^{12+} nanocluster is a 6-electron system ($N_0 = 6$).[14] No additional chloride ligands were detected in this case, in contrast to the two chlorides recently reported by Gonzàlez–Rosell et al. for DNA-Ag_{16}NC.[15] Our results are in line with the correlation proposed by Copp et al. that rod-like AgNCs with $N_0 = 6$ tend to fluorescence in the red region of the spectrum.[14]

While no structural information is currently available, the single predominant absorption peak around 540 nm and the limiting anisotropy value of ≈ 0.4 point towards a potential rod-like shape of $DNA_2[Ag_{18}]^{12+}$.[2]

Ratiometric excitation-intensity-dependent emission

Table 1 shows a large range of I_{Lu}/I_{Fl} ratios for different solvents and temperature ranges. These data suggest that restriction of mobility (either by lowering the temperature or increasing the viscosity) yielded a lower I_{Lu}/I_{Fl} ratio and generally increased the fluorescence decay time more significantly than the luminescence decay time. Since the Fluotime300 instrument (PicoQuant) used to record the steady-state spectra (Figure 1 and Table 1) has limited sensitivity above 800 nm, the full emission spectrum from 550 to 1000 nm was captured on a home-built microscope with a wavelength and intensity calibrated silicon-based camera (see Figure 5).[4d] Overlaying the two normalized spectra (Figure S10), showed significant differences in the I_{Lu}/I_{Fl} ratio, and allowed us to determine more accurately

the emission maximum of the long-lived state, which is actually centered at 846 nm. In order to elucidate the origin of the apparent discrepancy in the I_{Lu}/I_{Fl} ratio, emission spectra were measured at different excitation intensities. As shown in Figures 4 and 5, the I_{Lu}/I_{Fl} ratio strongly depends on the excitation intensity. While one would not directly expect an excitation-intensity-dependence of the I_{Lu}/I_{Fl} ratio if the luminescent state is being populated from the fluorescent state, previous results on other DNA-AgNCs have shown that the long-lived population in the luminescent state can be optically pumped back to the fluorescent state. This process is also referred to as optically activated delayed fluorescence (OADF).[16]

Figures 4 and 5 show continuous changes in the I_{Lu}/I_{Fl} ratio for excitation intensities ranging from 10^2 to 10^5 W/cm^2. This excitation range is commonly used in confocal and wide-field microscopy experiments. Hence, $DNA_2[Ag_{18}]^{12+}$ can be used as a molecular-scale excitation intensity meter. Calibration curves to relate I_{Lu}/I_{Fl} ratios with excitation intensity were created in both 10 mM NH_4OAc H_2O and D_2O solutions. While the I_{Lu}/I_{Fl} ratio is higher in D_2O than in H_2O, H_2O will in practice be easier to work with, since D_2O solutions will equilibrate over time with atmospheric water. Figure 4, together with Figure 5, displays three options, depending on the available hardware, of how to use the ratiometric emission properties of $DNA_2[Ag_{18}]^{12+}$ to construct a calibration curve for determining the excitation intensity.

In the first approach, emission spectra were recorded with a spectrometer (Figure 4A) and the intensities around the two emission maxima (i.e., 841–849 and 619–627 nm) were integrated to calculate the Lu/Fl ratio (Figure 4B). The 300 mm grating could not capture the entire range from 550
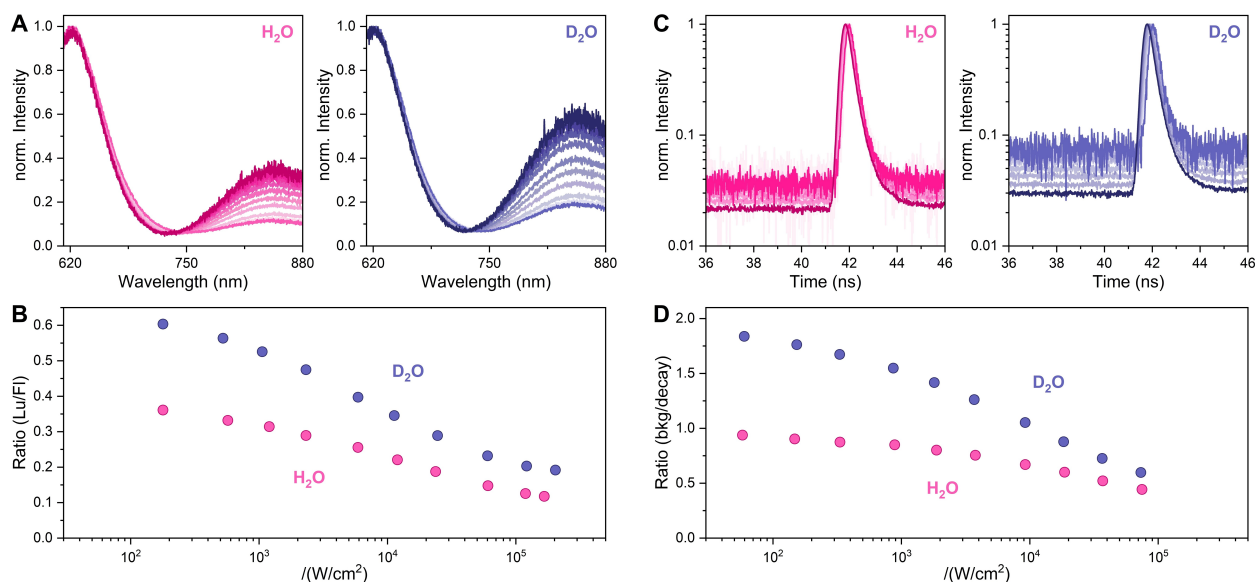
Figure 4. Excitation intensity studies of the dual emission from $DNA_2[Ag_{18}]^{12+}$ in 10 mM NH_4OAc H_2O (pink) and D_2O (blue) solutions using a spectrometer and TCSPC hardware. (A) Spectral changes as a function of excitation intensity ($\lambda_{exc} = 514$ nm, continuous wave). (B) Ratio between luminescence (Lu, centred at 845 nm) and fluorescence (Fl, centred at 623 nm) as a function of excitation intensity. (C) Time-resolved data as a function of excitation intensity ($\lambda_{exc} = 520$ nm, pulsed 78 MHz). (D) The ratio between the background (i.e., long-lived luminescence) and the fluorescence decay (bkg/decay) represents the luminescence-to-fluorescence ratio.
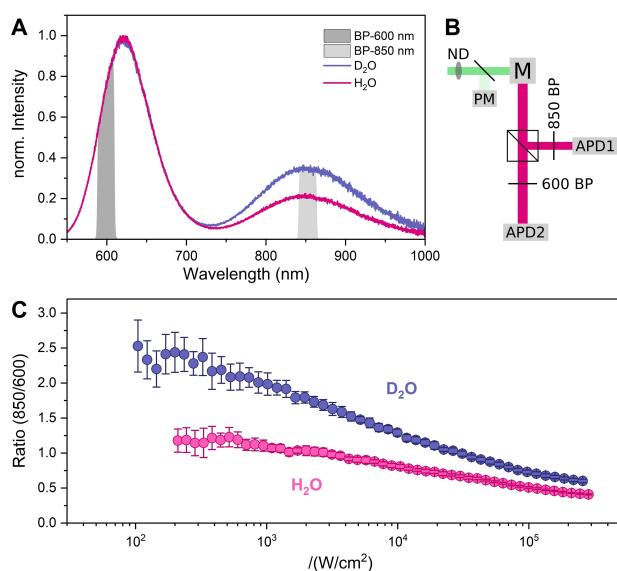
Figure 5. Excitation intensity studies of the dual emission from DNA$_2$-[Ag$_{18}$]$^{12+}$ in 10 mM NH$_4$OAc H$_2$O (pink) and D$_2$O (blue) solutions using a microscope setup with two band-pass filters in the detection path. (A) Normalized spectra of DNA$_2$[Ag$_{18}$]$^{12+}$ measured at room temperature (λ_{exc} = 514 nm, 11 kW/cm^2, CW). The filtered spectral regions for the fluorescence and luminescence are represented as gray regions. (B) Schematic of the setup used in the third approach. The excitation intensity is adjusted by a tuneable neutral density (ND) filter and is partially reflected by a coverslip for measuring the power with a power meter (PM). The light is guided into a microscope (M), which excites the DNA$_2$[Ag$_{18}$]$^{12+}$ solution. The emission is split with a 50:50 beam splitter cube and filtered by two band-pass (BP) filters; a 600 nm BP filter for the fluorescence and an 850 nm BP filter for the luminescence. The resulting emission is then detected on two different avalanche photodiodes (APDs). (C) The resulting ratios between the 850 nm filtered APD signal and the 600 nm filtered APD signal at different excitation intensities. The experimentally obtained data points (see Figures S15 and S16) were binned logarithmically in 50 intervals. The mean and standard deviations are presented.

to 1000 nm at once, but it allowed for determining the intensity of both maxima in one measurement when centered at 750 nm. Note that increasing the excitation intensity slightly broadens the fluorescence band on the red side in both H$_2$O and D$_2$O solutions. In order to check the reproducibility of the ratiometric response of DNA$_2$[Ag$_{18}$]$^{12+}$ over time, three different batches (freshly synthesized, 8 weeks and 14 weeks old) were measured on the same day. The absorption spectra of the three batches can be seen in Figure S11. While chemical stability of batches can be different and is often related to the purity of the collected fraction,[17] Figure S12 shows that the three batches with different age give very similar spectra and excitation-intensity-dependent *Lu*/*Fl* ratios. The *Lu*/*Fl* ratios are slightly different than the ratios presented in Figure 5A, which highlights the need for proper estimation of excitation power and control over experimental conditions.

The second approach is based on a standard TCSPC experiment (Figure 4C). The fluorescence photons (i.e., the photons encompassed by the fluorescence decay from 41 to 46 ns) were separated from the baseline of the entire time

window. The baseline corresponds to the photons emitted from the long-lived luminescent state, when minor contributions from dark counts and detector after pulsing events have been corrected for.[8] Then, the ratios between the luminescence and fluorescence photons (*bkg/decay*) were plotted against the excitation intensity (Figure 4D).

The last option, presented in Figure 5, is probably the easiest to implement in existing commercial microscopes. Here, the intensity of the two emitting states was directly measured using two band-pass (BP) filters in front of two detectors (600 nm for the fluorescence and 850 nm for the luminescence, see Figure 5A). Home-written LabVIEW software is used for simultaneously recording the signal of both detectors together with the excitation intensity, while a tunable neutral density filter allows for manually adjusting the excitation intensity (Figure 5B). Measuring multiple cycles where the excitation intensity is varied (Figures S13–S15) easily enables the collection of hundreds of data points. Here, the I_{Lu}/I_{Fl} ratio was calculated as the 850 nm band-pass signal divided by the 600 nm band-pass signal (*850/600*), and Figures 5C displays the calculated ratios for all collected cycles. The calibration curves reported in Figures 4 and 5 are only proxies for the true I_{Lu}/I_{Fl} ratios, i.e., where the entire integrated areas of both contributions are considered. It is in fact not necessary for equipment-specific calibration curves to establish the true I_{Lu}/I_{Fl} ratio. For example, one can often be limited by the available band-pass filters. The curves were overlaid to verify that the three different methods indeed gave calibration curves with the same shape and relative ratio changes. Figure S16 shows that the different calibration methods are in good agreement with each other.

Currently, we propose that the ratiometric excitation-intensity-dependent response originates from the optical depletion of the long-lived state resulting in a repopulation of the fluorescent state, a process known as OADF. For several other dual emissive metal cluster systems, thermally activated delayed fluorescence (TADF) has been reported as the mechanism for the regeneration of the fluorescent state from the long-lived state.[18] To exclude TADF for DNA$_2$[Ag$_{18}$]$^{12+}$, time-gated emission spectra were measured with a recently reported technique based on TCSPC and interferometry (see details in Supporting Information).[19] In this technique, emission spectra from the short- (e.g., fluorescence) or long-lived (e.g., phosphorescence or TADF) states can be disentangled temporally. If TADF occurs, besides the instant fluorescence response synchronized with the excitation pulse, unsynchronized fluorescence should also be present due to the much slower repopulation of the fluorescent state from the long-lived state. Figure S17 shows that TADF can be ruled out, since the fluorescence band only appears synchronized to the laser excitation pulse and is absent in the rest of the time window. Additionally, as highlighted previously, the I_{Lu}/I_{Fl} ratio decreases upon cooling (Table 1), which is the opposite as what one would expect for TADF, assuming all other rates are unaffected. Photon upconversion through triplet-triplet annihilation (TTA) can also be excluded as the explanation of the excitation-intensity-dependent ratiometric response, as the

diffusion driven process should also lead to unsynchronized fluorescence covering the whole time-to-amplitude converter (TAC) window. As a matter of fact, dilution of DNA_2-$[Ag_{18}]^{12+}$ by a factor of 100 yielded similar *bkg/decay* values (see Figure S18), which rules out diffusion-driven intermolecular interactions as the main cause of the excitation-intensity-dependent ratiometric response. Therefore, an intrinsic process like OADF is currently the most plausible explanation. Excitation-intensity-dependent deviations from expected fluorescence intensities for Rose Bengal[20] have previously been attributed to optically induced reversed intersystem crossing, which is conceptually similar to OADF.

Conclusion

The dual emission of $DNA_2[Ag_{18}]^{12+}$ was probed by steady-state and time-resolved measurements, to gain insight in the origin of the IRF-limited red fluorescence and the pronounced microsecond-lived NIR luminescence. During our investigations, we discovered that the ratio between luminescence and fluorescence (I_{Lu}/I_{Fl}) was not only temperature- and solvent-dependent, but also excitation-intensity-dependent. We proposed OADF as the mechanistic origin behind the excitation-intensity-dependent response as TADF and photon upconversion through TTA could be excluded. We presented three different approaches to construct excitation intensity calibration curves based on the ratiometric dual emission of $DNA_2[Ag_{18}]^{12+}$. The three different methods show that $DNA_2[Ag_{18}]^{12+}$ can be used as a molecular sized ratiometric excitation intensity probe.

Supporting Information

The authors have cited additional references within the Supporting Information.[21–27]

Conflict of Interest

The authors declare no conflict of interest.

Data Availability Statement

The data that support the findings of this study are available from the corresponding author upon reasonable request.

[1] J. T. Petty, J. Zheng, N. V. Hud, R. M. Dickson, *J. Am. Chem. Soc.* **2004**, *126*, 5207–5212.

[2] A. Gonzàlez–Rosell, C. Cerretani, P. Mastracco, T. Vosch, S. M. Copp, *Nanoscale Adv.* **2021**, *3*, 1230–1260.

[3] a) P. Mastracco, A. Gonzàlez–Rosell, J. Evans, P. Bogdanov, S. M. Copp, *ACS Nano* **2022**, *16*, 16322–16331; b) S. M. Copp, S. M. Swasey, A. Gorovits, P. Bogdanov, E. G. Gwinn, *Chem. Mater.* **2020**, *32*, 430–437; c) S. M. Copp, A. Gorovits, S. M. Swasey, S. Gudibandi, P. Bogdanov, E. G. Gwinn, *ACS Nano* **2018**, *12*, 8240–8247; d) S. M. Copp, P. Bogdanov, M. Debord, A. Singh, E. Gwinn, *Adv. Mater.* **2014**, *26*, 5839–5845.

[4] a) J. T. Petty, S. Carnahan, D. Kim, D. Lewis, *J. Chem. Phys.* **2021**, *154*, 244302; b) D. Lewis, C. Setzler, P. M. Goodwin, K. Thomas, M. Branham, C. A. Arrington, J. T. Petty, *J. Phys. Chem. C* **2023**, *127*, 10574–10584; c) V. Rück, C. Cerretani, V. A. Neacşu, M. B. Liisberg, T. Vosch, *Phys. Chem. Chem. Phys.* **2021**, *23*, 13483–13489; d) C. Cerretani, G. Palm-Henriksen, M. B. Liisberg, T. Vosch, *Chem. Sci.* **2021**, *12*, 16100–16105.

[5] Y. Shen, Z. An, H. Liu, B. Yang, Y. Zhang, *Angew. Chem. Int. Ed.* **2023**, *62*, e202214483.

[6] S. Ghosh, U. Ross, A. M. Chizhik, Y. Kuo, B. G. Jeong, W. K. Bae, K. Park, J. Li, D. Oron, S. Weiss, J. Enderlein, A. I. Chizhik, *J. Phys. Chem. Lett.* **2023**, *14*, 2702–2707.

[7] a) S. Wen, D. Li, Y. Liu, C. Chen, F. Wang, J. Zhou, G. Bao, L. Zhang, D. Jin, *J. Phys. Chem. Lett.* **2022**, *13*, 5316–5323; b) C. Würth, M. Kaiser, S. Wilhelm, B. Grauel, T. Hirsch, U. Resch-Genger, *Nanoscale* **2017**, *9*, 4283–4294.

[8] M. Liisberg, S. Krause, C. Cerretani, T. Vosch, *Chem. Sci.* **2022**, *13*, 5582–5587.

[9] A. Gonzàlez–Rosell, R. Guha, C. Cerretani, V. Rück, M. B. Liisberg, B. B. Katz, T. Vosch, S. M. Copp, *J. Phys. Chem. Lett.* **2022**, *13*, 8305–8311.

[10] J. Maillard, K. Klehs, C. Rumble, E. Vauthey, M. Heilemann, A. Fürstenberg, *Chem. Sci.* **2021**, *12*, 1352–1362.

[11] J. Chen, A. Kumar, C. Cerretani, T. Vosch, D. Zigmantas, E. Thyrhaug, *J. Phys. Chem. Lett.* **2023**, *14*, 4078–4083.

[12] S. A. Patel, M. Cozzuol, J. M. Hales, C. I. Richards, M. Sartin, J. C. Hsiang, T. Vosch, J. W. Perry, R. M. Dickson, *J. Phys. Chem. C* **2009**, *113*, 20264–20270.

[13] V. Rück, N. K. Mishra, K. K. Sørensen, M. B. Liisberg, A. B. Sloth, C. Cerretani, C. B. Mollerup, A. Kjaer, C. Lou, K. J. Jensen, T. Vosch, *J. Am. Chem. Soc.* **2023**, *145*, 16771–16777.

[14] S. M. Copp, D. Schultz, S. Swasey, J. Pavlovich, M. Debord, A. Chiu, K. Olsson, E. Gwinn, *J. Phys. Chem. Lett.* **2014**, *5*, 959–963.

[15] A. Gonzàlez–Rosell, S. Malola, R. Guha, N. R. Arevalos, M. Rafik, M. F. Matus, M. E. Goulet, E. Haapaniemi, B. B. Katz, T. Vosch, J. Kondo, H. Häkkinen, S. M. Copp, *J. Am. Chem. Soc.* **2023**, *145*, 10721–10729.

[16] a) T. Vosch, Y. Antoku, J. C. Hsiang, C. I. Richards, J. I. Gonzalez, R. M. Dickson, *Proc. Natl. Acad. Sci. USA* **2007**, *104*, 12616–12621; b) C. I. Richards, J. C. Hsiang, D. Senapati, S. Patel, J. Yu, T. Vosch, R. M. Dickson, *J. Am. Chem. Soc.* **2009**, *131*, 4619–4621; c) B. C. Fleischer, J. T. Petty, J. C. Hsiang, R. M. Dickson, *J. Phys. Chem. Lett.* **2017**, *8*, 3536–

3543; d) S. Krause, M. R. Carro-Temboury, C. Cerretani, T. Vosch, *Chem. Commun.* **2018**, *54*, 4569–4572; e) S. Krause, C. Cerretani, T. Vosch, *Chem. Sci.* **2019**, *10*, 5326–5331.

[17] M. Gambucci, C. Cerretani, L. Latterini, T. Vosch, *Methods Appl. Fluoresc.* **2019**, *8*, 014005.

[18] a) Z.-R. Yuan, Z. Wang, B.-L. Han, C.-K. Zhang, S.-S. Zhang, Z.-Y. Zhu, J.-H. Yu, T.-D. Li, Y.-Z. Li, C.-H. Tung, D. Sun, *Angew. Chem. Int. Ed.* **2022**, *61*, e202211628; b) Z. Han, X.-Y. Dong, P. Luo, S. Li, Z.-Y. Wang, S.-Q. Zang, T. C. W. Mak, *Sci. Adv.* **2020**, *6*, eaay0107.

[19] M. B. Liisberg, T. Vosch, *Commun. Mater.* **2023**, *4*, 57.

[20] J. M. Larkin, W. R. Donaldson, R. S. Knox, T. H. Foster, *Photochem. Photobiol.* **2002**, *75*, 221–228.

[21] A. M. Brouwer, *Pure Appl. Chem.* **2011**, *83*, 2213.

[22] J. R. Lakowicz, *Principles of fluorescence spectroscopy*, Springer New York, New York, **2006**.

[23] M. B. Liisberg, Z. Shakeri Kardar, S. M. Copp, C. Cerretani, T. Vosch, *J. Phys. Chem. Lett.* **2021**, *12*, 1150–1154.

[24] A. Perri, J. H. Gaida, A. Farina, F. Preda, D. Viola, M. Ballottari, J. Hauer, S. De Silvestri, C. D'Andrea, G. Cerullo, D. Polli, *Opt. Express* **2018**, *26*, 2270–2279.

[25] A. Perri, F. Preda, C. D'Andrea, E. Thyrhaug, G. Cerullo, D. Polli, J. Hauer, *Opt. Express* **2017**, *25*, A483-A490.

[26] J. Chen, M. E. Messing, K. Zheng, T. Pullerits, *J. Am. Chem. Soc.* **2019**, *141*, 3532–3540.

[27] M. Loos, C. Gerber, F. Corona, J. Hollender, H. Singer, *Anal. Chem.* **2015**, *87*, 5738–5744.

Supporting Information

A DNA-Stabilized Ag$_{18}^{12+}$ Cluster with Excitation-Intensity-Dependent Dual Emission

Vanessa Rück,[a] Mikkel B. Liisberg,[a] Christian Brinch Mollerup,[b] Yanmei He,[c] Junsheng Chen,[a] Cecilia Cerretani,*,[a] Tom Vosch*,[a]

[a]   Vanessa Rück, Mikkel B. Liisberg, Junsheng Chen, Cecilia Cerretani, Tom Vosch
      Department of Chemistry
      University of Copenhagen
      Universitetsparken 5, 2100 Copenhagen, Denmark.
      E-mail: cece@chem.ku.dk, tom@chem.ku.dk
[b]   Christian Brinch Mollerup
      Department of Forensic Medicine
      University of Copenhagen
      Frederik V's Vej 11, 2100 Copenhagen, Denmark.
[c]   Yanmei He
      Division of Chemical Physics and NanoLund
      Lund University
      P.O. Box 124, 22100 Lund, Sweden

Materials and Methods

1 $DNA_2[Ag_{18}]^{12+}$ Synthesis

Hydrated DNA oligonucleotide (Integrated DNA Technologies) with the sequence 5'-TGGACGGCGG-3' was mixed with $AgNO_3$ (Sigma Aldrich, ≥ 99.998%) in 10 mM ammonium acetate aqueous solution (NH_4OAc, Sigma Aldrich, ≥ 98%) at pH 7. Freshly prepared $NaBH_4$ (Sigma Aldrich, ≥ 99.99%) was added to the mixture after 15 min to reduce the silver cations and promote the formation of silver nanoclusters. The optimal ratio between the components was [DNA]:[$AgNO_3$]:[$NaBH_4$] = 30 µM: 150 µM: 75 µM. After synthesis, the sample was stored in the fridge for 6 days prior to high-performance liquid chromatography (HPLC) purification. In the end, the purified fraction was solvent exchanged to 10 mM NH_4OAc H_2O solution by spin-filtration with a 3 kDa cut-off membrane filter (Amicon Ultracel-3). Note that it is common that the synthesis ratio does not reflect the final stoichiometry obtained from mass spectrometry since the synthesis yield is usually far from 100 %.

2   HPLC purification

HPLC purification was performed using a preparative HPLC system from Agilent Technologies with an Agilent Technologies 1100 Series UV-Vis detector, an Agilent Technologies 1260 Infinity fluorescence detector and a Kinetex C18 column (5 µm, 100 Å, 250 × 4.6 mm), equipped with a fraction collector. The mobile phase was a gradient mixture of 35 mM triethylammonium acetate (TEAA) buffer in water (A) and methanol (B). The flow rate was set to 1 mL/min.
The elution gradient ranged from 5% to 95% B in 30 min. In the first 2 min it was kept constant at 5% B, then it was linearly increased to 30% B in the next 25 min, and finally in the 27-30 min interval, the gradient was rapidly risen to 95% B.
The collection was based on the AgNC absorbance at 540 nm, while monitoring also the DNA absorbance at 260 nm and the absorption of silver nanoparticles (λ = 450 nm). At the same time, both AgNC emission bands were monitored at 630 and 830 nm, exciting at 540 nm.
The run was followed by 5 min of washing with 95% B to remove any remaining sample from the column. As shown in the chromatograms in Figure S1, the purified fraction eluted around 19.2 min, which corresponds to approximately 22.2% B.

3   Spectroscopic measurements

Steady-state and time-resolved measurements were carried out in different media: 10 mM NH_4OAc H_2O solution, 10 mM NH_4OAc D_2O solution and 95% glycerol (5% 10 mM NH_4OAc H_2O), and at diverse temperatures: -196, 5, 25 °C. A description of the measurements at -196 °C is given in paragraph 3.2.6. For the cuvette measurements, the 10 mM NH_4OAc D_2O condition was prepared by adding a small volume of concentrated DNA-AgNC stock solution (20 µL) to the final solvent (2 mL), while for the microscope measurements, a solvent exchange of the DNA-AgNC containing H_2O solution into 10 mM NH_4OAc D_2O was performed.

3.1 Absorption measurements

Absorption spectra were measured with a Cary 300 UV-Vis spectrophotometer from Agilent Technologies using a deuterium lamp for ultraviolet radiation and a tungsten-halogen lamp for visible and near-infrared (NIR) radiation. All measurements were performed in a single-beam configuration with a "zero/baseline" correction, *i.e.*, measuring the 100%/0% transmittance with air as reference. The corresponding solvent spectra were measured separately and then subtracted from the samples' spectra. The absorbance of the AgNC-related transition was kept below 0.1 to avoid inner filter effects during emission measurements.

3.2 FluoTime300 instrument (PicoQuant)

3.2.1 Steady-state emission measurements

Steady-state fluorescence measurements were performed using a FluoTime300 instrument (PicoQuant). The fluorescence spectra were recorded by exciting the samples with a vertically-polarized 531 nm (LDH-D-TA-530B) picosecond-pulsed laser (PicoQuant). All emission spectra have been corrected for the wavelength dependency of the detector.

3.2.2 Quantum Yield (Q) measurements and calculations

The quantum yield of $DNA_2[Ag_{18}]^{12+}$ was determined in 10 mM NH_4OAc aqueous solution at 25 °C, using Cresyl Violet in ethanol as reference dye (Q_{ref} = 0.56).[1] Absorption and emission spectra of the DNA-AgNC and the reference compound were measured at five different concentrations, and the quantum yield was calculated according to the following formula:[2]

$$Q_{NC} = \frac{F_{NC}}{f_{A,NC}} \times \frac{f_{A,ref}}{F_{ref}} \times \frac{n_{NC}^2}{n_{ref}^2} \times Q_{ref} \quad \textbf{(1)}$$

where Q represents the quantum yield, F is the integrated emission spectrum (*i.e.*, the area under the fluorescence spectrum), f_A defines the fraction of absorbed light at the excitation wavelength (531 nm), and n is the refractive index of the medium where the compounds are dissolved in during the measurements. The subscripts *NC* and *ref* indicate the $DNA_2[Ag_{18}]^{12+}$ and Cresyl Violet, respectively. The emission spectra of $DNA_2[Ag_{18}]^{12+}$ were fitted with a Gaussian function to isolate the fluorescence band from the luminescence one.

3.2.3 Excitation spectra measurements

Unlike the emission measurements, excitation spectra were recorded with a QuantaMaster400 instrument from PTI/HORIBA with a xenon arc lamp, monitoring the emission at 620 and 840 nm. The spectra were measured in 10 mM NH_4OAc aqueous solution at room temperature, and then corrected for the wavelength dependency of the detector and for wavelength-dependent intensity difference in the excitation lamp.

3.2.4   Time-correlated single photon counting (TCSPC) measurements

Time-resolved fluorescence measurements were performed by exciting with a vertically-polarized 531 nm (LDH-D-TA-530B) picosecond-pulsed laser (PicoQuant).

For $DNA_2[Ag_{18}]^{12+}$ in 10 mM NH_4OAc H_2O and D_2O solutions at 5 and 25 °C, fluorescence decays were acquired at 625 nm, integrating 5 s in order to reach at least 10,000 counts in the maximum. However, since the decay curves were found to be instrument response function (IRF) limited, it was not possible to determine the fluorescence lifetimes in these conditions.

For $DNA_2[Ag_{18}]^{12+}$ in 95% glycerol and 5% 10 mM NH_4OAc H_2O solution at 5 and 25 °C, fluorescence decays were instead acquired at 610 nm, integrating 10 s. The decay curves were fitted with FluoFit v.4.6 software from PicoQuant, using a tri-exponential reconvolution model including the IRF. The average lifetimes $<\tau_{fl}>$, reported in Table 1, were calculated as the intensity-weighted average decay times at the monitored wavelength.[2]

3.2.5   Microsecond decay time measurements

Microsecond decay times were measured in burst mode by exciting at 531 nm. Emission intensities of $DNA_2[Ag_{18}]^{12+}$ in 10 mM NH_4OAc H_2O or D_2O were recorded at 840 nm, while the measurements in 95% glycerol were performed at 820 nm, given the blue-shift in the luminescence band. The integration time was set to 10 min. Every solvent and temperature condition required different settings that are summarized in Table S1.

Table S1. *Settings for burst mode measurements of $DNA_2[Ag_{18}]^{12+}$ in 10 mM NH_4OAc aqueous and deuterated solutions, as well as in 95% glycerol.*

Condition	Repetition rate	Effective sync rate	Burst length	# pulses	Period length	Duty cycle	Binning
H_2O 25 °C	40 MHz	1 kHz	375 µs	15,000	1.00 ms	37.5%	204.8 ns
D_2O 25 °C	40 MHz	300 Hz	1.25 ms	50,000	3.33 ms	37.5%	406.9 ns
95% Glycerol 5 °C	40 MHz	1 kHz	300 µs	12,000	1.00 ms	30%	102.4 ns
95% Glycerol 25 °C	40 MHz	1 kHz	300 µs	12,000	1.00 ms	30%	102.4 ns

3.2.6   Steady-state and time-resolved emission measurements at -196 °C

Low-temperature steady-state and time-resolved emission measurements were carried out in both 10 mM NH_4OAc H_2O and D_2O solutions. The measurements were performed by immersing an NMR tube with the sample in a transparent Dewar filled with liquid nitrogen (-196 °C). The Dewar was then placed in the cuvette compartment of a FluoTime300 instrument from PicoQuant. In order to limit the increased

scattering, two filters were used: a 527 nm band-pass filter (Semrock, FF01-527/20-25) in the excitation path and a 532 nm long-pass filter (Semrock, BLP01-532R-25) in the emission path.

The acquired steady-state emission spectra were corrected for the wavelength dependency of the detector.

Fluorescence decay curves were measured at 595 nm, given the blue-shift of the emission spectrum at -196 °C. The analysis of time-resolved data was performed with FluoFit v.4.6 software from PicoQuant. The decays were fitted with a bi-exponential reconvolution model including the IRF. The intensity-averaged decay times $<\tau_{fl}>$ (reported in table 1) were calculated as the intensity-weighted average decay times at the selected emission wavelength.[2]

Burst mode measurements were carried out by monitoring the emission at 785 nm using different settings for the two solvents.

For $DNA_2[Ag_{18}]^{12+}$ in 10 mM NH_4OAc H_2O solution, the repetition rate of the 531 nm laser was set to 21.3 MHz, with an effective sync rate of 200 Hz. The laser burst lasted 1.64 ms and consisted of 35,000 pulses (*i.e.,* every pulse was separated by 46.9 ns) followed by 3.36 ms where the laser was switched off (32.8% duty cycle). The binning was chosen to be 204.8 ns and the integration time was set to 10 min.

For the sample in the deuterated solvent, the repetition rate of the laser was also set to 21.3 MHz, but with an effective sync rate of 135 Hz. The burst length was 2.1 ms and comprised 45,000 pulses (*i.e.,* every pulse was separated by 46.7 ns) followed by 5.3 ms where the laser was turned off (28.5% duty cycle). The binning was set to 409.6 ns and the integration time was 10 min.

The intensity decays upon switching off the laser were tail-fitted with a bi-exponential function. Intensity traces and time constants can be found in Figures S3, S8 and Table 1.

3.2.7 Steady-state emission anisotropy measurements

Steady-state emission anisotropy was measured in 95% glycerol and 5% 10 mM NH_4OAc H_2O solution at 5 °C, exciting with a 531 nm pulsed laser.

Parallel (I_{VV}, I_{HH}) and perpendicular (I_{VH}, I_{HV}) emission spectra were recorded by changing the excitation and emission polarizers accordingly. These data were used to calculate the instrumental G factor ($G=I_{HV}/I_{HH}$) and the limiting emission anisotropy (r) of the DNA-AgNC:[2]

$$r = \frac{I_{VV} - G \cdot I_{VH}}{I_{VV} + 2 \cdot G \cdot I_{VH}} \quad (2)$$

3.3 Home-Built Microscope Setup

The detector of the FluoTime300 system (PicoQuant), used for most measurements, becomes increasingly insensitive beyond 800 nm. To circumvent the low efficiency in the NIR range and to obtain emission spectra with more accurate spectral profiles, we used our home-built confocal microscope for measuring representative emission spectra of $DNA_2[Ag_{18}]^{12+}$. Additionally, the setup was used to study the excitation-intensity-dependent dual emission of $DNA_2[Ag_{18}]^{12+}$ because of the higher excitation intensities obtainable

with a high numerical aperture objective. The fundamental microscope setup used for recording emission spectra will be described here, while the other setups employed for measuring the excitation-intensity-dependent dual emission will be described in the next section (3.3.1).

A fiber coupled continuous wave (CW) argon laser (CVI Melles-Griot 35MAP431-200) was used as an excitation source delivering a wavelength of 514.5 nm. The output of the fiber was expanded by a telecentric lens system and cleaned up by a 514 nm band-pass filter (LL01-514-25, Semrock) before it was reflected by a 30:70 beam splitter (XF122, Omega Optical) or a 514 dichroic mirror (LPD01-514RU-25 Semrock, only for the data presented in Figure S12) and sent through an oil immersion objective (UPlanSApo 100x, NA = 1.4, Olympus), which focused the laser onto the sample and collected the emission. The laser light was blocked by a 532 nm long-pass filter (BLP01-532-25, Semrock) and out-of-focus light was blocked by a 100 μm pinhole. The luminescence was sent through a spectrograph (Acton Research, SP 2356 spectrometer, 300 grooves/mm) onto a nitrogen cooled CCD camera (Princeton Instruments, SPEC-10:100B/LN-eXcelon) to record the spectra. As previously reported, the emission spectra were wavelength- and intensity-corrected using calibrated light sources.[3] Due to the lower detector sensitivity towards the near-infrared region, multiplication of the raw data with the correction file can result in larger noise in the near-infrared versus the visible region of the spectrum.

3.3.1 Excitation-intensity-dependent measurements

As reported in the manuscript, three methods were used for the excitation-intensity-dependent measurements. While all of the approaches are based on the same microscope setup above, there are some minor differences among the three. Each setup and the accompanying data analysis (i.e., how I_{Lu}/I_{Fl} ratio is calculated) will be outlined for each of the methods here.

In the <u>first approach</u>, emission spectra were measured, calibrated, and analyzed. The spectra were recorded using the setup described above. The luminescence (I_{Lu}) and fluorescence (I_{Fl}) intensities were calculated as the sum from 841-849 nm and 619-627 nm. For the excitation-intensity-dependency, the power of the excitation source was controlled with a variable neutral density filter (Thorlabs) and was measured, from the reflection of a flip mirror positioned in the beam path, with a power meter (S120VC, Thorlabs). After measuring the entire range of powers, the power value at the reflection was noted and subsequently measured on top of the microscope; this factor (*i.e.*, the power value on top of the microscope compared to that at the reflection) was used to calculate every power value on top of the microscope. The conversion from power (W) to intensity (W/cm^2) was done assuming a diffraction-limited focal volume.

In the <u>second approach</u>, TCSPC was used for assessing the I_{Lu}/I_{Fl} ratio. Since TCSPC requires a pulsed excitation source, we switched the argon laser with a pulsed fiber coupled (NKT Photonics, FD7-PM) continuum white-light laser (NKT Photonics, SuperK EXTREME EXB-6) with a repetition rate of 78 MHz. This delivered a wavelength of 520 nm by sending the continuum output through an acousto-optic tunable filter (NKT Photonics, SuperK SELECT). The output of the fiber was cleaned up by a 520 nm band-pass filter (Semrock, FF01-520/5-25). The remainder of the setup was similar to the one described above, apart from the detection site. In this case, the emission was directed towards and detected on an avalanche photodiode (CD3226, PerkinElmer) connected to a single photon counting board (SPC-830, Becker & Hickl). Since the fluorescence signal is short and IRF-limited, it only constitutes a small fraction of the time-

to-amplitude converter (TAC) window, while the long-lived luminescence appears as a flat signal in the entire TAC window. Accordingly, a time gate (41-46 ns) is defined, which encompasses the entire fluorescence signal, whereas the luminescence is only detected outside this time window. Thus, the mean luminescence signal is calculated outside the fluorescence time gate, and this value is subtracted from the fluorescence signal to correct for the residual luminescence within the time gate (see reference 4 for more details on time gating). In this way, the resulting sum of the fluorescence represents I_{Fl}. I_{Lu} is calculated as the sum of the entire TAC window subtracted by I_{Fl}. Note that dark counts and detector after pulsing events have been corrected for by subtracting a measurement of similar integration time with the laser blocked. The excitation intensity was controlled and recorded in a similar manner as described above.

In the third approach, two band-pass filtered APDs were used to simultaneously capture the fluorescence and luminescence signals, as well as the excitation intensity at high data collection rates. For this setup, the CW argon laser with an excitation wavelength of 514 nm was used again. While similar in the excitation path, the emission was instead directed towards a 50:50 beam splitter (Thorlabs) and then sent onto two APDs (CD3226, PerkinElmer) that were connected to a DAQ card (SCB-68, National Instruments). In front of each APD, a different band-pass filter was placed: a 600 nm band-pass filter (FF01-600/14-25, Semrock) for measuring the fluorescence (I_{Fl}) and an 850 nm band-pass filter (FF01-850/10-25, Semrock) to record the luminescence (I_{Lu}, see Figure 5A for band-pass filter profiles and Figure 5B for a schematic of the setup). The excitation intensity was measured with a power meter (S120VC, Thorlabs) from the reflection of a coverslip. Once again, a conversion factor to get the excitation intensity on top of the microscope was used, as described in the first approach. Accompanying LabVIEW software was written to simultaneously record the signals from both APDs as well as the excitation intensity. By using a variable neutral density filter (Thorlabs), it is possible to continuously adjust the excitation intensity and log the APD signals and the excitation intensity. Figure S11 displays how multiple cycles are recorded over the duration of a few minutes. From these cycles, one can plot I_{Lu} and I_{Fl} as a function of excitation intensity (Figure S12), and the I_{Lu}/I_{Fl} ratio from multiple cycles shows high reproducibility (Figure S13). In Figure 5, all recorded cycles are collected and presented.

3.3.2 Time-gated emission spectra measurements

For the recording of time-gated emission spectra, we employed a recently developed method.[4] Here, only a brief outline of the procedure will be given, while further details on the working principles can be found in Liisberg *et al*.[4,5] and Perri *et al*.[6]

The technique is based on two key elements, a TCSPC board and an interferometer, which provide the temporal and spectral aspects, respectively. We use a common-path birefringent interferometer (Translating-Wedge-based Identical pulses eNcoding System; TWINS, model GEMINI from NIREOS) that allows the easy collection of spectra in the visible and near-infrared regions.[7] In this setup, a decay is recorded with the TCSPC board at every wedge displacement of the interferometer, which effectively creates a 2D time-resolved interferometric map (TRIM, Figure S15a). From the ungated TRIM ($I_{UG}(t, x)$), which shows contributions from both the short-lived fluorescence and long-lived luminescence, it is possible to define a time gate that encompasses the fluorescence signal (*i.e.*, from 31-40 ns) and accordingly prepare time gated TRIMs of the fluorescence ($I_{Fl,TG}(t, x)$) and luminescence ($I_{Lu,TG}(t, x)$). Note that residual luminescence within the time gate has been corrected for by calculating a mean luminescence intensity ($<I>$) outside the defined time. This mean value is used to represent the

luminescence within the time gate, and is accordingly subtracted in case of $I_{Fl,TG}(t, x)$. The fluorescence only exhibits a short-lived signal within the defined time gate, while the long-lived luminescence appears constant in entire TAC window. Summation along the time axis shows integrated interferograms of the ungated ($I_{UG}(x)$), fluorescence gated ($I_{Fl,TG}(x)$), and luminescence gated ($I_{Lu}(x)$) data (Figure S15b). By Fourier transformation, and a series of calibrations (see Liisberg et al.[4] for details), it is possible to prepare 2D time-resolved emission maps (TREMs, Figure S15c) of the ungated and time-gated TRIMs. These TREMs show how the fluorescence and luminescence contributions have been disentangled from one another when time-gated (see $I_{Fl,TG}(t, \lambda)$ and $I_{Lu,TG}(t, \lambda)$). The integrated spectra (Figure S15d) clearly reveal that the fluorescence feature around 620 nm is entirely short-lived and the 850 nm luminescence feature is fully long-lived.

The setup for measuring time-gated emission spectra is essentially similar to the setup used for recording the excitation-intensity-dependence with TCSPC; with the only differences being the lack of a pinhole, the introduction of the TWINS device in the emission path, a change of repetition rate from 78 MHz to 13 MHz, and the use of a different APD (SPCM-AQRH-14-TR, Excelitas Technologies). Official LabVIEW routines from NIREOS and Becker & Hickl were modified and combined to allow for measuring TRIMs. All subsequent data analysis was conducted in MATLAB.

3.4 Femtosecond transient absorption (fs-TA) measurements

fs-TA experiments were performed by using a femtosecond pump-probe setup.[8] Laser pulses (796 nm, 60 fs pulse length, 4 kHz repetition rate) were generated by a regenerative amplifier (Solstice Ace) seeded by a femtosecond oscillator (Mai Tai SP, both Spectra Physics). For the pump the Topas C (Light Conversion) was used to obtain pulses with central wavelength located at 515 nm. Pump pulse energy was set to 0.1 µJ per pulse. The spot size was approximately 0.2 mm^2. For the probe we used the super-continuum generation from a thin CaF$_2$ plate. The mutual polarization between pump and probe beams was set to the magic angle (54.7°) by placing a Berek compensator in the pump beam. The steady-state absorption and emission spectra were recorded before and after the fs-TA measurements, in which no change was detected.

4 Mass spectrometry

Electrospray ionization-mass spectrometry measurements were performed with a Xevo G2-XS QTof (Waters Corporation), using negative ion mode with a 2 kV capillary voltage, 30 V cone voltage and no collision energy. Spectra were collected from 1000 to 4000 m/z, and with a scan time of 1 s. Source temperature was 80 °C with a cone gas flow of 45 L/h, and the desolvation temperature and gas flow were 150 °C and 450 L/h, respectively. The QTOF was calibrated using ESI-L Low Tune Mix (Agilent Technologies), which contained compounds in the mass range of 1034 to 2834 m/z. All samples were injected using an Acquity I-Class Plus system (Waters) with a flow-through needle autosampler, with a flow of 0.1 mL/min 50 mM NH$_4$OAc buffer at pH 7 – MeOH (80:20) and using 5 µL injection volume. The system was operated using UNIFI v.1.9.4 (Waters), and the final spectra were generated by averaging multiple spectra surrounding the apex of the observed peak.

The recorded data were analyzed and fitted with the open-source software EnviPat Web[9] (https://www.envipat.eawag.ch/index.php), together with a self-written MATLAB script. The MATLAB script was used to find the maximum of each isotope peak of the molecular ion and fit it with a single Gaussian function (Figure 3). The calculated average masses were 1628.53 and 2035.95 m/z with differences from the theoretical values of 0.01 and 0.04, respectively.

Adjacent peaks of the isotope pattern are spaced by 1/z, which defines the charge state z- of a m/z peak. The total charge of the DNA-AgNC corresponding to a certain m/z peak is equal to the number of silver cations, eN_+, minus the number of protons removed from the DNA, en_{pr}, to reach the total charge of **$-eZ$** (previously named z-) observed experimentally: **$-eZ = eN_+ - en_{pr}$**; where **e** is the elementary charge. Since n_{pr} protons are removed from the DNA-AgNC, the experimentally measured total mass **m** (in amu) is given by $m = m_{DNA} \cdot n_s + m_{Ag} \cdot (N_+ + N_0) - n_{pr}$; where N_+ is the number of silver cations, N_0 is the number of reduced silver atoms, m_{DNA} is the DNA mass, n_s is the number of DNA strands, and m_{Ag} is the silver atom mass. By varying the N_+ values, and thus n_{pr}, it was possible to establish the nanocluster charge (and the number of reduced silvers) that best matched the observed isotope pattern. The chemical formula and molecular mass reported in Figure 3 correspond to **$m + n_{pr}$** from the most abundant m/z peaks.

5   References

[1] A. M. Brouwer *Pure Appl. Chem.*, **2011**, *83* , 2213.

[2] J. R. Lakowicz *Principles of Fluorescence Spectroscopy*, 2006.

[3] M. B. Liisberg, Z. S. Kardar, S. M. Copp, C. Cerretani, T. Vosch *J. Phys. Chem. Lett.* **2021**, *12*, 1150–1154.

[4] M. B. Liisberg, T. Vosch, *Communications Materials* **2023**, *4*, article number: 57.

[5] M. B. Liisberg, S. Krause, C. Cerretani, T. Vosch *Chem. Sci.*, **2022**,*13*, 5582-5587.

[6] A. Perri, J. H. Gaida, A. Farina, F. Preda, D. Viola, M. Ballottari, J. Hauer, S. De Silvestri, C. D'Andrea, G. Cerullo, D. Polli *Opt. Express*, **2018**, 26, 2270-2279.

[7] A. Perri, F. Preda, C. D'Andrea, E. Thyrhaug, G. Cerullo, D. Polli, J. Hauer *Opt. Express* **2017**, *25*, A483-A490.

[8] J. Chen, M. E. Messing, K. Zheng, T. Pullerits, Journal of the American Chemical Society 2019, 141, 3532-3540.

[9] M. Loos, C. Gerber, F. Corona, J. Hollender, H. Singer *Anal. Chem.*, **2015**, *87*, 5738-5744.

HPLC Chromatograms
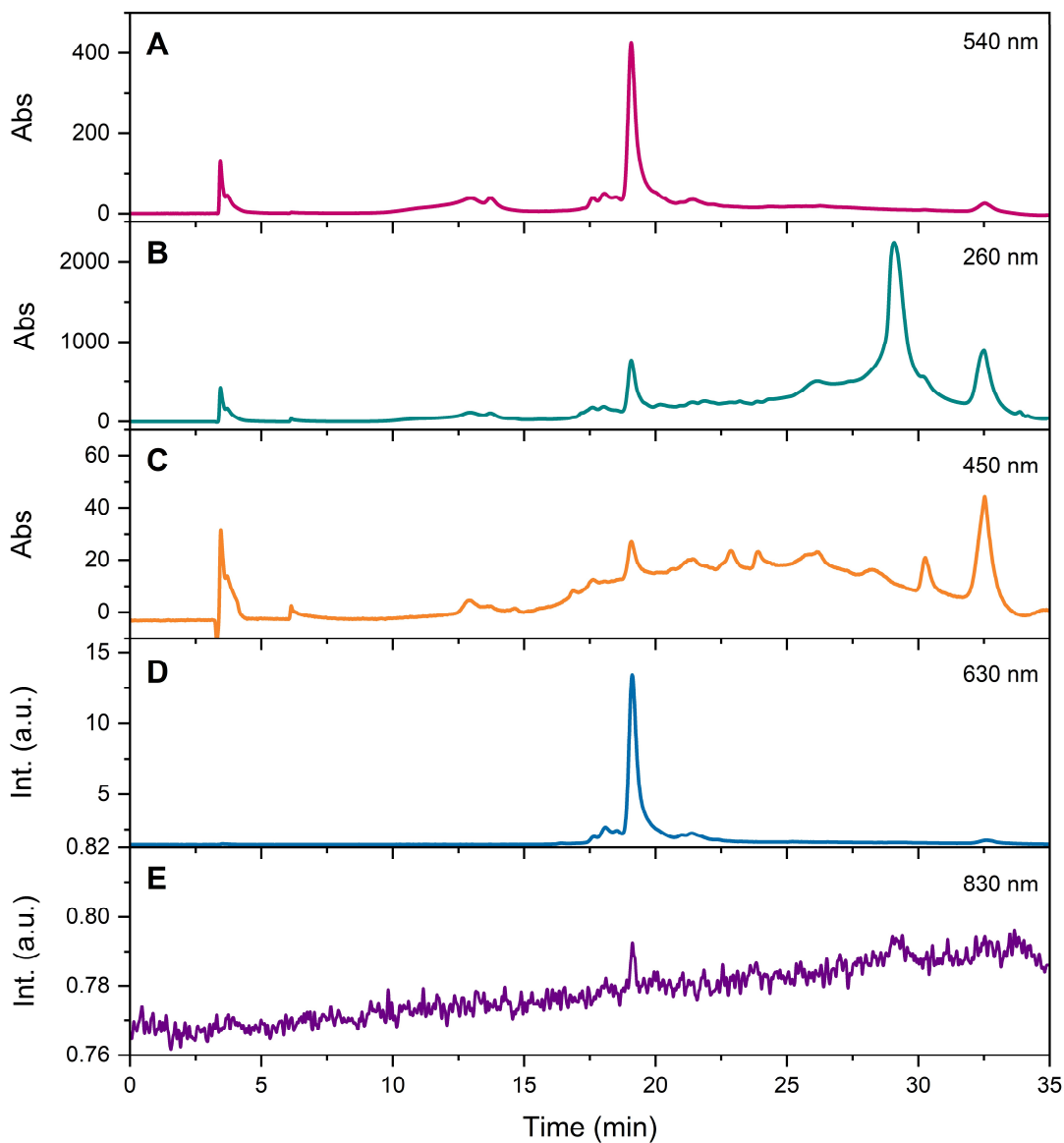
Figure S1. _HPLC chromatograms of DNA$_2$[Ag$_{18}$]$^{12+}$ synthesized in 10 mM NH$_4$OAc aqueous solution monitoring **A)** the main absorption peak of the AgNC at 540 nm, **B)** the DNA absorption at 260 nm, and **C)** the absorption of silver nanoparticles at 450 nm. The absorbance is given in mOD. **D)** and **E)** chromatograms that monitor the emission of DNA$_2$[Ag$_{18}$]$^{12+}$ at 630 and 830 nm (λ_{exc}= 540 nm), respectively. The fraction described in the manuscript was collected between 18.8 and 20.3 min._

Quantum Yield
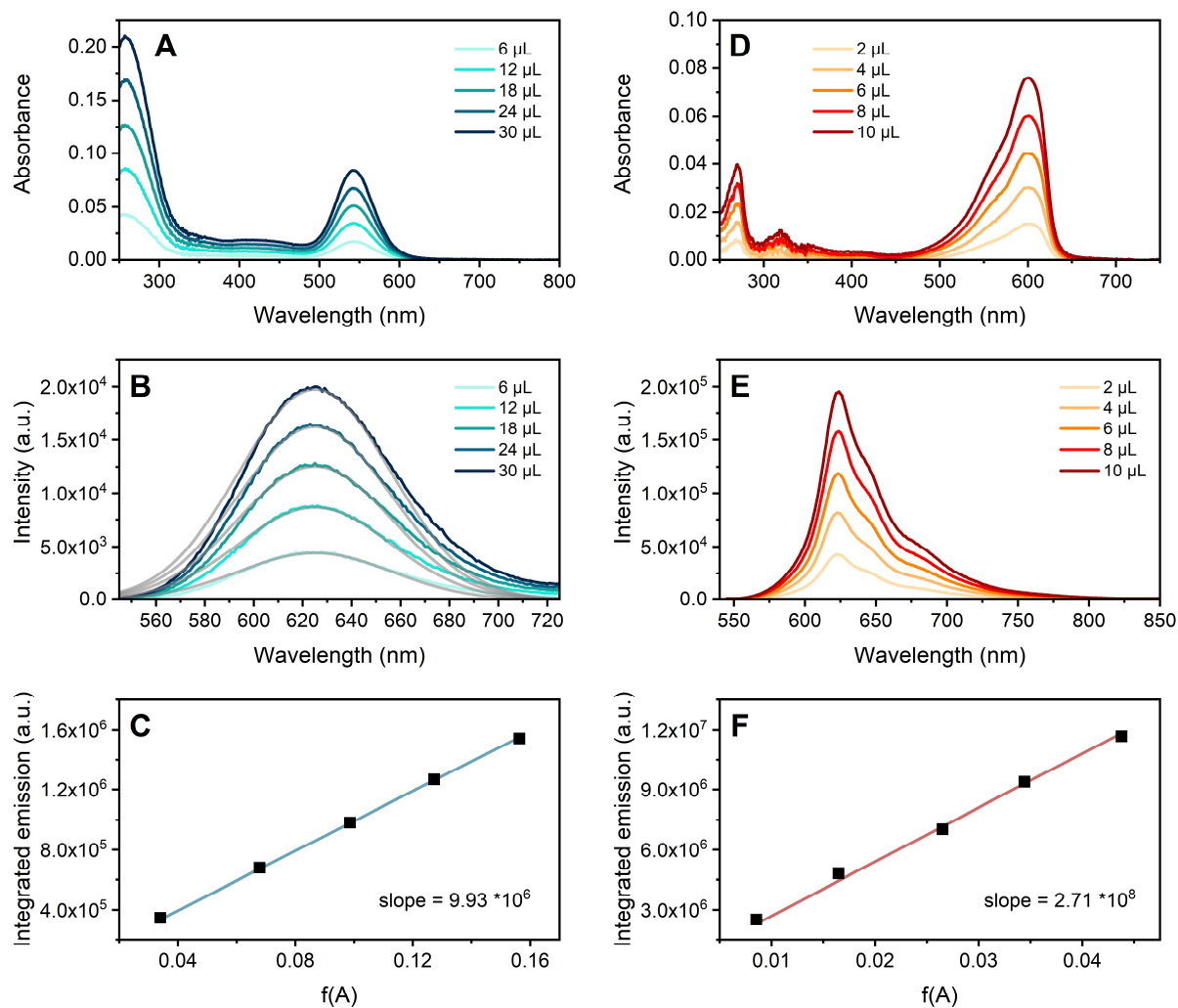
Figure S2. *Quantum yield measurements and calculations of DNA$_2$[Ag$_{18}$]$^{12+}$ in 10 mM NH$_4$OAc aqueous solution at 25 °C. **A)** absorption and **B)** emission spectra with the corresponding Gaussian fits (gray) of DNA$_2$[Ag$_{18}$]$^{12+}$. **D)** absorption and **E)** emission spectra of Cresyl Violet in absolute ethanol. The emission spectra were recorded by exciting at 531 nm. **C)** and **F)** Zero-intercept linear fit of the integrated fluorescence vs the fraction of absorbed light for the DNA-AgNC and reference dye, respectively. The slopes were used to calculate the Q of DNA$_2$[Ag$_{18}$]$^{12+}$.*

Steady-state and Time-resolved data
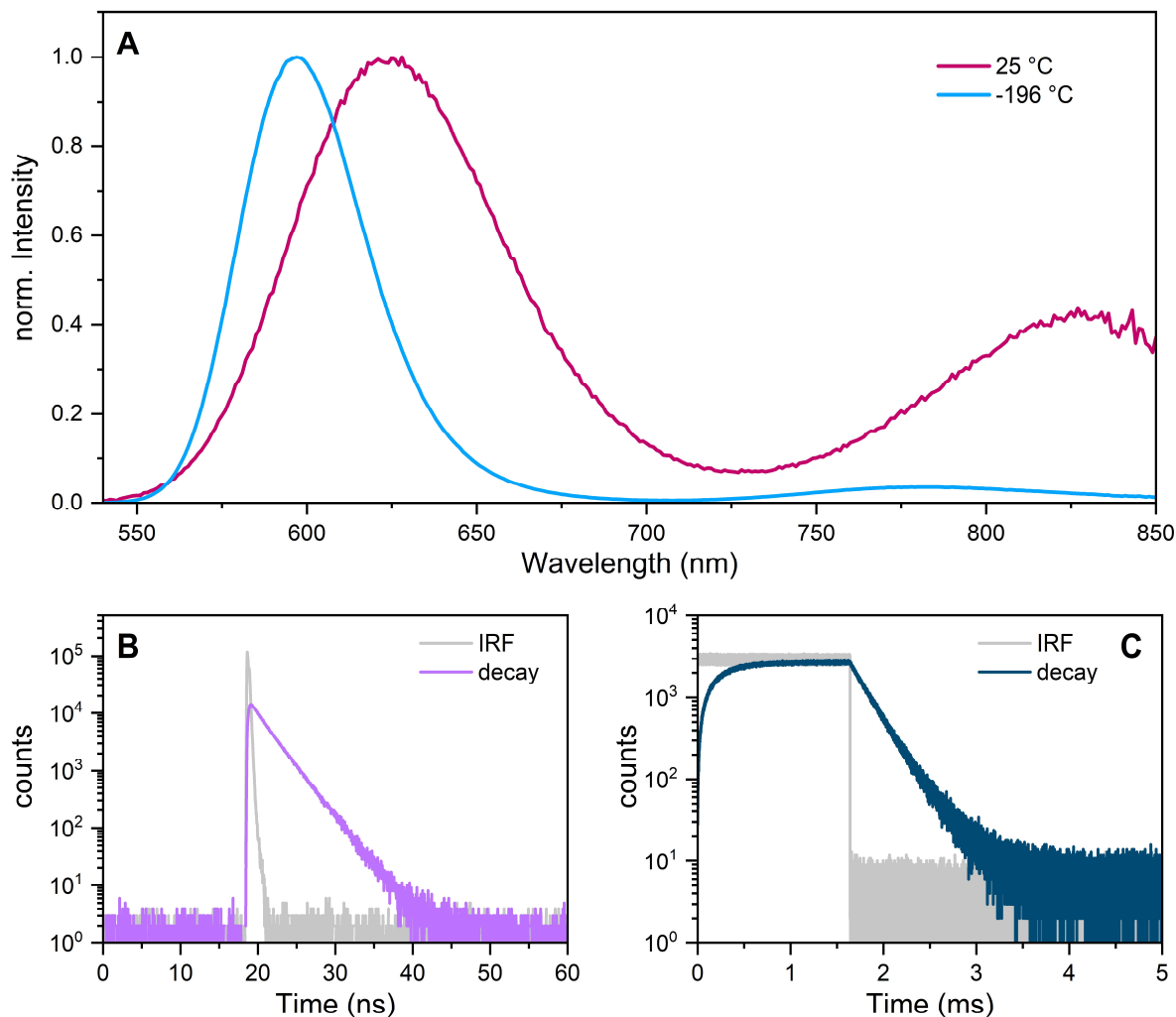
Figure S3. *A)* *Overlay of normalized steady-state emission spectra of DNA$_2$[Ag$_{18}$]$^{12+}$ in 10 mM NH$_4$OAc aqueous solution at 25 and -196 °C, exciting at 531 nm.* *B)* *Fluorescence decay of DNA$_2$[Ag$_{18}$]$^{12+}$ in 10 mM NH$_4$OAc H$_2$O solution at -196 °C measured at 595 nm (λ_{exc} = 531 nm), together with the IRF.* *C)* *Emission of DNA$_2$[Ag$_{18}$]$^{12+}$ in 10 mM NH$_4$OAc H$_2$O solution at -196 °C recorded at 785 nm (λ_{exc} = 531 nm) in burst mode, and IRF.*
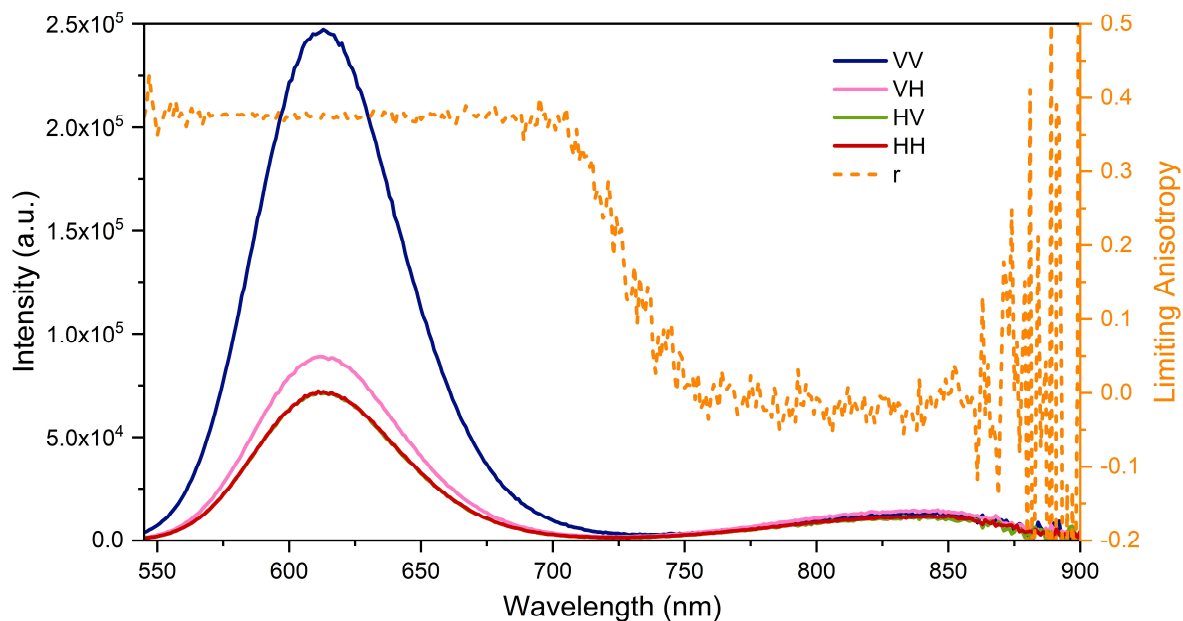
Figure S4. *Steady-state emission anisotropy measurements of DNA$_2$[Ag$_{18}$]$^{12+}$ in 95% glycerol and 5% 10 mM NH$_4$OAc H$_2$O solution at 5 °C, exciting at 531 nm. Parallel (VV, HH) and perpendicular (VH, HV) emission spectra are shown along with the calculated limiting anisotropy trace (r).*
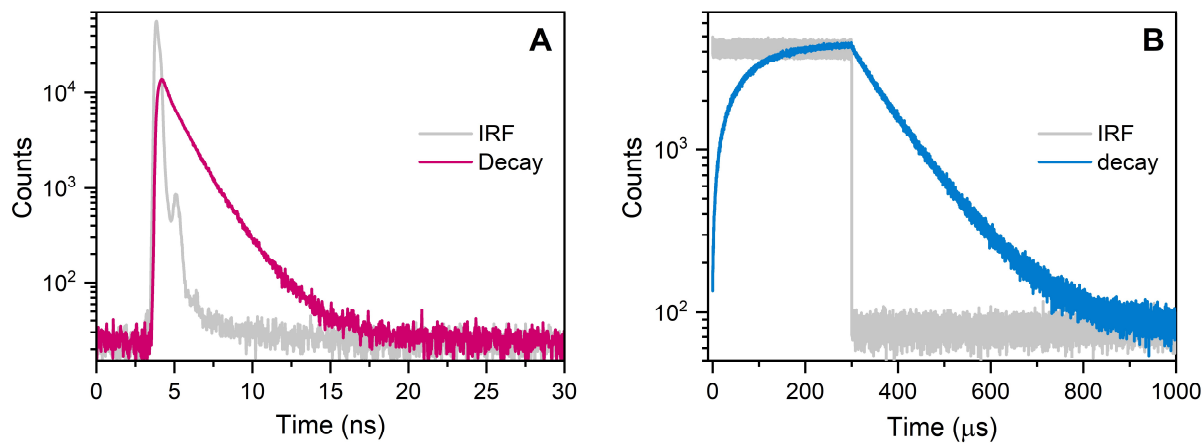
Figure S5. *Time-resolved emission data of DNA$_2$[Ag$_{18}$]$^{12+}$ in 95% glycerol and 5% 10 mM NH$_4$OAc aqueous solution at 5 °C, exciting at 531 nm. **A)** Fluorescence decay measured at 610 nm, together with the IRF; and **B)** emission recorded in burst mode at 820 nm, along with the corresponding IRF.*
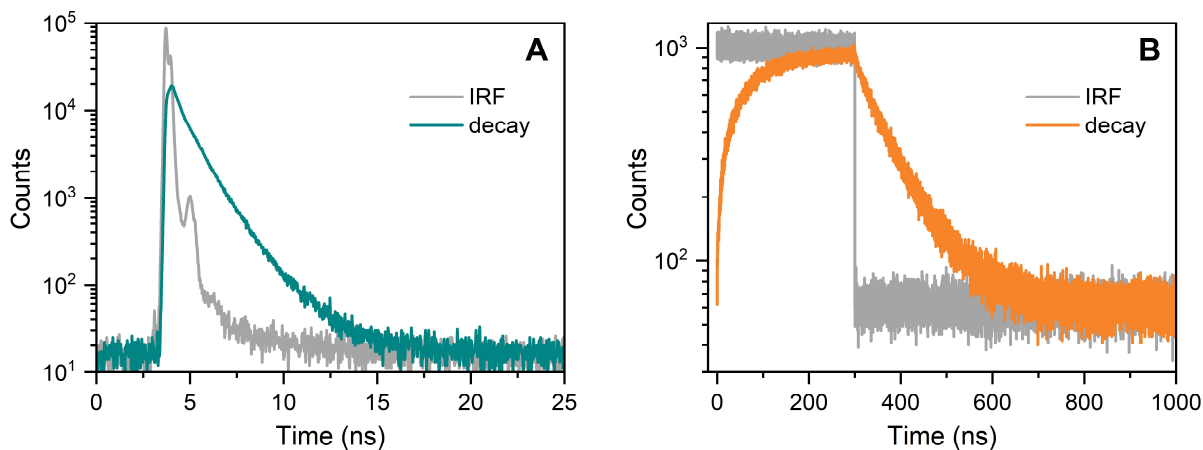
Figure S6. *Time-resolved emission data of DNA$_2$[Ag$_{18}$]$^{12+}$ in 95% glycerol and 5% 10 mM NH$_4$OAc aqueous solution at 25 °C, exciting at 531 nm.* ***A)*** *Fluorescence decay measured at 610 nm, together with the IRF; and* ***B)*** *emission recorded in burst mode at 820 nm, along with the corresponding IRF.*
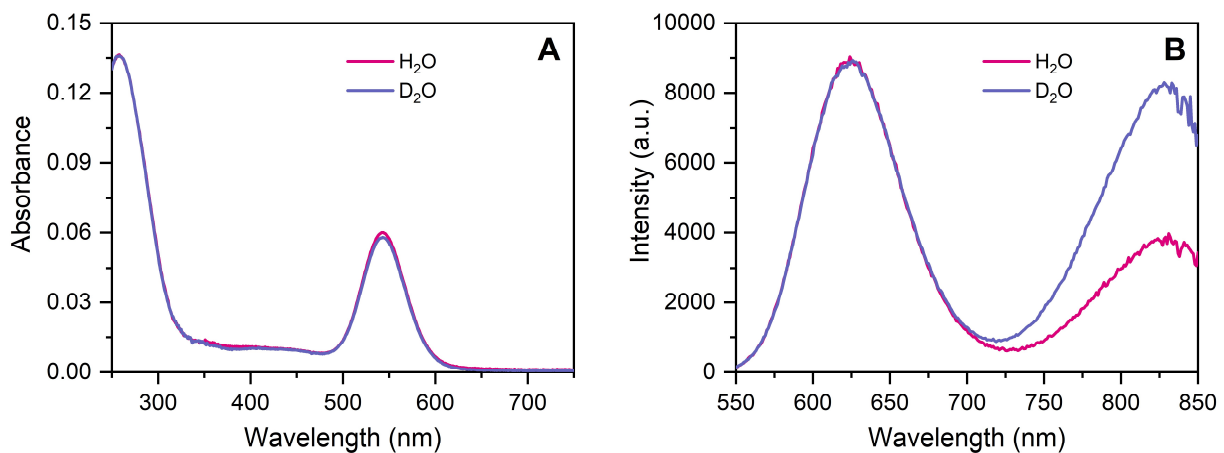
Figure S7. *Comparison of steady-state spectra for DNA$_2$[Ag$_{18}$]$^{12+}$ in 10 mM NH$_4$OAc H$_2$O (pink) and D$_2$O (violet) solutions at room temperature. Overlay of* ***A)*** *absorption spectra and* ***B)*** *emission spectra, exciting at 531 nm.*
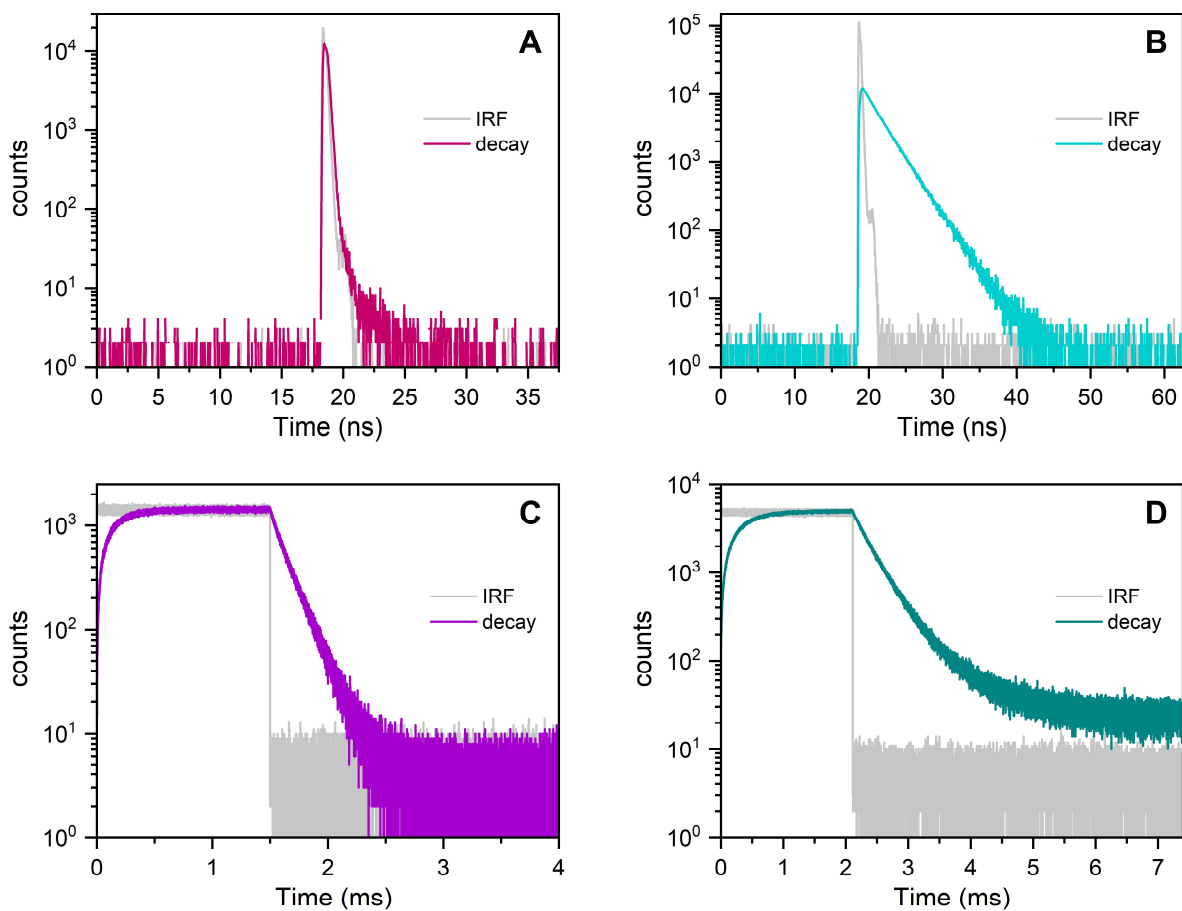
Figure S8. *Time-resolved emission data of DNA$_2$[Ag$_{18}$]$^{12+}$ in 10 mM NH$_4$OAc deuterated solution at 25 °C (A and C) and -196 °C (B and D), exciting at 531 nm. Fluorescence decay measured at **A)** 625 nm and **B)** 595 nm, together with the IRF. Emission recorded in burst mode at **C)** 840 nm and **D)** 785 nm, along with the corresponding IRFs.*
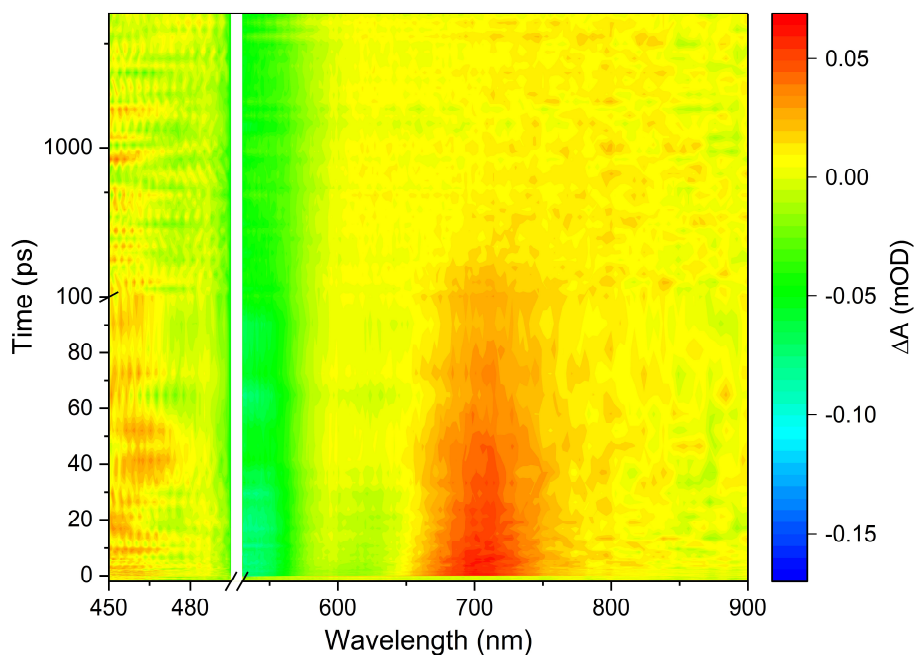
Figure S9. *Pseudo-color representation of femtosecond transient absorption (fs-TA) spectra of DNA$_2$[Ag$_{18}$]$^{12+}$ in 10 mM NH$_4$OAc aqueous solution. The laser scatter in the range of 495 - 530 nm is not shown.*
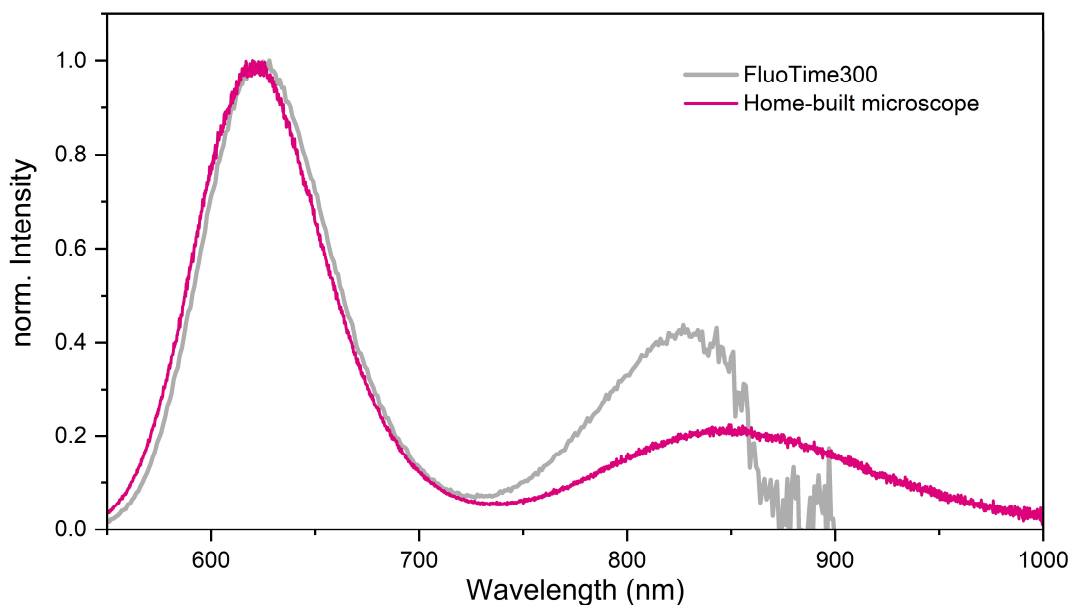
Figure S10. *Comparison of emission spectra of DNA$_2$[Ag$_{18}$]$^{12+}$ in 10 mM NH$_4$OAc aqueous solution recorded at room temperature with a FluoTime300 instrument (λ_{exc} = 531 nm) and on our home-built microscope (λ_{exc} = 514 nm). Note that due to the limited sensitivity above 800 nm, the I_{Lu}/I_{Fl} ratios obtained from the FluoTime300 instrument might be less reliable than measured with the home-built microscope.*

Excitation-intensity-dependent measurements
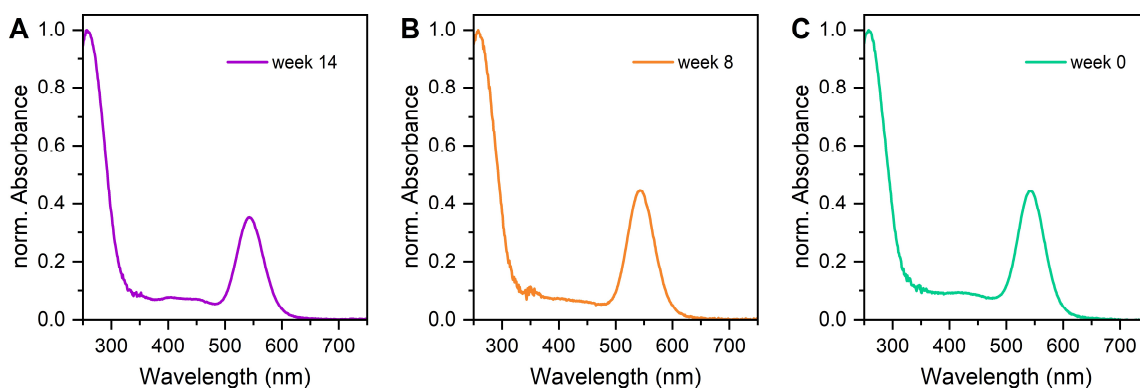
Figure S11. *Normalized absorption spectra of three different batches of DNA$_2$[Ag$_{18}$]$^{12+}$ in 10 mM NH$_4$OAc.* ***A)*** *Oldest batch, 14 weeks after HPLC purification. This batch was also used for recording the data in the main article at an earlier time point.* ***B)*** *Newer batch, 8 weeks after HPLC purification.* ***C)*** *Freshly prepared batch, 0 weeks after HPLC purification.*
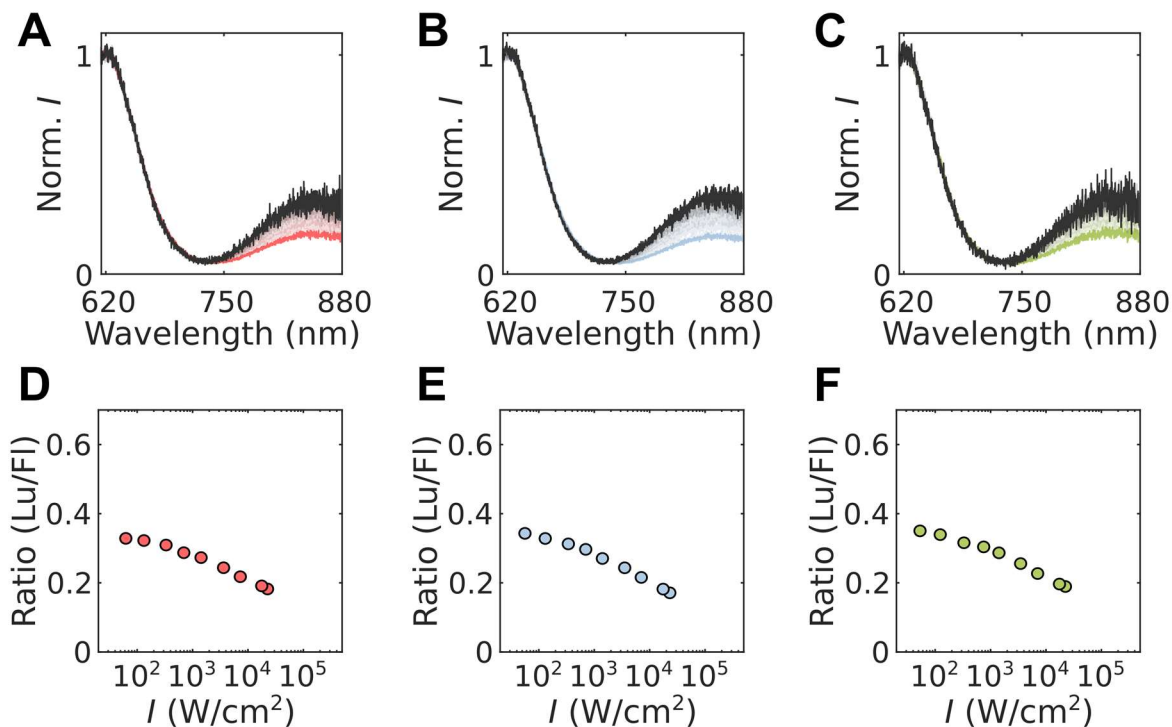
Figure S12. *Emission spectra and excitation-intensity-dependent Lu/Fl ratios of three different batches of DNA$_2$[Ag$_{18}$]$^{12+}$ in 10 mM NH$_4$OAc with different ages. The age is specified from the moment of HPLC purification. The corresponding absorption spectra of the three batches can be found in Figure S11.* ***A)*** *and* ***D)*** *Batch that was 14 weeks old.* ***B)*** *and* ***E)*** *Batch that was 8 weeks old.* ***C)*** *and* ***F)*** *Batch that was freshly synthesized and HPLC purified, 0 weeks old.*
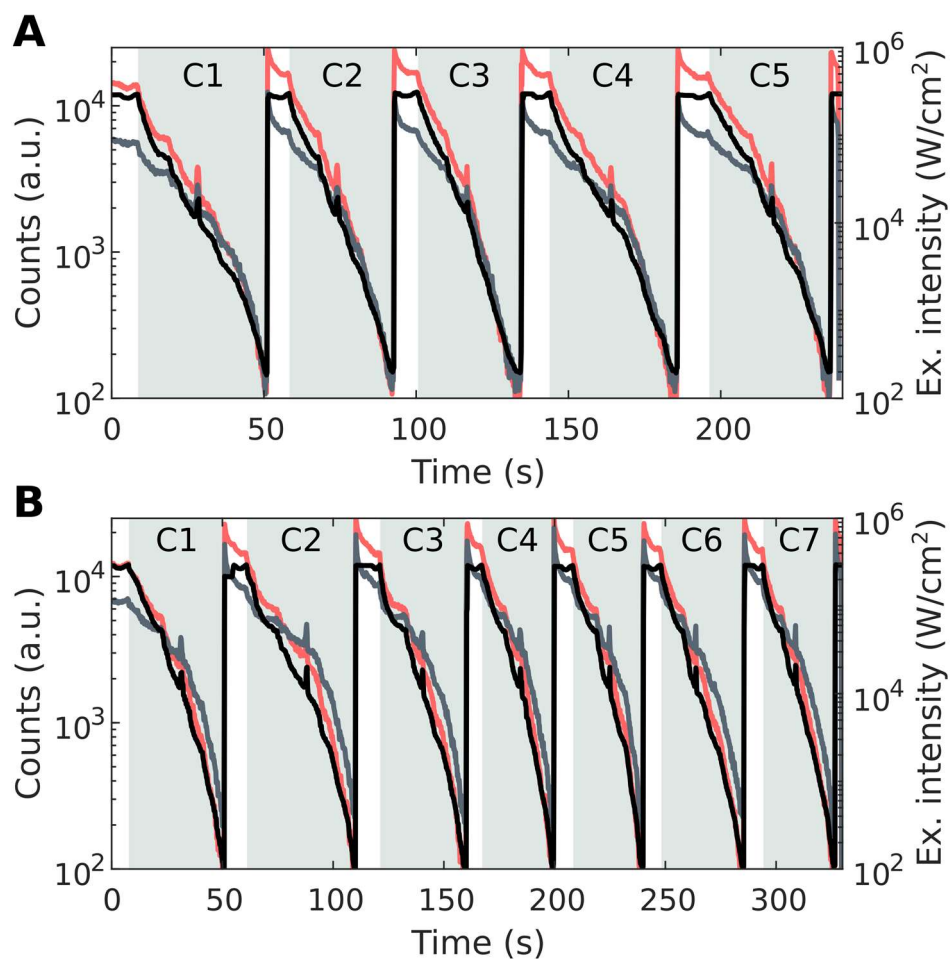
Figure S13. _Third approach (section 3.3.1) for assessing the excitation-intensity-dependency of DNA$_2$[Ag$_{18}$]$^{12+}$ dual emission with the use of a two-APD setup. The fluorescence (red), luminescence (gray), and excitation intensity (black) are simultaneously recorded. This is done for DNA$_2$[Ag$_{18}$]$^{12+}$ in both 10 mM NH$_4$OAc **A)** H$_2$O and **B)** D$_2$O solutions at room temperature. Multiple cycles (C1-C5/C7) are measured, and the corresponding time ranges (gray areas) are used for subsequent data analysis. More details can be found in section 3.3.1._
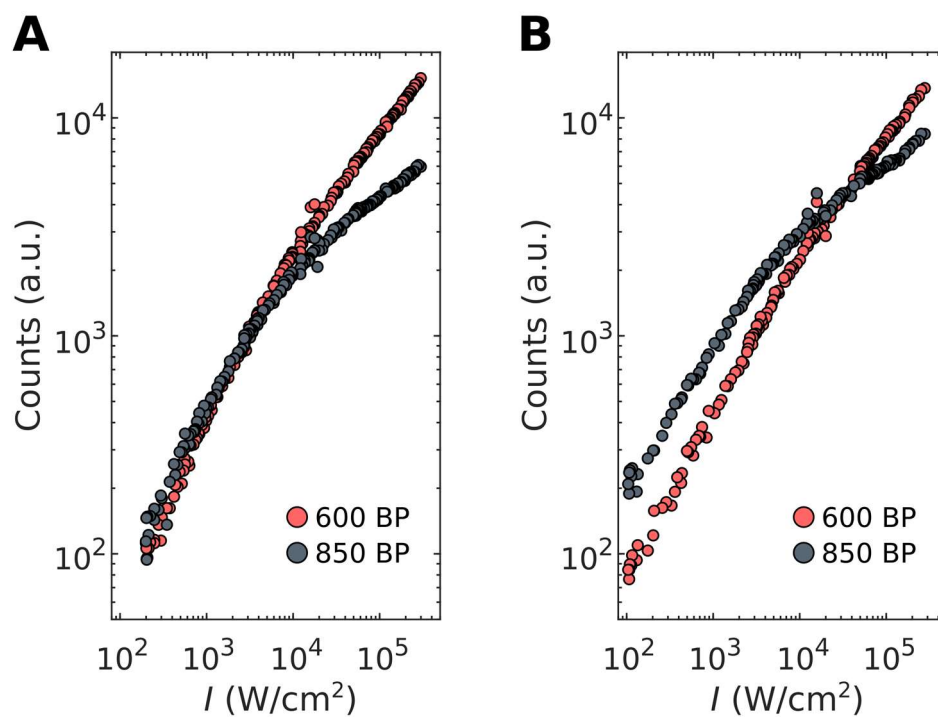
Figure S14. *Fluorescence and luminescence as a function of excitation intensity for a single cycle. The fifth cycle of the data presented in Figure S13 is extracted, and the fluorescence (600 BP) and luminescence (850 BP) are plotted as a function of excitation intensity. This is done for DNA$_2$[Ag$_{18}$]$^{12+}$ in both 10 mM NH$_4$OAc **A)** H$_2$O and **B)** D$_2$O solutions at room temperature.*
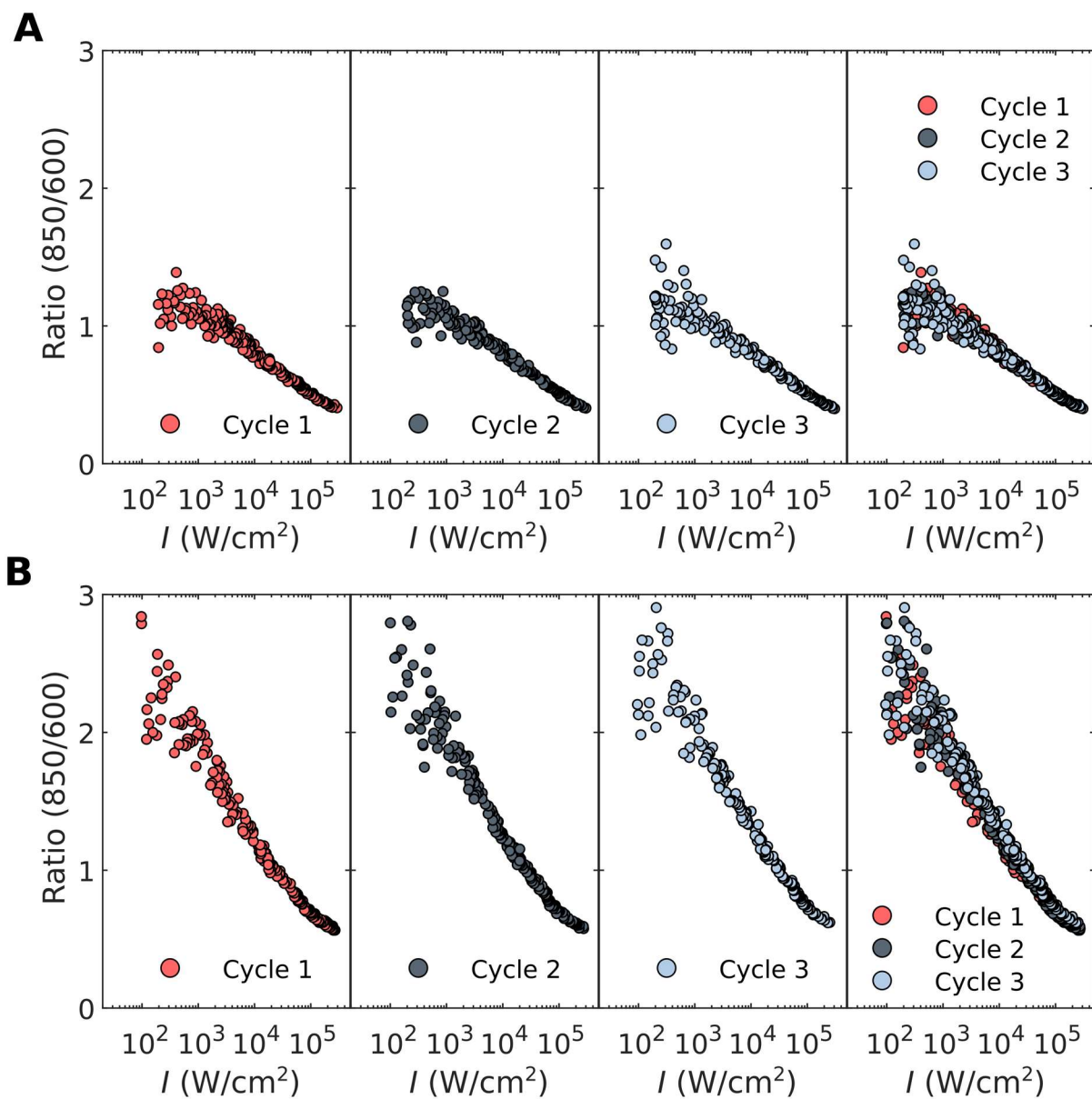
Figure S15. *Ratio between luminescence and fluorescence (850/600) as a function of excitation intensity for multiple cycles. Three cycles from the data reported in Figure S13 are extracted and the ratio between the luminescence (850 BP) and fluorescence (600 BP) is presented as a function of excitation intensity. This is done for DNA$_2$[Ag$_{18}$]$^{12+}$ in 10 mM NH$_4$OAc **A)** H$_2$O and **B)** D$_2$O solutions at room temperature. In both cases, a very high reproducibility between cycles can be observed.*
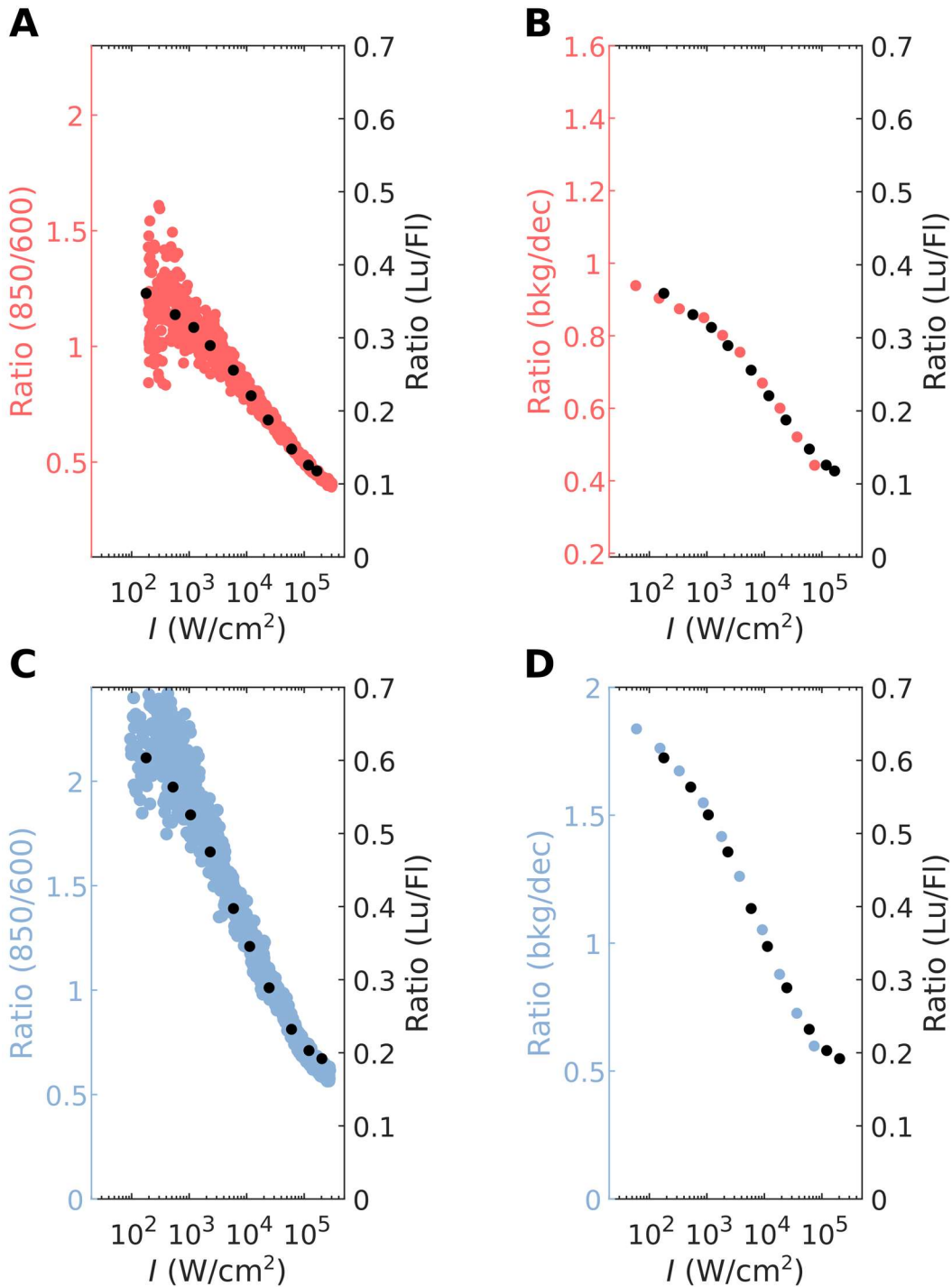
Figure 16. *Comparison between calibration curves obtained with the three different approaches described in section 3.3.1. The excitation-intensity-dependent ratios extracted with each method (Figures 4 and 5) are overlaid and rescaled on different y-axes to show the mutual agreement between the shape and relative ratio change.* ***A)*** *Comparison between the first and third approach for DNA$_2$[Ag$_{18}$]$^{12+}$ in 10 mM NH$_4$OAc aqueous solution.* ***B)*** *Comparison between the first and second method in 10 mM NH$_4$OAc H$_2$O solution.* ***C, D)*** *Similar to* ***A, B)*** *but in in 10 mM NH$_4$OAc deuterated solution.*

Interferometer measurement

A

$I_{UG}(t, x)$ $I_{Fl,TG}(t, x)$ $I_{Lu,TG}(t, x)$

B

C

$I_{UG}(t, \lambda)$ $I_{Fl,TG}(t, \lambda)$ $I_{Lu,TG}(t, \lambda)$

D
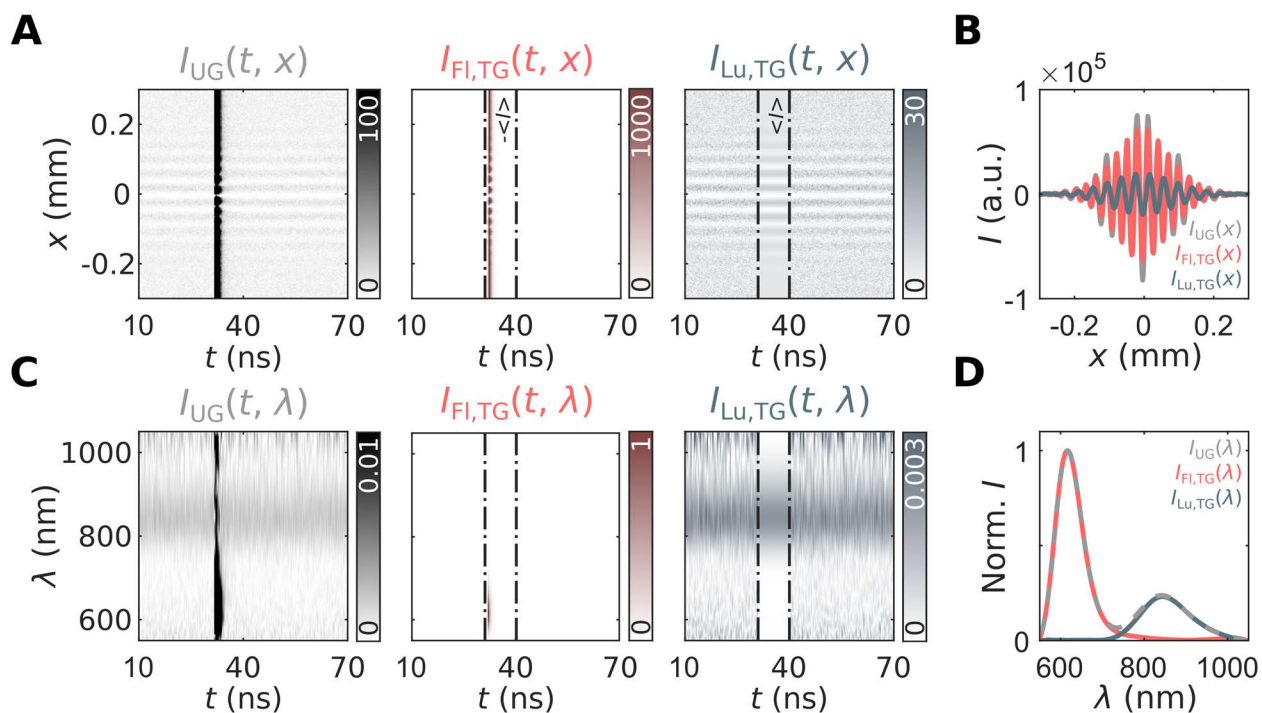
Figure S17. *Time-gated emission spectra of DNA$_2$[Ag$_{18}$]$^{12+}$ in 10 mM NH$_4$OAc aqueous solution measured at room temperature under 520 nm (13 MHz) excitation. **A)** Ungated ($I_{UG}(t, x)$), fluorescence-gated ($I_{Fl,TG}(t, x)$), and luminescence-gated ($I_{Lu,TG}(t, x)$) TRIMs. **B)** Overlay of the integrated TRIMs. **C)** Ungated ($I_{UG}(t, \lambda)$), fluorescence-gated ($I_{Fl,TG}(t, \lambda)$), and luminescence-gated ($I_{Lu,TG}(t, \lambda)$) TREMs normalized to the maximum of $I_{UG}(t, \lambda)$. Note that different limits are used for each of the TREMs to highlight the different contributions. **D)** Resulting spectra of the interferograms in **B**).*

Concentration-dependent measurements

A

B
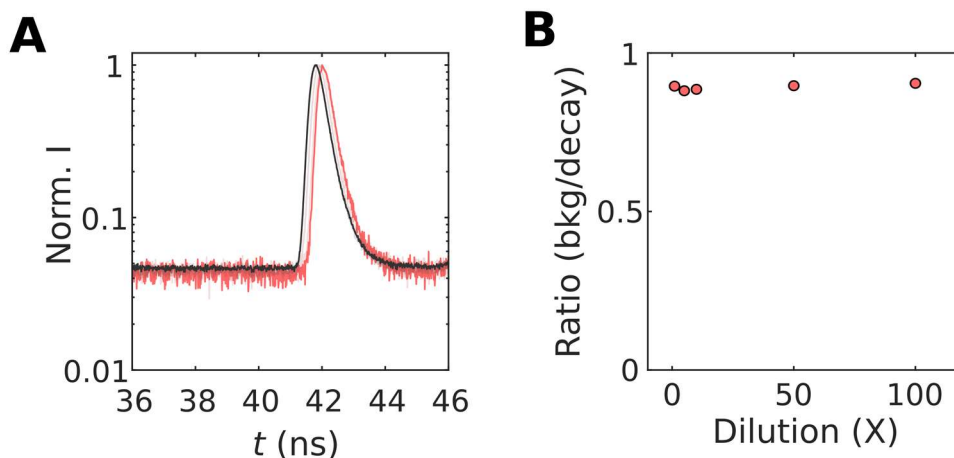
Figure S18. *Concentration dependence of the ratiometric response of DNA$_2$[Ag$_{18}$]$^{12+}$, measured using the TCSPC approach. **A)** Time-resolved data (λ_{exc} = 520 nm, 78 MHz, 528 W/cm^2) for 1X (~ 96 µM based on the DNA absorbance, black curve) and 100X dilutions (red curve). **B)** Bkg/decay ratio for 1X (~ 96 µM based on the DNA absorbance), 5X, 10X, 50X and 100X dilutions. Note that based on the signal of the 100X dilution measurement, it is fair to assume that further dilution by another factor of 100 (~10 nM) should still be measurable using the ratiometric approach.*

22

Publication 3

Bioconjugation of a Near-Infrared DNA-Stabilized Silver Nanocluster to Peptides and Human Insulin by Copper-Free Click Chemistry.

Vanessa Rück, Narendra K. Mishra, Kasper K. Sørensen, Mikkel B. Liisberg, Ane B. Sloth, Cecilia Cerretani, Christian B. Mollerup, Andreas Kjaer, Chenguang Lou, Knud J. Jensen, and Tom Vosch.

Article
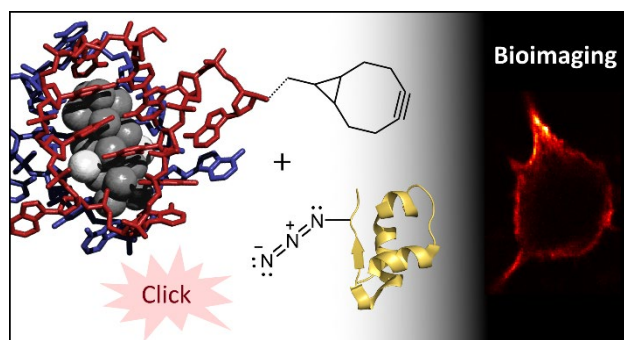
Bioconjugation of a Near-Infrared DNA-Stabilized Silver Nanocluster to Peptides and Human Insulin by Copper-Free Click Chemistry

Vanessa Rück, Narendra K. Mishra, Kasper K. Sørensen, Mikkel B. Liisberg, Ane B. Sloth, Cecilia Cerretani, Christian B. Mollerup, Andreas Kjaer, Chenguang Lou, Knud J. Jensen, and Tom Vosch*

Read Online

ACCESS | Metrics & More | Article Recommendations | Supporting Information

ABSTRACT: DNA-stabilized silver nanoclusters (DNA-AgNCs) are biocompatible emitters with intriguing properties. However, they have not been extensively used for bioimaging applications due to the lack of structural information and hence predictable conjugation strategies. Here, a copper-free click chemistry method for linking a well-characterized DNA-AgNC to molecules of interest is presented. Three different peptides and a small protein, human insulin, were tested as labeling targets. The conjugation to the target compounds was verified by MS, HPLC, and time-resolved anisotropy measurements. Moreover, the spectroscopic properties of DNA-AgNCs were found to be unaffected by the linking reactions. For DNA-AgNC-conjugated human insulin, fluorescence imaging studies were performed on Chinese hamster ovary (CHO) cells overexpressing human insulin receptor B (hIR-B). The specific staining of the CHO cell membranes demonstrates that DNA-AgNCs are great candidates for bioimaging applications, and the proposed linking strategy is easy to implement when the DNA-AgNC structure is known.

Bioimaging

Click
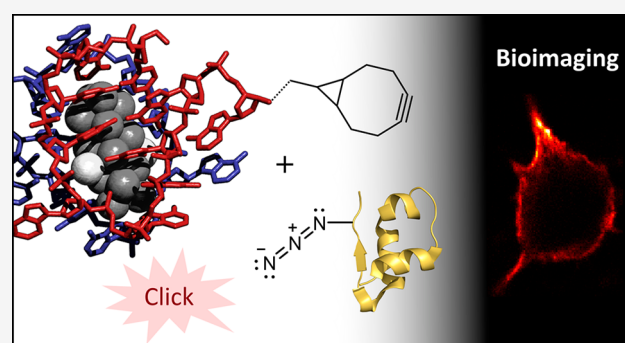
■ INTRODUCTION

DNA-stabilized silver nanoclusters (DNA-AgNCs) were first introduced by Petty et al. in 2004,[1] and have become known for their tunable emission, high brightness, large Stokes shift, and interesting photophysical properties.[2] Usually, less than 30 silver atoms and cations are embedded in one or more DNA strands with an overall diameter below 2 nm.[2] The DNA oligomer acts both as a scaffold to prevent aggregation into bigger particles and as a programmable tool to generate atomically precise clusters.[3−8] Hence, tuning the DNA template results in a wide palette of DNA-AgNCs with emission spanning from the visible to the near-infrared (NIR) range.[2] Due to the large variability provided by the four natural nucleotides alone, the photophysical properties of DNA-AgNCs can be modified in a myriad of different ways.[2,9] Additionally, simple modifications of the nucleobases, e.g., replacing guanosine with inosine, whose structures solely differ in one amino group, can dramatically affect the fluorescence decay time and quantum yield, as was recently demonstrated.[10−13] DNA-AgNCs are interesting not only for unraveling and understanding the origin of luminescence in small metal clusters but also for their use as fluorophores. Most DNA-AgNCs possess fluorescent states along with microsecond-lived states, which can be either dark or luminescent. The presence of the long-lived state enables the possibility of optically

activated delayed fluorescence (OADF) and upconversion fluorescence (UCF).[14,15] Since the emission is on the anti-Stokes side of the secondary excitation laser, these approaches allow background-free imaging. Moreover, the high brightness of some clusters in the near-infrared region[16] makes them promising candidates for imaging biological samples, e.g., tissues and cells, characterized by high autofluorescence. However, limited work has been done on attaching functional groups to DNA-AgNCs in order to promote conjugation to targets of interest,[17] which is key to improving their potential as fluorophores in bioimaging applications.[18−21] A likely problem is that the linker can influence the interactions of the nucleobases with the AgNC, leading to changes in the spectroscopic properties or loss of stability of the DNA-AgNC. Here, we demonstrate a bioconjugation strategy for an NIR-emitting DNA-AgNC with a known structure.[22] Our approach is based on the copper-free click reaction achieved by strain-promoted azido-alkyne cycloaddition (SPAAC).[23−25] The
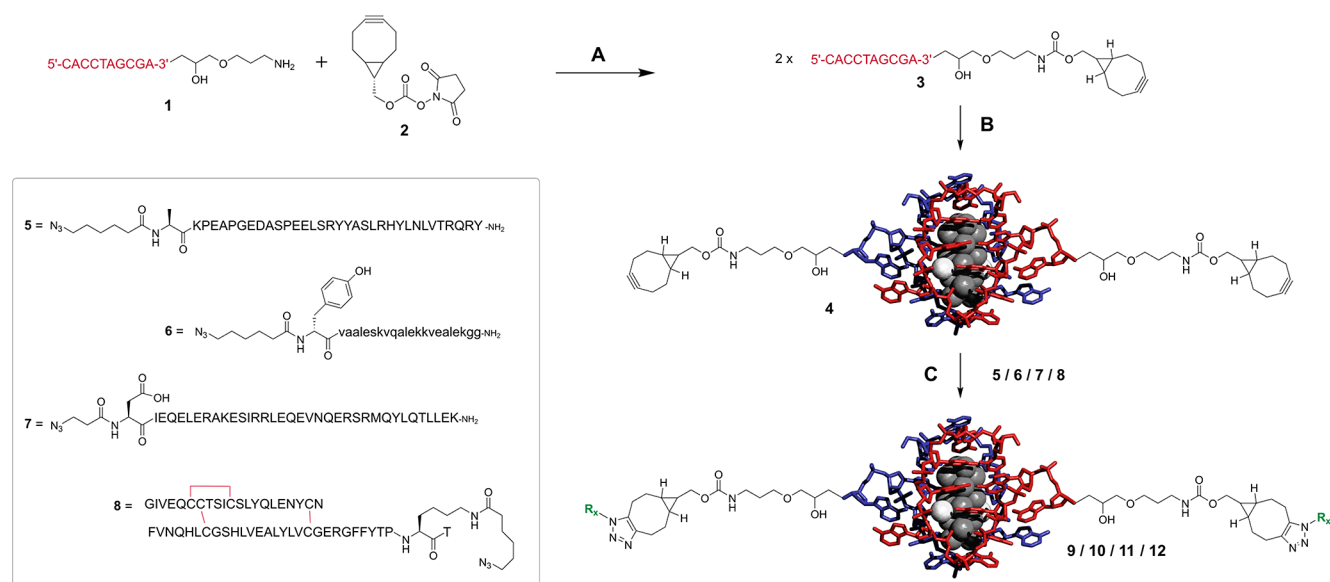
Figure 1. Scheme for the synthesis and conjugation of DNA-BCN-Ag16NC (**4**) with three peptides and a small protein: PYY-peptide (**5**), d-peptide (**6**), coiled-coil peptide (**7**), and human insulin (**8**). **9**, **10**, **11**, and **12** are the conjugated products of compound **4** to peptides **5**, **6**, **7** and protein **8**, respectively. The DNA-Ag$_{16}$NC structure was made in Pymol using PDB accession code 6JR4.[22]

spontaneous addition of a reactive, ring-strained alkyne to an azido group eliminates the need for a metal catalyst like copper, which is cytotoxic.[24]

Particularly, we prove the successful conjugation of the NIR emissive DNA-Ag$_{16}$NC[22,26,27] to three different peptides of various sizes as well as a small protein, human insulin (hI). For hI conjugated to DNA-Ag$_{16}$NC, confocal fluorescence microscopy was performed to visualize human insulin receptor B (hIR-B) overexpressed in Chinese hamster ovary (CHO) cells. In addition, emission spectra and fluorescence lifetime images were recorded to prove that the photophysical properties of DNA-Ag$_{16}$NCs are not affected by the cellular environment, a problem (e.g., quenching or spectral shifts) that can occur with other fluorophores.[28] To the best of our knowledge, this is the first time that SPAAC has been used to successfully conjugate biomolecules to purified DNA-AgNCs.

RESULTS AND DISCUSSION

Synthesis of BCN-Terminated DNA-Ag$_{16}$NC. To evaluate our proposed strategy, the well-characterized DNA-Ag$_{16}$NC was chosen. This specific DNA-AgNC was selected for several reasons. First, it is an NIR emitter with a very large Stokes shift (5600 cm^{-1})[26,29] and has a decent quantum yield (0.26)[26] compared to other fluorophores in the same emission range.[30] Moreover, it was recently found that DNA-Ag$_{16}$NC has a red-shifted μs-lived state, which could be used to generate OADF, opening up the possibility of time-gated background-free imaging.[27] Additionally, it could be used as a suitable two-photon fluorophore for measuring blood flow velocities in living mice.[31] Most importantly, the structure is known,[22] which is crucial in the rational design of our conjugation experiments. Crystallographic data show that the AgNC is well-protected by the DNA template, and thus it displays remarkable chemical stability over time.

The DNA-Ag$_{16}$NC is formed by two 10-base DNA sequences 5′-CACCTAGCGA-3′.[22] Based on the structure, the 5′-ends are not available for conjugation, since the cytosines are coordinated by Ag atoms. The attachment of a

functional group in this position, as well as one of the internal positions, could affect the formation of the AgNC and alter the spectroscopic properties. In contrast, the A$_{10}$ nucleotides at the 3′-ends do not interact with the AgNC.[22] Since the removal of A$_{10}$ was proven not to affect the photophysical properties of Ag$_{16}$NC,[32] the 3′-end position was selected for attaching a reactive linking group.

For the copper-free click reaction, a ring-strained alkyne is required; thus, we opted for bicyclononyne (BCN), which is the smallest ring-strained alkyne that can be easily dissolved in water. BCN enables highly efficient and bio-orthogonal conjugation to peptides and proteins when exposed to an azide-containing counterpart.[23−25] In order to attach a BCN group to the 3′-end of 5′-CACCTAGCGA-3′, the DNA was ordered with a primary amine bound to the A$_{10}$ position (compound **1**, see Figure 1).

The first step was the synthesis of compound **3** (step A in Figure 1). Compound **1**, dissolved in phosphate-buffered saline (PBS) and triethylamine, was mixed with BCN-NHS-ester (compound **2**) dissolved in acetonitrile (see Supporting Information (SI) for further details). The BCN-terminated DNA (compound **3**) was then purified by spin-filtration. Liquid chromatography mass spectrometry (LCMS) showed that the desired compound **3** was obtained (Figure S1). Afterward, compound **3** was used to prepare the BCN-terminated DNA-Ag$_{16}$NC (compound **4**, step B in Figure 1). Briefly, compound **3** was mixed with AgNO$_3$ in 10 mM ammonium acetate (NH$_4$OAc), to which a freshly prepared NaBH$_4$ solution was added after 15 min to promote the formation of the AgNC. The final ratio between the components was [DNA]:[AgNO$_3$]:[NaBH$_4$] = 25 μM:187.5 μM:93.75 μM, based on a previously published protocol.[26]

After synthesis, the reaction mixture was stored in the refrigerator for 1−3 days prior to high-performance liquid chromatography (HPLC) purification. Details on the HPLC method and the corresponding chromatograms can be found in the SI. Finally, the purified fraction was solvent exchanged with 10 mM NH$_4$OAc by spin-filtration. As can be seen in Figure 2A, a single peak is present in the LCMS chromato-
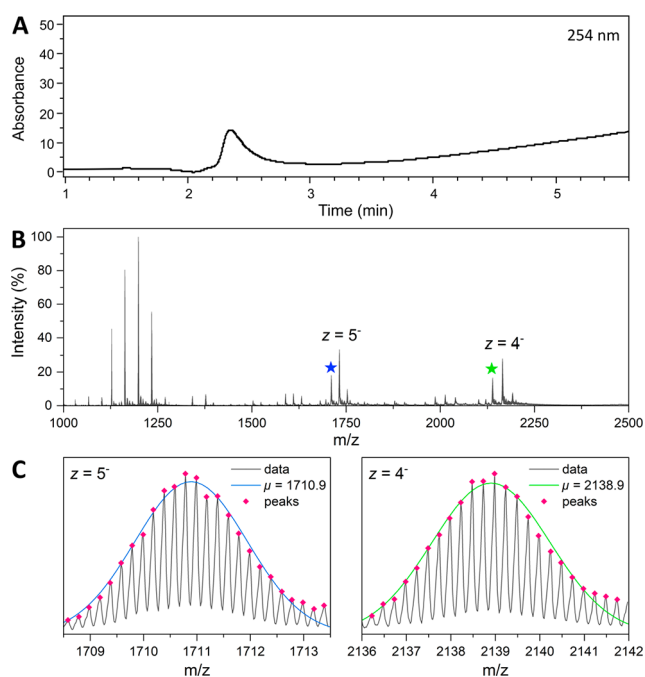
Figure 2. LCMS data for compound **4**. (A) Chromatogram monitoring the absorbance at 254 nm, given in mOD. Compound **4** elutes at approximately 2.4 min. See Figure S3 for the corresponding mass spectrum. (B) Mass spectrum of compound **4** measured on a different mass spectrometer (see SI). The stars indicate the peaks related to compound **4** with 16 silver atoms. (C) Zoomed-in views of the marked peaks in the mass spectrum for $z = 5^-$ and 4^- peaks, along with the corresponding Gaussian fits and average molecular masses (μ). See SI for further details on why the mass ratio is off by approximately 2 amu.

Figure 3. Normalized absorption (solid lines) and emission spectra (dashed lines, $\lambda_{exc} = 507.5$ nm) of the original DNA-Ag$_{16}$NC and the DNA-BCN-Ag$_{16}$NC (compound **4**) in 10 mM NH$_4$OAc at room temperature. See Figure S20 for the full absorption spectrum of compound **4**.

gram, which indicates that mainly compound **4** was obtained, and no byproducts were present. However, compound **4** highly fragmented with the applied LCMS conditions (see Figure S3). Even though this is common for DNA-AgNCs,[1,33,34] Gonzàlez-Rosell et al. have recently managed to obtain the mass spectrum of DNA-Ag$_{16}$NC and unraveled that the chemical structure of the silver cluster is $[Ag_{16}Cl_2]^{8+}$.[35] Using similar experimental conditions,[35] compound **4** was further analyzed by a different mass spectrometer, which enabled us to confirm that the DNA-BCN-Ag$_{16}$NC was successfully synthesized. The mass spectrum is reported in Figure 2B, where $z = 5^-$ and 4^- peaks are highlighted. These peaks correspond to the mass of DNA-Ag$_{16}$NC with two BCN groups attached (Figure 2C). Interestingly, additional peaks corresponding to DNA-BCN-AgNC with a larger number of silver atoms could also be observed in the mass spectrum. These extra silver ions are not part of the AgNC core, but are most likely coordinated to the triple bond of the BCN group.[36] A detailed explanation of why we believe these additional silver cations are coordinated to the triple bond and how this affects the MS measurement can be found in the SI.

Spectroscopic characterization of compound **4** showed that the photophysical properties are unaltered by the attachment of the BCN groups (Table 1 and Figures 3, S20−S21). The absorption and emission maxima are at 524 and 743 nm, respectively, and the average fluorescence decay time $\langle \tau \rangle$ remains at around 3.26 ns. Time-resolved fluorescence anisotropy measurements were used to determine the hydrodynamic volume of compound **4** and all conjugates.

Compared to DNA-Ag$_{16}$NC alone (10.14 nm^3), the hydrodynamic volume of compound **4** increased, as expected, to 12.18 nm^3, due to the addition of the two BCN groups (Table 1 and Figure 1).

Conjugation of Compound 4 to Peptides and hI. After compound **4** was successfully synthesized, we proceeded with the copper-free click reactions to three azido-modified peptides (PYY-peptide **5**, d-peptide **6**, coiled-coil peptide **7**)[37−39] and a small azido-modified protein, human insulin (compound **8**),[40] as shown in step C of Figure 1. The copper-free click reaction of compound **4** with each peptide was carried out at 18 °C by shaking the mixture at 350 rpm for 72 h. Analytical HPLC and LCMS analysis confirmed that each reaction was completed after 72 h (more details can be found in the SI). Several temperatures and reaction times were tested, and these reaction conditions were found to give the highest yields. The LCMS chromatograms of compounds **9**, **10**, and **11** are shown in Figure 4A−C, where mainly single peaks are present, while the corresponding mass spectra can be found in Figures S13−15. Compounds **9**−**11** retained the color of the original DNA-Ag$_{16}$NC solution, confirming that DNA-Ag$_{16}$NC is stable under the applied reaction conditions. This observation was further verified by spectroscopic characterization. Figure S22 shows that absorption and emission spectra of compounds **9**−**11** remain unchanged compared to compound **4** (see also Table 1). Reaction of the peptides with DNA-BCN-Ag$_{16}$NC was also proven by time-resolved anisotropy measurements. Unlike the original DNA-Ag$_{16}$NC and compound **4**, the time-resolved anisotropy data of compounds **9**−**11** could be best fitted with two rotational correlation times. The first rotational correlation time (θ_1) was fixed in the fit to the value of compound **4**, representing the local motion of the DNA-Ag$_{16}$NC part, while the second component (θ_2) was left free and was significantly longer, representing the rotation of the entire construct (Table 1).

The latter indicates that the overall hydrodynamic volume increased due to conjugation with the peptides. However, we could not confirm with certainty that the value of θ_2 matched with the addition of the peptides. First, the error in the calculated hydrodynamic volume is large when the rotational correlation time is significantly longer than the fluorescence decay time. Second, no hydrodynamic volumes for the three peptides could be found in literature.

Next, we applied the click reaction to a therapeutically relevant protein, human insulin. This well-studied protein is essential in the regulation of glucose metabolism and diabetes

Table 1. Steady-State and Time-Resolved Fluorescence Data, Along with Time-Resolved Anisotropy Data of DNA-Ag$_{16}$NC, DNA-BCN-Ag$_{16}$NC (Compound 4) and DNA-BCN-Ag$_{16}$NC Conjugated to Three Peptides and a Protein (Compounds 9−12)[a]

Compound	λ_{abs} (nm)	λ_{em} (nm)	$\langle\tau\rangle$ (ns)	r_1	θ_1 (ns)	r_2	θ_2 (ns)	V_{hydro1} (nm^3)	V_{hydro2} (nm^3)
DNA-Ag$_{16}$NC	526	746	3.22	0.388	2.19	–	–	10.14	–
4	524	743	3.26	0.382	2.63	–	–	12.18	–
9	525	738	3.07	0.117	2.63*	0.246	6.77	12.18	31.35
10	525	740	3.07	0.233	2.63*	0.143	7.06	12.18	32.66
11	523	741	3.24	0.322	2.63*	0.0548	3.28	12.18	15.18
12	526	734	3.10	0.174	2.63*	0.207	8.60	12.18	39.80

[a]λ_{abs} and λ_{em} are the absorption and emission maxima, $\langle\tau\rangle$ is the intensity-weighted average decay time monitored at 740 nm (λ_{exc} = 507.5 nm), r is the fundamental anisotropy, θ is the rotational correlation time, and V_{hydro} is the calculated hydrodynamic volume. The subscripts 1 and 2 refer to the two components derived from the biexponential fit of the anisotropy data measured at 740 nm, exciting at 507.5 nm (see SI and Figures S20−S25 for further details on the spectroscopic measurements). *This value was fixed based on the rotational correlation time of compound **4**.
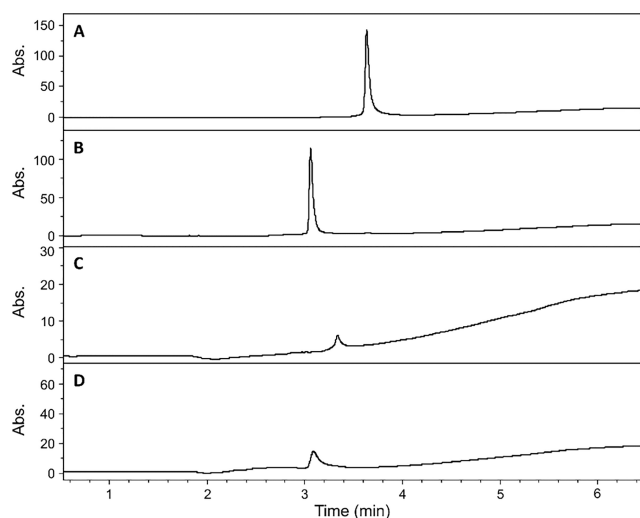
Figure 4. (A−D) Chromatograms of compounds **9**, **10**, **11**, and **12** (λ_{abs}= 254 nm), respectively. The absorbance is given in mOD. The corresponding mass spectra can be found in Figures S13−15 and S18. All four compounds have a long shelf life; see Figure S28.

treatment. The copper-free click reaction was carried out in water by adding compound **8** to compound **4**. The reaction mixture was shaken at 850 rpm for 36 h at 37 °C. LCMS analysis confirmed that the reaction was successful, as could be seen from the single peak around 3.1 min (see Figures 4D and S18). Absorption and emission spectra of compound **12** remained unchanged compared to the DNA-BCN-Ag$_{16}$NC (see Figure S24). Also for compound **12**, two rotational correlation times were needed to satisfactorily fit the time-resolved anisotropy data. The first rotational correlation time (θ_1) represented the movement of the DNA-BCN-Ag$_{16}$NC part, while the second component (θ_2) was significantly longer (Table 1). The hydrodynamic volume calculated from θ_2 was found to be 39.80 nm^3. The monomer of bovine insulin, which is similar in size to human insulin, has been reported to have a hydrodynamic radius of 1.4 nm.[41] For a spherical approximation, this yields a volume of 11.50 nm^3. Even though the combined hydrodynamic volume is not a simple addition, the value of 39.80 nm^3 for compound **12** seems to indicate that DNA-BCN-Ag$_{16}$NC reacts with two hI units.

Bioimaging of hI-Conjugated DNA-Ag$_{16}$NC. Fluorescence imaging studies were carried out on Chinese hamster ovary (CHO) cells with hI-conjugated DNA-Ag$_{16}$NC (compound **12**) to demonstrate that our linking strategy provides a

straightforward labeling protocol and makes DNA-Ag$_{16}$NCs suitable for bioimaging applications. Prior to bioimaging studies, the chemical stability of compound **4** in the cell medium was tested by recording emission spectra over time. Figure S26 displays a negligible drop in the emission intensity, confirming the good chemical stability of DNA-BCN-Ag$_{16}$NCs with no decomposition of the compound and potential release of silver. Therefore, we can assume that the insulin conjugate (compound **12**) shows similar behavior since the stability of the DNA-Ag$_{16}$NC is most likely the critical part of the construct. Afterward, the photostability of compound **4** in the cell medium was also verified by continuously irradiating the sample for 2 h (excitation power = 1.67 mW yielding approximately 0.1 W/cm^2). As shown in Figure S27, compound **4** has good photostability, since only a minor decrease in the fluorescence intensity can be observed.

For the fluorescence imaging experiments, CHO cells overexpressing human insulin receptor B (hIR-B) were used.[42] The CHO cells were first fixed, incubated with compound **12** or DNA-Ag$_{16}$NC (as control) for 15 min, and then imaged in both bright field and confocal fluorescence microscopy configurations (see SI for details).

Figure 5A−B shows that compound **12** was mostly localized on the cell membrane. To verify that the observed emission is not due to autofluorescence, emission spectra were recorded from the stained regions. Figure 5E confirms that the recorded fluorescence in Figure 5B is indeed from insulin-conjugated DNA-Ag$_{16}$NCs, as the expected Gaussian-like emission band centered at 730 nm was obtained. It should be noted that upon increasing the concentration of compound **12**, the labeling was no longer limited to the outer membrane but covered the entire cell (Figure S29). This concentration-dependent staining of CHO cells is in line with previously reported findings by Ghosh et al.[43] To exclude the possibility that some of the staining was due to nonspecific interactions of DNA-Ag$_{16}$NCs with the fixed CHO cells, similar experiments were performed with DNA-Ag$_{16}$NCs alone (Figure 5C−D). As shown by the blue spectrum in Figure 5E, no significant emission could be detected when using similar staining concentrations and imaging conditions. All DNA-Ag$_{16}$NCs were clearly removed during the washing step before imaging (see SI for more details). Consequently, only autofluorescence, similar to unstained CHO cells, was detected in the control experiment (see Figure S30). Additionally, fluorescence lifetime imaging microscopy (FLIM) was performed, and the recorded images and data can be found in Figures 5F−G and S31. The fluorescence decays acquired for every pixel were
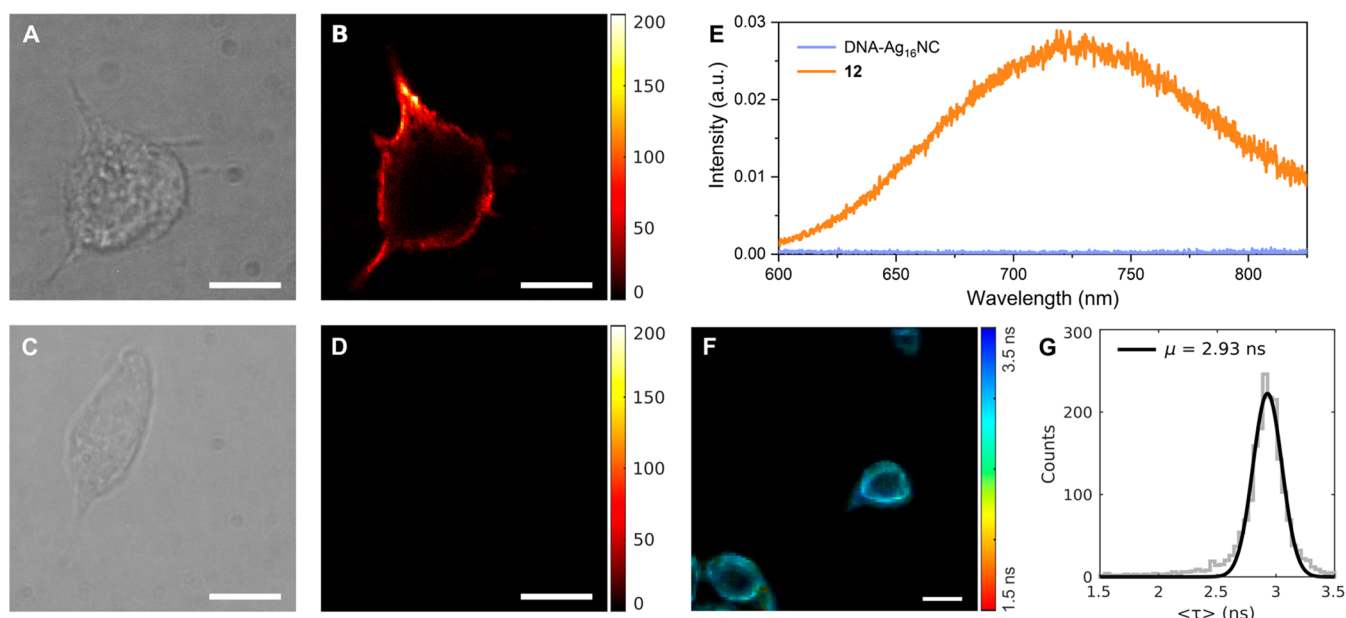
Figure 5. Imaging of fixed CHO cells overexpressing hIR-B receptors. (A) Bright-field and (B) confocal images of CHO cells stained with approximately 100 nM compound **12**. (C) Bright-field and (D) confocal images of CHO cells stained with approximately 100 nM DNA-Ag$_{16}$NCs. (E) Emission spectra (λ_{exc} = 520 nm) of CHO cells stained with compound **12** (orange curve) and DNA-Ag$_{16}$NCs only (light blue trace). (F) FLIM image of CHO cells overexpressing hIR-B labeled with approximately 300 nM DNA-Ag$_{16}$NC-hI (compound **12**) and (G) corresponding histogram of fitted fluorescence decay times. A Gaussian fit to the distribution yields a mean value (μ) of 2.93 ns. Scale bars: 10 μm.

fitted with a biexponential reconvolution function, including the autogenerated instrument response function (IRF). The mean value of 2.93 ns from the Gaussian fit distribution of the fluorescence decay times is very close to that obtained from bulk measurements (3.10 ns, see Table 1), indicating that compound **12** was not significantly affected by the cellular environment. Furthermore, compound **12** was localized on the CHO cell membranes, in agreement with the confocal fluorescence intensity image in Figure 5B.

In the end, a cell viability assay was carried out to evaluate the applicability of DNA-Ag$_{16}$NCs to living cells. CHO cells were incubated with increasing concentrations (ranging from 50 nM to 1 μM) of DNA-Ag$_{16}$NC and compound **12** along with human insulin (azido-hI) as a control. After 4 h, approximately 90% of the cells were still viable when treated with concentrations up to 500 nM. On the other hand, a 30% drop was recorded for cells incubated with a 1 μM concentration of DNA-Ag$_{16}$NC and compound **12**, while human insulin did not significantly affect the cell viability (see SI and Figure S32 for further details). Overall the concentrations used for the bioimaging experiments (100−300 nM) do not appear to be toxic for living cells.

CONCLUSIONS

We demonstrated successful copper-free click reactions between NIR emissive DNA-Ag$_{16}$NCs and peptides of different sizes as well as a small protein. The described approach focused on the rational design of DNA-BCN-Ag$_{16}$NC, based on the addition of the BCN group at the 3′-end of the original sequence. As proven by the mass spectrometry data, the presence of the linkers does not affect the formation of DNA-Ag$_{16}$NC, and the photophysical properties remain unaltered. The conjugated compounds were analyzed by MS, HPLC, and time-resolved anisotropy measurements. As shown for the human insulin adduct, we

were able to image CHO cells with DNA-Ag$_{16}$NCs by achieving good and specific staining of the membranes. Control experiments excluded the possibility of nonspecific binding. Furthermore, spectral and lifetime measurements confirmed that the spectroscopic properties of DNA-Ag$_{16}$NCs were preserved in biologically relevant environments.

The described site-specific conjugation of DNA-AgNCs via SPAAC is a promising approach to generate fluorescent labels from DNA-AgNCs once their structures become available. This avoids tedious testing of the DNA sequence positions in order to find a suitable nucleobase where the linker can be attached. Particularly, the DNA-AgNC should have at least a noninteracting nucleobase in the stabilizing DNA strand to make it suitable for the click reaction, while retaining the original photophysical properties. The proposed strategy can open up new application possibilities and hopefully stimulate other research groups to use this new class of emitters to address biologically relevant problems.

ASSOCIATED CONTENT

Supporting Information

The Supporting Information is available free of charge at https://pubs.acs.org/doi/10.1021/jacs.3c04768.

Material and Methods section, experimental details on the synthesis, LCMS, MS, HPLC purification and spectroscopic characterization, as well as staining procedure and confocal imaging. (PDF)

AUTHOR INFORMATION

Corresponding Author

Tom Vosch − *Department of Chemistry, University of Copenhagen, 2100 Copenhagen, Denmark;* orcid.org/0000-0001-5435-2181; Email: tom@chem.ku.dk

Authors

Vanessa Rück − *Department of Chemistry, University of Copenhagen, 2100 Copenhagen, Denmark;* orcid.org/0000-0002-7403-3118

Narendra K. Mishra − *Department of Chemistry, University of Copenhagen, 1871 Frederiksberg C, Denmark*

Kasper K. Sørensen − *Department of Chemistry, University of Copenhagen, 1871 Frederiksberg C, Denmark*

Mikkel B. Liisberg − *Department of Chemistry, University of Copenhagen, 2100 Copenhagen, Denmark;* orcid.org/0000-0001-7623-5453

Ane B. Sloth − *Department of Clinical Physiology and Nuclear Medicine, Copenhagen University Hospital − Rigshospitalet, 2100 Copenhagen, Denmark; Cluster for Molecular Imaging, Department of Biomedical Sciences, University of Copenhagen, 2200 Copenhagen, Denmark*

Cecilia Cerretani − *Department of Chemistry, University of Copenhagen, 2100 Copenhagen, Denmark;* orcid.org/0000-0002-3048-5438

Christian B. Mollerup − *Department of Forensic Medicine, University of Copenhagen, 2100 Copenhagen, Denmark;* orcid.org/0000-0001-8187-6474

Andreas Kjaer − *Department of Clinical Physiology and Nuclear Medicine, Copenhagen University Hospital − Rigshospitalet, 2100 Copenhagen, Denmark; Cluster for Molecular Imaging, Department of Biomedical Sciences, University of Copenhagen, 2200 Copenhagen, Denmark;* orcid.org/0000-0002-2706-5547

Chenguang Lou − *Department of Physics, Chemistry and Pharmacy, University of Southern Denmark, 5230 Odense M, Denmark;* orcid.org/0000-0002-9521-8285

Knud J. Jensen − *Department of Chemistry, University of Copenhagen, 1871 Frederiksberg C, Denmark;* orcid.org/0000-0003-3525-5452

Complete contact information is available at:
https://pubs.acs.org/10.1021/jacs.3c04768

Notes

The authors declare no competing financial interest.

■ REFERENCES

(1) Petty, J. T.; Zheng, J.; Hud, N. V.; Dickson, R. M. DNA-Templated Ag Nanocluster Formation. *J. Am. Chem. Soc.* **2004**, *126*, 5207−5212.

(2) Gonzàlez-Rosell, A.; Cerretani, C.; Mastracco, P.; Vosch, T.; Copp, S. M. Structure and luminescence of DNA-templated silver clusters. *Nanoscale Advances* **2021**, *3*, 1230−1260.

(3) Copp, S. M.; Gorovits, A.; Swasey, S. M.; Gudibandi, S.; Bogdanov, P.; Gwinn, E. G. Fluorescence color by data-driven design of genomic silver clusters. *ACS Nano* **2018**, *12*, 8240−8247.

(4) Copp, S. M.; Swasey, S. M.; Gorovits, A.; Bogdanov, P.; Gwinn, E. G. General Approach for Machine Learning-Aided Design of DNA-Stabilized Silver Clusters. *Chem. Mater.* **2020**, *32*, 430−437.

(5) Sharma, J.; Yeh, H.-C.; Yoo, H.; Werner, J. H.; Martinez, J. S. Silver nanocluster aptamers: in situ generation of intrinsically fluorescent recognition ligands for protein detection. *Chem. Commun.* **2011**, *47*, 2294−2296.

(6) Yeh, H.-C.; Sharma, J.; Han, J. J.; Martinez, J. S.; Werner, J. H. A DNA-Silver Nanocluster Probe That Fluoresces upon Hybridization. *Nano Lett.* **2010**, *10*, 3106−3110.

(7) Petty, J. T.; Giri, B.; Miller, I. C.; Nicholson, D. A.; Sergev, O. O.; Banks, T. M.; Story, S. P. Silver Clusters as Both Chromophoric Reporters and DNA Ligands. *Anal. Chem.* **2013**, *85*, 2183−2190.

(8) Latorre, A.; Somoza, A. DNA-Mediated Silver Nanoclusters: Synthesis, Properties and Applications. *ChemBioChem.* **2012**, *13*, 951−958.

(9) Gonzàlez-Rosell, A.; Guha, R.; Cerretani, C.; Rück, V.; Liisberg, M. B.; Katz, B. B.; Vosch, T.; Copp, S. M. DNA Stabilizes Eight-Electron Superatom Silver Nanoclusters with Broadband Down-conversion and Microsecond-Lived Luminescence. *J. Phys. Chem. Lett.* **2022**, *13*, 8305−8311.

(10) Zhang, Y.; He, C.; de La Harpe, K.; Goodwin, P. M.; Petty, J. T.; Kohler, B. A single nucleobase tunes nonradiative decay in a DNA-bound silver cluster. *J. Chem. Phys.* **2021**, *155*, 094305.

(11) Zhang, Y.; He, C.; Petty, J. T.; Kohler, B. Time-Resolved Vibrational Fingerprints for Two Silver Cluster-DNA Fluorophores. *J. Phys. Chem. Lett.* **2020**, *11*, 8958−8963.

(12) Petty, J. T.; Ganguly, M.; Yunus, A. I.; He, C.; Goodwin, P. M.; Lu, Y.-H.; Dickson, R. M. A DNA-Encapsulated Silver Cluster and the Roles of Its Nucleobase Ligands. *J. Phys. Chem. C* **2018**, *122*, 28382−28392.

(13) Cerretani, C.; Liisberg, M.; Rück, V.; Kondo, J.; Vosch, T. The effect of inosine on the spectroscopic properties and crystal structure of a NIR-emitting DNA-stabilized silver nanocluster. *Nanoscale Advances* **2022**, *4*, 3212−3217.

(14) Fleischer, B. C.; Petty, J. T.; Hsiang, J. C.; Dickson, R. M. Optically Activated Delayed Fluorescence. *J. Phys. Chem. Lett.* **2017**, *8*, 3536−3543.

(15) Krause, S.; Carro-Temboury, M. R.; Cerretani, C.; Vosch, T. Anti-Stokes fluorescence microscopy using direct and indirect dark state formation. *Chem. Commun.* **2018**, *54*, 4569−4572.

(16) Neacşu, V. A.; Cerretani, C.; Liisberg, M. B.; Swasey, S. M.; Gwinn, E. G.; Copp, S. M.; Vosch, T. Unusually large fluorescence quantum yield for a near-infrared emitting DNA-stabilized silver nanocluster. *Chem. Commun.* **2020**, *56*, 6384−6387.

(17) Choi, S.; Dickson, R. M.; Yu, J. Developing luminescent silver nanodots for biological applications. *Chem. Soc. Rev.* **2012**, *41*, 1867−1891.

(18) Antoku, Y.; Hotta, J. I.; Mizuno, H.; Dickson, R. M.; Hofkens, J.; Vosch, T. Transfection of living HeLa cells with fluorescent poly-cytosine encapsulated Ag nanoclusters. *Photochemical and Photobiological Sciences* **2010**, *9*, 716−721.

(19) Yu, J.; Choi, S.; Dickson, R. M. Shuttle-Based Fluorogenic Silver-Cluster Biolabels. *Angew. Chem., Int. Ed.* **2009**, *48*, 318−320.

(20) Richards, C. I.; Hsiang, J. C.; Senapati, D.; Patel, S.; Yu, J.; Vosch, T.; Dickson, R. M. Optically modulated fluorophores for selective fluorescence signal recovery. *J. Am. Chem. Soc.* **2009**, *131*, 4619−4621.

(21) Choi, S.; Yu, J.; Patel, S. A.; Tzeng, Y.-L.; Dickson, R. M. Tailoring silver nanodots for intracellular staining. *Photochemical & Photobiological Sciences* **2011**, *10*, 109−115.

(22) Cerretani, C.; Kanazawa, H.; Vosch, T.; Kondo, J. Crystal structure of a NIR-Emitting DNA-Stabilized Ag16 Nanocluster. *Angewandte Chemie - International Edition* **2019**, *58*, 17153−17157.

(23) Agard, N. J.; Prescher, J. A.; Bertozzi, C. R. A Strain-Promoted [3 + 2] Azide-Alkyne Cycloaddition for Covalent Modification of Biomolecules in Living Systems. *J. Am. Chem. Soc.* **2004**, *126*, 15046−15047.

(24) Kim, E.; Koo, H. Biomedical applications of copper-free click chemistry: in vitro, in vivo, and ex vivo. *Chemical Science* **2019**, *10*, 7835–7851.

(25) Dommerholt, J.; Schmidt, S.; Temming, R.; Hendriks, L. J. A.; Rutjes, F. P. J. T.; van Hest, J. C. M.; Lefeber, D. J.; Friedl, P.; van Delft, F. L. Readily Accessible Bicyclononynes for Bioorthogonal Labeling and Three-Dimensional Imaging of Living Cells. *Angew. Chem., Int. Ed.* **2010**, *49*, 9422–9425.

(26) Bogh, S. A.; Carro-Temboury, M. R.; Cerretani, C.; Swasey, S. M.; Copp, S. M.; Gwinn, E. G.; Vosch, T. Unusually large Stokes shift for a near-infrared emitting DNA-stabilized silver nanocluster. *Methods and Applications in Fluorescence* **2018**, *6*, 024004.

(27) Liisberg, M.; Krause, S.; Cerretani, C.; Vosch, T. Probing Emission of a DNA-Stabilized Silver Nanocluster from the Sub-Nanosecond to Millisecond Timescale in a Single Measurement. *Chemical Science* **2022**, *13*, 5582–5587.

(28) Lakowicz, J. R. *Principles of fluorescence spectroscopy*; Springer: 2006.

(29) Chen, J.; Kumar, A.; Cerretani, C.; Vosch, T.; Zigmantas, D.; Thyrhaug, E. Excited-State Dynamics in a DNA-Stabilized Ag16 Cluster with Near-Infrared Emission. *J. Phys. Chem. Lett.* **2023**, *14*, 4078–4083.

(30) East, A. K.; Lucero, M. Y.; Chan, J. New directions of activity-based sensing for in vivo NIR imaging. *Chemical Science* **2021**, *12*, 3393–3405.

(31) Wang, X.; Liisberg, M. B.; Nolt, G. L.; Fu, X.; Cerretani, C.; Li, L.; Johnson, L. A.; Vosch, T.; Richards, C. I. DNA-AgNC Loaded Liposomes for Measuring Cerebral Blood Flow Using Two-Photon Fluorescence Correlation Spectroscopy. *ACS Nano* **2023**, DOI: 10.1021/acsnano.3c04489.

(32) Cerretani, C.; Kondo, J.; Vosch, T. Removal of the A10 adenosine in a DNA-stabilized Ag16 nanocluster. *RSC Adv.* **2020**, *10*, 23854–23860.

(33) Vosch, T.; Antoku, Y.; Hsiang, J. C.; Richards, C. I.; Gonzalez, J. I.; Dickson, R. M. Strongly emissive individual DNA-encapsulated Ag nanoclusters as single-molecule fluorophores. *Proc. Natl. Acad. Sci. U.S.A.* **2007**, *104*, 12616–12621.

(34) Gwinn, E. G.; O'Neill, P.; Guerrero, A. J.; Bouwmeester, D.; Fygenson, D. K. Sequence-Dependent Fluorescence of DNA-Hosted Silver Nanoclusters. *Adv. Mater.* **2008**, *20*, 279–283.

(35) Gonzàlez-Rosell, A.; Malola, S.; Guha, R.; Arevalos, N. R.; Rafik, M.; Matus, M. F.; Goulet, M. E.; Haapaniemi, E.; Katz, B. B.; Vosch, T.; Kondo, J.; Häkkinen, H.; Copp, S. M. Chloride ligands on DNA-stabilized silver nanoclusters. *J. Am. Chem. Soc.* **2023**, *145*, 10721–10729.

(36) Fang, G.; Bi, X. Silver-catalysed reactions of alkynes: recent advances. *Chem. Soc. Rev.* **2015**, *44*, 8124–8173.

(37) Beck-Sickinger, A. G.; Jung, G. Structure-activity relationships of neuropeptide Y analogues with respect to Y1 and Y2 receptors. *Biopolymers* **1995**, *37*, 123–142.

(38) Lou, C.; Boesen, J. T.; Christensen, N. J.; Sørensen, K. K.; Thulstrup, P. W.; Pedersen, M. N.; Giralt, E.; Jensen, K. J.; Wengel, J. Self-Assembly of DNA-Peptide Supermolecules: Coiled-Coil Peptide Structures Templated by d-DNA and l-DNA Triplexes Exhibit Chirality-Independent but Orientation-Dependent Stabilizing Cooperativity. *Chem.—Eur. J.* **2020**, *26*, 5676–5684.

(39) Ljubetic, A.; Lapenta, F.; Gradisar, H.; Drobnak, I.; Aupic, J.; Strmsek, Z.; Lainscek, D.; Hafner-Bratkovic, I.; Majerle, A.; Krivec, N.; Bencina, M.; Pisanski, T.; Velickovic, T. C.; Round, A.; Carazo, J. M.; Melero, R.; Jerala, R. Design of coiled-coil protein-origami cages that self-assemble in vitro and in vivo. *Nat. Biotechnol.* **2017**, *35*, 1094–1101.

(40) Østergaard, M.; Mishra, N. K.; Jensen, K. J. The ABC of Insulin: The Organic Chemistry of a Small Protein. *Chem.—Eur. J.* **2020**, *26*, 8341–8357.

(41) Wang, P.; Wang, X.; Liu, L.; Zhao, H.; Qi, W.; He, M. The Hydration Shell of Monomeric and Dimeric Insulin Studied by Terahertz Time-Domain Spectroscopy. *Biophys. J.* **2019**, *117*, 533–541.

(42) Mannerstedt, K.; Mishra, N. K.; Engholm, E.; Lundh, M.; Madsen, C. S.; Pedersen, P. J.; Le-Huu, P.; Pedersen, S. L.; Buch-Månson, N.; Borgström, B.; Brimert, T.; Fink, L. N.; Fosgerau, K.; Vrang, N.; Jensen, K. J. An Aldehyde Responsive, Cleavable Linker for Glucose Responsive Insulins. *Chem.—Eur. J.* **2021**, *27*, 3166–3176.

(43) Ghosh, S.; Chattoraj, S.; Bhattacharyya, K. Solvation Dynamics and Intermittent Oscillation of Cell Membrane: Live Chinese Hamster Ovary Cell. *J. Phys. Chem. B* **2014**, *118*, 2949–2956.

Supporting Information

Bioconjugation of a Near-Infrared DNA-Stabilized Silver Nanocluster to Peptides and Human Insulin by Copper-Free Click Chemistry

Vanessa Rück,[a] Narendra K. Mishra,[b] Kasper K. Sørensen,[b] Mikkel B. Liisberg,[a] Ane B. Sloth,[c,d] Cecilia Cerretani,[a] Christian B. Mollerup,[e] Andreas Kjaer,[c,d] Chenguang Lou,[f] Knud J. Jensen,[b] and Tom Vosch[a,*]

a. Department of Chemistry, University of Copenhagen, Universitetsparken 5, 2100 Copenhagen, Denmark.
b. Department of Chemistry, University of Copenhagen, Thorvaldsensvej 40, 1871 Frederiksberg C, Denmark.
c. Department of Clinical Physiology and Nuclear Medicine, Copenhagen University Hospital – Rigshospitalet, Blegdamsvej 9, 2100 Copenhagen, Denmark.
d. Cluster for Molecular Imaging, Department of Biomedical Sciences, University of Copenhagen, Blegdamsvej 3B, 2200 Copenhagen, Denmark.
e. Department of Forensic Medicine, University of Copenhagen, Frederik V's Vej 11, 2100 Copenhagen, Denmark.
f. Department of Physics, Chemistry and Pharmacy, University of Southern Denmark, Campusvej 55, 5230 Odense M, Denmark.

Table of Contents

Graphical Content:

1. Materials and Liquid chromatography mass spectrometry (LCMS)

<u>Chemicals:</u>

All DNA oligomers as well as the nuclease-free water were purchased from Integrated DNA Technologies (IDT). Recombinant human insulin was bought from Thermo Fisher. BCN-NHS-ester, $AgNO_3$ ($\geq$ 99.998%), ammonium acetate (NH_4OAc, $\geq$ 98%), $NaBH_4$ ($\geq$ 99.99%) and all other chemicals were purchased from Sigma-Aldrich and used as received without further purification. MilliQ water was used for aqueous preparations.

TentaGel R 0.18 mmol/g was purchased from Rapp Polymere GmbH. All L and D amino acids (Iris Biotech GmbH) were Nα-Fmoc protected and with the following side-chain protection groups: tert-butyl ether for serine, tyrosine and threonine; tert-butyl ester for aspartic acid and glutamic acid; trityl for asparagine and glutamine; 2,2,4,6,7-pentamethyldihydrobenzofuran-5-sulfonyl for arginine; and tert-butyloxycarbonyl for lysine. Azido-hexanoic acid and azidoacetic acid were purchased from Merck Life Science.

N,N-dimethylformamide (DMF) , N-methylpyrrolidone (NMP), N-[(1H-benzotriazol-1-yl)(dimethylamino) methylene]-N-methylmethanaminium hexafluorophosphate N-oxide (HBTU), 1-Hydroxy-7-azabenzotriazole (HOAt), trifluoroacetic acid (TFA), piperidine and N,N-diisopropylethylamine (DIPEA) were bought from Iris Biotech GmbH; while acetonitrile, formic acid, triethylsilane (TES), and dichloromethane (DCM) were purchased from Honeywell.

<u>LCMS:</u>

The DNA-BCN (compound **3**), DNA-stabilized silver nanocluster (DNA-BCN-Ag$_{16}$NC, compound **4**), purified peptides (compounds **5-7**), human insulin (compound **8**) and bioconjugates (compounds **9-12**) were analyzed by ultra-high pressure liquid chromatography mass spectrometry (UHPLC-MS). This was done by using a rapid separation liquid chromatography (RSLC) Dionex Ultimate 3000 instrument (Thermo Scientific) coupled to an Impact HD quadrupole time of flight mass spectrometer (QTOF). The ionization conditions were as follows: positive mode, end plate offset 500 V/841 nA, capillary 3500 V/2509 nA, nebulizer 2.2 bar, dry gas (N_2) 10 L/min, dry temperature 220 ˚C, hexapole 40.5 V, quadrupole 35.5 V.

A kinetex C18 column (EVO, 2.6 μm, 100 Å, 50 × 2.1 mm, Phenomenex) was used for compounds **3** and **5-7**, whereas an Aeris C4 column (3.6 μm, widepore, 200 Å, 50 × 2.1 mm, Phenomenex) was used for compounds **4** and **8-12**. All analyses were performed with a flow rate of 0.4 mL/min. The elution gradient was a mixture of 0.1 % formic acid in MilliQ H_2O (A) and acetonitrile (B); and was varied as follows: 0-1 min 5 % B, 1-5 min increase from 5 % to 100 % B, 5-6 min 100 % B, 6-6.2 min 100 % to 5 % B and finally 6.2-7.5 min 5 % B.

For compounds **4** and **9-12**, it was not possible to observe the corresponding molecular ion peaks in the mass spectra, but the DNA-BCN strand and the conjugates could be detected, respectively, with one or more silver cations attached. Compound **4** was further analyzed by mass spectrometry with different ionization conditions in order to observe the molecular ion peak.

2. Conjugation of DNA with BCN and synthesis of DNA-BCN-Ag$_{16}$NC

Conjugation of DNA with (1R,8S,9s)-Bicyclo[6.1.0]non-4-yn-9-ylmethyl N-succinimidyl carbonate (BCN):

In a typical reaction, 1 eq. of amino-modified DNA (compound **1**, 3.93 µmol, 12.62 mg) was dissolved in 2 mL PBS buffer (pH 7.35) and then added to 10 eq. of BCN-NHS-ester (compound **2**, 39.3 µmol, 11.45 mg) dissolved in 2 mL acetonitrile, followed by 10 eq. of triethylamine (39.2 µmol, 4 µL). The total volume of the reaction mixture was 4.004 mL. The reaction was shaken for 24 hours at 500 rpm. The unreacted DNA oligomers and BCN-NHS-ester were removed by spin-filtration with nuclease-free water (5 times), using a 3 kDa cut-off filter. Finally, the product (compound **3**) was analyzed using LCMS, see Figure S1.

LCMS Details: Molecular formula of DNA-BCN: $C_{113}H_{148}N_{40}O_{63}P_{10}$
Molecular weight [M]: 3384.38 g/mol
Observed: $[M+2H]^{2+}$: 1692.83, $[M+3H]^{3+}$: 1128.88, $[M+4H]^{4+}$: 846.91
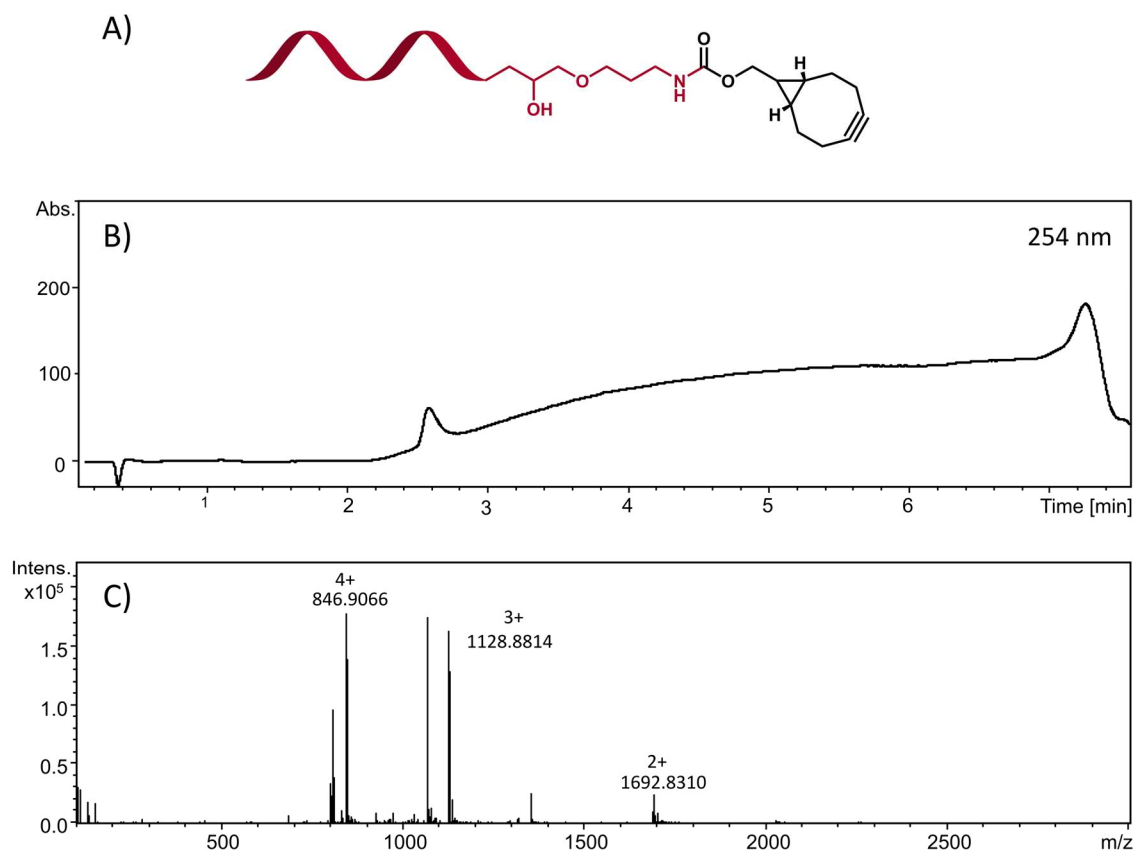
Figure S1: (A) Schematic representation of the structure, (B) LCMS chromatogram and (C) mass spectrum of DNA-BCN (compound **3**) after purification. Absorption is given in mOD.

Synthesis and HPLC purification of DNA-BCN-Ag$_{16}$NC:

Hydrated DNA oligonucleotide functionalized with BCN (compound **3**) was mixed with AgNO$_3$ in 10 mM NH$_4$OAc solution (pH = 7.0). Freshly prepared NaBH$_4$ was added to the solution after 15 minutes in order to reduce the silver cations and promote the formation of silver clusters. The optimal ratio between the components was [DNA]:[AgNO$_3$]:[NaBH$_4$] = 25 µM: 187.5 µM: 93.75 µM, based on a previously published protocol.[1] After synthesis, the sample was stored in the fridge for 1-3 days prior to high-performance liquid chromatography (HPLC) purification. In the end, the purified fraction was solvent exchanged to 10 mM NH$_4$OAc by spin-filtration with 3 kDa cut-off membrane filters to ensure good stability of DNA-BCN-Ag$_{16}$NCs over time.

The HPLC purification of compound **4** was performed using a preparative HPLC system from Agilent Technologies with an Agilent Technologies 1260 Infinity fluorescence detector, an Agilent Technologies 1100 Series UV-Vis detector, and an Aeris C4 column (3.6 µm, widepore, 200 Å, 50 x 2.1 mm, Phenomenex). The mobile phase was a gradient mixture of 35 mM triethylammonium acetate (TEAA) buffer in MilliQ water (A) and methanol (B). The flow rate was set to 1 mL/min. The elution gradient ranged from 5 % to 75 % B in 16 minutes. In the first 2 minutes, the concentration of B was kept constant at 5 % and then linearly increased to 75 % B in 14 minutes (ΔB = 5 % B/min). Afterwards, the gradient was increased to 95 % for 2 minutes and kept at the same percentage for two more minutes. Finally, the gradient was rapidly decreased to 5 % B within 2 minutes and kept constant for two more minutes. The collection was based on the absorbance at 530 nm. As shown in the chromatograms in Figure S2, the retention time of the pure fraction is around 12.3 minutes (≈ 56 % B). Therefore, a fraction between 11.5 to 13 minutes was collected. The detailed HPLC method and detector configurations are summed up in Table S1.

The concentration of the pure compound **4** was determined based on the DNA absorption peak since the molar extinction coefficient of compound **4** is not known. Based on the crystal structure of DNA-Ag$_{16}$NC, two DNA strands stabilize the Ag$_{16}$NC.[2] Therefore the DNA-Ag$_{16}$NC concentration is always half of that of DNA, which is the value reported in the sections below. In addition, the DNA-BCN-Ag$_{16}$NC has a larger absorption at 260 nm with respect to the DNA-Ag$_{16}$NC, because the BCN group absorbs at this wavelength. As a result of this, there is some uncertainty on the estimated concentration of the DNA-BCN-Ag$_{16}$NC.

*Table S1: HPLC method and configuration of UV-Vis (DADs) and fluorescence (FLD) detectors for DNA-BCN-Ag$_{16}$NC (compound **4**).*

Time (min)	Solvent B	Detectors	
0-2	5 %	DAD$_1$: 530 nm	FLD$_1$: 730 nm
2-16	5-75 %	DAD$_2$: 450 nm	(λ_{exc}= 530 nm)
16-18	75-95 %	DAD$_3$: 260 nm	
18-20	95 %		
20-22	95-5 %		
22-25	5 %		
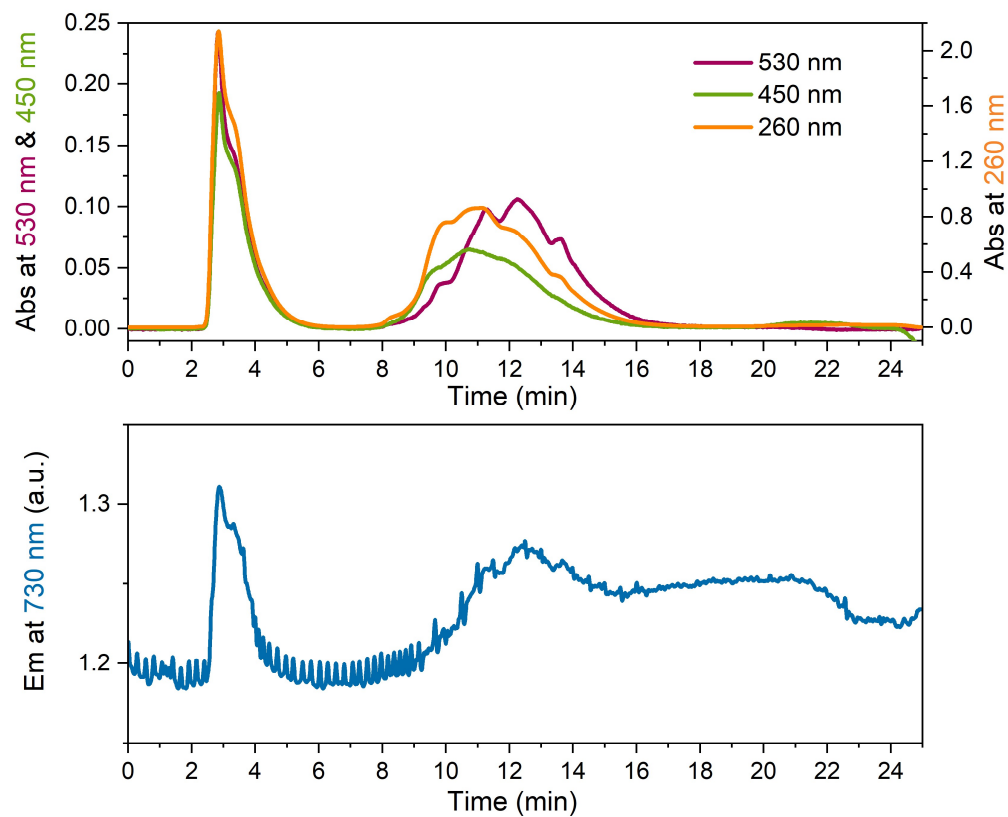
*Figure S2: HPLC chromatograms of DNA-BCN-Ag$_{16}$NCs (compound **4**) monitoring the absorption at 530 nm, 450 nm and 260 nm, and the fluorescence signal at 730 nm (exciting at 530 nm).*

LCMS of DNA-BCN-Ag$_{16}$NC:
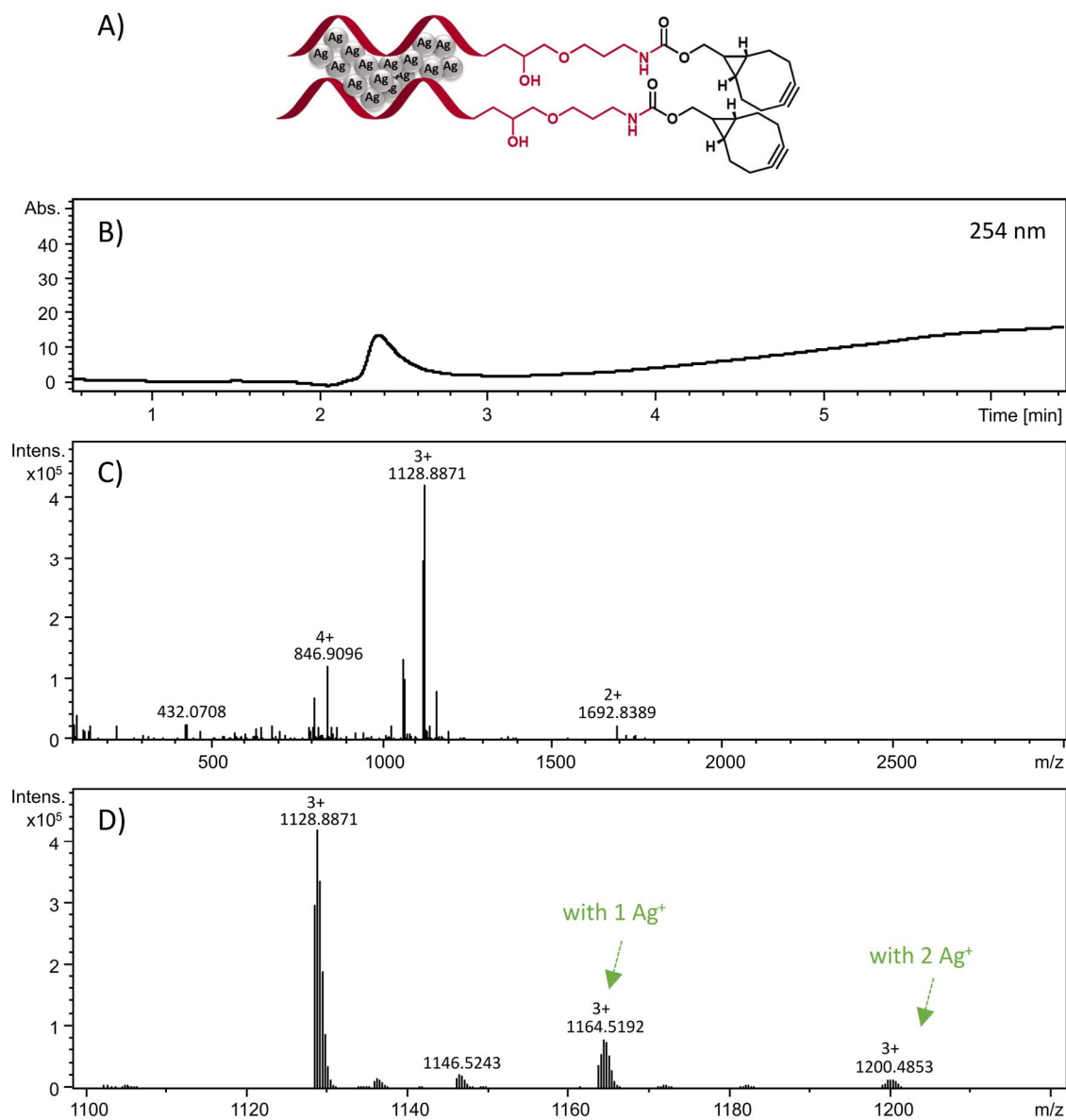
Figure S3: (A) Schematic representation, (B) LCMS chromatogram and (C) mass spectrum of compound **4**. Because of fragmentation, the molecular ion peak could not be observed. (D) Zoomed-in view of mass spectrum of compound **4** highlighting m/z peaks with one or two silver ions after fragmentation. Absorption is given in mOD.

LCMS Details: Molecular formula of DNA-BCN: $C_{113}H_{148}N_{40}O_{63}P_{10}$
Molecular weight [M]: 3384.38 g/mol
Observed: $[M+2H]^{2+}$: 1692.84, $[M+3H]^{3+}$: 1128.89, $[M+4H]^{4+}$: 846.91
$[M+2H+Ag]^{3+}$: 1164.52, $[M+1H+2Ag]^{3+}$: 1200.49

Mass spectrometry

Additional ESI-MS measurements were performed with a Xevo G2-XS QTof (Waters Corporation, Milford, MA, USA), using negative ion mode with a 2 kV capillary voltage, 30 V cone voltage and no collision energy. Spectra were collected from 1000 to 4000 m/z, and with a scan time of 1 second. Source temperature was 80 °C with a cone gas flow of 45 L/h, and the desolvation temperature and gas flow were 150 °C and 450 L/h, respectively. The QTOF was calibrated using ESI-L Low Tune Mix (Agilent Technologies, Santa Clara, CA, USA), which contained compounds in the mass range of 1034 to 2834 m/z. All samples were injected using an Acquity I-Class Plus system (Waters) with a flow-through needle autosampler, with a flow of 0.1 mL/min 50 mM NH_4OAc buffer at pH 7 – MeOH (80:20) and using 5 µL injection volume. The system was operated using UNIFI v.1.9.4 (Waters), and the final spectra were generated by averaging multiple spectra surrounding the apex of the observed peak.

The recorded data were analyzed and fitted with the open-source software EnviPat Web[3] (https://www.envipat.eawag.ch/index.php).

Detailed MS investigation of DNA-BCN-Ag$_{16}$NC:

The mass spectrum reported in Figure 2B shows fragments of DNA-BCN-AgNC up to around 1650 m/z and a few molecular ion peaks corresponding to the DNA-BCN-AgNC with different numbers of Ag atoms. The two peaks centered at 1710.89 m/z and 2138.90 m/z are related to the adduct with 16 silvers and 5^- and 4^- charge states, respectively. These peaks are approximately 2 amu off compared to the expected mass, indicating potential hydrogenation of the triple bond of the BCN group. Additionally, adducts with 17 and even 18 silvers are more common than the dominant 16-silver complex observed for DNA-Ag$_{16}$NC. These two findings lead to the conclusion that there are additional silver cations bound to the triple bond of the BCN group prior to mass spectrometry measurements. A detailed explanation is provided below.

In order to check that the chosen mass spectrometry method was suitable, the mass spectrum of DNA-Ag$_{16}$NC alone was measured in negative ion mode. Figure S4A shows two main peaks centered at 1555.55 m/z and 1944.68 m/z, which are related to 5^- and 4^- charge states, respectively. These peaks match the isotopic distribution of the $(DNA)_2Ag_{16}Cl_2$ reported by Gonzàlez-Rosell *et al.*[4] with a total nanocluster charge of 8^+ that corresponds to 6 reduced silvers.[4] This means that direct injection of DNA-Ag$_{16}$NC in the ESI-MS yields the expected molecular mass and oxidation state.
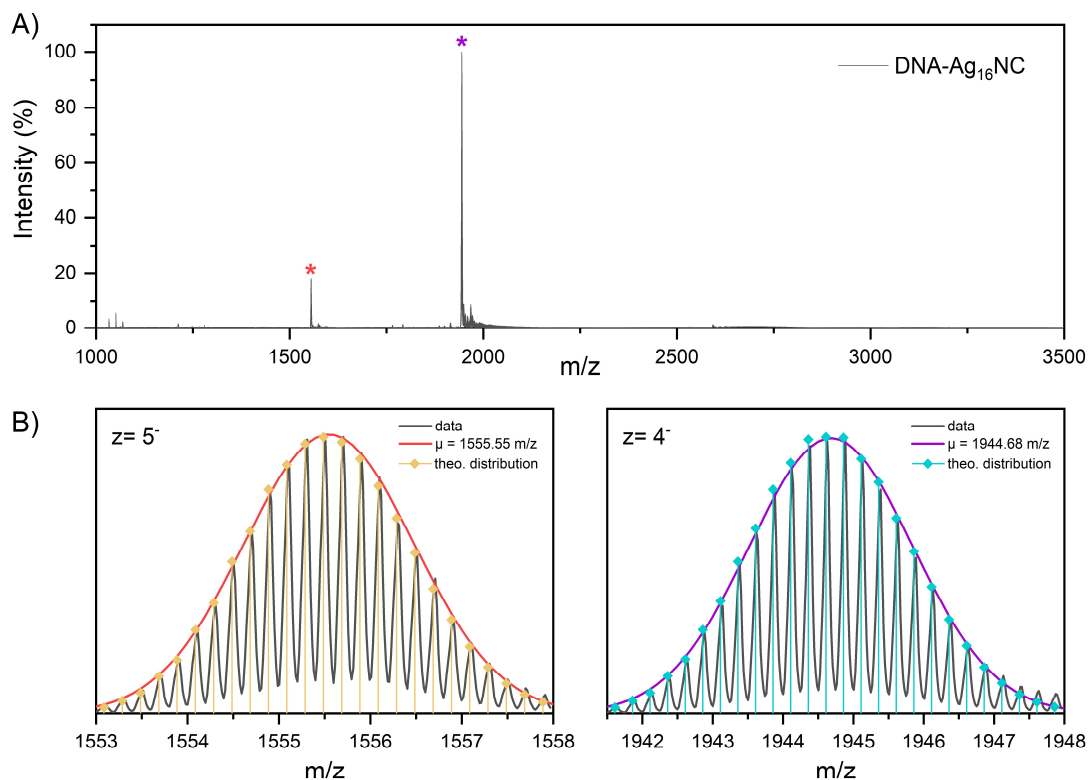
Figure S4: (A) Mass spectrum of DNA-Ag$_{16}$NC measured in negative ion mode. The red and purple stars indicate the peaks related to (DNA)$_2$[Ag$_{16}$Cl$_2$]$^{8+}$ with 5$^-$ and 4$^-$ charge states, respectively. (B) Zoomed-in views of the marked peaks in the mass spectrum for z= 5$^-$ and 4$^-$, together with the corresponding theoretical isotopic distributions for the reported average masses.

However, the mass spectrometry data of DNA-BCN-Ag$_{16}$NC seems to be approximately 2 amu off compared to the predicted molecular mass. As can be seen in Figure 2B-C, as well as Figures S5 and S6, the peaks corresponding to z= 5$^-$ and z= 4$^-$ for the complexes with 16 and 17 silvers, could be best fitted to molecular masses that amount to the expected masses with 2 additional amu. The most plausible explanation is that there are, on average, two extra hydrogens due to the reduction (hydrogenation) of the triple bond of the BCN group. While at first glance this looks problematic and might indicate that some of the triple bonds are indeed double bonds, a detailed investigation uncovered that this was the result of the direct injection of the sample in the MS instrument and the presence of Ag$^+$ cations coordinated to the BCN triple bond. It seems that this combination causes the hydrogenation of the triple bond in the MS instrument.
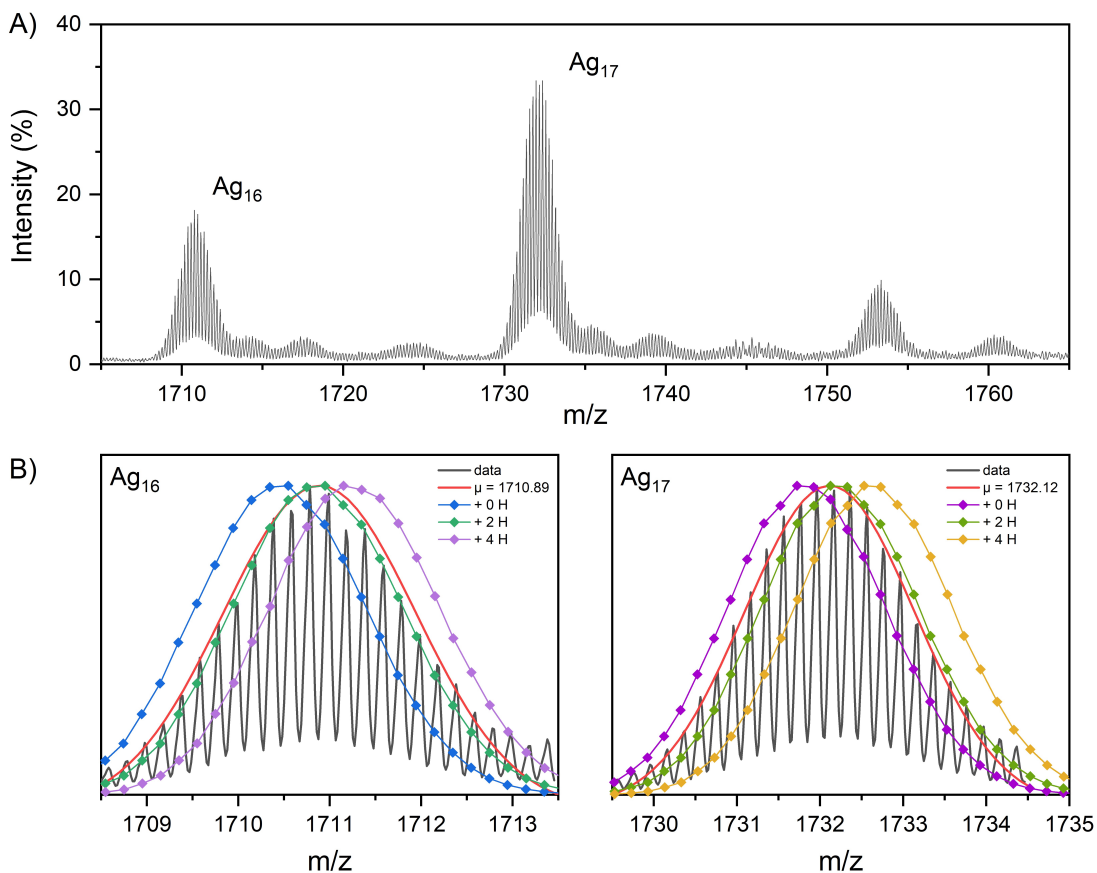
*Figure S5: (A) Zoomed-in view of the z= 5⁻ peaks reported in Figure 2B for compound **4**. (B) Experimental isotopic distributions of (DNA-BCN)₂[Ag₁₆Cl₂]⁸⁺and (DNA-BCN)₂[Ag₁₇Cl₂]⁹⁺ with the corresponding Gaussian fits (solid red) and the theoretical isotopic distributions in the absence of additional hydrogen atoms and with two and four extra hydrogens.*

MS Details:

(DNA-BCN)₂**Ag₁₆**Cl₂: Molecular formula: $C_{226}H_{296}Ag_{16}Cl_2N_{80}O_{126}P_{20}$ → [M]: 8565.55 g/mol
Observed: $[M_{obs}]^{5-}$: 1710.89 → (DNA-BCN)₂[Ag₁₆Cl₂]⁸⁺ + ≈2H

(DNA-BCN)₂**Ag₁₇**Cl₂: Molecular formula: $C_{226}H_{296}Ag_{17}Cl_2N_{80}O_{126}P_{20}$ → [M]: 8673.42 g/mol
Observed: $[M_{obs}]^{5-}$: 1732.12 → (DNA-BCN)₂[Ag₁₇Cl₂]⁹⁺ + ≈2H
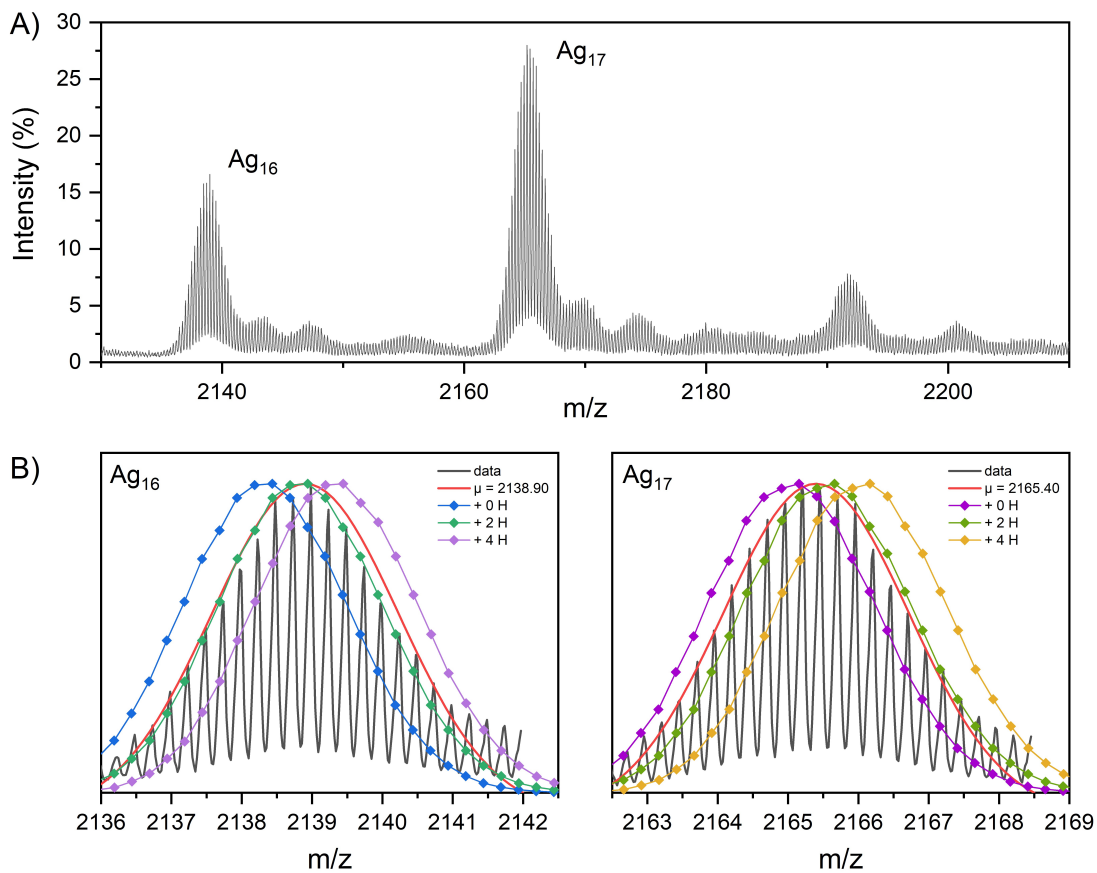
*Figure S6: (A) Zoomed-in view of the z= 4⁻ peaks reported in Figure 2B for compound **4**. (B) Experimental isotopic distributions of (DNA-BCN)₂[Ag₁₆Cl₂]⁸⁺and (DNA-BCN)₂[Ag₁₇Cl₂]⁹⁺ with the corresponding Gaussian fits (solid red) and the theoretical isotopic distributions in the absence of additional hydrogen atoms and with two and four extra hydrogens.*

MS Details:

(DNA-BCN)₂**Ag₁₆**Cl₂: Molecular formula: $C_{226}H_{296}Ag_{16}Cl_2N_{80}O_{126}P_{20}$ → [M]: 8565.55 g/mol
Observed: $[M_{obs}]^{4-}$: 2138.90 → (DNA-BCN)₂[Ag₁₆Cl₂]⁸⁺ + ≈2H

(DNA-BCN)₂**Ag₁₇**Cl₂: Molecular formula: $C_{226}H_{296}Ag_{17}Cl_2N_{80}O_{126}P_{20}$ → [M]: 8673.42 g/mol
Observed: $[M_{obs}]^{4-}$: 2165.40 → (DNA-BCN)₂[Ag₁₇Cl₂]⁹⁺ + ≈2H

First, we confirmed that the reduction was not caused by NaBH$_4$. This was done by adding NaBH$_4$ to the sole BCN-DNA (compound **3**) with the same ratio used for the synthesis of DNA-BCN-Ag$_{16}$NC. Figure S7 shows that the addition of NaBH$_4$ does not affect the triple bond since the same molecular ion peak is observed in the presence and absence of the reducing agent. This peak corresponds to the expected isotopic distribution of the BCN-DNA strand with intact/non-reduced BCN group.
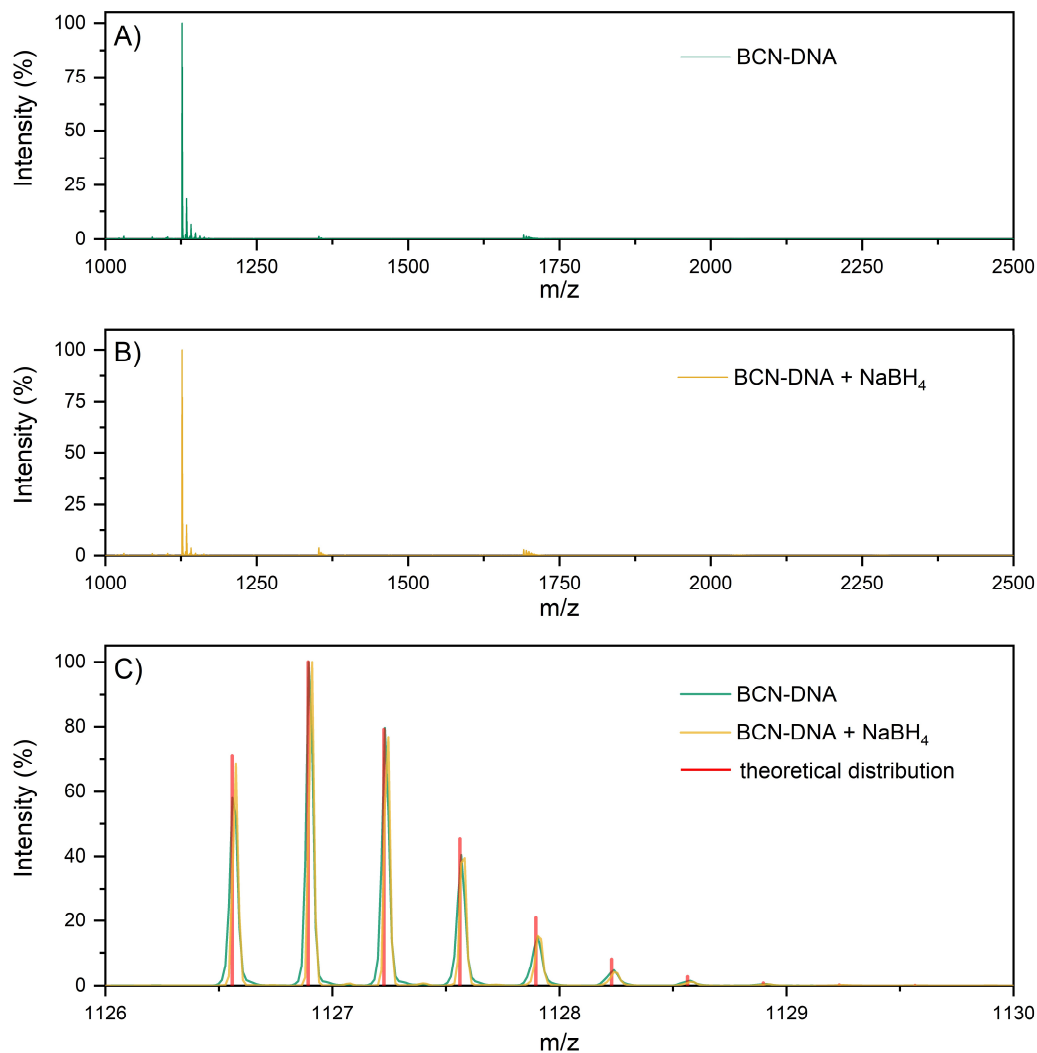
Figure S7: Mass spectra of (A) BCN-DNA and (B) BCN-DNA treated with NaBH$_4$ measured in negative ion mode with the ESI-MS instrument. (C) Overlay of the spectra in (A) and (B) together with the theoretical isotopic distribution. The peaks correspond to z= 3$^-$. The observed average mass is [M-3H]$^{3-}$= 1127.11 g/mol, which confirms that no reduction of the BCN group occurs.

On the other hand, addition of Ag^+ cations affect the integrity of the triple bonds when BCN-DNA is measured using direct injection in the LCMS instrument in positive ion mode. Figure S8 shows the mass spectra of the BCN-DNA alone (green) and with the addition of a small amount of $AgNO_3$ (yellow), along with the theoretical isotopic distributions of the BCN-DNA strand with intact (blue) and reduced (red) triple bond of the BCN group.
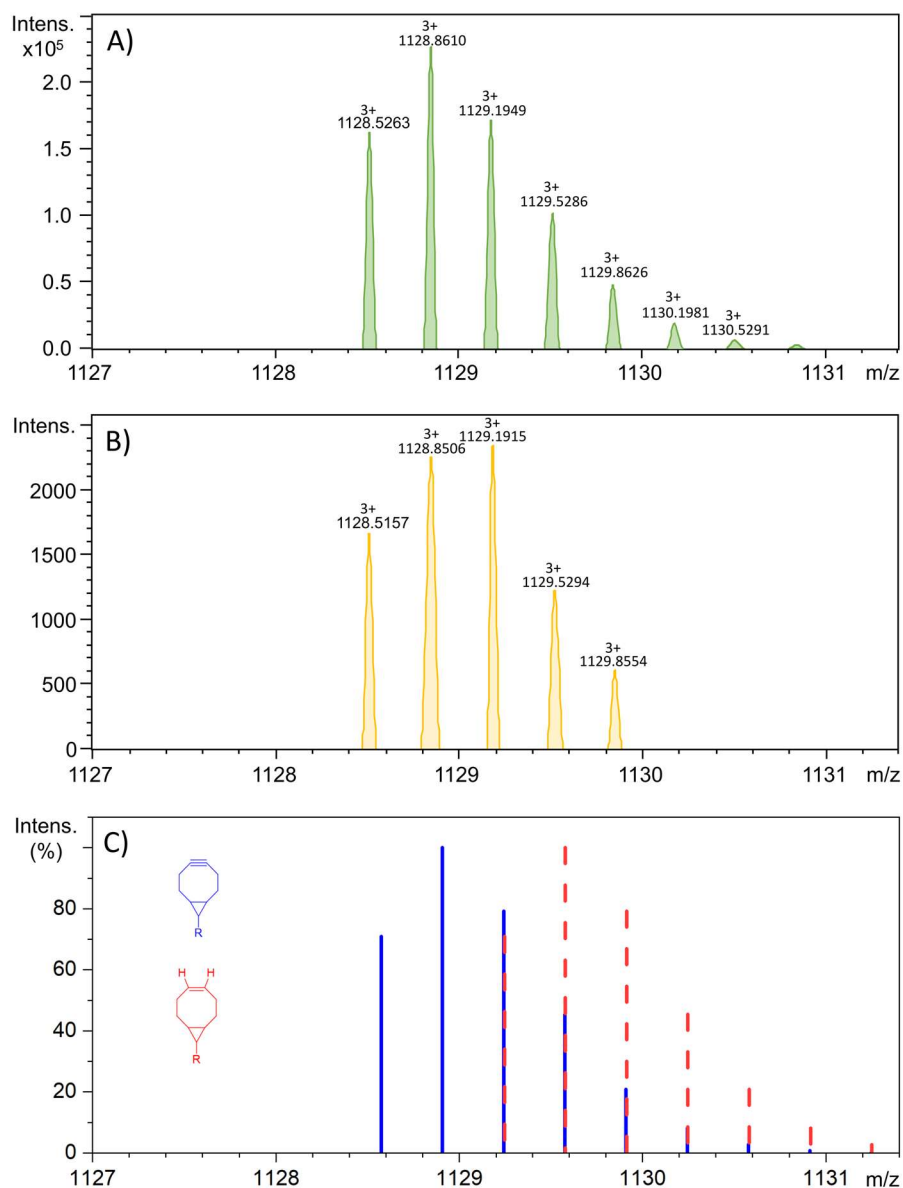
Figure S8: Mass spectra of (A) BCN-DNA and (B) BCN-DNA treated with AgNO₃ measured in positive ion mode, using the LCMS instrument described in section 1. The peaks correspond to z= 3⁺. (C) Theoretical isotopic distributions of the BCN-DNA strand with intact (blue) and reduced (red) triple bond of the BCN group.

The peak in Figure S8B has a different isotopic distribution, overall shifted to higher m/z, than that of Figure S8A for the intact BCN triple bond, thus one can deduce that the triple bonds are hydrogenated in the presence of silver cations upon direct injection.

That this reduction happens in the MS and that the BCN triple bond is intact in the original solution can be seen in the LCMS data in Figure S9. Figure S9A shows that when DNA-BCN-Ag$_{16}$NC was directly injected in the LCMS instrument, the peak related to the BCN-DNA fragment is characterized by an isotopic distribution corresponding to a partly hydrogenated triple bond. However, if DNA-BCN-Ag$_{16}$NC was first sent through a column (Figure S9B), where the LC solvents could wash off the extra silver cations, the BCN-DNA fragment peak displays the isotopic distribution of the non-reduced BCN triple bond. The latter proves that the DNA-BCN-Ag$_{16}$NC is unaltered in solution and that there are additional silver cations coordinated to the triple bond. This also explains why for DNA-Ag$_{16}$NC reported in Figure S4 and Gonzàlez-Rosell *et al.*[4] mainly an Ag$_{16}$ adduct is observed, while for DNA-BCN-AgNC in Figures 2B, S5 and S6, the dominant peak corresponds to the Ag$_{17}$ complex. It is worth noticing that the presence of Ag$^+$ bound to the triple bond might slow down the copper-free click reaction, but does not prevent the formation of the bioconjugates with the peptides and human insulin since the BCN triple bond stays intact. This can be clearly seen in the LCMS data reported in Figure 4 and below, where only single peaks of the desired products can be observed.
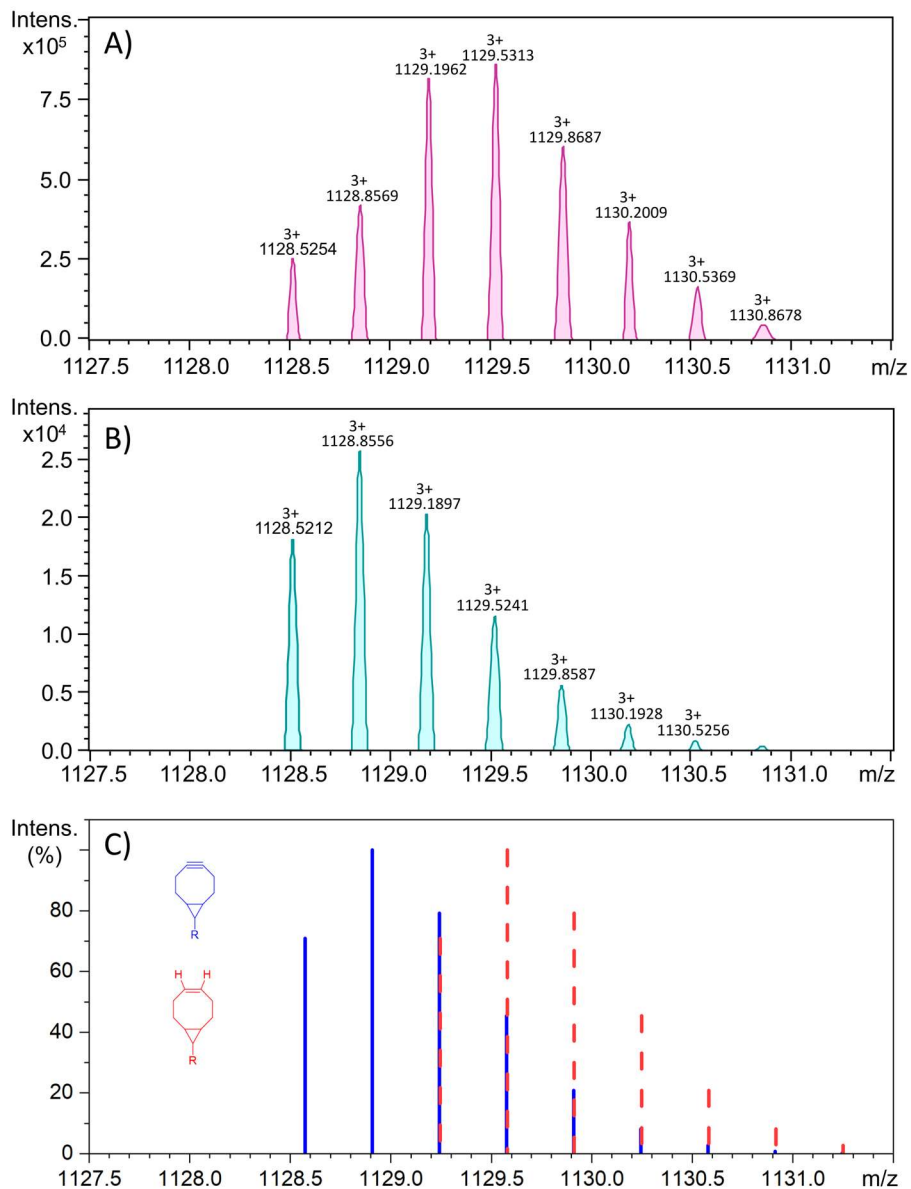
Figure S9: (A) and (B) Zoomed-in views of the mass spectra of DNA-BCN-Ag$_{16}$NC in the 1127.5 – 1131.5 m/z range, recorded in positive ion mode, using the LCMS instrument described in section 1. The peaks correspond to z= 3$^+$. (A) Peak related to the BCN-DNA fragment collected after direct injection of the sample in the LCMS instrument. (B) Peak corresponding to the BCN-DNA fragment collected after sending the sample first through the LC column, where the solvents could wash off the extra silver cations. (C) Theoretical isotopic distributions of the BCN-DNA strand with intact (blue) and reduced (red) triple bond of the BCN group.

3. Conjugation of DNA-BCN-Ag$_{16}$NC to peptides

Synthesis of azido-hexanoyl PYY-/coiled-coil-/d-peptides:

The peptides were synthesized using a Biotage® Initiator + Alstra™ microwave peptide synthesizer applying a standard protocol.[5] The deprotection of the first 20 amino acids was carried out first with piperidine-DMF (2:3) for 3 minutes, followed by piperidine-DMF (1:4) for 15 minutes. After each deprotection step, a washing procedure was performed twice with NMP and once with DCM, then the resin was washed with DMF at 70 °C for one minute. For the incorporation of the amino acids, the coupling was carried out at 75 °C for 10 minutes by using 5.2 eq. of Fmoc-amino acid, 5.2 eq. of HOAt, 5 eq. of HBTU, and 9.4 eq. of DIEA in NMP. After the coupling was done, the resin was washed twice with NMP.

From the 20th residue onwards the deprotection step with piperidine-DMF (1:4) lasted 25 minutes instead of 15 minutes. The coupling reaction was performed twice. Double coupling was also carried out for all arginines regardless of their placements.

After synthesis, the azido group was anchored at the N-terminal of the peptide. For coiled-coil peptide (BCRSN), the azido-propanoic acid was used, whereas azido-hexanoic acid was chosen for PYY- and d-peptide. The coupling was performed with 2 eq. of azido acid, 2 eq. of HOAt, 1.8 eq. of HBTU, and 3.8 eq. of DIEA in NMP per 1 eq. of peptide. The reaction was carried out at room temperature (RT) for 120 minutes. The latter reaction was repeated, and afterwards, the resin was washed three times with DMF and six times with DCM. Then the peptide was cleaved from the resin using 95 % TFA/ 3 % H$_2$O/ 2 % TES for 2 hours. Later, the TFA was removed under nitrogen flow. Finally, the peptide was precipitated with cold diethyl ether.

The product was isolated on a reversed-phase high-performance flash chromatography (RP-HPFC) Selekt system from Biotage, using a C18 column (SNAP Ultra C18 50 g, Biotage) and CH$_3$CN/H$_2$O with 0.1% formic acid as solvents. The elution consisted of a linear gradient of 5-50 % CH$_3$CN over 20 minutes, and the flow rate was set to 50 mL/min. The collected fractions were analyzed via LCMS in order to determine the purity, see Figures S10-S12. Finally, the purified fractions were lyophilized.

Note: PYY (3-36) is a metabolic hormone from the rat. Coiled-coil peptide originates from Bcr-Abl Oncoprotein. D-peptide is a designed coiled-coil peptide.

LCMS of azido-hexanoyl-PYY (3-36)-peptide:

A)

N$_3$—[structure]—K–P–E–A–P–G–E–D—A–S–P–E–E–L–S–R–Y–Y—A–S–L–R–H–Y–L–N–L–V—T–R–Q–R–Y—NH$_2$
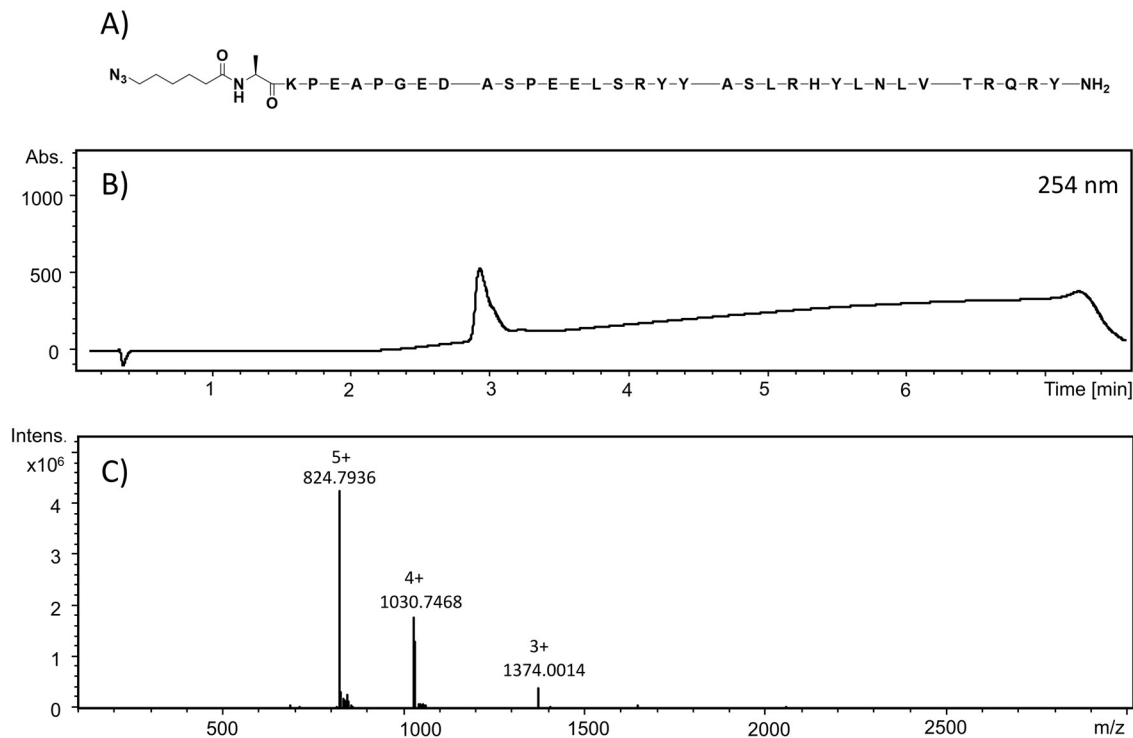
Figure S10: (A) Structure, (B) LCMS chromatogram and (C) mass spectrum of azido-hexanoyl-PYY (3-36)-peptide (compound **5**). Absorption is given in mOD.

LCMS Details: Molecular formula of azido-hexanoyl-PYY (3-36): C$_{182}$H$_{281}$N$_{55}$O$_{55}$
Molecular weight [M]: 4119.58 g/mol
Observed: [M+3H]$^{3+}$: 1374.00, [M+4H]$^{4+}$: 1030.75, [M+5H]$^{5+}$: 824.79

17

LCMS of azido-hexanoyl-d-peptide:
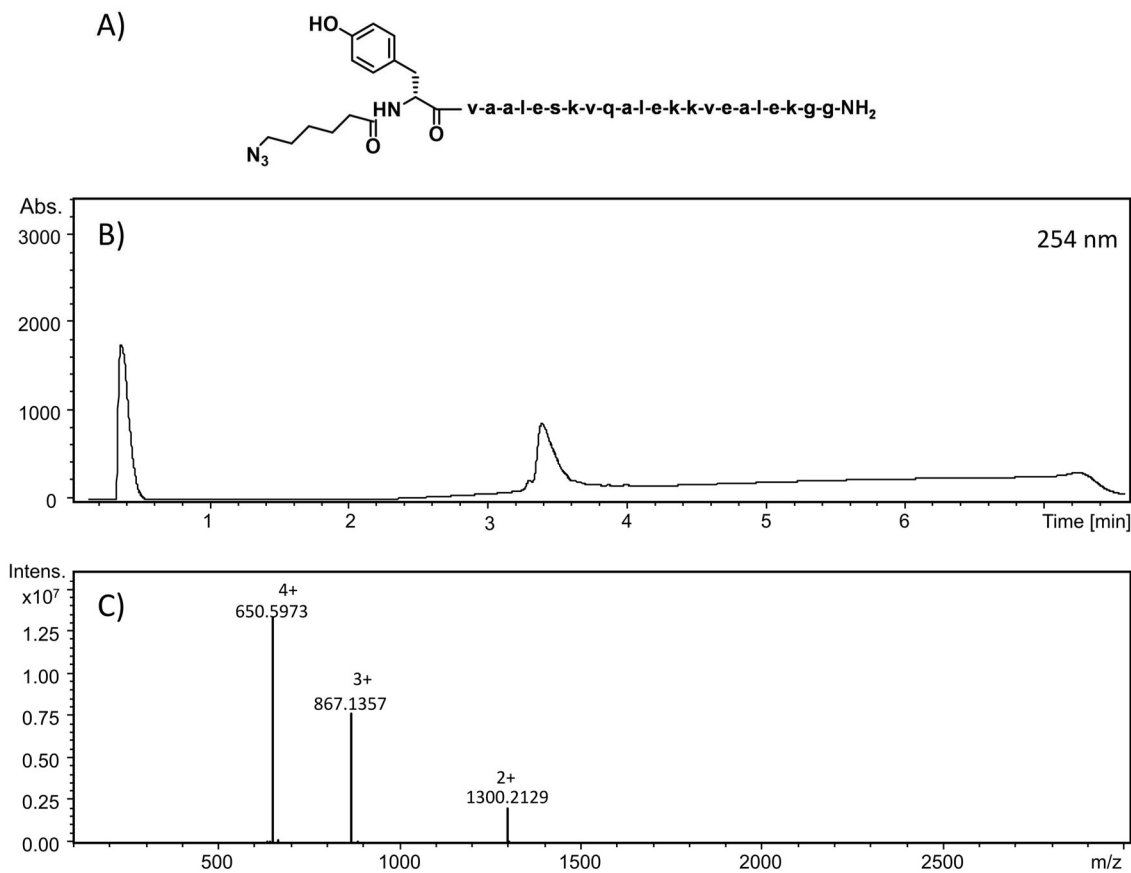
Figure S11: (A) Structure, (B) LCMS chromatogram and (C) mass spectrum of azido-hexanoyl-d-peptide (compound **6**). All amino acids have D configuration. Absorption is given in mOD.

LCMS Details: Molecular formula of azido-hexanoyl-d-peptide: $C_{116}H_{195}N_{31}O_{36}$
Molecular weight [M]: 2600.02 g/mol
Observed: $[M+2H]^{2+}$: 1300.21, $[M+3H]^{3+}$: 867.14, $[M+4H]^{4+}$: 650.60

LCMS of azido-propanoyl-coiled-coil-peptide:

A)

B)

C)
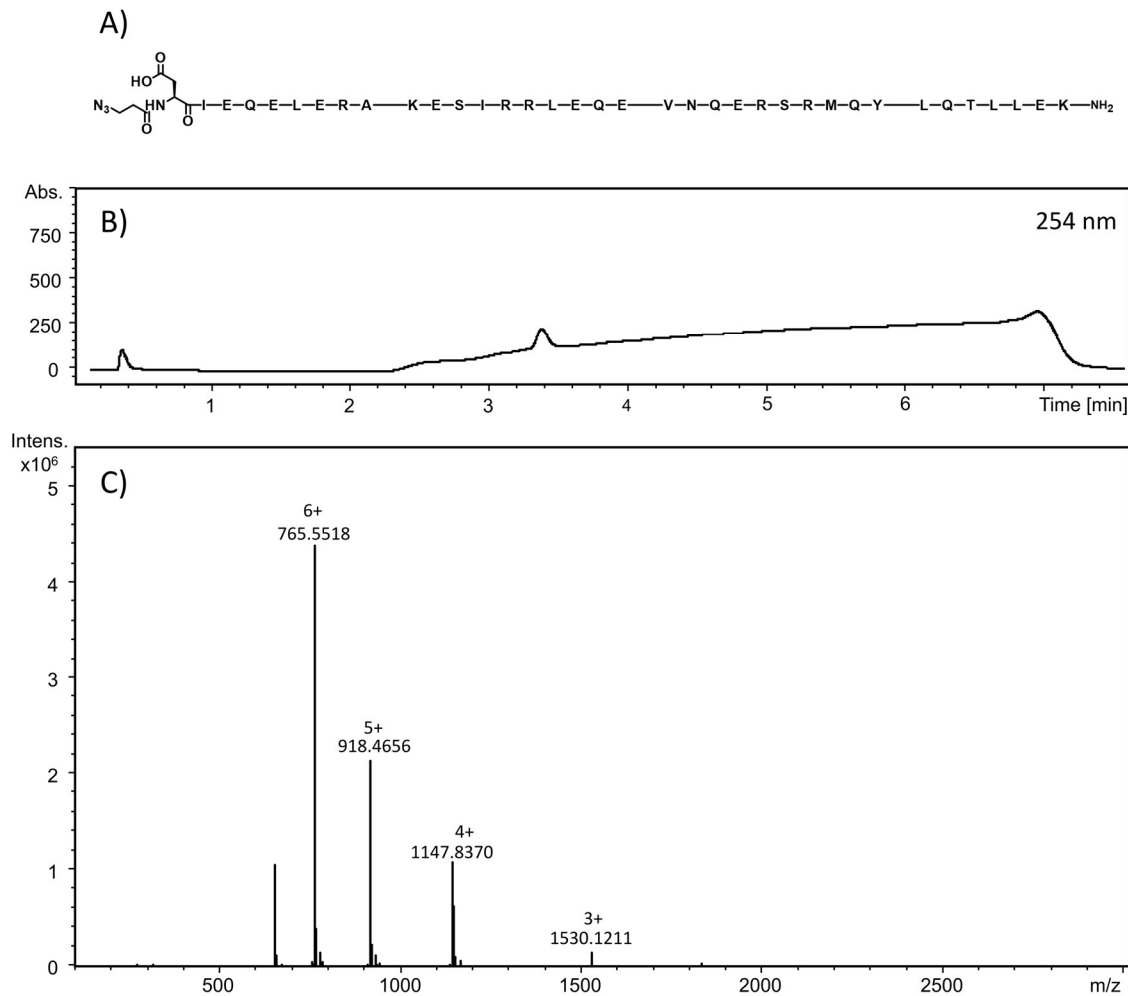
*Figure S12: (A) Structure, (B) LCMS chromatogram and (C) mass spectrum of azido-propanoyl-coiled-coil-peptide (compound **7**). Absorption is given in mOD.*

LCMS Details: Molecular formula of azido-propanoyl-coiled-coil-peptide: $C_{192}H_{322}N_{62}O_{66}S$
Molecular weight [M]: 4587.35 g/mol
Observed: $[M+3H]^{3+}$: 1530.12, $[M+4H]^{4+}$: 1147.84, $[M+5H]^{5+}$: 918.47, $[M+6H]^{6+}$: 765.55

Conjugation of DNA-BCN-Ag$_{16}$NC with PYY (3-36)-peptide:

An adequate amount of compound **4** (117.5 µM, 20 µL) was mixed with 18.4 µL of 163 µM PYY peptide (compound **5**) dissolved in MilliQ water. Then, MilliQ water was added to reach the final volume of 40 µL. The reaction mixture was shaken at 350 rpm for 48 hours at 18 °C. The reaction was monitored at different time intervals. After 48 hours the peptide was completely consumed, but a small amount of DNA-BCN-Ag$_{16}$NCs was still present, therefore further 10 µL of PYY (3-36) with a concentration of 163 µM were added. After 72 hours, the reaction mixture was purified 10 times using a 10 kDa cut-off membrane filter to remove any byproducts. LCMS analysis verified that the reaction was completed and the sample was pure. However, compound **9** fragmented during LCMS and only the mass of the DNA-BCN-PYY could be detected.

LCMS Details: Molecular formula of DNA-BCN-PYY (3-36): $C_{295}H_{429}N_{95}O_{118}P_{10}$
Molecular weight [M]: 7503.96 g/mol
Observed: $[M+4H]^{4+}$: 1876.90, $[M+5H]^{5+}$: 1501.51, $[M+6H]^{6+}$: 1251.42, $[M+7H]^{7+}$: 1072.79, $[M+10H]^{10+}$: 751.25
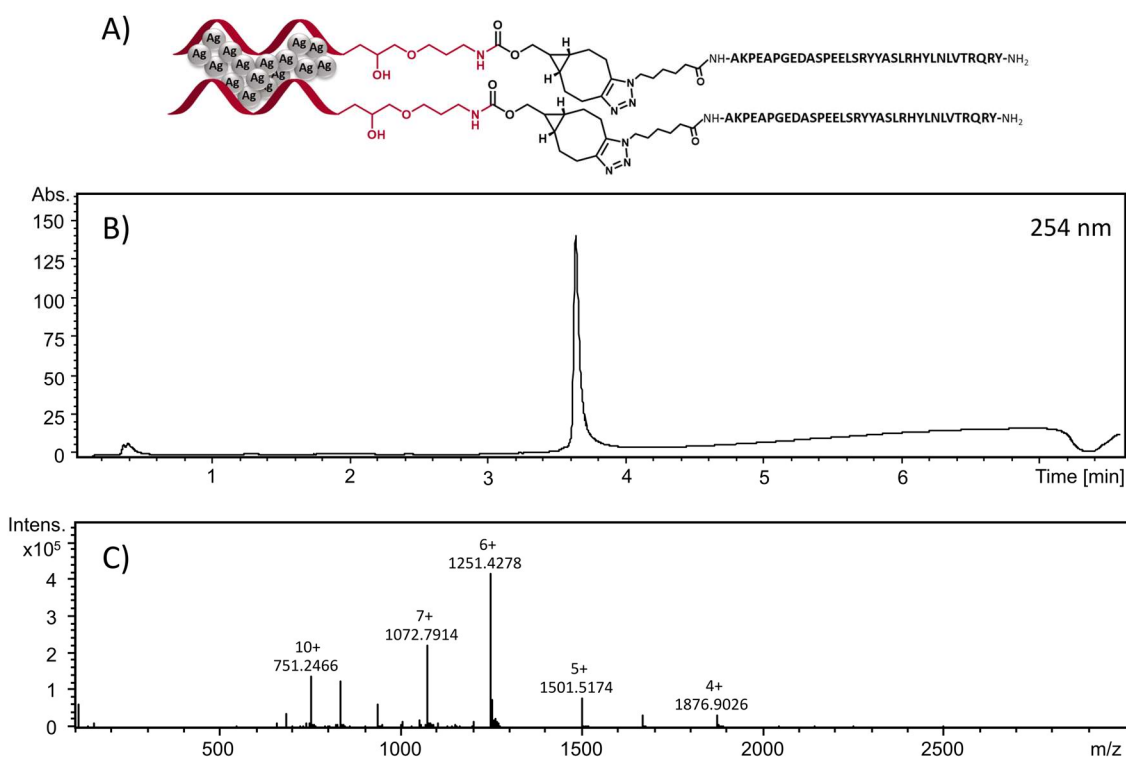
*Figure S13: (A) Schematic representation of the structure, (B) LCMS chromatogram, and (C) mass spectrum of compound **9**. Note that M corresponds to the DNA-BCN-PYY (3-36) fragment. Absorption is given in mOD.*

Conjugation of DNA-BCN-Ag$_{16}$NC with d-peptide:

9.0 μL of d-peptide (679 μM) dissolved in MilliQ water was mixed with 20 μL of compound **4** (117.5 μM). Later, MilliQ water was added to reach a final volume of 40 μL. The final concentrations of DNA-BCN-Ag$_{16}$NCs and d-peptide were 58.75 μM and 152.78 μM, respectively. The reaction mixture was shaken at 350 rpm for 72 hours at 18 °C. After 72 hours, the reaction mixture was spin-filtered 10 times using a 10 kDa cut-off membrane filter to get the pure product **10**. LCMS analysis confirmed that the reaction was completed and no byproducts were present, even though compound **10** fragmented during LCMS. Only the mass of the DNA-BCN-d-peptide could be observed.

LCMS Details: Molecular formula of DNA-BCN-d-peptide: C$_{229}$H$_{343}$N$_{71}$O$_{99}$P$_{10}$
Molecular weight [M]: 5984.399 g/mol
Observed: [M+3H]$^{3+}$: 1995.363, [M+4]$^{4+}$: 1496.770, [M+6H]$^{6+}$: 998.170
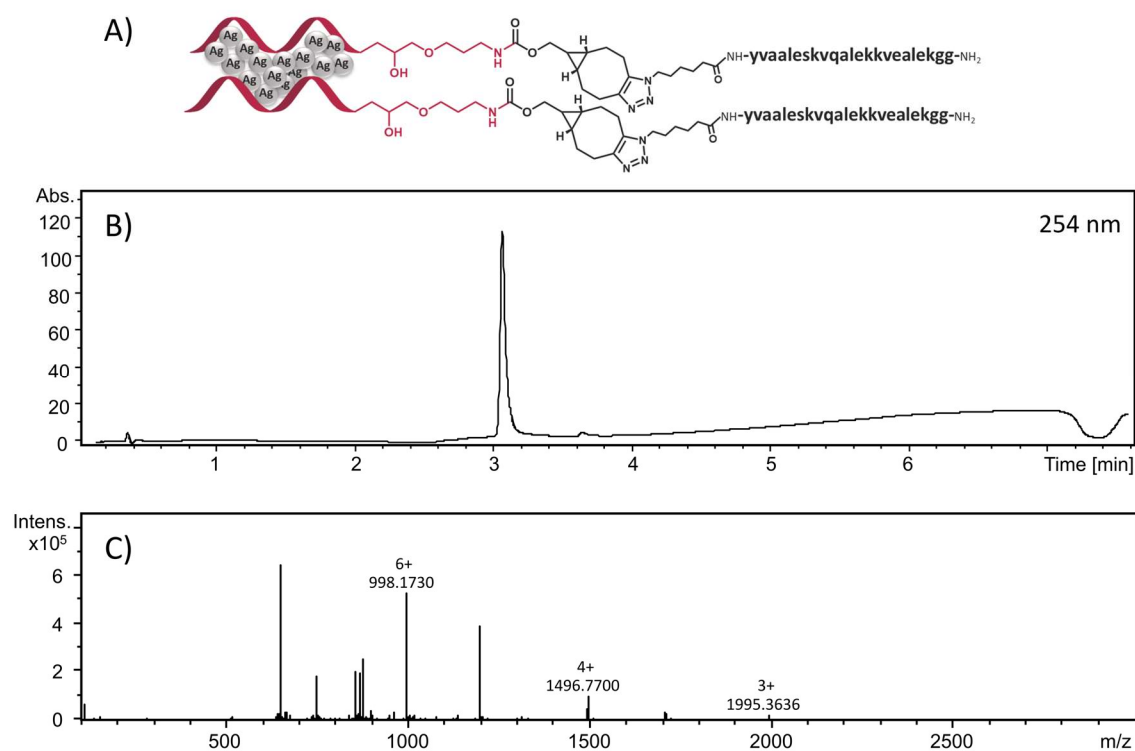
Figure S14: (A) Schematic representation of the structure, (B) LCMS chromatogram and (C) mass spectrum of compound **10**. Note that M represents the mass of the DNA-BCN-d-peptide fragment. Absorption is given in mOD.

Conjugation of DNA-BCN-Ag$_{16}$NC with coiled-coil peptide:

20 μL of compound **4** (117.50 μM) was mixed with 7.2 μL of coiled-coil peptide (414 μM) dissolved in MilliQ water. Afterwards, MilliQ water was added to achieve a final volume of 40 μL. The reaction mixture was shaken at 350 rpm for 72 hours at 18 °C. After 72 hours, the reaction mixture was purified 10 times using a 10 kDa cut-off membrane filter to get the pure product **11**. LCMS analysis confirmed that the reaction was completed and the sample was pure. However, compound **11** fragmented during LCMS, and only the mass of DNA-BCN-coiled-coil-peptide was detected.

LCMS Details: Molecular Formula of DNA-BCN-Coiled-coil-peptide: C$_{305}$H$_{470}$N$_{102}$O$_{129}$P$_{10}$S
Molecular weight [M]: 7971.50 g/mol

Observed: [M+4H]$^{4+}$: 1994.01, [M+5H]$^{5+}$: 1595.40, [M+6H]$^{6+}$: 1329.66
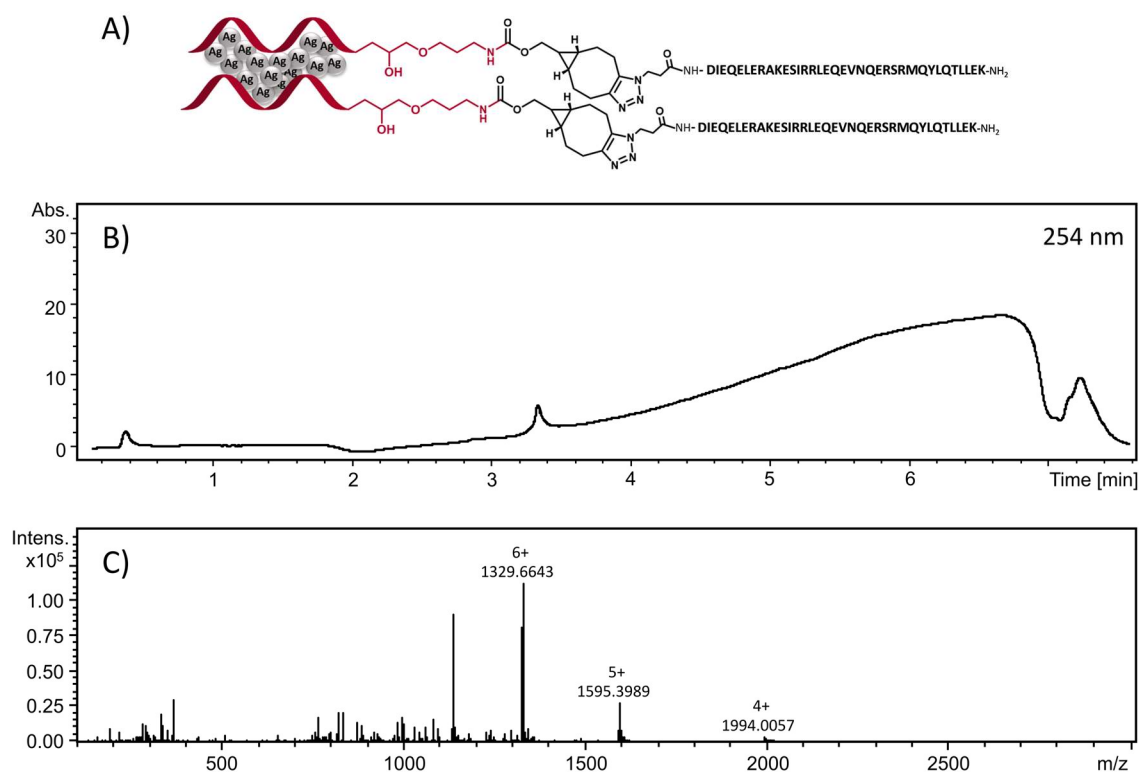
*Figure S15: (A) Schematic representation of the structure, (B) LCMS chromatogram and (C) mass spectrum of compound **11**. Note that M corresponds to the molecular weight of the DNA-BCN-coiled-coil-peptide fragment. Absorption is given in mOD.*

4. Conjugation of DNA-BCN-Ag$_{16}$NC to human insulin (hI)

Synthesis of azido-hexanoyl-hI:
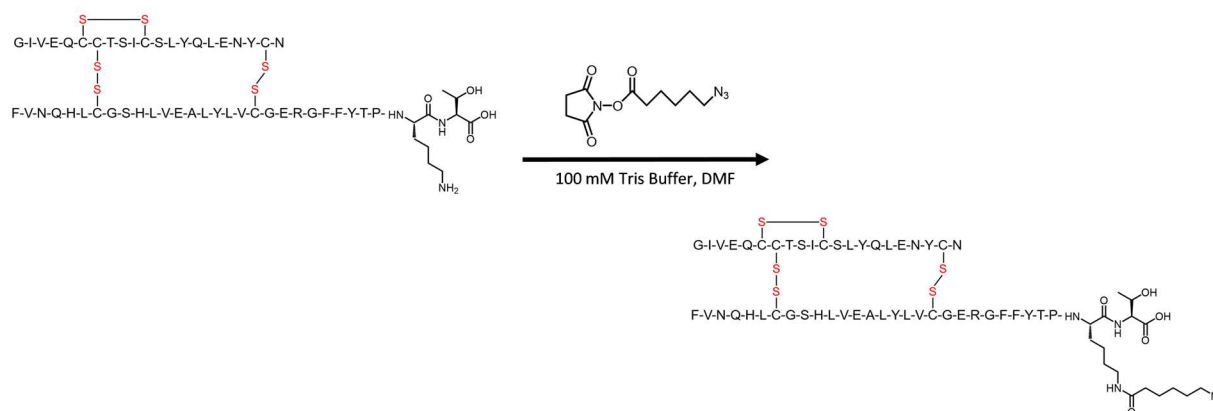
Figure S16: Reaction scheme of azido-hexanoyl-hI (compound 8).

Human insulin was modified and purified based on the protocol reported in reference 6. Briefly, human insulin (100 mg, 17.2 µmol) was suspended in 1.0 mL of 0.1 M Tris Buffer, and the pH was adjusted with NaOH (0.2 M) to 10.5 to dissolve it completely. 6-Azido-hexanoyl-NHS ester (34.0 µmol, 8.7 mg) dissolved in DMF (2.0 mL) was added dropwise to the solution over 5 minutes, and the reaction was stirred for 15 minutes. The completion of the reaction was confirmed by LCMS analysis. Then the reaction mixture was diluted with 10.0 mL MilliQ water and the pH was adjusted to 7.8. The product was isolated on an RP-HPFC Isolera system (Biotage), using a C18 column (SNAP Ultra C18 50 g, Biotage). A mixture of CH$_3$CN/MilliQ H$_2$O with 0.1% formic acid was used as eluent with a linear gradient of 5-50 % CH$_3$CN over 20 minutes, and a flow rate of 50 mL/min was chosen.[6] Each collected fraction was analyzed via LCMS (chromatograms not shown) in order to determine purity, and only the pure fractions were combined. Afterwards, CH$_3$CN was removed using a rotatory evaporator. LCMS confirmed that the product (compound **8**) was successfully obtained and the corresponding chromatogram is reported in Figure S17. In the end, the product was lyophilized.

LCMS details: Molecular formula of azido-hexanoyl-hI: C$_{263}$H$_{392}$N$_{68}$O$_{78}$S$_6$
Molecular weight [M]: 5946.79 g/mol
Observed: [M+3H]$^{3+}$: 1982.90, [M+4H]$^{4+}$: 1487.42, [M+5H]$^{5+}$: 1190.14
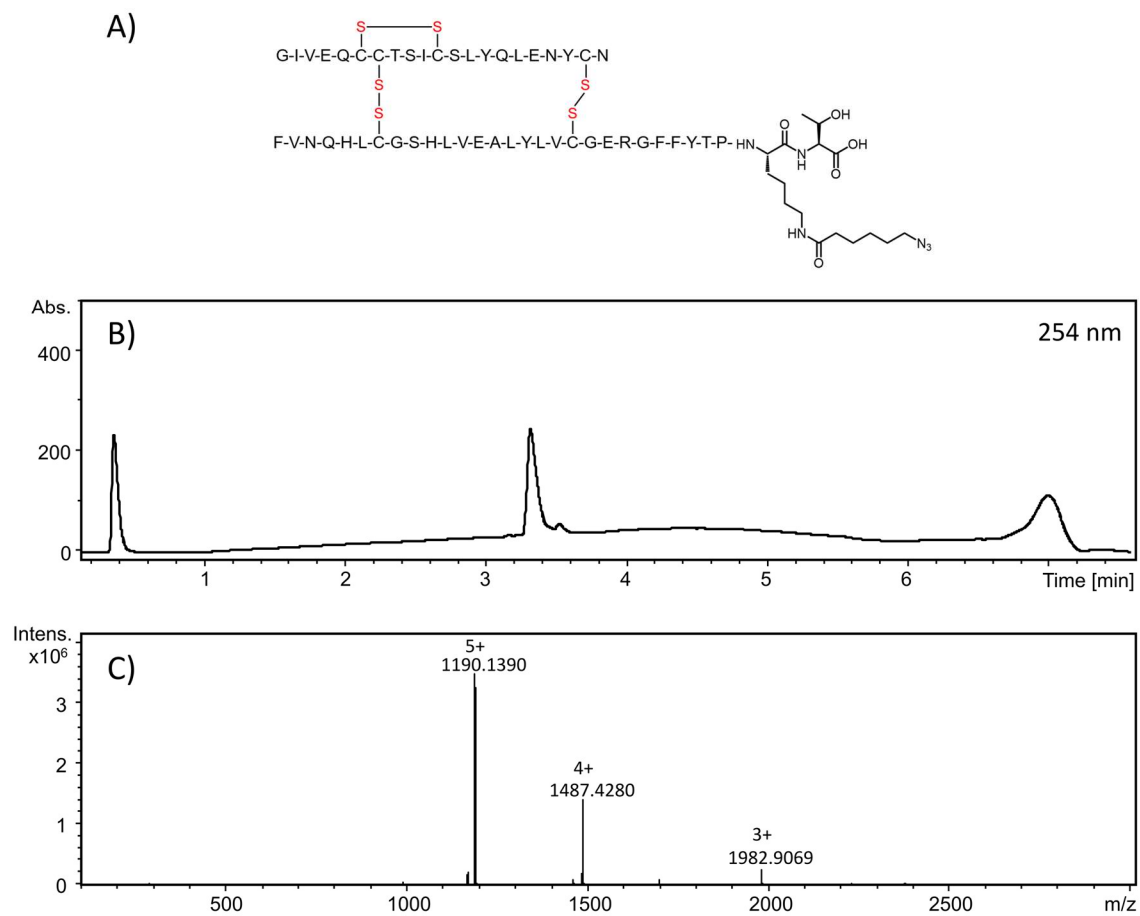
*Figure S17: (A) Structure, (B) LCMS chromatogram of the combined fractions from the RP-HPFC Isolera System and (C) mass spectrum of azido-hexanoyl-hI (compound **8**), eluted at around 3.3 minutes. Absorption is given in mOD.*

Conjugation of DNA-BCN-Ag$_{16}$NC with azido-hexanoyl-hI:

20 µL of compound **4** (57.5 µM) was added to an aqueous solution of azido-hexanoyl-hI (247 µM, 12.1 µL) and the volume was then adjusted to 40 µL by adding 7.9 µL of MilliQ water. The final concentrations of compound **4** and **8** were 28.75 µM and 74.72 µM, respectively. The reaction mixture was shaken at 850 rpm for 36 hours at 37 °C. Before LCMS analysis, the reaction mixture was purified 3 times using a 10 kDa cut-off membrane filter. The LCMS chromatogram (Figure S18B) shows only one peak, confirming that the desired product was obtained and the reactants were fully consumed. However, compound **12** fragmented during LCMS and only the mass of DNA-BCN-hI was observed. For this reason, the chromatogram of DNA-BCN-hI was compared to that of the hI-conjugated DNA-BCN-Ag$_{16}$NC. As displayed in Figure S19, the two retention times are different, which proves that compound **12** formed with the applied reaction conditions, despite the absence of the molecular ion peak in the mass spectrum (Figure S18C). The Human Insulin structure was created in Pymol using the PDB ascension code 4EY9.

LCMS Details: Molecular formula of DNA-BCN-hI: $C_{376}H_{540}N_{108}O_{141}P_{10}S_6$:
Molecular weight [M]: 9331.17 g/mol

Observed: $[M+4H]^{4+}$: 2333.86, $[M+5H]^{5+}$: 1867.08, $[M+6H]^{6+}$: 1556.07, $[M+7H]^{7+}$: 1333.91, $[M+9H]^{9+}$: 1037.70
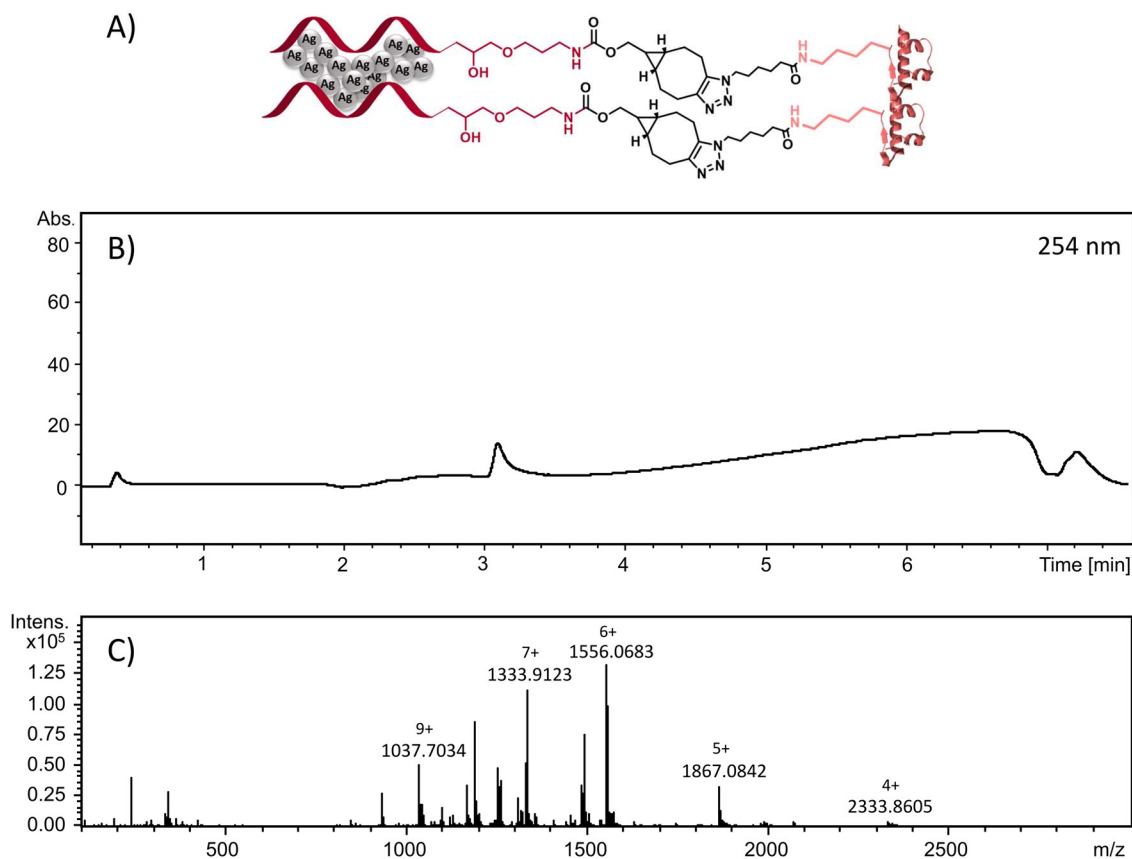
Figure S18: (A) Schematic representation of the structure, (B) LCMS chromatogram and (C) mass spectrum of compound 12 (elution time 3.1 minutes). Note that M corresponds to the fragment of DNA-BCN-hI. Absorption is given in mOD.
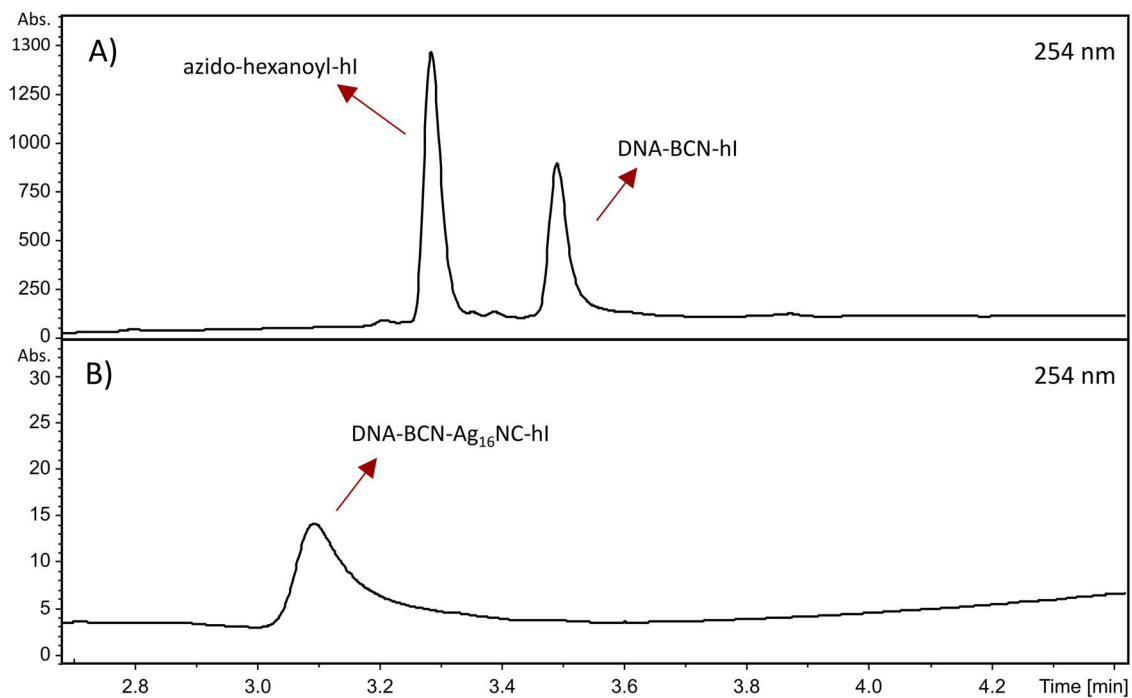
*Figure S19: Comparison between LCMS chromatograms of (A) DNA-BCN-hI and (B) compound **12**. For displaying purposes, only the interval from 2.7 to 4.4 min is shown. Absorption is given in mOD.*

5. Spectroscopic measurements

Absorption measurements:

Absorption spectra were carried out on two different UV-Vis spectrophotometers: a Cary 300 from Agilent Technologies or a Lambda 1050 from Perkin Elmer using a deuterium lamp for ultraviolet radiation and a tungsten-halogen lamp for visible and near-infrared radiation. The measurements were performed in a single-beam configuration with a 0/100% transmittance baseline correction. Every spectrum was subtracted by the corresponding blank absorption spectrum.

Steady-state emission and excitation measurements:

Steady-state fluorescence measurements were performed using a FluoTime300 instrument (PicoQuant) with a 507.5 nm picosecond-pulsed laser (LDH-PC-510, PicoQuant) as excitation source.
The excitation spectra were measured with a QuantaMaster400 from PTI/HORIBA with a xenon arc lamp to monitor the emission at 730 nm. All spectra were corrected for the wavelength dependency of the detector and the excitation spectra were additionally corrected for the lamp power. For all fluorescence measurements, the absorbance of the investigated compound was kept below 0.1 at the excitation wavelength in order to avoid inner filter effects.

Time-correlated single-photon counting (TCSPC):

Time-resolved fluorescence measurements were performed using a FluoTime300 instrument from PicoQuant with a vertically-polarized pulsed laser at 507.5 nm (LDH-PC-510, PicoQuant) as excitation source. The integration time was chosen to be 10 s and the repetition rate was set to 20 MHz in order to reach at least 10,000 counts in the maximum at 740 nm. The data analysis was performed with FluoFit v.4.6 software (PicoQuant). The decays were fitted with a multi-exponential reconvolution model including the IRF. The amplitude (α_i) and decay time (τ_i) components were used to calculate the intensity-weighted average decay time, $<\tau>$,[8] reported in Table 1.

In addition, time-resolved anisotropy measurements of DNA-Ag$_{16}$NC, DNA-BCN-Ag$_{16}$NC (compound **4**) and all conjugates (compounds **9-12**) were performed by recording both parallel and perpendicular fluorescence intensity decays at 740 nm. The samples were excited at 507.5 nm with a vertically-polarized laser (LDH-P-C-510, PicoQuant). The anisotropy data were fitted with the same software from PicoQuant, using a multi-exponential reconvolution model for the decay time and a mono- or bi-exponential function for the rotational correlation time (θ), including the IRF. One θ exponent was employed for DNA-Ag$_{16}$NC and compound **4**, while two exponents were used for all the conjugates (compounds **9-12**), assuming that the first θ refers to the DNA-BCN-Ag$_{16}$NC rotation and the second θ describes the rotational correlation time of the entire conjugate (see Table 1). The hydrodynamic volume (V_{hydro}) was then calculated according to the following equation:[8]

$$\theta = \frac{\eta \cdot V_{hydro}}{k_B \cdot T}$$

where η is the dynamic viscosity of the solvent, T is the absolute temperature and k_B is the Boltzmann constant.
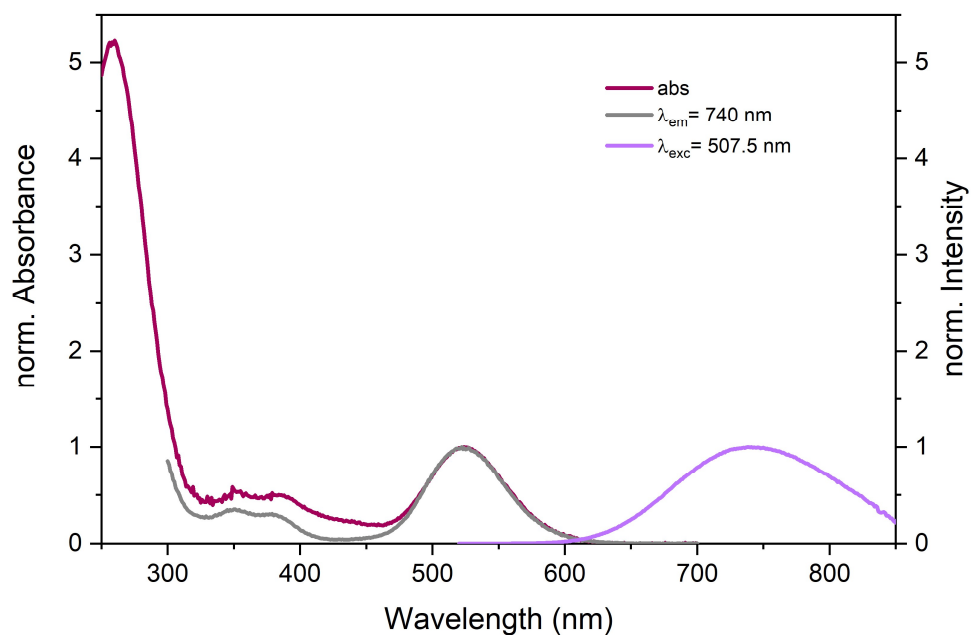
*Figure S20: Normalized absorption, excitation and emission spectra of purified DNA-BCN-Ag$_{16}$NC (compound **4**) in 10 mM NH$_4$OAc, recorded at room temperature.*
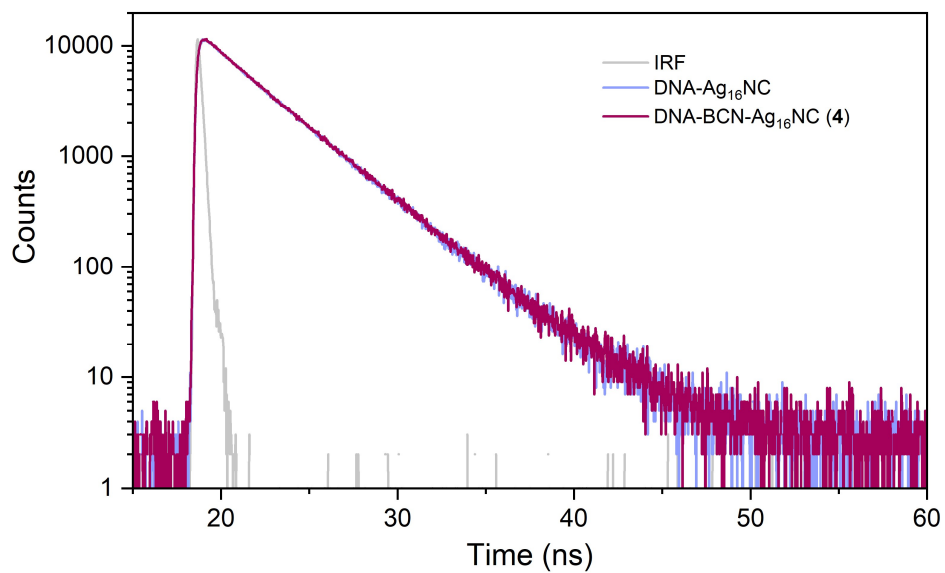
*Figure S21: Fluorescence decays of DNA-Ag$_{16}$NC and DNA-BCN-Ag$_{16}$NC (compound **4**) in 10 mM NH$_4$OAc measured at 740 nm (λ_{exc}= 507.5 nm) at room temperature. The decays were fitted with a bi-exponential reconvolution function, and the respective intensity-weighted average decay times are reported in Table 1. The gray trace is the instrument response function (IRF).*
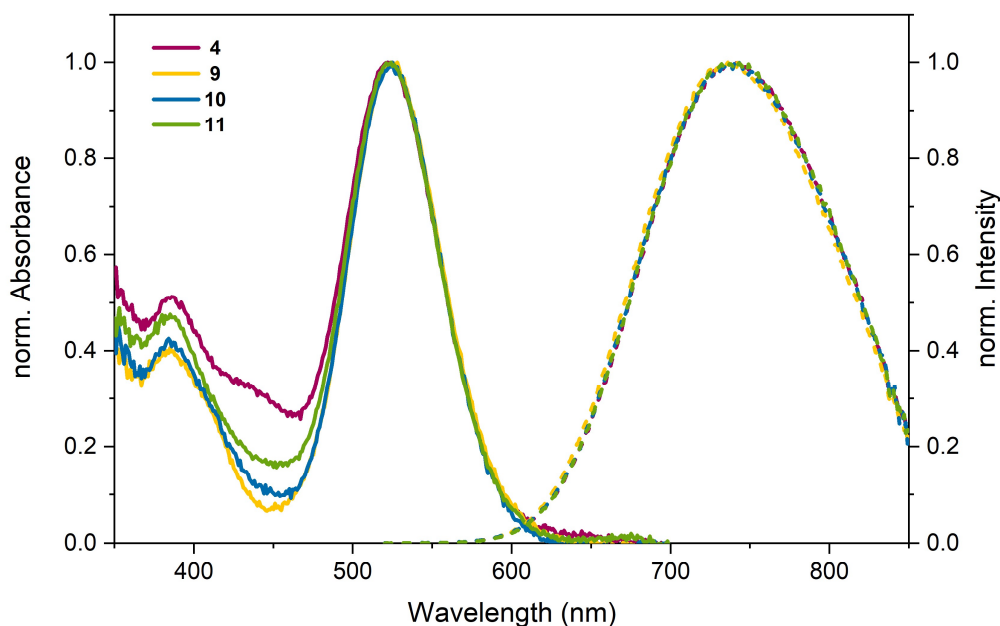
*Figure S22: Comparison of normalized absorption and emission spectra ($\lambda_{exc}= 507.5$ nm) of DNA-BCN-Ag$_{16}$NC (compound **4**) and all conjugated peptide products (compounds **9-11**) in 10 mM NH$_4$OAc at room temperature.*
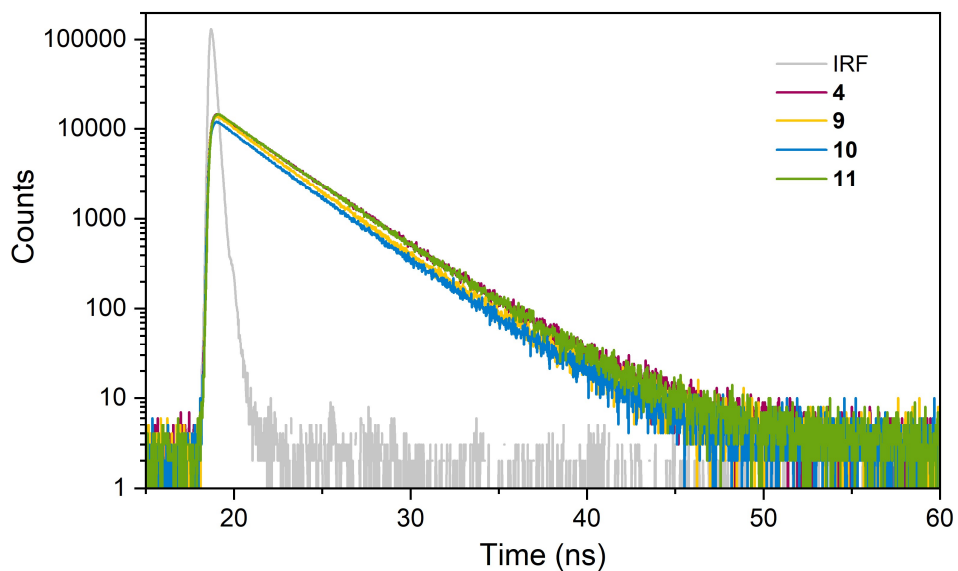
*Figure S23: Fluorescence decay curves of compounds **4, 9-11** in 10 mM NH$_4$OAc recorded at 740 nm at room temperature. All samples were excited at 507.5 nm. The decays were fitted with a tri-exponential reconvolution model, and the corresponding intensity-weighted average decay times are reported in Table 1. The gray trace is the instrument response function (IRF).*
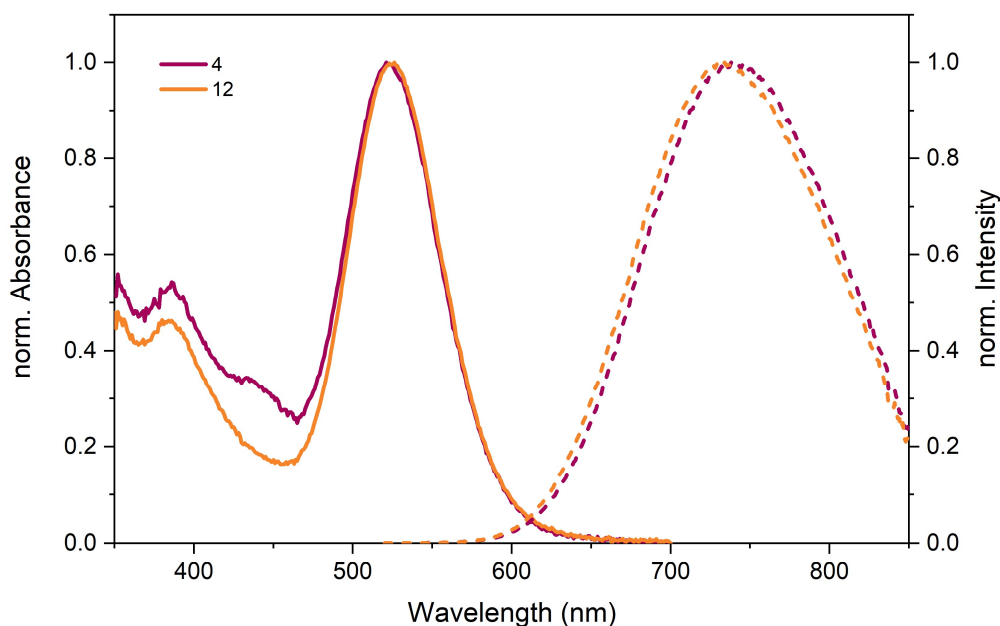
*Figure S24: Normalized absorption and emission spectra (λ_{exc}= 507.5 nm) of DNA-BCN-Ag$_{16}$NC (compound **4**) and the conjugated DNA-BCN-Ag$_{16}$NC-hI (compound **12**) measured in 10 mM NH$_4$OAc at room temperature.*
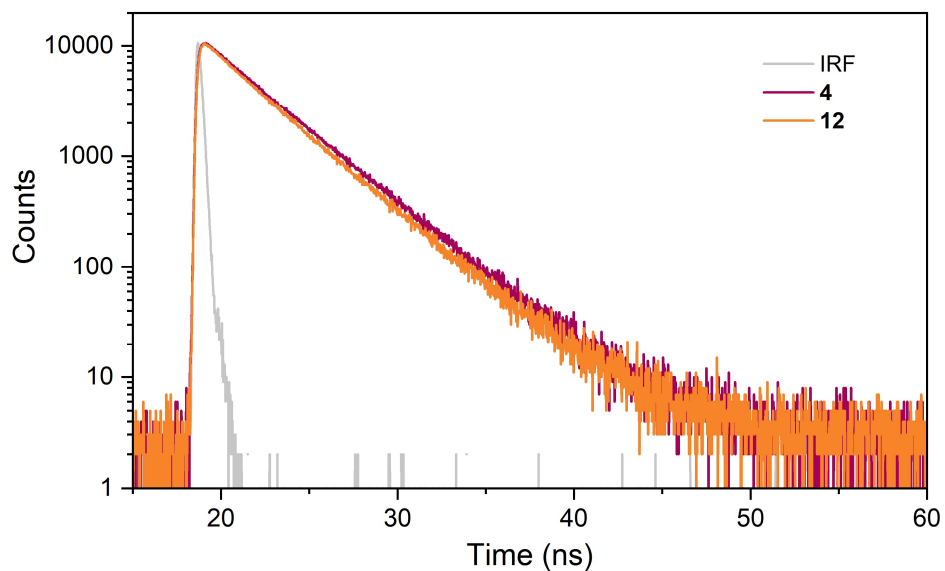
*Figure S25: Fluorescence decays of DNA-BCN-Ag$_{16}$NC (compound **4**) and DNA-BCN-Ag$_{16}$NC-hI (compound **12**) in 10 mM NH$_4$OAc measured at 740 nm (λ_{exc}= 507.5 nm) at room temperature. Both decay traces were fitted with a bi-exponential reconvolution model, and the respective intensity-weighted average decay times are reported in Table 1. The gray trace is the instrument response function (IRF).*
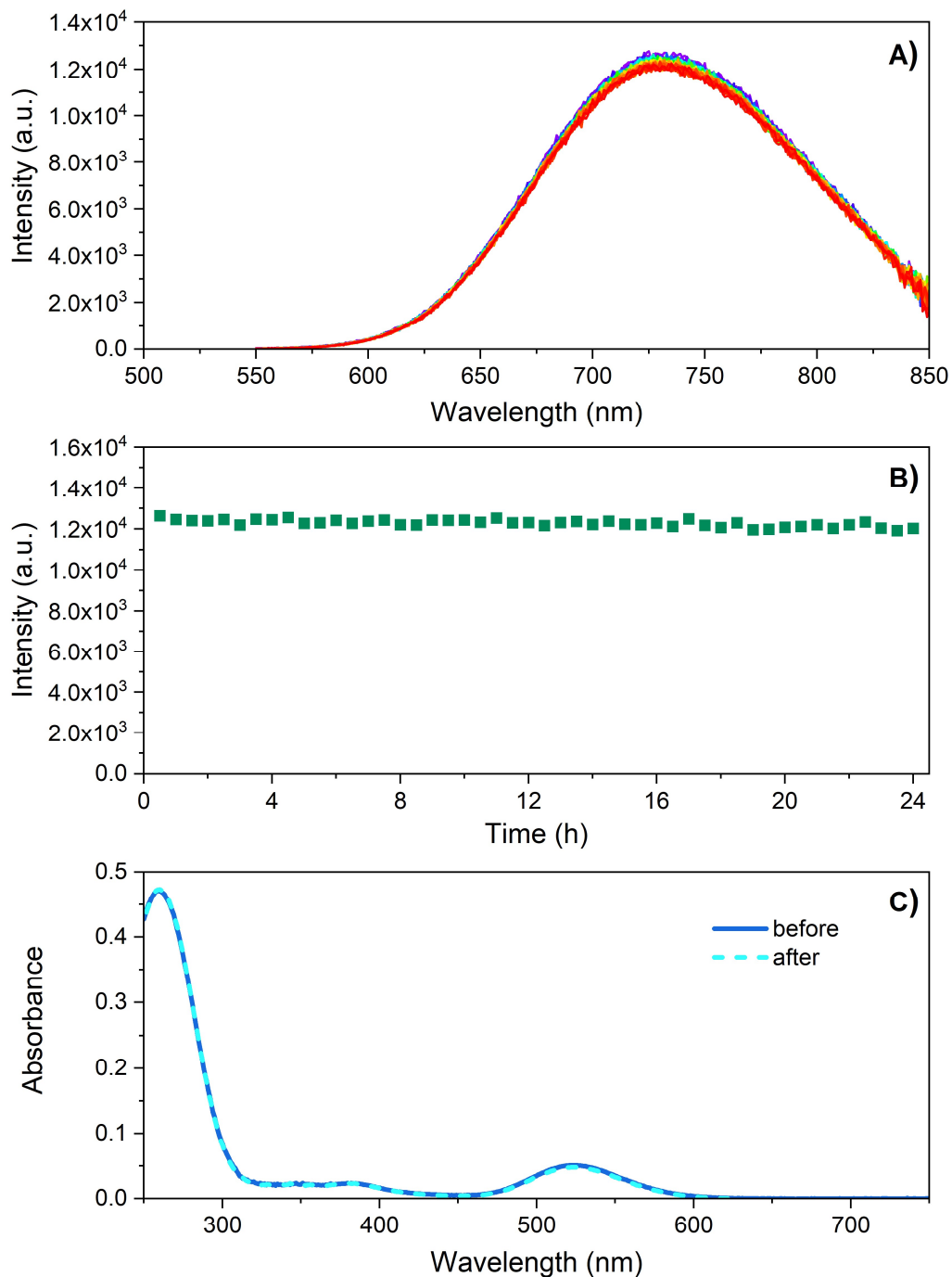
*Figure S26: Chemical stability test of DNA-BCN-Ag$_{16}$NC (compound **4**) in 2 mM KNO$_3$ and 100 mM NaNO$_3$ at 25 ˚C. (A) Emission spectra recorded every 30 minutes over a period of 24 hours, exciting at 507.5 nm. The laser source was blocked in between measurements. (B) Emission maxima plotted as a function of time. (C) Absorption spectra before the emission measurements and after 24 hours.*
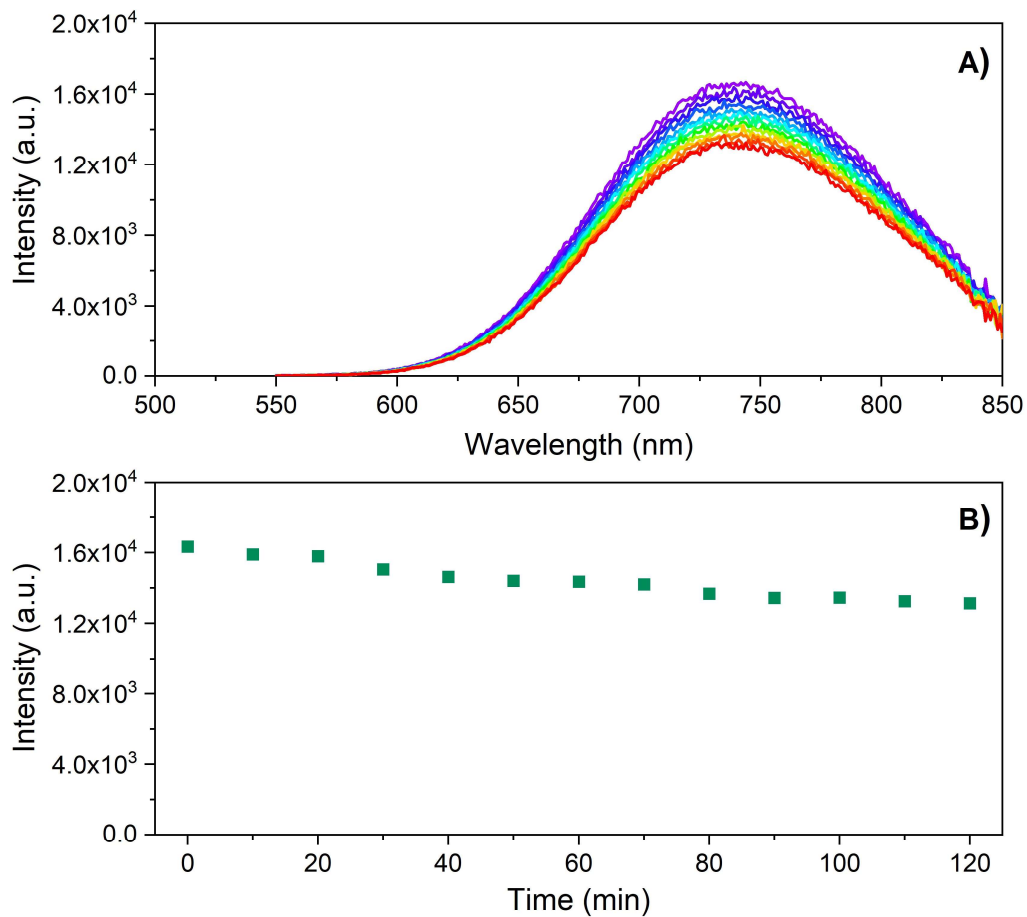
Figure S27: Photostability test of DNA-BCN-Ag$_{16}$NC in 2 mM KNO$_3$ and 100 mM NaNO$_3$ at 25 ˚C. (A) Emission spectra recorded every 10 minutes for 2 hours, exciting at 507.5 nm. The laser source was not blocked in between measurements. The intensity of the laser was 1.67 mW resulting in 95 mW/cm^2. (B) Emission maxima plotted as a function of time.
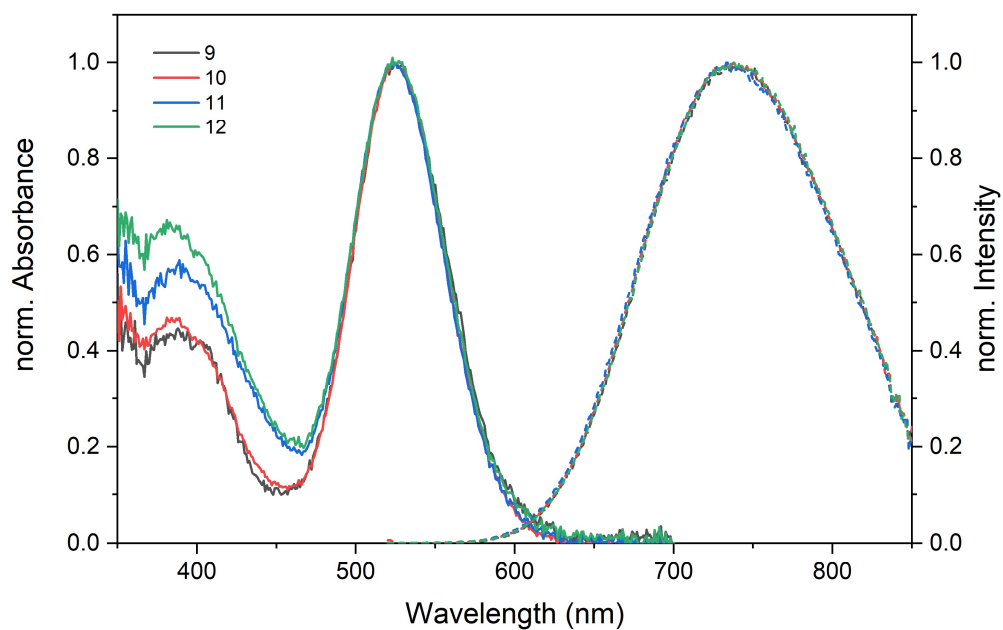
*Figure S28: Normalized absorption and emission spectra (λ_{exc}= 507.5 nm) of seven-month-old conjugates (compounds **9-12**) in 10 mM NH₄OAc at 25 ˚C. The samples were stored at 4 ˚C.*

6. Cell Imaging

Cell sample preparation:

A monoclonal Chinese hamster ovary (CHO) cell line overexpressing the human insulin receptor B (hIR-B) was established by transfecting a hIR-B expressed plasmid (HG11081-UT, Sino Biological Inc.) into CHO cells (European Collection of Authenticated Cell Cultures) followed by hygromycin (10687010, Invitrogen) treatment and selection of a clonal cell-line with high hIR-B expression. The cells were cultivated in F-12K Nut Mix 1X (Gibco) supplemented with 10 % fetal bovine serum (Gibco), 1 % penicillin/streptomycin (10,000 U/mL, Gibco), and 750 µg/mL hygromycin (MedChemExpress). The cells were seeded into 8-well slides (Nunc^{TM} Lab-Tek^{TM} II chambered cover glass) at densities of 50,000 cells per well and kept at 37 °C and 5 % CO_2 for 2 hours or overnight. The cells were washed with phosphate-buffered saline (1x PBS) and were fixed by adding 150 µL 4 % formaldehyde in 1x PBS and incubated for 20 minutes at room temperature (RT). Afterwards, they were washed and stored in 1x PBS at 4 °C.

The fixed cells were labeled with DNA-Ag$_{16}$NCs or compound **12** by incubating approximately 100 nM sample for 15 min in a 2 mM KNO_3 and 100 mM $NaNO_3$ medium. The stained cells were subsequently washed three times with the medium and imaged immediately after.

Confocal microscope setup:

A home-built confocal microscope setup was used for the imaging of CHO cells. A fiber-coupled (FD7-PM, NKT Photonics) pulsed continuum white-light laser (SuperK EXTREME EXB-6, NKT Photonics) at ≈11 MHz was used as an excitation source delivering a wavelength of 520 nm by sending the continuum output through an acousto-optic tunable filter (AOTF; SuperK SELECT, NKT Photonics). The output of the fiber was expanded and collimated by a lens system and cleaned up by a 520 nm band-pass filter (FF01-520/5, Semrock) and 561 nm short-pass filter (SP01-561RU, Semrock) before it was reflected by a 30:70 beam splitter (XF122, Omega Optical) and sent through an oil immersion objective (UPlanSApo 100x, NA = 1.4, Olympus). The excitation intensity measured on top of the microscope was 9 W/cm^2. The objective focused the laser onto the sample, which was positioned on a piezo-driven stage (Physik Instrumente, E-710.4CL), and the emission was collected by the same objective. The laser light was blocked by three long-pass filters [(BLP01-532LP, Semrock), (BLP01-561R, Semrock), and (BLP01-647R, Semrock)] and out-of-focus light was blocked by a 100 µm pinhole. The resulting emission was detected on an avalanche photodiode (CD3226, PerkinElmer).

Emission spectra were recorded by redirecting the fluorescence through a spectrograph (SP 2356 spectrometer, 300 grooves/mm, Acton Research) onto a nitrogen-cooled CCD camera (SPEC-10:100B/LN-eXcelon, Princeton Instruments). The spectra were wavelength- and intensity-calibrated, as previously described.[9]

Bright-field images of the CHO cells were recorded on the same confocal microscope, but with a CMOS camera (DCC1545M, Thorlabs) and light from an incandescent light bulb.

Fluorescence Lifetime Imaging microscopy (FLIM) setup:

FLIM experiments were performed on a second confocal microscope, which was essentially the same as the setup described above; but with a different avalanche photodiode (SPCM-AQRH-14-TR, Excelitas) and scanner (LPS300, Mad City Labs). The laser repetition rate was changed to 13 MHz to ensure that the entire decay was captured in the time to amplitude window, and the excitation intensity was increased to 150 W/cm^2. A pixel dwell time of 8 ms was used for FLIM imaging. Afterwards, the data was analyzed in SPCImage (Becker & Hickl), where the decay at each pixel was fitted with a bi-exponential reconvolution model including the IRF (auto-generated in SPCImage) and was subsequently exported and plotted in MATLAB R2020b.
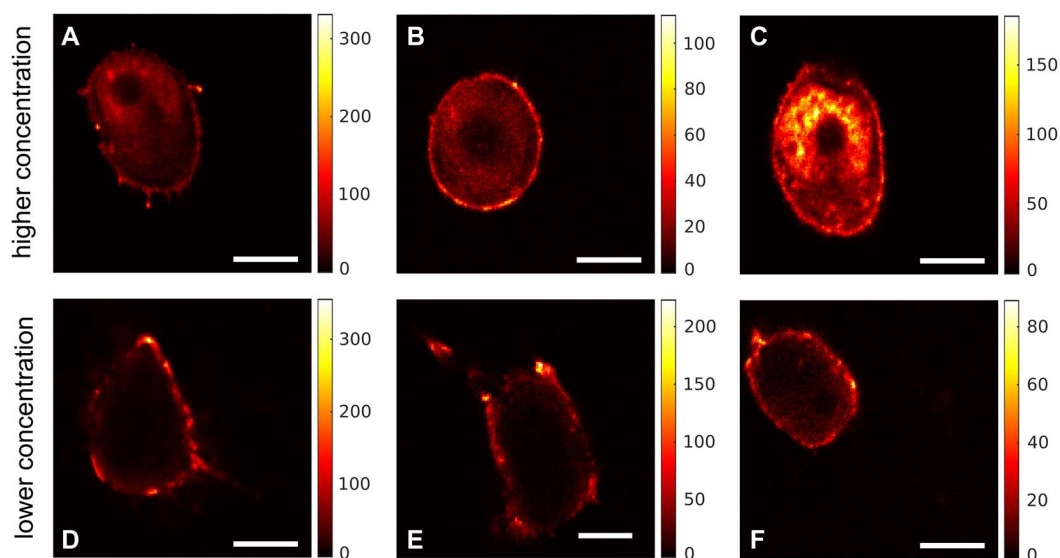
*Figure S29: Concentration dependency experiment. Confocal images of CHO cells incubated with DNA-BCN-Ag$_{16}$NC-hI (compound **12**) for 15 min. (A), (B) and (C) show the CHO cells stained with compound **12** with a concentration of 1 µM, while (D), (E) and (F) display cells incubated with 100 nM of the same conjugate. Scale bars: 10 µm.*
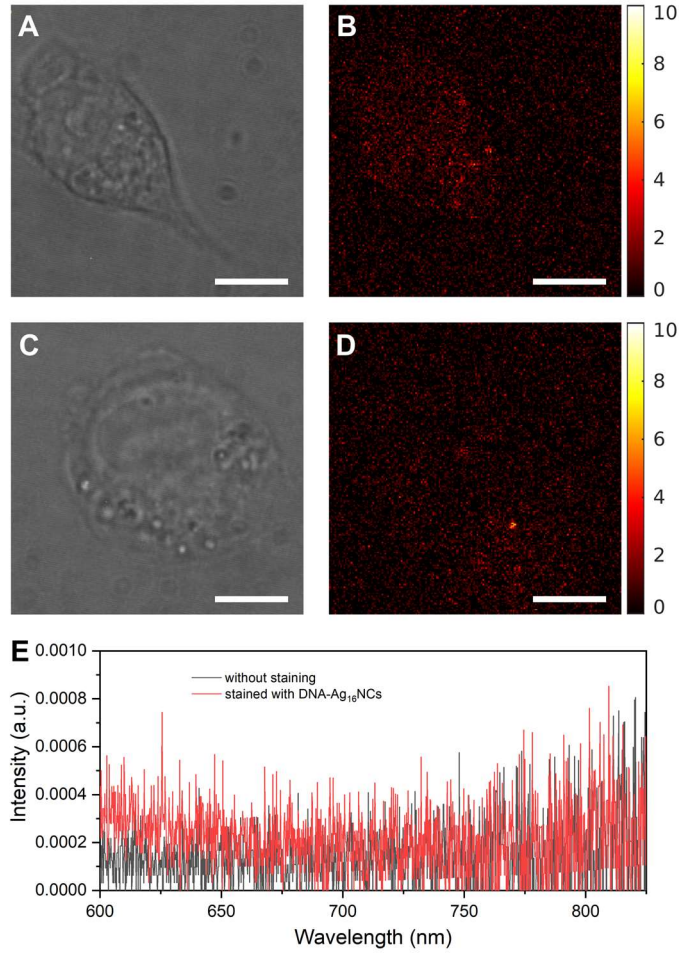
Figure S30: CHO cells auto-fluorescence. (A) Bright-field and (B) confocal image of CHO cells stained with 100 nM DNA-Ag$_{16}$NCs. (C) Bright-field and (D) confocal image of CHO cells without staining. Scale bar: 10 μm. (E) Emission spectra (λ$_{exc}$= 520 nm) of CHO cells stained with (red) and without (gray) DNA-Ag$_{16}$NCs. In both cases, only minimal auto-fluorescence could be detected.
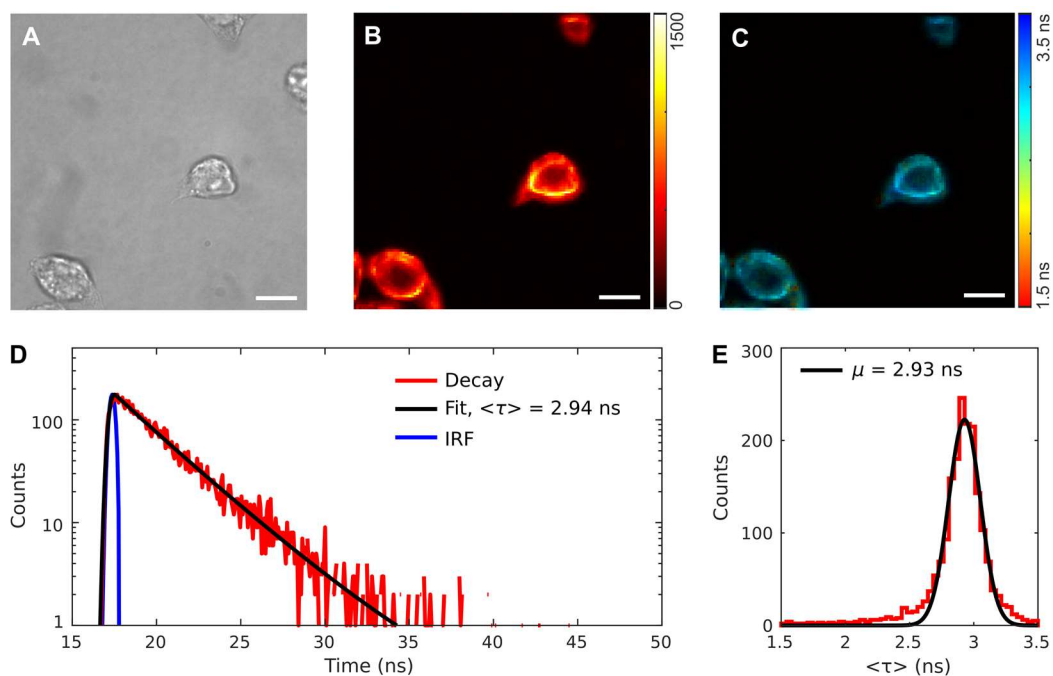
*Figure S31: FLIM imaging of CHO cells overexpressing hIR-B, labeled with approximately 300 nM DNA-Ag$_{16}$NC-hI (compound **12**): (A) Bright-field, (B) fluorescence intensity/confocal and (C) FLIM image. Scale bars: 10 µm. (D) Exemplary decay fitted with a bi-exponential reconvolution model including the IRF (auto-generated in SPCImage) yields an intensity-weighted average decay time of 2.94 ns. (E) Histogram of fitted fluorescence decay times. A Gaussian fit to the distribution yields a mean value (µ) of 2.93 ns.*

Viability Assay:

To assess the cell toxicity of DNA-Ag$_{16}$NC, compound **12** and azido-hI, Cell Proliferation Reagent WST-1 (Roche) was used. The assay relies on the conversion of the tetrazolium salt, WST-1, to the strongly absorbing formazan product (monitored at 440 nm) by viable cells. Thus, a higher degree of absorption indicates more viable cells. For the assay, the hIR-B overexpressing CHO cells were seeded into 96-well plates ($\approx$ 40,000 cells per well) in 100 µL buffer medium (F-12 K Nut Mix + Hygromycin). They were then treated with either DNA-Ag$_{16}$NC, compound **12**, or human insulin (azido-hI) at final concentrations of 50, 100, 200, 500, and 1000 nM (this was performed in triplicates). After 30 minutes, 10 µL of Cell Proliferation Reagent WST-1 were added to each well and allowed to incubate for 4 hours at 37 °C. The plate was shaken thoroughly for 1 minute, and the absorption at 440 nm (formazan absorption maximum) and 660 nm (background level reading) was measured on an ELISA reader (FLUOstar Omega, BMG LABTECH).

A series of controls was included to calculate the relative viability for each condition. To determine the background level of the compounds and non-metabolically converted WST-1, for each of the compounds and concentrations, their absorption was measured in buffer with Cell Proliferation Reagent WST-1 without cells. To assess the viable level of untreated cells, wells were incubated with cells in buffer and Cell Proliferation Reagent WST-1. Finally, the absorption of the medium together with Cell Proliferation Reagent WST-1 was measured to determine the background level of absorption (due to non-metabolic conversion) for the untreated cells.

Therefore, to calculate the relative viability for each condition, the absorption of every measured data point was firstly corrected for the background level, A_{440}-A_{660}. The absorption of the compound, medium, and Cell Proliferation Reagent WST-1 was subtracted from the absorption of the treated cells, while only the absorption of the medium and Cell Proliferation Reagent WST-1 was subtracted from the untreated cells. Finally, the relative viability was calculated as the absorption of treated cells divided by untreated cells. Presented in Figure S32 are the mean and standard deviation (measured in triplicates) of the relative viability for each condition.
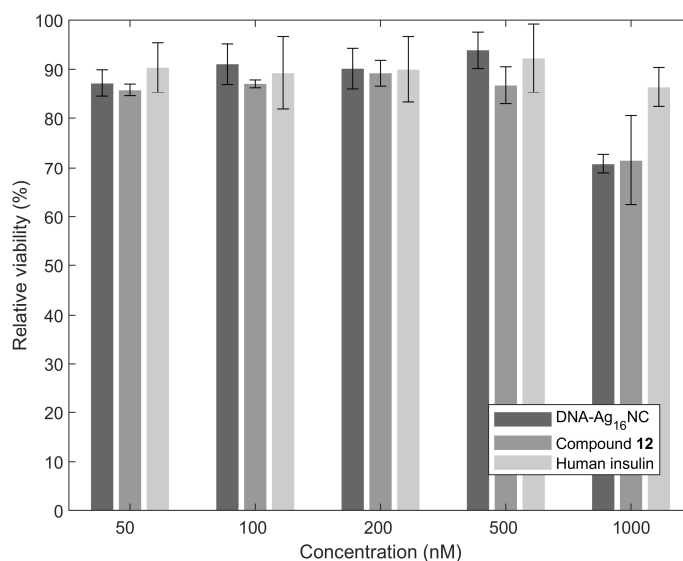
*Figure S32: Relative viability of cells treated with DNA-Ag$_{16}$NC, compound **12**, and human insulin (azido-hI) for 4 hours compared to untreated cells based on a WST-1 colorimetric assay.*

7. References

[1] S. A. Bogh, M. R. Carro-Temboury, C. Cerretani, S. M. Swasey, S. M. Copp, E. G. Gwinn and T. Vosch, *Methods and applications in fluorescence*, **2018**, 6, 024004.

[2] C. Cerretani, H. Kanazawa, T. Vosch, J. Kondo, *Angewandte Chemie - International Edition*, **2019**, 58, 17153-17157.

[3] M. Loos, C. Gerber, F. Corona, J. Hollender, H. Singer, Analytical Chemistry, **2015**, 87(11), 5738-5744.

[4] A. Gonzalez-Rosell, S. Malola, R. Guha, N. Arevalos, M. Matus, M. Goulet, et al., ChemRxiv. Cambridge: Cambridge Open Engage; **2023**; This content is a preprint and has not been peer-reviewed.

[5] K. J. Jensen, P. T. Shelton, S. L. Pederson, "Peptide synthesis and applications" Springer protocol, Method in Molecular Biology.

[6] K. S. Sorensen, N. K. Mishra, M. P. Paprocki, K. J. Jensen, *ChemBioChem,* **2021**, *22*, 1818-1822.

[7] Fávero-Retto, M. P.; Palmieri, L. C.; Souza, T. A. C. B.; Almeida, F. C. L.; Lima, L. M. T. R., Structural meta-analysis of regular human insulin in pharmaceutical formulations. *European Journal of Pharmaceutics and Biopharmaceutics* **2013,** *85* (3, Part B), 1112-1121.

[8] J. R. Lakowicz, *Principles of fluorescence spectroscopy*, Springer, 2006.

[9] M. B. Liisberg, Z. Shakeri Kardar, S. M. Copp, C. Cerretani and T. Vosch, *The Journal of Physical Chemistry Letters*, **2021**, 12, 1150-1154.

8. Author Contributions

V.R. and C.C. synthesized the DNA-AgNCs and performed the spectroscopic measurements. N.K.M. carried out the conjugation reactions. M.B.L. and V.R. performed the confocal microscopy and FLIM measurements. K.K.S. carried out the LCMS measurements. C.B.M. carried out the MS measurements. A.B.S. and A.K. handled and prepared the CHO cells for imaging. C.L. performed initial synthesis test reactions. T.V. and K.J.J. conceived the experiments. The paper was written with input from all authors.

Publication 4

How Inert is Single-Stranded DNA Towards DNA-Stabilized Silver Nanoclusters? A Case Study.

Vanessa Rück, Cecilia Cerretani, Tom Vosch.
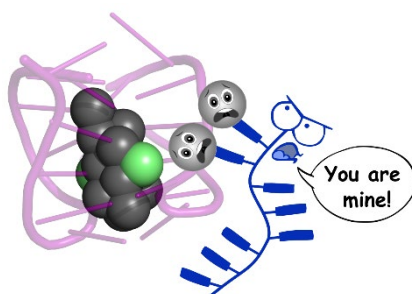
How Inert is Single-Stranded DNA Towards DNA-Stabilized Silver Nanoclusters? A Case Study

Vanessa Rück,[a] Cecilia Cerretani,[a] and Tom Vosch*[a]

A case study, detailing the effect of different DNA oligomers on a NIR-emitting DNA-stabilized silver nanocluster (DNA-AgNC), is reported. The presence of single-stranded DNA oligomers was found to adversely affect the chemical stability of $(DNA)_2[Ag_{16}Cl_2]^{8+}$ with distinct degrees of destruction depending on the DNA sequence. To increase the chemical stability of the DNA-AgNC, we implemented two protection strategies. First, hybridization of the bare DNA strands with the corresponding complementary sequences dramatically reduced the destruction of $(DNA)_2[Ag_{16}Cl_2]^{8+}$, as demonstrated by the decreased drops in both the absorption and emission spectra. Secondly, saturation of the free DNA oligomers with silver cations left $(DNA)_2[Ag_{16}Cl_2]^{8+}$ intact. Our investigation can thus provide an easy-to-implement approach to discover DNA sequences that are intrinsically less reactive towards preformed DNA-AgNCs, and give an idea on how to protect DNA-AgNCs from bare DNA strands.

Introduction

Self-assembly of DNA oligomers with silver atoms and cations results in the formation of DNA-stabilized silver nanoclusters (DNA-AgNCs) with molecule-like spectroscopic properties.[1] By changing the scaffolding DNA sequence, emission wavelength, decay time, quantum yield and Stokes shift can be varied in nearly unlimited ways.[1a,2] The synthesis is straightforward and consists of mixing three compounds: DNA, silver nitrate and a reducing agent, in an aqueous solution. The synthesis results in the DNA-AgNC of interest along with byproducts like unwanted DNA-AgNCs, silver nanoparticles, bare DNA and DNA strands complexed with a diverse number of silver cations. The presence of these side products can compromise the chemical stability of the compound of interest and/or hinder its use in specific applications (e.g., labeling). Although it was demonstrated in the early days how DNA-AgNCs chemically evolve over time,[3] to date purification is still not considered standard practice in the field.

A commonly used concept is the extension of the DNA sequence that stabilizes a specific AgNC with an extra segment suitable for hybridization (a hybridization tail).[4] It is thus reasonable to ask how "inert" this hybridization tail is in the synthesis process, i.e., whether the silver cations would also bind to the hybridization tail region, preventing the Watson-Crick (W-C) base pair formation upon hybridization with a complementary DNA strand. It is worth noticing that this, of course, does not exclude the possibility of silver-mediated interactions between the tail strand and the intended hybridization target. By now, there are several examples available in literature that establish the presence of silver-mediated DNA strands hybridized via both Watson-Crick (e.g., C–G) and non-Watson-Crick base pairs (e.g., C–C).[5] The presence of reports in literature where perfectly complementary DNA strands were still able to stabilize emissive DNA-AgNCs illustrates this idea, highlighting the disruptive power of silver.[4]

Recently, we demonstrated the conjugation of a NIR emissive $(DNA)_2[Ag_{16}Cl_2]^{8+}$ to a variety of peptides and human insulin using click chemistry.[6] When dissolved in 10 mM ammonium acetate (NH_4OAc), this specific DNA-AgNC is very stable over time (years), and has a surprisingly good chloride resistivity. As such, this would be the ideal candidate to test whether the "hybridization tails" (single-stranded DNA segments) affect the chemical stability of the wrapped AgNC, and if so, which methods could be employed to prevent its destruction. We have previously reported for a red-emitting DNA-AgNC that free single-stranded DNA (ssDNA) had a negative impact on the chemical stability.[7] In this case study, however, we used three different ssDNA sequences to assess the level of sequence-dependent reactivity towards $(DNA)_2[Ag_{16}Cl_2]^{8+}$. We also show that pre-hybridization of the hybridization tail with its complementary part offered some increased protection for $(DNA)_2[Ag_{16}Cl_2]^{8+}$, and even better results were obtained by passivating the hybridization tails with silver cations. Our results highlight the need to revisit the idea that hybridization tails are inert by default and promote only Watson-Crick base pair hybridization when the complementary strand is added.

[a] V. Rück, C. Cerretani, T. Vosch
Department of Chemistry and Nanoscience Center
University of Copenhagen
Universitetsparken 5, 2100 Copenhagen, Denmark
E-mail: tom@chem.ku.dk

ChemPhotoChem

Research Article
doi.org/10.1002/cptc.202400014

Chemistry
Europe
European Chemical
Societies Publishing

Results and Discussion

Destruction of $(DNA)_2[Ag_{16}Cl_2]^{8+}$ by ssDNA

$(DNA)_2[Ag_{16}Cl_2]^{8+}$ consists of two 5′-CACCTAGCGA-3′ strands, a cluster of 16 silver atoms and two chloride ions bound to the silver cluster.[8]

Table 1 reports the three hybridization tails (Strands 1–3) used in this study, together with the corresponding 12- and 15-base complementary strands. Strand 1 contains the same sequence motif (CACCTAGCGA) as the original oligomer used to stabilize $(DNA)_2[Ag_{16}Cl_2]^{8+}$, while Strand 2 comprises only six bases of the original sequence (CACCTA). Strand 3 is an unrelated sequence, rich in thymines and adenines, which are known to have a lower affinity for silver.

Before exploring the effect of adding the three different strands to $(DNA)_2[Ag_{16}Cl_2]^{8+}$, we measured the chemical stability of $(DNA)_2[Ag_{16}Cl_2]^{8+}$ in 10 mM NH$_4$OAc and in nuclease-free water to establish a baseline. Figure 1 shows that in 10 mM NH$_4$OAc (A) both the absorption and emission intensity are virtually unaltered over a period of 24 hours, while a very minor, but constant drop of about 5 % was observed in nuclease-free water (B). Given the overlapping nature of the spectra, the emission intensity at 735 nm of each spectrum is plotted in Figure 1C as a function of time. Addition of salts during or after the synthesis can have an impact on the chemical stability and on the type of DNA-AgNC that is formed.[9] Given the endless number of combinations of salts, pH and buffers, we proceeded to use the nuclease-free water as medium to test the chemical stability of $(DNA)_2[Ag_{16}Cl_2]^{8+}$ with the three strands and their hybridized versions. It is worth noticing that the DNA tails were first hybridized and then added to the $(DNA)_2[Ag_{16}Cl_2]^{8+}$ solution (see SI for details on the sample composition). Figure 2 displays the effect of adding the bare Strands 1, 2 and 3 to $(DNA)_2[Ag_{16}Cl_2]^{8+}$. The cytosine-rich sequences, Strands 1 and 2, caused dramatic changes to the absorption and emission spectra of $(DNA)_2[Ag_{16}Cl_2]^{8+}$, wiping out around 80 % of the compound in 24 hours. On the other hand, the thymine-rich Strand 3 caused a more moderate drop of around 20 % in

Table 1. Overview of DNA sequences used in this study.

Name	Sequence
Strand1	5′-CTC TAC **CAC CTA GCG A**AC-3′
Strand1-comp12	3′-GTG GAT CGC TTG-5′
Strand1-comp15	3′-ATG GTG GAT CGC TTG-5′
Strand2	5′-CTC TAC **CAC CTA** CAT CAC-3′
Strand2-comp12	3′-GTG GAT GTA GTG-5′
Strand2-comp15	3′-ATG GTG GAT GTA GTG-5′
Strand3	5′-TTG TTA AAT ATG TTG CTT-3′
Strand3-comp12	3′-TTA TAC AAC GAA-5′
Strand3-comp15	3′-AAT TTA TAC AAC GAA-5′

Figure 1. Absorption and emission spectra of $(DNA)_2[Ag_{16}Cl_2]^{8+}$ in (A) 10 mM NH$_4$OAc and (B) nuclease-free water measured at room temperature over a period of 24 hours. Emission spectra were acquired every hour exciting at 507 nm. (C) Fluorescence intensity from (A) and (B) at 735 nm, normalized to the initial value.

Figure 2. Effect of Strands 1–3 (A–C) on the absorption and emission spectra of $(DNA)_2[Ag_{16}Cl_2]^{8+}$ nanoclusters in nuclease-free water at room temperature. The emission spectra were recorded exciting at 507 nm. The red trace represents the sole $(DNA)_2[Ag_{16}Cl_2]^{8+}$ solution. The other trace colors display the same sample with either Strand 1, 2 or 3 over time. Orange indicates the mixture of the DNA-AgNC with the specific Strand after 0 hours; yellow after 1 hour; green after 2 hours; light blue after 4 hours; dark blue after 6 hours and purple after 24 hours.

ChemPhotoChem

Research Article
doi.org/10.1002/cptc.202400014

Chemistry Europe
European Chemical
Societies Publishing

24 hours. These results indicate that even though the AgNC is well-encapsulated by two DNA strands, all three additional sequences can interact over time with the silver atoms and cations, leading to the destruction of $[Ag_{16}Cl_2]^{8+}$ cluster.

Time-correlated single photon counting experiments also reveal that the remaining $(DNA)_2[Ag_{16}Cl_2]^{8+}$ nanoclusters after 24 hours have a similar fluorescence decay time as before the addition of the strands, see Figure S2. This excludes any major quenching effects and confirms that the presence of free DNA strands influences the stability of the $(DNA)_2[Ag_{16}Cl_2]^{8+}$ cluster. This is why purification with HPLC, SEC or gel electrophoresis is key. Interestingly, while significant research has been done in finding DNA sequences that stabilize emissive AgNCs, very limited research has been carried out in discovering unreactive DNA sequences,[10] and it is often assumed that hybridization tails are inert in molecular beacon schemes.[11]

Protection of $(DNA)_2[Ag_{16}Cl_2]^{8+}$ by Pre-Hybridization

Next, we tested whether pre-hybridization of Strands 1, 2 and 3 with either 12- or 15-nucleobase complementary oligomers could prevent the destruction of $(DNA)_2[Ag_{16}Cl_2]^{8+}$. Details on the hybridization and gel electrophoresis of Strands 1, 2 and 3 are reported in the SI. Figure S3 shows the image of the gel, confirming that hybridization indeed took place. Addition of the hybridized Strands 1, 2 and 3 to $(DNA)_2[Ag_{16}Cl_2]^{8+}$ cluster solution led to a reduced drop of only ~20 to 30%, depending on the sequence (Figure 3 and Figures S4–6). The gel electrophoresis was solely used to confirm the hybridization, but not as a purification method, thus it is likely that a small fraction of non-hybridized strands was still present when the hybridized tails were added to $(DNA)_2[Ag_{16}Cl_2]^{8+}$. This might explain why full protection was not observed, and why the same trend as that in Figure 1 was found for the three strands. Our data indicates also that there is no significant difference between bare overhangs of 3 and 6 nucleotides in the hybridized segments, since very similar responses were recorded (Figure 3). Overall, the hybridization of free DNA appears to be a promising protection strategy.
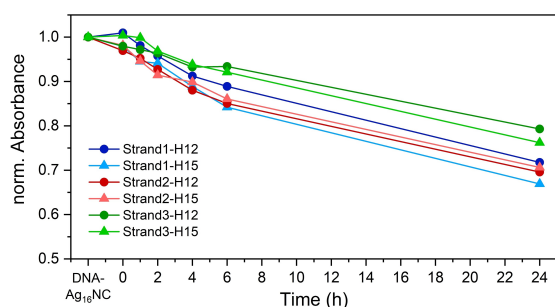
Protection of $(DNA)_2[Ag_{16}Cl_2]^{8+}$ by Silver Cations

Finally, we verified the effect of incubating Strands 1, 2 and 3 with silver ions. Different amounts of $AgNO_3$ were added to the bare oligomers in order to make the silver cations bind to the nucleobases. This approach was previously used for a red-emitting DNA-AgNC, and turned out to be very effective in leaving the cluster intact.[9b] Petty et al. also showed that addition of 8 equivalents of Ag^+ to DNA-AgNC in 10% serum dramatically slowed down their destruction.[12] Addition of an 18-fold amount of silver ions with respect to the DNA concentration of Strands 1, 2 or 3 (which represents one silver per nucleobase) yielded full protection of $(DNA)_2[Ag_{16}Cl_2]^{8+}$. Figure 4 shows that in all three cases, only a 5% drop was observed in the absorption spectra. But this drop is similar for $(DNA)_2[Ag_{16}Cl_2]^{8+}$ alone when dissolved in nuclease-free water (Figure 1). When the concentration was less than one silver per nucleobase, i.e., in the case of 5- and 10-fold $AgNO_3$, the results varied, but a trend could be observed. The lower the amount of silver, the less stable $(DNA)_2[Ag_{16}Cl_2]^{8+}$ was (Figure 4). We note that high binding constants have been previously reported for the interaction of DNA with Ag^+.[13] Similar results were also found when monitoring the fluorescence instead of the absorption (see Figures S7–9). Interestingly, in the case of 10× and 18× $AgNO_3$, the fluorescence increased above the initial value, but one should note that absolute intensity measurements are more prone to deviations than the ratiometric absorption measurements, and given the small effect we refrain from drawing any conclusions at this point. Our results indicate

Figure 3. Absorption values at 525 nm over a period of 24 hours for $(DNA)_2[Ag_{16}Cl_2]^{8+}$ incubated with pre-hybridized Strands. The absorbance was normalized to the initial value of $(DNA)_2[Ag_{16}Cl_2]^{8+}$ only.
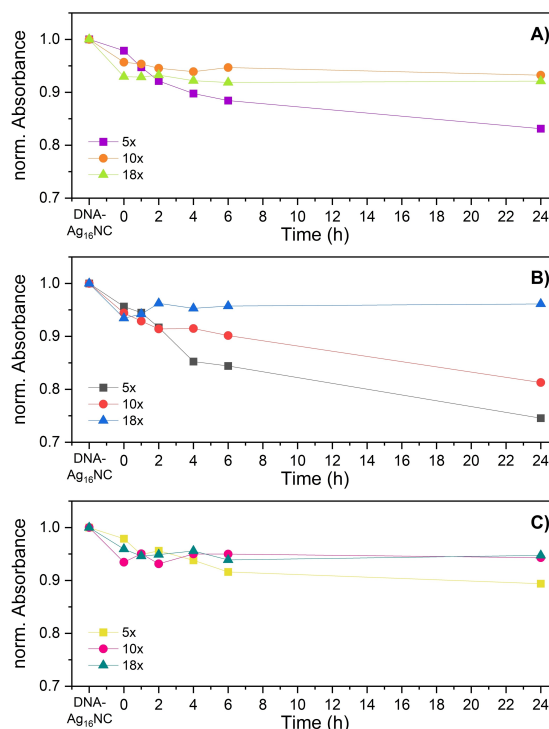
Figure 4. Pre-incubation of Strands 1, 2 and 3 (A-C) with 5-, 10- and 18-fold $AgNO_3$ with respect to the concentration of the Strands. The absorbance was normalized to the initial value of the sole $(DNA)_2[Ag_{16}Cl_2]^{8+}$, and was monitored over time up to 24 hours.

ChemPhotoChem

Research Article
doi.org/10.1002/cptc.202400014

Chemistry Europe
European Chemical
Societies Publishing

that pre-incubation of Strands 1, 2 and 3 with one silver ion per nucleobase seems to passivate the strands and provide full chemical protection for $(DNA)_2[Ag_{16}Cl_2]^{8+}$. While our results indicate that Ag^+ passivates the free DNA stands, Setzler et al. recently reported that addition of extra Ag^+ and H_2 gas can restore oxidized AgNCs.[14]

Conclusions

Our case study using the well-characterized $(DNA)_2[Ag_{16}Cl_2]^{8+}$ cluster shows that free DNA strands can have a detrimental impact on the chemical stability of DNA-AgNCs. Different levels of destruction were observed among the three sequences, indicating that the destruction is sequence-dependent and there might be less- or non-reactive motifs. Our study can thus become an easy-to-implement screening platform to discover inert DNA sequences. Additionally, we presented two protection approaches. Our data proved that hybridized DNA strands are far less reactive and the observed limited reactivity may have been from free non-hybridized DNA strands. Lastly, passivation of bare DNA segments with silver cations seems the best strategy to prevent the destruction of DNA-AgNCs. While very effective, it might also hinder the possibility of Watson-Crick base pairing, which is usually the purpose of hybridization tails.

Supporting Information

The authors have cited an additional reference within the Supporting Information.[15]

Conflict of Interests

The authors declare no conflict of interest.

Data Availability Statement

The data that support the findings of this study are available in the supplementary material of this article.

[1] a) A. Gonzàlez-Rosell, C. Cerretani, P. Mastracco, T. Vosch, S. M. Copp, *Nanoscale Adv.* **2021**, *3*, 1230–1260; b) D. Schultz, E. G. Gwinn, *Chem. Commun.* **2012**, *48*, 5748–5750.

[2] S. M. Copp, D. Schultz, S. Swasey, J. Pavlovich, M. Debord, A. Chiu, K. Olsson, E. Gwinn, *J. Phys. Chem. Lett.* **2014**, *5*, 959–963.

[3] C. M. Ritchie, K. R. Johnsen, J. R. Kiser, Y. Antoku, R. M. Dickson, J. T. Petty, *J. Phys. Chem. C* **2007**, *111*, 175–181.

[4] a) H.-C. Yeh, J. Sharma, J. J. Han, J. S. Martinez, J. H. Werner, *Nano Lett.* **2010**, *10*, 3106–3110; b) P. Shah, A. Rørvig-Lund, S. B. Chaabane, P. W. Thulstrup, H. G. Kjaergaard, E. Fron, J. Hofkens, S. W. Yang, T. Vosch, *ACS Nano* **2012**, *6*, 8803–8814; c) J. T. Petty, S. P. Story, S. Juarez, S. S. Votto, A. G. Herbst, N. N. Degtyareva, B. Sengupta, *Anal. Chem.* **2012**, *84*, 356–364.

[5] a) Q. Sun, X. Xie, Y. Song, L. Sun, *Biomaterials* **2022**, *26*, 9; b) A. Ono, S. Cao, H. Togashi, M. Tashiro, T. Fujimoto, T. Machinami, S. Oda, Y. Miyake, I. Okamoto, Y. Tanaka, *Chem. Commun.* **2008**, 4825–4827; c) J. Kondo, Y. Tada, T. Dairaku, Y. Hattori, H. Saneyoshi, A. Ono, Y. Tanaka, *Nat. Chem.* **2017**, *9*, 956–960; d) S. M. Swasey, E. G. Gwinn, *New J. Phys.* **2016**, *18*, 045008; e) J. Müller, *Coord. Chem. Rev.* **2019**, *393*, 37–47.

[6] V. Rück, N. K. Mishra, K. K. Sørensen, M. B. Liisberg, A. B. Sloth, C. Cerretani, C. B. Mollerup, A. Kjaer, C. Lou, K. J. Jensen, T. Vosch, *J. Am. Chem. Soc.* **2023**, *145*, 16771–16777.

[7] M. Gambucci, G. Zampini, G. Quaglia, T. Vosch, L. Latterini, *ChemPhotoChem* **2021**, *5*, 369–375.

[8] A. Gonzàlez-Rosell, S. Malola, R. Guha, N. R. Arevalos, M. F. Matus, M. E. Goulet, E. Haapaniemi, B. B. Katz, T. Vosch, J. Kondo, H. Häkkinen, S. M. Copp, *J. Am. Chem. Soc.* **2023**, *145*, 10721–10729.

[9] a) R. Guha, M. Rafik, A. Gonzàlez-Rosell, S. M. Copp, *Chem. Commun.* **2023**, *59*, 10488–10491; b) M. Gambucci, C. Cerretani, L. Latterini, T. Vosch, *Methods Appl. Fluoresc.* **2020**, *8*, 014005.

[10] a) D. Schultz, S. M. Copp, N. Markešević, K. Gardner, S. S. R. Oemrawsingh, D. Bouwmeester, E. Gwinn, *ACS Nano* **2013**, *7*, 9798–9807; b) S. M. Copp, D. E. Schultz, S. Swasey, E. G. Gwinn, *ACS Nano* **2015**, *9*, 2303–2310.

[11] a) Y.-A. Kuo, C. Jung, Y.-A. Chen, H.-C. Kuo, O. S. Zhao, T. D. Nguyen, J. R. Rybarski, S. Hong, Y.-I. Chen, D. C. Wylie, J. A. Hawkins, J. N. Walker, S. W. J. Shields, J. S. Brodbelt, J. T. Petty, I. J. Finkelstein, H.-C. Yeh, *Adv. Mater.* **2022**, *34*, 2204957; b) P. R. O'Neill, K. Young, D. Schiffels, D. K. Fygenson, *Nano Lett.* **2012**, *12*, 5464–5469; c) H.-C. Yeh, J. Sharma, I.-M. Shih, D. M. Vu, J. S. Martinez, J. H. Werner, *J. Am. Chem. Soc.* **2012**, *134*, 11550–11558; d) P. Shah, R. Nagda, I. L. Jung, Y. J. Bhang, S.-W. Jeon, C. S. Lee, C. Do, K. Nam, Y. M. Kim, S. Park, Y. H. Roh, P. W. Thulstrup, M. J. Bjerrum, T.-H. Kim, S. W. Yang, *ACS Nano* **2020**, *14*, 8697–8706.

[12] J. T. Petty, B. Sengupta, S. P. Story, N. N. Degtyareva, *Anal. Chem.* **2011**, *83*, 5957–5964.

[13] a) J. T. Petty, O. O. Sergev, A. G. Kantor, I. J. Rankine, M. Ganguly, F. D. David, S. K. Wheeler, J. F. Wheeler, *Anal. Chem.* **2015**, *87*, 5302–5309; b) H. Torigoe, I. Okamoto, T. Dairaku, Y. Tanaka, A. Ono, T. Kozasa, *Biochimie* **2012**, *94*, 2431–2440.

[14] C. J. Setzler, C. A. Arrington, D. Lewis, J. T. Petty, *J. Phys. Chem. B* **2023**, *127*, 10851–10860.

[15] S. A. Bogh, M. R. Carro-Temboury, C. Cerretani, S. M. Swasey, S. M. Copp, E. G. Gwinn, T. Vosch, *Methods Appl. Fluoresc.* **2018**, *6*, 024004.

RESEARCH ARTICLE

The presence of bare DNA oligomers adversely affects the chemical stability of the $(DNA)_2[Ag_{16}Cl_2]^{8+}$ nanocluster which is important for biological applications. To keep the DNA-stabilized Ag nanocluster intact, two protection strategies are implemented: hybridization of the DNA strands with the corresponding complementary sequences, and passivation of the DNA oligomers with silver cations." change to "The presence of bare DNA oligomers adversely affects the chemical stability of the $(DNA)_2[Ag_{16}Cl_2]^{8+}$ nanocluster, which is important for biological applications. To keep the DNA-stabilized silver nanocluster intact, two protection strategies are implemented: hybridization of the DNA strands with the corresponding complementary sequences, and passivation of the DNA oligomers with silver cations.

You are mine!
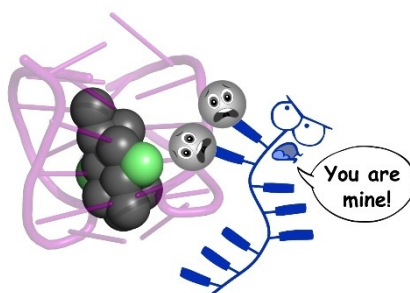
V. Rück, C. Cerretani, T. Vosch*

1 – 5

How Inert is Single-Stranded DNA Towards DNA-Stabilized Silver Nanoclusters? A Case Study

Supporting Information

How Inert is Single-Stranded DNA Towards DNA-Stabilized Silver Nanoclusters? A Case Study.

Vanessa Rück,[a] Cecilia Cerretani,[a] Tom Vosch*[a]

[a] Department of Chemistry and Nanoscience Center
     University of Copenhagen
     Universitetsparken 5, 2100 Copenhagen, Denmark.
     E-mail: tom@chem.ku.dk

Materials and Methods

1 Synthesis and HPLC purification of $(DNA)_2[Ag_{16}Cl_2]^{8+}$

The one-pot synthesis and HPLC purification were carried out as previously reported.[1]

Hydrated DNA oligonucleotide (Integrated DNA Technologies) with the sequence 5'-CACCTAGCGA-3' was mixed with $AgNO_3$ (Sigma Aldrich, ≥ 99.998%) in 10 mM ammonium acetate aqueous solution (NH_4OAc, Sigma Aldrich, ≥ 98%) at pH 7. Freshly prepared $NaBH_4$ (Sigma Aldrich, ≥ 99.99%) was added to the mixture after 15 min to reduce the silver cations and promote the formation of silver nanoclusters. The optimal ratio between the components was $[DNA]:[AgNO_3]:[NaBH_4]$ = 25 μM: 187.5 μM: 93.75 μM. After synthesis, the sample was stored in the fridge for 3 days before high-performance liquid chromatography (HPLC) purification. In the end, the purified fraction was solvent exchanged to 10 mM NH_4OAc by spin-filtration with a 3 kDa cut-off membrane filter (Amicon Ultracel-3).

HPLC purification was performed using a preparative HPLC system from Agilent Technologies with an Agilent Technologies 1100 Series UV-Vis detector, an Agilent Technologies 1260 Infinity fluorescence detector and a Kinetex C18 column (Phenomenex, 5 μm, 100 Å, 250 × 4.6 mm), equipped with a fraction collector. The mobile phase was a gradient mixture of 35 mM triethylammonium acetate (TEAA) buffer in water (A) and methanol (B). The flow rate was set to 1 mL/min.

In the first 2 min the elution gradient was kept constant at 20% B, then it was linearly increased to 40% B in the next 20 min, and finally in the 22-24 min interval, the gradient was rapidly risen to 95% B. The collection was based on the absorbance at 530 nm. The AgNC emission band was monitored at 730 nm, exciting at 530 nm. The run was followed by 6 min of washing with 95% B to remove any remaining sample from the column. The chromatogram can be found in Reference 1. Absorption spectra before and after purification can be found in Figure S1. The absorption spectra before HPLC shows the presence of multiple side products, including most likely silver nanoparticles.

2 Spectroscopic measurements

2.1 Absorption measurements

Absorption spectra were measured with a Cary 300 UV-Vis spectrophotometer from Agilent Technologies using a deuterium lamp for ultraviolet radiation and a tungsten-halogen lamp for visible and near-infrared (NIR) radiation. All measurements were performed in a single-beam configuration with a "zero/baseline" correction, *i.e.*, measuring the 100%/0% transmittance with air as reference. The corresponding solvent spectra were measured separately and then subtracted from the samples' spectra. The absorbance of the AgNC-related transition was kept below 0.1 to avoid inner filter effects during emission measurements.

2.2 FluoTime300 instrument (PicoQuant)

2.2.1 Steady-state emission measurements

Steady-state fluorescence measurements were performed using a FluoTime300 instrument (PicoQuant). The fluorescence spectra were recorded by exciting the samples with a vertically-polarized 507 nm picosecond-pulsed laser (LDH-PC-510, PicoQuant). All emission spectra have been corrected for the wavelength dependency of the detector.

2.2.2 Time-correlated single photon counting (TCSPC) measurements

Time-resolved fluorescence measurements were carried out on a FluoTime300 instrument (PicoQuant) by exciting with a vertically-polarized 531 nm picosecond-pulsed laser (LDH-D-TA-530B, PicoQuant).

Fluorescence decays were acquired at 740 nm integrating 15-90 s to reach at least 10,000 counts at the maximum. The decay curves were fitted with FluoFit v.4.6 software from PicoQuant, using a bi-exponential reconvolution model including the instrument response function (IRF).

3 Stability tests

3.1 Nuclease-free water *vs* 10 mM NH$_4$OAc

Stability tests of $(DNA)_2[Ag_{16}Cl_2]^{8+}$ in nuclease-free water (Integrated DNA Technologies) and 10 mM NH$_4$OAc were carried out by measuring emission spectra every hour over 24 hours. The excitation light was blocked between measurements, and the sample was kept at 25 °C and stirred. Absorption spectra were also measured before starting the fluorescence measurements and after 24 hours.

3.2 DNA strands, pre-hybridized or pre-incubated strands

Stability tests of $(DNA)_2[Ag_{16}Cl_2]^{8+}$ with bare ssDNA, pre-hybridized strands or pre-incubated oligomers with AgNO$_3$ were performed in nuclease-free water. The final concentration ratio of DNA-AgNC to Strand 1, 2 or 3 was always 2 µM: 4 µM. The concentration of DNA-AgNC was determined from the absorption of the DNA. Absorption, emission spectra and fluorescence decays were recorded over a period of 24 hours (0 h, 1 h, 2 h, 4 h, 6 h and 24 h). The first point of each stability test was the DNA-AgNC alone, followed by the addition of Strands 1-3, hybridized double-stranded DNA (dsDNA) or passivated DNA oligomers with Ag$^+$ cations (0 h). The samples were kept at 25 °C and stirred.

4   Hybridization

4.1   Hybridization

For the hybridization, 200 µM of Strand 1-3 and 200 µM of the corresponding complementary strand, either 12- or 15-bases long, were mixed with 50 mM NaCl in nuclease-free water. The mixtures were heated at 90 °C for 2 min and then cooled down in steps of 10 °C every 5 min until 20 °C were reached. The samples were then kept at a constant temperature of 20 °C for 25 min. The obtained dsDNA solutions were finally used without further purification.

4.2   Gel electrophoresis

Gel electrophoresis was performed with a non-denaturing gel (15%). For a non-denaturing 15% polyacrylamide gel, 2 mL 10x TBE buffer, 7.5 mL 40% acrylamide/bisacrylamide and 7.5 mL Milli-Q water were mixed. Afterwards, 24 µL Tetramethylethylenediamine (TEMED) and 120 µL of freshly prepared 10% (w/v) ammonium persulfate (APS) were added and mixed thoroughly. The acrylamide was poured between the glass plates and a comb was inserted.

A MiniProtean Tetra Cell system from Bio-Rad was used for the gel electrophoresis. The samples were prepared as follows: 5 µL of the DNA samples (2 mM) were mixed with 1 µL TriTrack DNA Loading dye (Thermo Scientific) and 0.5 µL 100x SYBR gold (Thermo Scientific), and then applied on a 15% non-denaturing polyacrylamide gel. The GeneRuler Ultra Low Range DNA Ladder (Thermo Scientific) was used as a reference. The electrophoresis was conducted in 1x TBE buffer at a constant voltage of 100 V for 2 hours. The gel image was taken with a Gel Doc EZ Imager from Bio-Rad.

5   Incubation with AgNO₃

The ssDNA oligomers were incubated with 18-, 10- or 5-fold $AgNO_3$ in order to passivate the strands with silver cations. First, Strand 1, 2 or 3 was incubated with the respective amount of $AgNO_3$ for 30 min at room temperature. The mixture was then added to the DNA-AgNC solution without further purification.

6   References

[1]   S. A. Bogh, M. R. Carro-Temboury, C. Cerretani, S. M. Swasey, S. M. Copp, E. G. Gwinn, T. Vosch, Methods Appl. Fluoresc. 2018, 6, 024004.
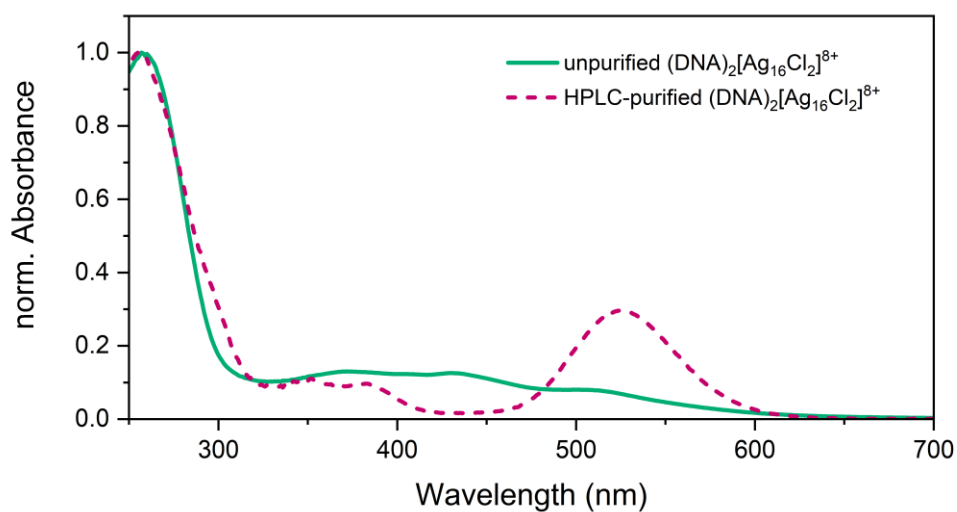
Figure S1. *Normalized absorption spectra of (DNA)$_2$[Ag$_{16}$Cl$_2$]$^{8+}$ before and after HPLC purification in 10 mM NH$_4$OAc at room temperature.*
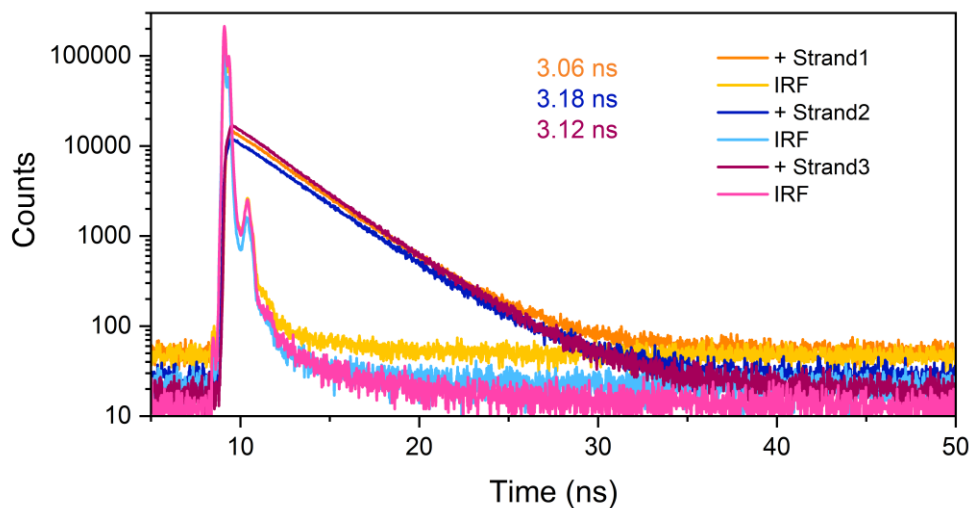
Figure S2. *Fluorescence decays of (DNA)$_2$[Ag$_{16}$Cl$_2$]$^{8+}$ mixed with Strand 1 (orange), Strand 2 (dark blue) or Strand 3 (dark pink) in nuclease-free water after 24 hours. The traces were recorded at 740 nm, exciting at 531 nm. The intensity-weighted average decay times are reported with the same color as the fluorescence traces they correspond to. The intensity-weighted average decay time of the sole (DNA)$_2$[Ag$_{16}$Cl$_2$]$^{8+}$ in 10 mM NH$_4$OAc at 25 °C is 3.26 ns.[1]*
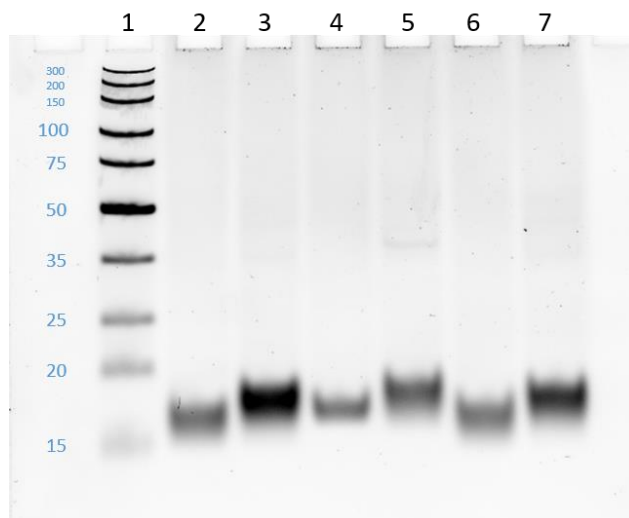
Figure S3. _15% non-denaturing polyacrylamide gel of hybridized strands stained with SYBR gold after 2 hours at 100 V._ **Lane 1** _DNA Ladder;_ **Lane 2** _Strand2 + Strand2-comp12;_ **Lane 3** _Strand2 + Strand2-comp15;_ **Lane 4** _Strand3 + Strand3-comp12;_ **Lane 5** _Strand3 + Strand3-comp15;_ **Lane 6** _Strand1+ Strand1-comp12;_ **Lane 7** _Strand1 + Strand1-comp15._
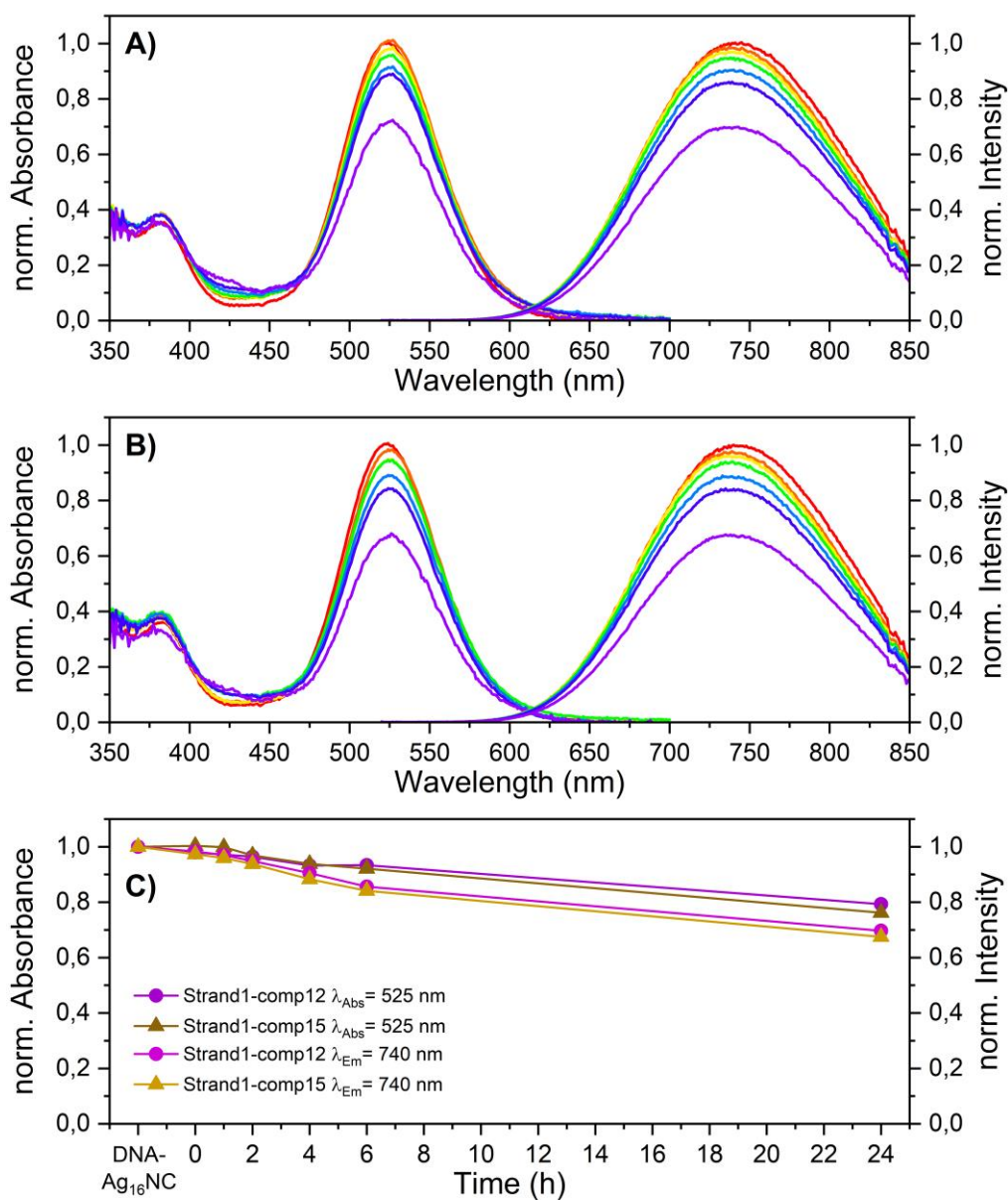
Figure S4. *Normalized absorption and emission spectra of DNA$_2$[Ag$_{16}$Cl$_2$]$^{8+}$ with hybridized Strand1-comp12 (A) and with Strand1-comp15 (B) in nuclease-free H$_2$O at 25 °C. The spectra were monitored over time up to 24 hours. The red color represents the sole DNA-AgNC solution. The other colors indicate the same sample with hybridized Strand1-comp12 or Strand1-comp15 at different time points. Orange indicates the mixture after 0 hours; yellow after 1 hour; green after 2 hours; light blue after 4 hours; dark blue after 6 hours and purple after 24 hours. (C) Absorption and emission maxima as a function of time for A and B, normalized by the values recorded for the DNA$_2$[Ag$_{16}$Cl$_2$]$^{8+}$ only.*
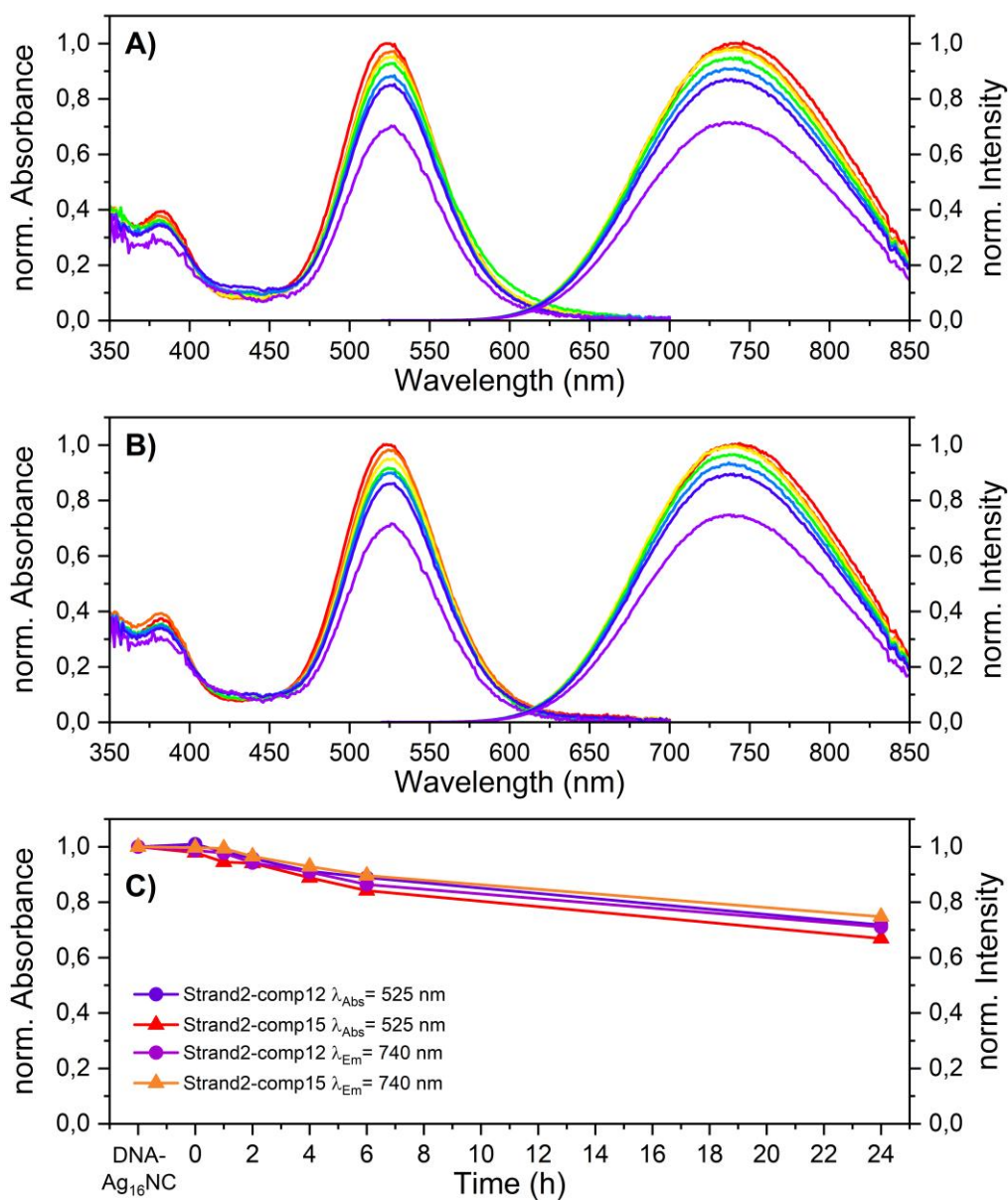
Figure S5. *Normalized absorption and emission spectra of $DNA_2[Ag_{16}Cl_2]^{8+}$ with hybridized Strand2-comp12 (A) and with Strand2-comp15 (B) in nuclease-free H_2O at 25 °C. The spectra were recorded over time up to 24 hours. The red color represents the sole DNA-AgNC solution. The other colors indicate the same sample with hybridized Strand2-comp12 or Strand2-comp15 at different time points. Orange indicates the mixture after 0 hours; yellow after 1 hour; green after 2 hours; light blue after 4 hours; dark blue after 6 hours and purple after 24 hours. (C) Absorption and emission maxima as a function of time for A and B, normalized by the values recorded for the $DNA_2[Ag_{16}Cl_2]^{8+}$ only.*
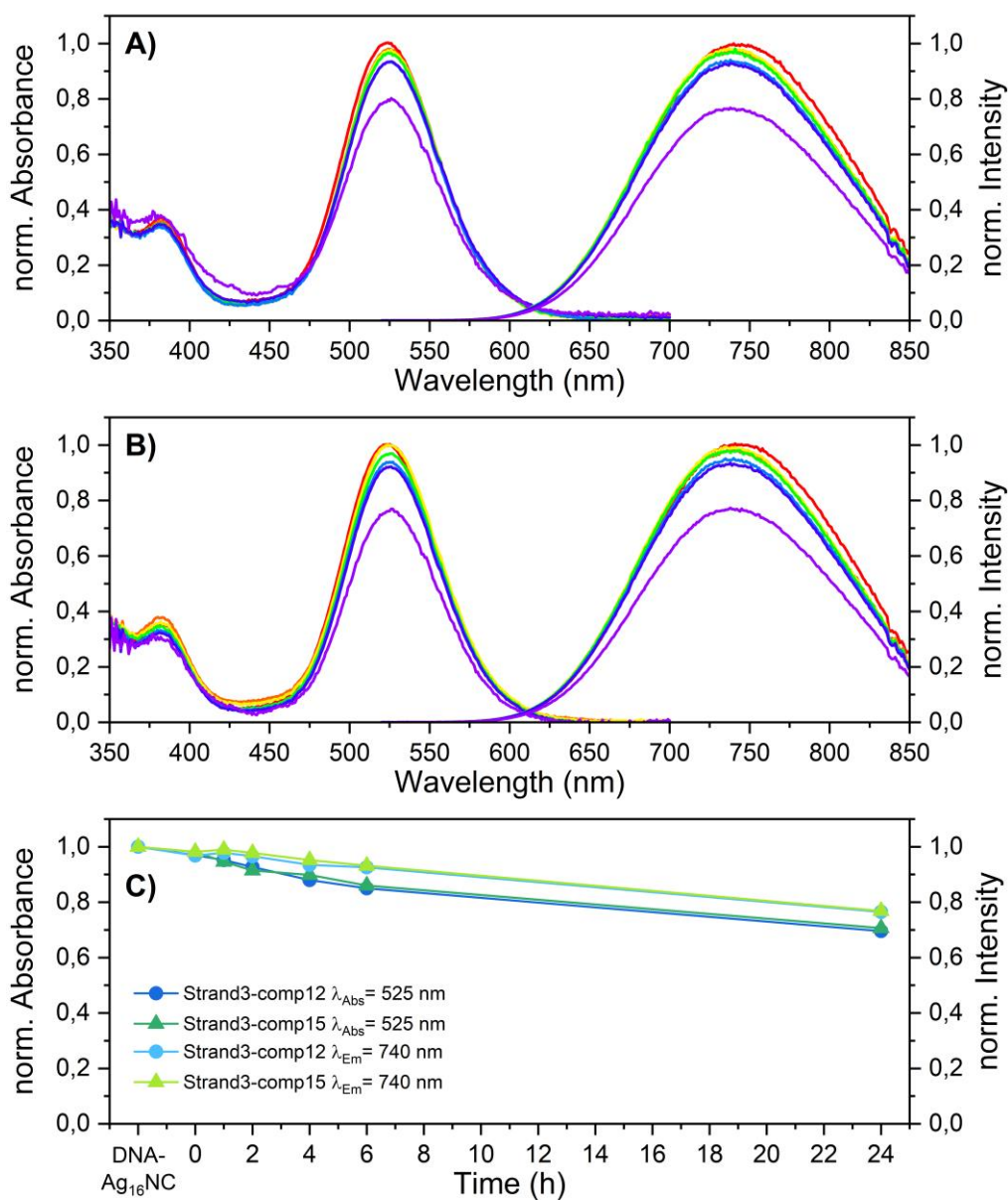
Figure S6. *Normalized absorption and emission spectra of $DNA_2[Ag_{16}Cl_2]^{8+}$ with hybridized Strand3-comp12 (A) and with Strand3-comp15 (B) in nuclease-free H_2O at 25 °C. The spectra were monitored over time up to 24 hours. The red color represents the sole DNA-AgNC solution. The other colors display the same sample with hybridized Strand3-comp12 or Strand3-comp15 at different time points. Orange indicates the mixture after 0 hours; yellow after 1 hour; green after 2 hours; light blue after 4 hours; dark blue after 6 hours and purple after 24 hours. (C) Absorption and emission maxima as a function of time for A and B, normalized by the values recorded for the $DNA_2[Ag_{16}Cl_2]^{8+}$ only.*
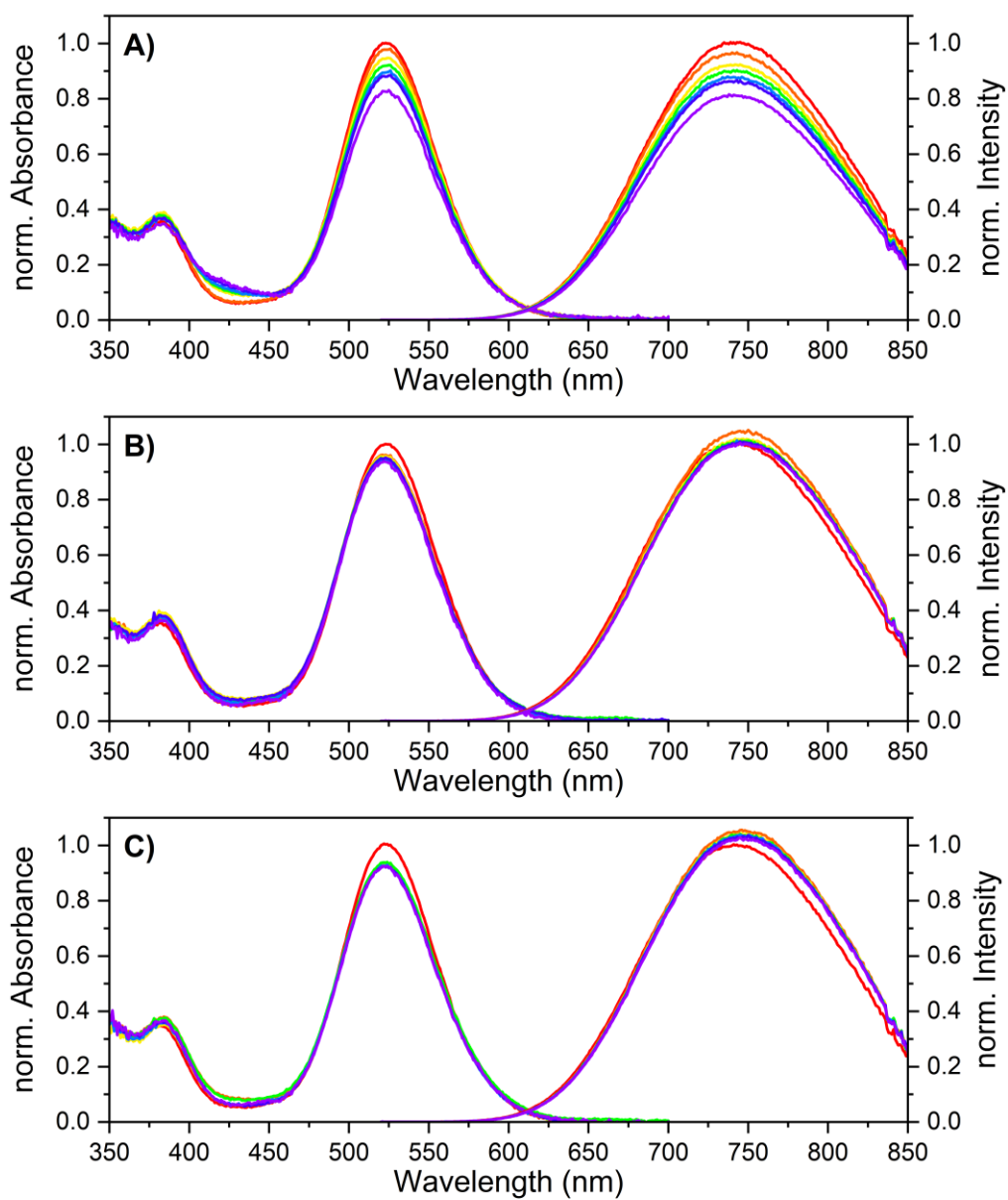
Figure S7. *Normalized absorption and emission spectra of DNA$_2$[Ag$_{16}$Cl$_2$]$^{8+}$ with pre-incubated Strand 1 with 5x (A), 10x (B) and 18x (C) AgNO$_3$ in nuclease-free H$_2$O at 25 °C, monitored over time. The red color represents the sole DNA-AgNC solution, orange indicates the mixture of the DNA-AgNC with the specific Strand1/Ag$^+$ after 0 hours; yellow after 1 hour; green after 2 hours; light blue after 4 hours, dark blue after 6 hours, and purple after 24 hours.*
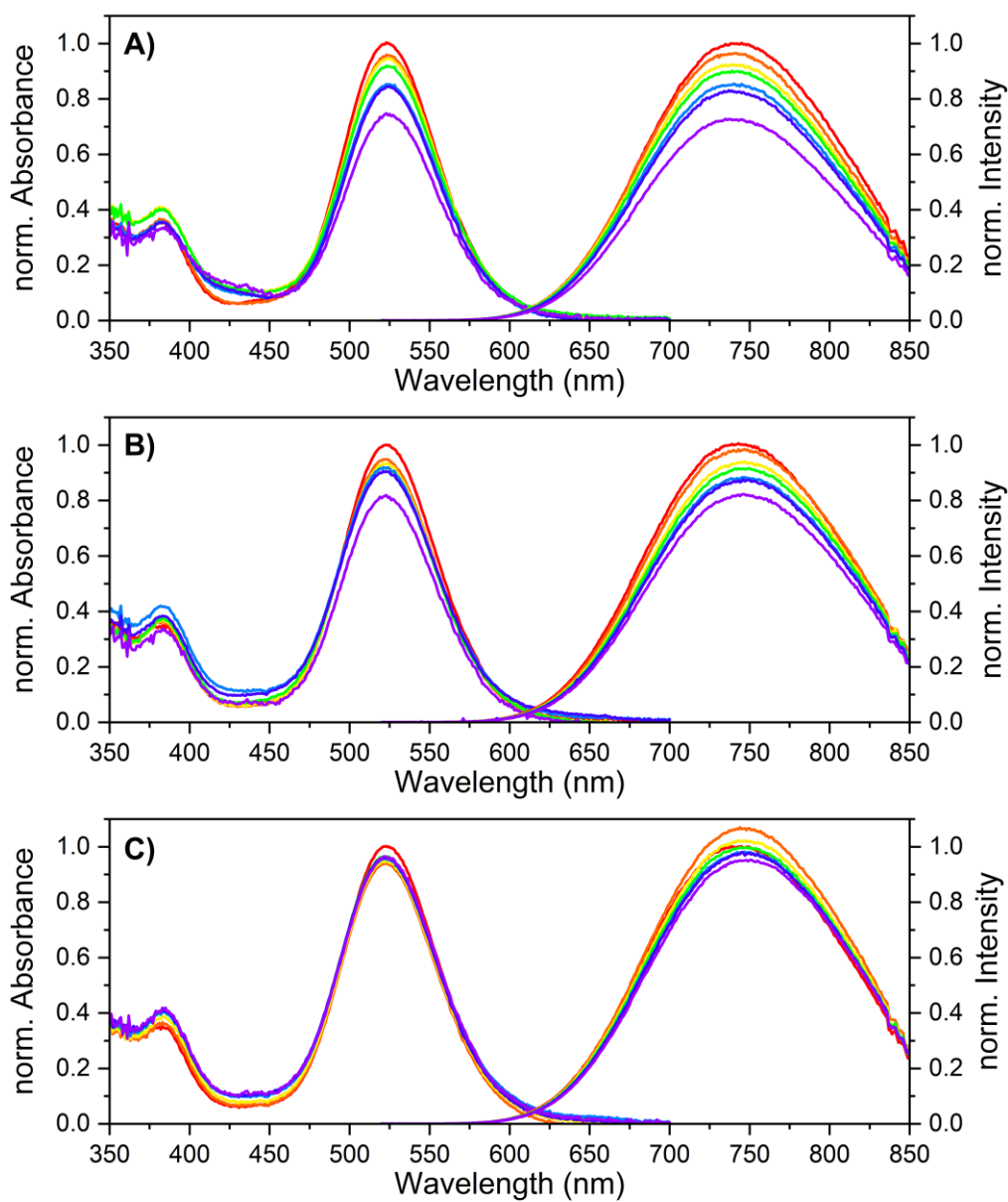
Figure S8. *Normalized absorption and emission spectra of DNA$_2$[Ag$_{16}$Cl$_2$]$^{8+}$ with pre-incubated Strand 2 with 5x (A), 10x (B) and 18x (C) AgNO$_3$ in nuclease-free H$_2$O at 25 °C, monitored over time. The red color represents the sole DNA-AgNC solution, orange indicates the mixture of the DNA-AgNC with the specific Strand2/Ag$^+$ after 0 hours; yellow after 1 hour; green after 2 hours; light blue after 4 hours, dark blue after 6 hours, and purple after 24 hours.*
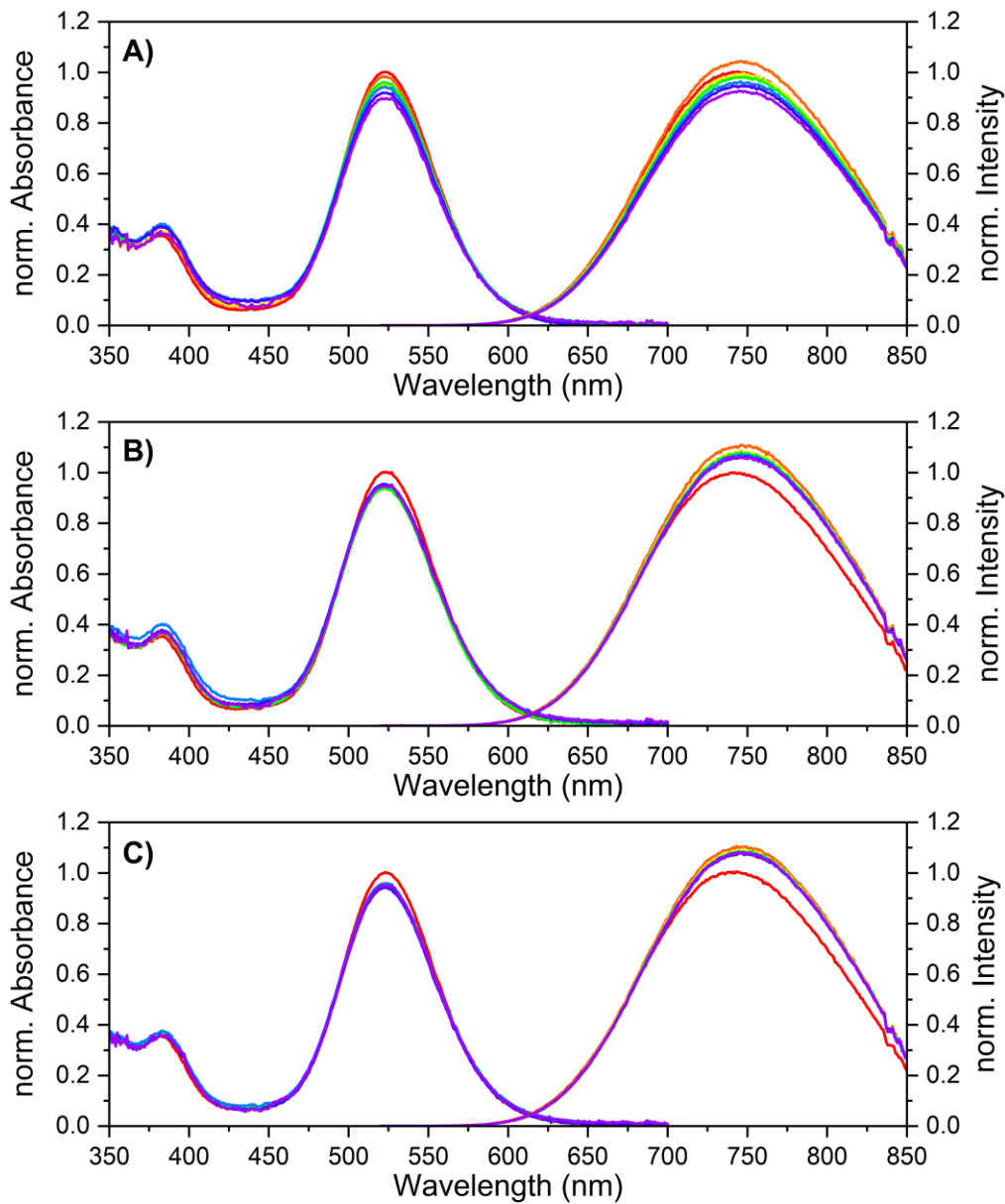
Figure S9. *Normalized absorption and emission spectra of DNA$_2$[Ag$_{16}$Cl$_2$]$^{8+}$ with pre-incubated Strand 3 with 5x (A), 10x (B) and 18x (C) AgNO$_3$ in nuclease-free H$_2$O at 25 °C, monitored over time. The red color represents the sole DNA-AgNC solution, orange indicates the mixture of the DNA-AgNC with the specific Strand3/Ag$^+$ after 0 hours; yellow after 1 hour; green after 2 hours; light blue after 4 hours, dark blue after 6 hours, and purple after 24 hours.*